PHYSICAL AND MATHEMATICAL MODELLING OF THE SYNOVIAL JOINT AND CARTILAGE REPAIR PRODUCTS

by

Anthony G. Herbert BE, MSc

A project submitted in partial fulfilment of the requirements for the degree of

Doctor of Engineering in Medical Devices

2013

DTC in Medical Devices
University of Strathclyde, Glasgow
Glasgow, Scotland

DECLARATION

This thesis is the result of the author's original research. It has been composed by the author and has not been previously submitted for examination which has led to the award of a degree.

Signed:
Date:

ACKNOWLEDGEMENTS

First and foremost, the author wishes to express his sincerest gratitude to Dr. Richard Black for his help, advice and support throughout the duration of this project. A combination of great expertise and always finding time for his students made this project possible. I greatly appreciate it! Secondly, I would also like to offer my thanks to Dr. Phil Riches who provided immeasurable insight and support in the field of tissue mechanics. Again, without your help Phil, I would have been lost. Thank you! In addition, thanks are expressed to Prof's Sean McKee & Stephen Wilson for their help in the mathematical modelling performed.

The author would also like to thank the technical support of the Bioengineering Department. In particular, this is extended to Mr. Davie Robb & Mr. Stevie Murray for their consultation and the construction of all the various test rigs and apparatus described within this thesis. This was always performed at the highest standards of professionalism, whilst still within the atmosphere of wit and Scottish banter I have grown accustomed to. I will miss the chats in the workshop. Gratitude must also be given to Mr. Brian Cartlidge who managed to recover all of my files and data after a computer virus attack. Brian, you saved my bacon!

Throughout my time at Strathclyde, I have been lucky enough to make some great friends, particularly those who shared the 10am coffee breaks with me each morning. Ewan Dougall, Ewan Bennett, John Burns & Dylan Dowd, thanks for the memories. I think we can all agree that many a far reaching issue was discussed at these gatherings. However, we were ultimately unsuccessful in settling on a protocol for the prevention and cure of global warming. I would also like to say cheers to all the guys involved in going for the "spontaneous" curry nights during all the weeks. Never short of good curry and banter.

ABSTRACT

There is a growing incidence of younger patients contracting joint disease. Osteochondral Autograft Transfer (OAT) remains a widely adopted surgical technique to treat the presence of osteochondral lesions in the knee. In this procedure, grafts of cartilage and bone are harvested from a non-load bearing site and used to replace the damaged tissue, predominately at a load bearing location. However, it is not well understood if a mismatch exists between the mechanical properties of the graft tissues and those of the local environment in which they are placed.

To investigate this, a number of the key mechanical properties of cartilage and bone are determined in tibiofemoral and patellorfemoral locations, using a porcine model analogue. These include the strength of the bone but also the aggregate modulus, Poisson's ratio and frictional properties of the cartilage. It was discovered significant variations do exist between the sites of interest for many of these parameters and, should this translate to human models, may have implications for the integration and survival of osteochondral grafts. However, some evidence of relative immaturity in the porcine model was found, which may have had an influence on the results.

Possible alternatives to OAT include tissue engineering, which has gained substantial momentum in clinical settings, and the use of allograft tissues. However, the health and viability of these osteochondral repair products is highly dependent on the environment in which they are developed (tissue engineered tissues) or stored (allograft tissues). The preliminary design and development stages of a novel bioreactor/joint simulator capable of producing physiologically relevant mechanical stimulus are discussed. It is hoped that this device can eventually be employed to grow site-specific osteochondral tissues or store osteochondral allografts in a mechanically beneficial environment.

TABLE OF CONTENTS

LIST OF FIGURES

LIST OF TABLES

1 Background

1.1 The Knee

The knee is arguably one of the most complex joints in the human body and consists of two primary joint structures; the tibiofemoral and patellofemoral joints. It is positioned between the two largest lever arms in the body making it particularly prone to injury (Mow and Hung, 2001). This susceptibility to injury is all the greater if one considers that the knees of average young men and women experience 5400 and 4700 daily loading cycles respectively and more than 10^8 over a lifespan (Neu et al., 2008). Furthermore, peak joint loads in the knee can vary from 1.9 to 7.2 times body weight during any one loading cycle (Komistek et al., 2005).

The knee is located between the two longest bones of the leg; the femur and tibia (figure 1-1). Both the tibiofemoral and patellofemoral joints are synovial joints, consisting of synovial fluid filled capsule that surrounds the articulating bones. At the inferior end of the femur are the femoral condyles. The medial and lateral condyles form the convex elements of the tibiofemoral joint and articulate against the corresponding concave compartments created by the meniscus in the tibial plateau. Between the condyles lies the intercondylar notch which extends superiorly to the patellofemoral (trochlear) groove. It is along this furrowed surface that the patella slides under flexion and extension of the knee (Mow and Hung, 2001).

Covering the articulating surfaces of the bones is approximately 1-2mm of articular (hyaline) cartilage. This light grey, almost translucent material provides an effective, self-lubricating bearing surface to transmit load and motion. Cartilage is not a shock absorber. It is so thin that its capacity to absorb energy is minor in comparison to the eccentric contractions of muscles and the energy absorption in the bones either side of the joint (Martin et al., 1998).

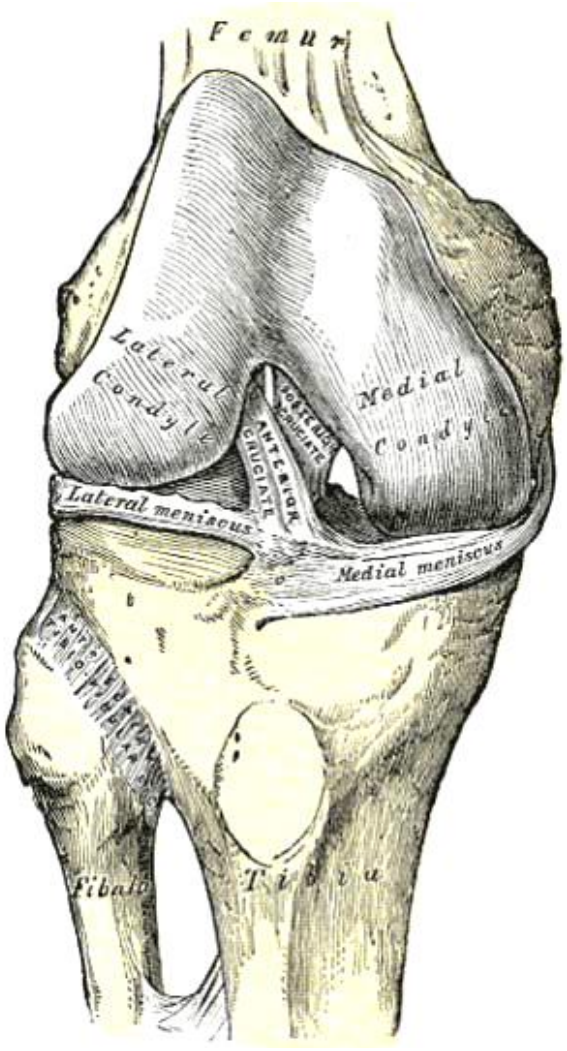

Figure 1-1. Anterior view of the knee with patellar elements, collateral ligaments and joint capsule removed (Gray, 1973).

1.2 Articular Cartilage

1.2.1 Structure

Cartilage is a connective tissue composing primarily of an extracellular matrix (mostly composed of water) and a sparse quantity of cells. The extracellular matrix primarily consists of collagen and proteoglycan (PG) molecules. Cartilage is structurally heterogeneous and is divided into four zones; the superficial, transitional (middle), deep and calcified zones (figure 1-2).

The superficial zone is the thinnest and has itself a surface and deep layer. The surface layer consists of random, flat bundles of collagen fibrils, while the deeper layer consists of dense collagen fibres parallel to the plane of the surface. This zone is structured so as to resist shear stresses. The strength and stiffness of the collagen fibres is greater in parallel with the split lines than perpendicular. The surface layer is crimped, and so not entirely smooth. The deeper layer possesses elongated chondrocytes whose long axis is parallel to the surface. The water content in the superficial zone is approximately 80% which decreases linearly to 65% in the deep zone (Mow and Hung, 2001).

The transitional zone contains collagen fibrils with larger diameters than those located in the superficial zone and are also ordered in a less parallel pattern. The chondrocytes are spherical in shape and randomly dispersed. In the deep zone there are large bundles of collagen running perpendicular to the plane of the surface. Water content is low and chondrocytes are round and stacked perpendicularly on top of one another. The calcified zone marks the transition between soft cartilage tissue and stiff subchondral bone. This zone is separated from the deep zone by a 2-5μm thick border called the tidemark. The collagen fibres in the deep zone anchor the cartilage to the bone by inserting themselves into the subchondral bone (Mow and Hung, 2001).

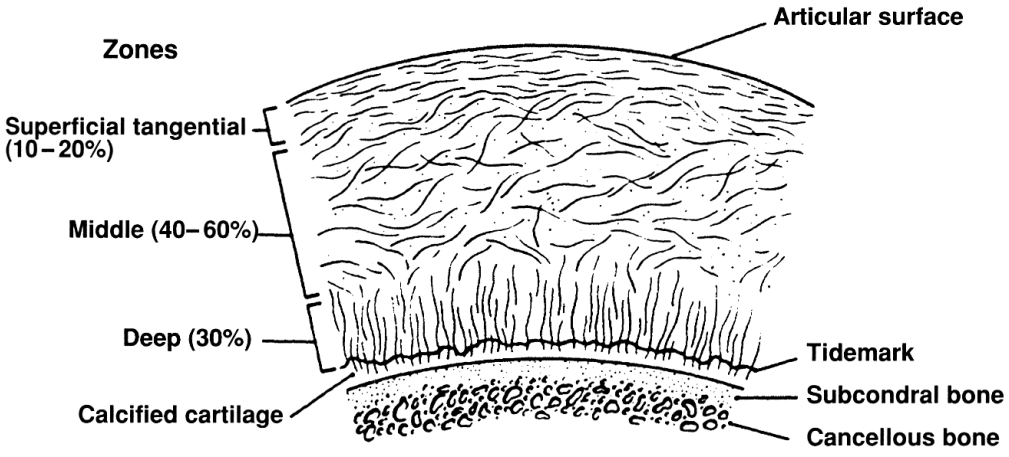

Figure 1-2. Cross-section of articular cartilage revealing the various zones through its depth (Mow et al., 1992).

1.2.2 Cells

The cells of articular cartilage (chondrocytes) account for less than 10% of the tissues volume. They vary in size and density according to location. They are highly metabolically active cells and are responsible for the synthesis and degradation of the matrix. Chondrocytes are isolated, lie in lacunae, and receive their nourishment through the diffusion of substrates through the extracellular matrix. In different cartilages of the body, chondrocytes have different synthetic activities. In articular cartilage, they specialise in producing Type II collagen and proteoglycan which form the majority of the extracellular matrix (Mow and Hung, 2001).

1.2.3 Extracellular Matrix

The structural macromolecules consist of collagen, proteoglycan and other proteins such as glycoproteins and lipids. The collagen in cartilage is similar to the insoluble fibrous protein found in bone, but has a slightly different structure. The basic biological unit of collagen is tropocollagen, a structure composed of three procollagen polypeptide chains, or alpha chains, coiled into left-handed helixes that are further coiled about each other into a right-handed triple helix. Each chain is composed of about a 1000 coiled around

each other to form a spiral. Tropocollagen is rich in glycine, proline, hydroxyproline and hydroxylysine. But the triple helix of cartilage contains three identical alpha chains, whereas bone has two identical and one different. Hyaline cartilage is primarily composed of Type II collagen and is responsible for the tensile strength of the tissue. The inter-molecular and intra-molecular cross-links between collagen fibrils act to add further strength and stability (Mow et al., 1992, Mow and Hung, 2001).

In addition, molecular chains from the glycosaminoglycan and polysaccharide found in proteoglycan play a role. Proteoglycans are a group of glycoproteins formed of subunits of disaccharides linked together and joined to a protein core (figure 1-3). They are found in relatively large proportions in hyaline cartilage. The glycosaminoglycan part of the proteoglycan (95%) contains sugars that are both negatively electrostatically charged and are attracted to water (Mow and Hung, 2001). Due to the large numbers of negative charges, monosaccharides repel one another as much as possible. The resulting structure resembles a "bottle brush". In cartilage proteoglycan, the species of glycosaminoglycans include chondroitin sulphate and keratin sulphate. The linkage between the carbohydrate chain and the protein is most commonly through a trihexoside and a serine residue respectively. A glycosidic bond is formed between the xylose and hydroxyl group of the serine (Champe and Harvey, 1987). The proteoglycan monomers associate with the molecule of the hyaluronic acid to form proteoglycan aggregates. The association is not covalent, but occurs primarily through ionic interactions between the core protein and the hyaluronic acid. The association is stabilised by additional small proteins called link proteins (Mow et al., 1992, Mow and Hung, 2001).

Both collagen II fibres and proteoglycan molecules are interlaced with one another providing additional mechanical strength by forming a complex composite structure (figure 1-4) (Mow et al., 1992). This solid phase has a low permeability which is due to a high frictional resistance to fluid flow. This causes a high interstitial fluid pressurisation in the fluid phase contributing to >90% of the instantaneous load transmission of the tissue. However, this decreases with time as fluid is exuded.

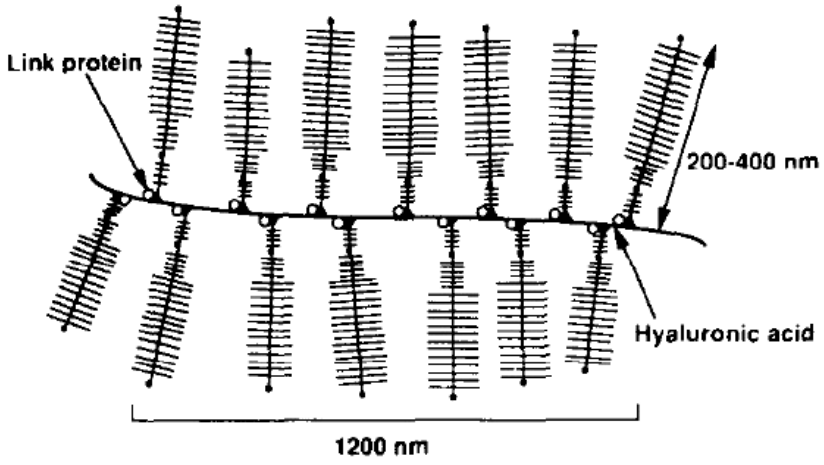

Figure 1-3. Proteoglycan macromolecule (Mow et al., 1992).

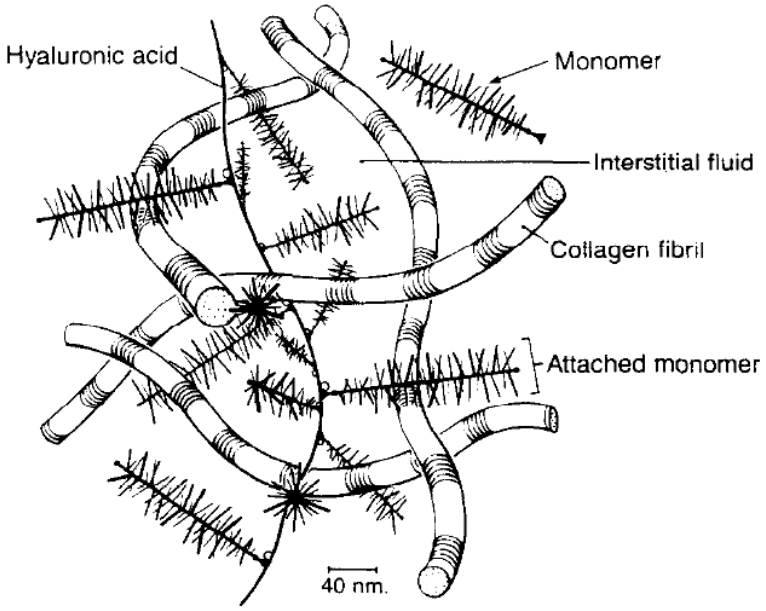

Figure 1-4. Proteoglycan molecules are interweaved with collagen II fibrils to form a porous composite structure (Mow et al., 1992).

1.3 Introduction to Osteochondral Transfer Therapy

Osteochondral transfer therapy, particularly a variation of it known as Osteochondral Autograft Transfer (OAT), is a well-established technique for the repair of both chondral and osteochondral defects in cartilaginous joints, particularly in the knee. The procedure is a relatively simple concept which involves the harvesting of small, cylindrically shaped plugs of healthy cartilage and underlying bone from a relatively non-load bearing site and transplanting them into the site of an osteochondral lesion (Brown et al., 2009, Leitman and Morgan, 2005, Miniaci et al., 2007). This is achieved via a recipient socket prepared at the injured location into which the plugs are press-fitted. OAT is often referred to as mosaicplasty, where in concept multiple cylindrical plugs may be employed to match the natural curvature of cartilage surface at the damaged area, thus maintaining overall joint congruence (Miniaci et al., 2007). These plugs should maintain similar biomechanical properties as intact cartilage and, once healed, produce a durable hyaline cartilage surface (Treme and Miller, 2008).

OAT is performed as a one-step procedure and can be accomplished either open or arthroscopically with little expense. Furthermore, since the graft is autologous, there is no risk of disease transmission or transplant/host incompatibility (Miniaci et al., 2007). The donor sites, should they be left open, will refill with new bone material up to approximately 3mm from the surface and disorganised fibrocartilage scar thereafter (Brown et al., 2009). Alternatively, allograft or synthetic materials may be utilised to fill these voids. However, the OAT process does suffer from a number of limitations, namely: possible donor site morbidity, the limited amount of donor material available, the inability to completely match the topology of the graft to the site of injury, poor integration into the surrounding area, and newly altered tissue mechanics due to the surgery. Other variations of osteochondral transfer therapy such as allograft transfer and the tissue engineering of replacement cartilage constructs may help to overcome some of these difficulties, but often at the cost of introducing additional inherent problems. As a

result, no gold standard of treatment exists at present, but for the most part this thesis shall focus on the OAT route of treatment.

1.4 Osteochondral Autograft Transfer

1.4.1 Surgical Procedure

Implementing an arthroscopic method, anterolateral and anteromedial ports may be used. Prior to donor harvest, a thorough diagnostic arthroscopy including inspection of the chondral surface and the pathology of meniscal and ligamentous structures is advised (Leitman and Morgan, 2005). The donor sites of choice are either the margin of the lateral femoral condyle or the interchondylar notch (Brown et al., 2009) or possibly the superior margin of the medial chondyle (Miniaci et al., 2007). The margins of the femoral condyles are useful for harvesting convex surfaces suitable for condylar areas, whereas the interchondylar notch provides concave surfaces suitable for reconstruction of sites such as trochlear groove (Miniaci et al., 2007).

Sizing instruments are used to measure the number and size of the plugs that will be required. The knee is manipulated to bring the donor harvest area into view of either the medial or lateral portal (depending on the harvest site selected). Harvesting kits such as OATS (Arthrex) or Acuflex Mosaicplasty (Smith & Nephew) are used as standard. The harvesting chisel tool is placed perpendicularly flush to the donor tissue and impacted to a depth of approximately 15mm. Twisting the instrument 180 degrees dislodges the core, allowing for removal (Leitman and Morgan, 2005). This can be achieved via two abrupt twists of 90 degrees (Brown et al., 2009). The plug is then inspected for obliquity through a window in the harvesting tool. The recipient site is prepared in much the same manner. The knee is manipulated to bring the site to the appropriate portal. A core is creating using a harvester 1mm smaller in diameter than the donor plug, which is impacted once more to a depth of approximately 15mm and twisted (Leitman and Morgan, 2005). However, in the case of larger defects and where more than one graft is required, a drill may be used to create the receiving core. All that remains is the transfer

of the donor plug. A depth stop is implemented on the harvesting tool (containing plug) to limit the passage of the plug into the recipient site. The end of the harvester is placed at the core orifice, and ensuring alignment is correct, a plunger pin is lowered, often by tapping a surgical mallet, until it reaches the depth stop. Upon withdrawal of the harvester, it should be observed that the depth stop succeeded in leaving the plug approximately 1mm proud. Finally an oversized tamp is used to seat the graft flush with the local chondral surface (Brown et al., 2009, Leitman and Morgan, 2005).

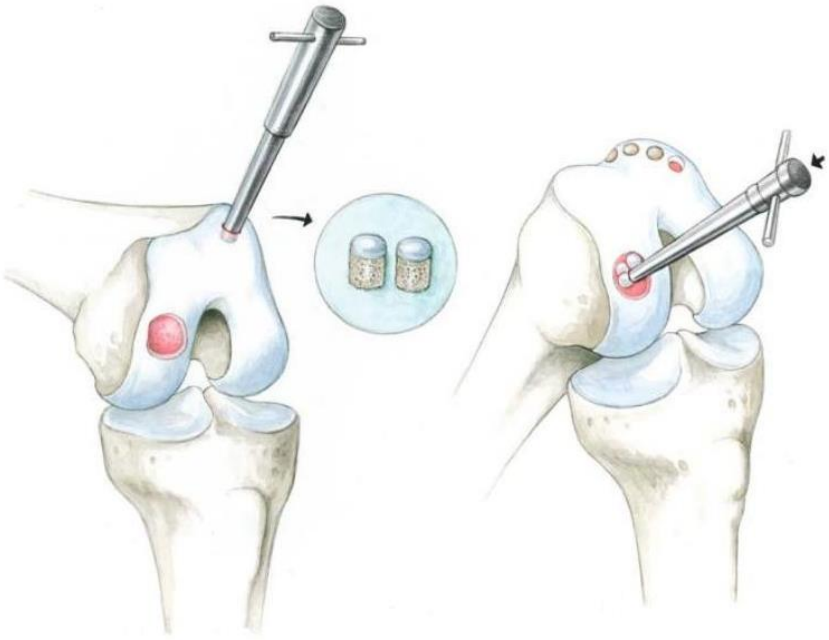

(a) **(b)**

Figure 1-5. Osteochondral autograft transfer (a) the defect site is prepared and osteochondral plugs harvested (from the edge of the lateral condyle in this instance), (b) the plugs are then inserted into the prepared site (Erggelet and Mandelbaum, 2008).

In the surgical procedure care is taken to ensure that the graft is seated both at the distal osseous end and flush at the articular surface. In fact, if the plug is too short then spongiosa taken from the harvest site is used to fill in the core as required and if the plug is too long, the core is shortened a little with a burr (Erggelet and Mandelbaum, 2008).

1.4.2 Fixation of Osteochondral Grafts

Primary to the survival of osteochondral grafts is adequate and correct fixation. Eliminating post-operative micro-motion is imperative in enhancing the overall longevity of the treatment. This is hardly surprising given that poor fixation has often been the cause of failure in joint arthroplasty therapies for some time.

Duchow et al. measured the repeated pull-out strength of porcine osteochondral plugs of different length and diameter by towing a 2mm screw threaded into them (rate 10mm/min) (Duchow et al., 2000). Results followed intuition; the more surface contact area a graft possessed, the more force was necessary to remove it. For a give diameter of 11mm, the failure loads of 10mm long grafts (mean 47N) were significantly lower than those of the 15mm long grafts (mean 93N) and 20mm long grafts (mean 110N). Reinserting the 15mm long grafts and retesting the pull-out strength showed the mean failure load to drop from 93 to 44N on second insertion and from 44 to 32N on third insertion. Abrasion of material on the contacting surfaces of both the plug and receiving site as well as permanent deformation are the most likely explanations for these load reductions. Changing the contact area by altering the diameter showed an increase in the mean failure load from 41 to 92N for two sets of plugs of equal length (15mm) but different diameters (8 & 11mm respectively). Finally, the standard harvesting method of turning the surgical chisel to dislodge the plug was assessed against graft removal by levering the instrument. Levering was found to break the distal ends of the grafts obliquely, reducing the contact area and accordingly the pull-out force was also found to diminish from means of 52 to 32N.

Whiteside et al. assessed sections of porcine femoral condyles for pull-out and push-in strength both on the day of graft insertion and after a week in tissue culture (Whiteside et al., 2003). It was postulated that this model could be representative of a patient's knee directly after surgery and after a week of boney in-growth. Graft plugs of 6.4mm diameter, 12mm length were fitted to drill-hole channels of 6.4mm diameter. Push-in

and push-out strengths were defined as the load to initiate slippage and translation of the grafts in each case. A schematic of the porcine sections with pull-out, push-in methods used is displayed in figure 1-6.

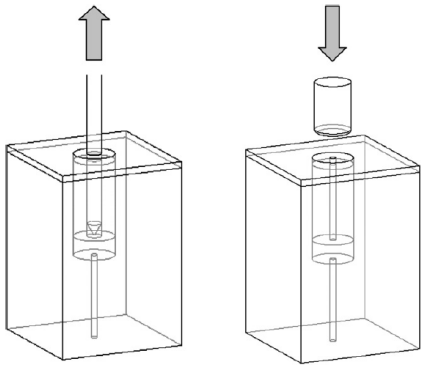

Figure 1-6. Sections of porcine femoral condyle with pull-out and push-in of osetochondral plugs (Whiteside et al., 2003).

Mean pull-out strengths decreased from approximately 120N to just under 90N, whereas mean push-in strengths decreased from approximately 150N to 80N. Furthermore, the elastic modulus of the subchondral bone was determined using an indentor before and after culture, but no significant difference was found to occur. It was concluded that the results demonstrated a substantial deterioration in such grafts in the immediate post-operative period which could be a threat to congruency and newly formed blood vessels. This may be overcome however, as it has been demonstrated that the bottoming of osteochondral grafts can lead to improved adherence (Kock et al., 2006, Kordas et al., 2005) and the use of bioresorbable bone cement has also been shown to boost graft fixation (Changoor et al., 2006).

Using the Acuflex mosaicplasty system, Kordas et al. inserted 15mm long plugs into drill-holes of varying depth in porcine femoral condyles (Kordas et al., 2005). Push-in forces were recorded from a 7mm proud position, to flush, and then to 3mm below the articular surface. The mean forces for pushing grafts flush were 36.58, 43.33 & 118.13N for drill holes of 20, 15 & 12mm in height respectively. There was no significant

difference between the 20 & 15mm drill-hole groups; the little difference that does occur is most likely due to the end of the plug contacting the end of the receiving hole and bottoming out. However, contact of the osseous end alone occurs and no compaction. This is not the case with the 12mm drill-hole group. The effort required to compact the plug (end) sufficiently enough to achieve a flush surface is observed in the rise of the mean force to 118.l3N. The mean forces required to push the plugs 3mm deeper were 122.5, 249.33 & 377.25N for the 20, 15 & 12mm holes respectively. Quite a large increase of force (≈36 to 122N) occurs in the 20mm drill-hole cases to drive the plug down further even though bottoming or compaction of bone still does not take place. Additionally, in the 15mm deep holes, a larger degree of force is required to compact the plug the same 3mm that was seen previously in the 12mm drill-hole cases (≈118 to 249N). This demonstrates that a significant effort is required to overcome the static inertia due to friction after the plugs have become stationary, seemingly more so when grafts have already reached the bottom of the hole. Thus, it was suggested that primary stability is better when grafts and drill holes are the same length and, based on the magnitudes of forces recorded, excessive force must be used for shorter holes. Cartilage may be damaged by such overloading, the relevance of which will be discussed in detail at a later stage.

Kock et al. determined the forces required to push osteochondral plugs into defect sites from a position of being 5mm proud, to flush, and then to 2mm below flush (rate 0.5mm/s) (Kock et al., 2006). This was performed for two variations of defect site in cadaveric femoral condyles. One variation was cored to the exact correct depth for a perfect osteochondral fit, whereas the other was 5mm deeper than required. This was to simulate what is referred to as “bottomed” and “unbottomed” plugs. Additionally, various lengths of osteochondral plugs were employed (8, 12, & 16mm), but the same diameter (6mm) was used in all cases.

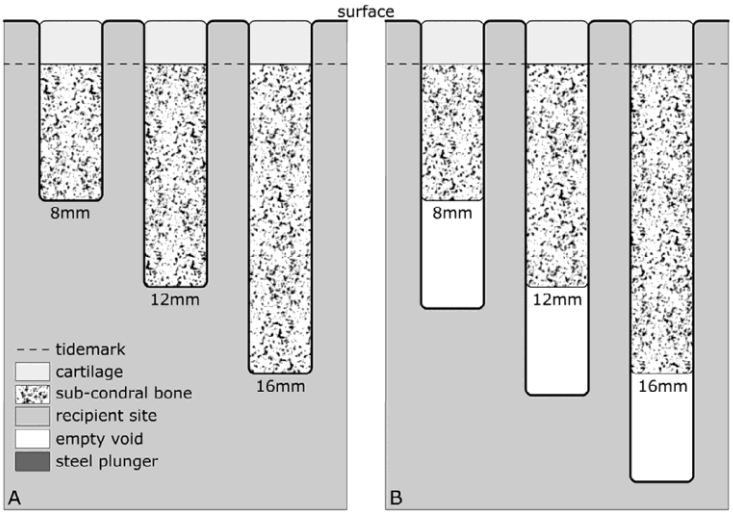

Figure 1-7. (a) 3 "bottomed plugs" of length 8, 12 &16mm, (b) 3 "unbottomed plugs" of same lengths mentioned in (a) (Kock et al., 2006).

Not surprisingly, no significance differences were recorded in the amount of force required to displace the plugs to a flush level for both "bottomed" and "unbottomed" cases (means of 143, 150 & 138N for 8, 12 & 16mm lengths respectively). In "unbottomed" cases, more force was required to cause displacement below the surface for the 12mm plugs than the 8mm plugs (means 171 vs. 123N). This is presumably due to larger surface contact areas and frictional resistance that are present as a result of the additional length. However, the force required to displace the 16mm long plugs below the surface was less than the 12mm plugs (151 vs. 171N). This is contrary to the surface area argument, but perhaps more abrasion occurs when longer plugs are fitted, meaning a loss of contact resistance occurs. In the "bottomed" cases, it was generally observed that more force was required to displace shorter plugs below the chondral surface (means of 528, 384 & 294N for 8, 12 & 16mm lengths respectively). It was thus concluded that short "bottomed" plugs would perform best in a clinical setting.

It is clear that when the "bottomed" plugs were displaced below the surface, the distal osseous ends became compacted. Since the same displacement of 2mm was used in all cases, the shorter the plug, the larger the compressive strain it encountered and the more compact the bone would become at the distal ends. Thus, it is not surprising that the

shorter plugs required more force for insertion. Such compaction is not prescribed for surgery, nor is it imaginable that it could occur naturally postoperatively. It has already been shown that often compaction leads to excessive forces of the grafts (Kordas et al., 2005). Hence, the general consensus is to bottom-out grafts at the osseous end whilst maintaining articular congruence at the opposing end.

Perhaps another route towards this goal is the use of cement in the fixation process. In this manner, grafts could be implanted without the need for impaction, much like the stems of cemented hip prostheses. Changoor et al. used an resorbable calcium sulphate cement (MIIG X3) to anchor grafts in various configurations in 20mm diameter defects and measured the push-out strength of 6mm sections with an indentor (Changoor et al., 2006). The configurations consisted of 5 distinct groups; (A) 12x4.5mm diameter grafts, (B) 5x6.5mm diameter grafts, (C) a combination of 4x4.5mm & 4x6.5mm diameter grafts, cement alone and finally intact bone. Interface failure was defined as the load and corresponding stress at the 1% offset strain point. Interface failure stresses were then found by dividing this load by the contacting area of the grafts. These results are presented in figure 1-8.

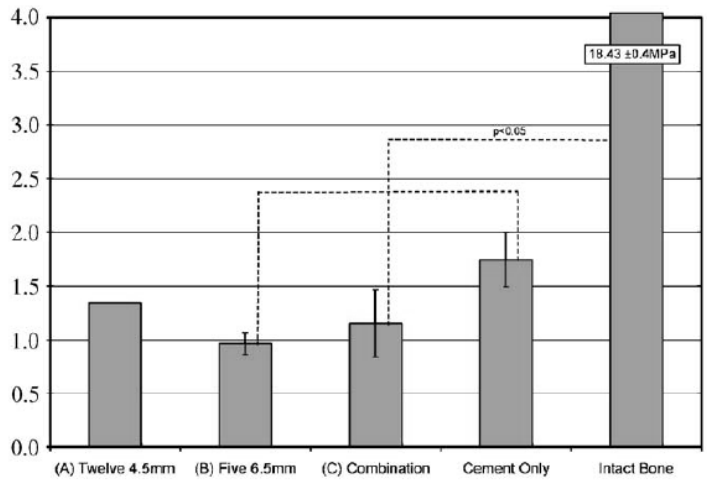

Figure 1-8. Interface falure stresses for groups (A), (B), & (C), cement only and intact bone (Changoor et al., 2006).

The construct to host interface failure stresses were measured at approximately 1.4, 1, 1.15, 1.75, & 18.5MPa for groups (A), (B), (C), with cement only and with the intact bone respectively. This work can be readily compared to the push-in experiments documented by Whiteside et al. (Whiteside et al., 2003). The reader is asked to recall that a failure load of 150N was required to cause translation of a 6.4 diameter, 12mm long graft. This corresponds to an interface failure stress of 0.62MPa. All configurations of osteochondral plug with bone cement are almost twice as high as this, clearly indicating a marked increase in graft stability. However, in a clinical setting it is unlikely that configuration (A) would be adopted due to the amount of material needed. Nevertheless, performing mosaicplasty with the added aid of such bone cement may offer rewards. It has been shown that the cement can serve as a temporary scaffold into which bone incorporation occurs at approximately 8 weeks (Kelly and Wilkins, 2004). However, it is doubtful that implant micromotion of the implanted osteochondral grafts may be controlled whilst osteointegration is concurrently achieved.

1.4.3 Influence of Surgical Preparation

1.4.3.1 The Effects of Impact Loading

Whiteside et al. examined the effect of impacting the articular surface during graft delivery on chondrocyte death (Whiteside et al., 2005). It was proposed that significant death of chondrocytes occurs within the articular surface of osteochondral grafts during the process of implantation itself. To test this hypothesis, two different experiments were designed; (1) measuring the effects of large single impact load and (2) measuring the effects of smaller multiple impacts to deliver a graft. In order to achieve this, a custom-made instrument with known mass was built and fitted with accelerometers to deliver 4.5mm diameter osteochondral plugs. It was discovered that for single impact loading a logarithmic relationship emerged between the applied impact energy and the depth to which chondrocyte death occurs below the articular surface (figure 1-9).

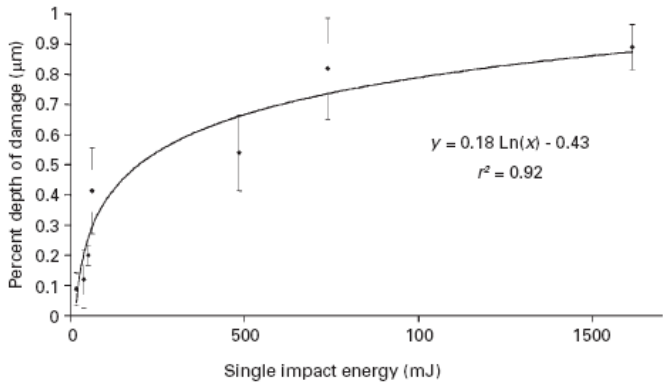

Figure 1-9. The relationship between impact energy & the percentage depth of chondrocyte death (Whiteside et al., 2005).

Given the previous discussion on the fixation of osteochondral plugs and the forces required to push or pull them, it may be of use to view the forces and stresses imparted onto the grafts in this study. The corresponding peak forces and stress for each of the impact energy levels applied in the study are displayed in table 1-1.

Table 1-1. The corresponding peak forces and stresses for each applied impact energy (Whiteside et al., 2005).

Impact energy (mJ)	Peak impact force (N)	Peak impact stress (MPa)
15	84.04	5.29
37	210.11	13.21
49	280.14	17.62
61	350.18	22.02
484	763.30	48.02
739	942.90	59.32
1615	1309.09	87.56

When applying multiple impacts to the grafts it was found that the mean force of impact predicted the depth of cell death more so than the number of impacts applied. Hence, insertion using multiple low level impacts is more beneficial than a single large impact delivery to the site of interest. Another interesting discovery was that when plugs bottomed-out, reaction forces were larger than the forces to overcome the press-fit interference (an order of magnitude larger). Hence, it is clear great care must be taken if bottoming of the plugs is desired. Whiteside et al. (Whiteside et al., 2005) suggest that

the recipient hole be deeper to ensure this does not occur, essentially suggesting that plugs be "unbottomed". However, it has already been demonstrated that that fixation in these cases is inferior to "bottomed" plugs. Hence this author suggests the following;

- If plugs must be "unbottomed" then insertion is practiced in combination with resorbable bone cement.
- If "bottoming" is desired, a steady application of force is applied to the grafts rather than impacts, a viscoelastic tip on the plunger could help absorb reaction forces when they occur. Given magnitude of forces describe for the pushing-in of plugs described in the "Fixation of Osteochondral Grafts" section, it possibly may be achieved by a steady hand or screw driven stage.
- The use of bone cement in conjunction with the suggestion for "bottoming" above. Of course, in any of the cases where resorbable bone cement is used, it is essential to ensure that the rate of new bone matrix growth is appropriate to the degree of cement degradation. Cement will also provide a seal around the graft is achieved at all time and prevent contaminant bone resorption by the infiltration of synovial fluid at the boney interfaces.

Pylawka et al. investigated the effect of repeated insertion impact force on cell viability in adult bovine osteochondral plugs (Pylawka et al., 2007). This was examined immediately after insertion and after 48 hours and 7 days in culture. An 8mm OATS (Arthrex) system was employed to harvest the grafts which were then inserted using a tamp (modified to include a 1kN load cell) and a surgical hammer. Grafts were 10mm in length with receiving holes >10mm indicating no bottoming of the plugs occurred. Peak forces were found to increase from mean initial values of 25N (recorded during the initial alignment of the graft) to 307N, before it decreased again towards the end of the insertion matching process. On average 18 taps were necessary for insertion. A typical load profile recorded during insertion is shown in figure 1-10. What is most noticeable about figure 1-10 is the very short duration over which loads and loading is applied.

Typically, load application was found to last <10 milliseconds with peak loading rates measuring up to mean values of 133kN/s.

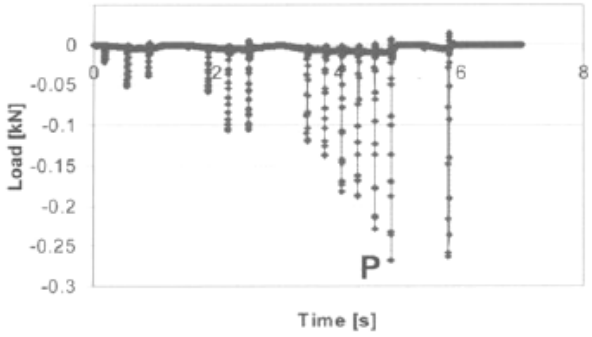

Figure 1-10. Typical load profile recorded for insertion of 8mm diameter osteochondral plug (Pylawka et al., 2007).

This loading on the cartilage surface translated into the measurements of cell viability which was significantly lower for impacted plugs over controls at time zero. Cell death levels were found to be 60% in the superficial zone for all groups at all time points, indicating this is by far the most affected region of the cartilage. Cell viability decreased for both groups at 48 hours and 7 days but differences between the groups were no longer significant. Culture in this case may be used to model *in vivo* changes in cell viability after graft implantation, but the loss of cell viability in culture is an issue of even more concern when dealing with osteochondral allografts. This matter will be discussed in greater detail at a later stage.

Patil et al. measured the effect of varied repeated insertion load on chondrocyte viability and GAG release in osteochondral grafts (Patil et al., 2008). This was achieved using a "drop tower" apparatus where a weight was dropped from different heights in a controlled manner upon an extruder within a harvesting tool to simulate the loads applied from a mallet to a tamp. 5 repeated loads of 200, 400 & 800N were applied and compared to a "sham" control group where grafts were harvested but not loaded

thereafter. Figure 1-11 displays the results of the varying loads on cell viability in the different cartilaginous zones.

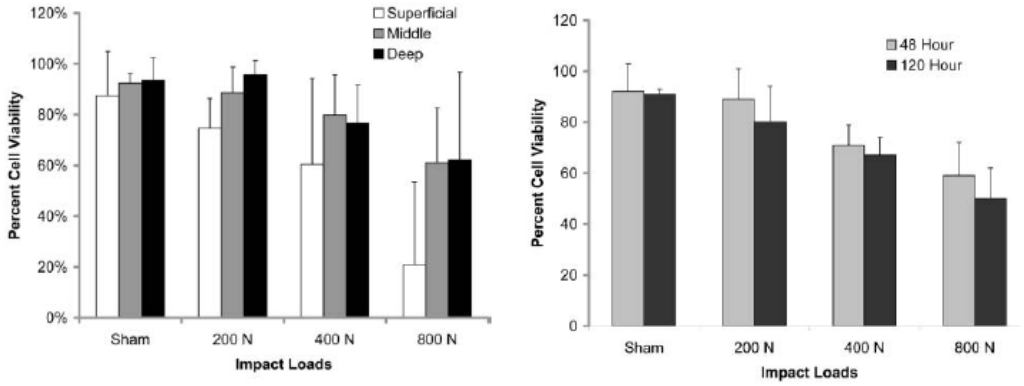

Figure 1-11. Cell viability of (a) chondral zones and (b) overall chondral depth at 48 & 120 hours for varying repeated impacts (Patil et al., 2008).

Cell viability was found to decrease in all zones with increased load but was found to be most affected in the superficial zone for all impact levels which agrees with the work of Pylawka et al. (Pylawka et al., 2007). This was a feature that became more prominent with greater loads and significantly so at 800N. The outcome of these loading scenarios on global chondrocyte viability after 48 & 120 hours in culture was also investigated. Little difference was found between the time periods for a given impact load but as the magnitude of the impacts increased the cell viability decreased linearly to approximately 50% at 800N. Interestingly, when GAG release was measured the reverse was the case, as for the control and for each impact level, significant differences were observed between the 48 & 120 hours, but these GAG levels remained unchanged with increasing load impact.

1.4.3.2 The Effects of Instrument Design

The choice of instrument used in harvesting may also influence the cell viability of the cartilage in osteochondral grafts. Huntley et al. investigated the influence of the

harvesting tool used on cell viability in the peripheral contact margins of osteochondral plugs (Huntley et al., 2005a). Fresh human tissue was obtained from 11 knees at the time of total knee arthroplasty and osteochondral plugs were harvested using a 4.5mm diameter Acuflex (Smith & Nephew) osteotome. A confocal laser scanning microscope was used to acquire images of *in situ* chondrocytes and the mean margins of cell death were calculated using the following expression;

$$d = 1000(r - \sqrt{\{r^2 - (2rA/p)\}}) \qquad \textbf{Equation 1-1}$$

Where;
d is the mean margin cell death (μm),
r is the radius of the graft (mm),
A is the concordant area of cell death (mm^2),
p is the perimeter of the graft (mm).

Substantial marginal cell death was observed in the superficial zone (mean 382μm) with over 99% cell viability seen more centrally. The effects of the osteotome were then compared to incisions using a scalpel blade by splitting the grafts and creating demiplugs. A mean margin of cell death of 390.3μm was discovered at the curved edges compared to a significantly lower value of 34.8μm at the site of the scalpel cut. Similar findings were found when the cartilage alone was incised and the bone left intact.

In a follow-up study by the group it was proposed that cutting-tip of the Acuflex (Smith & Nephew) system was sub-optimal, with injury to cartilage occurring due to compression of the graft edges by an internal bevel within the device (Huntley et al., 2005b). For the purposes of comparison, the group engineered their own harvesting tool without an internal bevel, designated the "Lissimore" osteotome, and quantified the margins of chondrocyte death for grafts harvested by both devices. Schematic sections of both devices are displayed in figure 1-12.

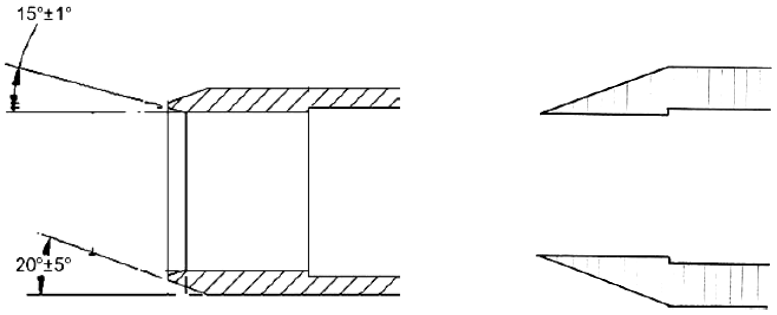

(a) **(b)**

Figure 1-12. Osteotomes used for harvesting grafts, (a) the Acuflex 4.5mm internal diameter osteotome and (b) the "Lissimore" osteotome (Huntley et al., 2005b).

It was discovered that the 4.5mm diameter Acuflex osteotome yielded grafts with a mean margin of cell death of 315.3μm in the superficial zone, whereas the 5mm diameter "Lissimore" osteotome yielded a significantly lower value of 117.8μm. Furthermore, transverse sections of the plugs revealed Acuflex generally caused cell death in all zones, but "Lissimore" tended to exhibit sparing in the mid and deep zones, with significant cell viability in these regions. It was also discovered that after processing the plug diameter of the Acuflex grafts increased by 10.9% compared to an increase of 3.3% in the "Lissimore" system. This may reflect the presence of the internal bevel in the Acuflex tool, which forces more tissue into its core and is re-expanded after removal. In addition, it may be the case that the expansion is due to swelling caused by damage to the cartilage matrix by the bevel. It is most likely that the expansion is caused by a combination of these suggestions.

So far the effects of the surgical process on the osteochondral grafts themselves have been discussed. However, it cannot be forgotten, that the core that receives the plugs requires preparation with surgical instruments also, leading one to believe that chondrocyte damage can occur in this area in much the same way it occurs in the grafts. Vizesi et al. compared the healing response of osteochondral defects created with either a punch or a drill in ovine knees at 4 and 26 weeks after surgery (Vizesi et al., 2007). Time zero radiographs showed there was minimal trauma to the surrounding cartilage

with the punched defect, whereas major deformation was evident with the drilled defect. Intraoperative observations of the punched defects highlighted clearly defined edges with no evidence of obvious scoring. In contrast, drilled defects had a rough appearance around the perimeter. Interestingly, the drilled group had a significantly better histological appearance at 4 weeks. This was attributed to small quantities of hyaline-like cartilage found in the defects which was not found in the punched group at the same time point. However, at 26 weeks the reverse was the case, with the punched group presenting a much greater decline in subchondral bone resorption, bonding of the repair tissue with bridges across the defect and a higher concentration of proteoglycans. Thus, it can be concluded that drilled defects cause a more aggressive inflammatory response consistent with the radiographic images and intraoperative observations of damaged tissue, which in turn leads to spontaneous healing in the short term. In the long term however, punched defects promote a superior and controlled degree of healing.

1.4.3.3 The Effects of Osmolarity

To help limit the damaging influences of the harvesting instrument Amin et al. investigated the choice, and more specifically the osmolarity, of the irrigating fluid used in theatre (Amin et al., 2008). Full chondral explants were retrieved from adult bovine metacarpophalangeal joints and exposed to a varying medium osmolarity (0-480mOsm) for 90 seconds to allow chondrocytes to respond to the altered environment. Using a scalpel, a full thickness articular defect was imparted upon the samples, which were then placed in a solution of the same osmolarity for 2.5 hours before being transferred to a control medium for further incubation for 7 days. Finally, cell death of the samples was assessed at 2.5 hours and 7 days using confocal microscopy, the results of which are displayed in figure 1-13.

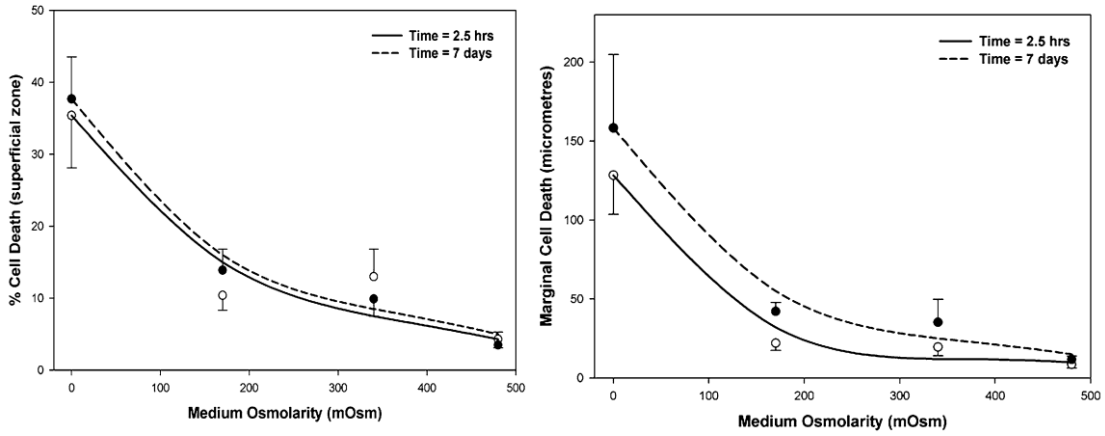

(a) **(b)**

Figure 1-13. Percentage cell death in the superficial zone (a) and marginal cell death (b) as a function of osmolarity and time (Amin et al., 2008).

A very clear decline is observed between 0mOsm (i.e. distilled water) and 480mOsm in both terms of percentage cell death in the superficial zone and marginal cell death around the initial wound. The authors suggest that this decline is due to the reduced swelling of chondrocytes at higher osmolarities. An alteration in medium osmolarity leads to rapid movement of water across the plasma membrane leading to increased cell volume. Thus, at low medium osmolarity, chondrocytes are more likely to be injured by the scalpel cut by virtue of their increased size. Furthermore, there was no significant difference in the values of % cell death and marginal cell death for varying osmolarity at 2.5 hours and 7 days. This implies that the majority of damage occurs within the 2.5 hour period immediately after the scalpel injury.

One final point is that the 0mOsm marginal cell death is consistent with those recorded by Huntley et al. in assessing the "Lissimore" device (Huntley et al., 2005b). This should be the case as the "Lissimore" tool employs a straight cutting edge much like the scalpel used in this study. Hence, it is likely that by using the "Lissimore" instrument in combination with an irrigation fluid of high osmolarity, cell death can be largely prevented promoting a corresponding increase in integration.

1.4.4 Donor site morbidity

Although adequate filling of defects with fibrocartilage scar does occur, the principal disadvantages of OAT are nevertheless still associated with the graft harvesting site (Treme and Miller, 2008). The majority of studies concentrate their efforts on recovery at the site of implantation rather than the site of harvest. However, a limited number focus on the harvest location or indeed both areas in tandem (Al-Shaikh et al., 2002, Hangody and Fules, 2003, Iwasaki et al., 2009, Iwasaki et al., 2007, LaPrade and Botker, 2004, Paul et al., 2009, Reddy et al., 2007).

In a case report spanning 24 months, LaPrade and Botker specifically followed the progress of two patients demonstrating fibrocartilage hypertrophy causing pain and locking of the joint (LaPrade and Botker, 2004). This necessitated abrasion of the overgrowths in both patients and in one case the introduction of allograft plugs to the site.

Using the Lysholm knee scale, Al-Shaikh assessed 19 patients who underwent OAT for treatment of osteochondral lesions of the talus using harvests from the knee (Al-Shaikh et al., 2002). This scale scores a patient out of 100 on the existence of a limp, use of walking aids, locking of the knee, giving way sensation, pain, swelling, and stair climbing and squatting. Excellent scores were reported (mean 97) with only 2 patients suffering from mild knee pain at an average follow-up time of 16 months. It was also discovered that patient age correlated with knee scores, with those below 30 years gaining better results than those above 30 years. In a similar study, Reddy et al. reported an average Lysholm score of 81 in a group of 15 patients with lesions of the talus indicating some loss of function (Reddy et al., 2007). However, more significantly perhaps, no negative effect was observed with regard to the number of plugs harvested in any patient in the group. Using a patient population of 831, Hangody and Fules reported that only slight donor site disturbances existed in 3% of patients within a 10 year period (Hangody and Fules, 2003). Pain at the harvest site was found to be absent

for 95% of the population at 6 weeks and 98% at 1 year. Paul et al. studied the follow-up progression of 112 patients who underwent treatment of talus lesions over a minimum of 2 years (Paul et al., 2009). A mean Lysholm score of 89 was again encouraging. Interestingly unlike Al-Shaikh et al. (Al-Shaikh et al., 2002), no correlation was found to exist between patient age and clinical outcome, but like Reddy et al. (Reddy et al., 2007) neither the size nor the number of plugs harvested affected the recovery score. Furthermore, it was indicated that a higher body mass index had a negative effect on patient scores, with a decrease of one point in the Lysholm score for every point increase in body mass index.

Finally, Iwasaki et al. studied 11 competitive athletes who underwent OAT for osteochondral defects of the elbow joint (Iwasaki et al., 2007). With follow-up periods ranging from 12-65 months, the Lysholm score for the donor knees was 100 in all but one case who scored 96 at 13 months. Additionally, magnetic resonance images reported good defect fill in the majority of cases and all athletes returned to their previous level of competitiveness. In a similar and more recent study by Iwasaki et al., a mean Lysholm score value of 99.6 was recorded over a range of 24-87 months in 19 athletic patients (Iwasaki et al., 2009). However, the patient selection periods would seem to suggest some of the same patients were used in both of this group's studies.

1.4.5 Clinical Results

Excellent to good results have been found to occur in 66-92% of femoral implantation cases depending on the source study used (Treme and Miller, 2008). Wang et al. found similar results in 80% of patients (Wang, 2002), whereas it was 83% of cases with Chow et al. (Chow et al., 2004). The upper value of the quoted range relates to the previously mentioned study performed by Hangody and Fules (Hangody and Fules, 2003). In this review, the authors found excellent to good results in 92% of femoral condyle implantations, 79% of patellar and/or trochlear mosaicplasties and 94% of talar implantations.

1.5 Osteochondral Allografts

Although literature suggests that there are relatively few cases of donor site morbidity, one possible means to avoid such instances is the use of allografts. Furthermore, allografts can provide structurally mature articular cartilage matrix with viable chondrocytes and have no size limitations, thus overcoming the issue of limited autograft harvest material in a patient (Feeley and Williams III, 2009). In many respects, cartilage is an ideal transplantation material as it is avascular, aneural and relatively immunoprivileged by virtue of the chondrocyte fixation within the matrix (Bugbee and Ostempowski, 2006). This gives protection from the host immune surveillance and so allows for chondrocyte survival without tissue matching or immunosuppression (McCulloch et al., 2007). However, the latter comment does not account for the presence of subchondral bone and the medium the tissue is stored in, to which the immunogenicity of these areas will be touched on later.

1.5.1 Storage Effects on Osteochondral Allografts

1.5.1.1 Structural, Mechanical & Biochemical Effects

Besides the procurement of the material and the technically demanding surgery, one of the principle complexities involved is the storage of the transplant material. Traditionally, osteochondral allograft material has been transplanted within 1 week of sourcing, but due to safety concerns involving bacterial contamination and disease transmission, in addition to logistical issues, this may be extended to as much as 40-42 days (Allen et al., 2005, Williams et al., 2003). Although it appears that maintenance of the extracellular matrix is achieved, significant decreases in chondrocyte viability, viable cell density and metabolic activity have been observed within time periods of just 30 days (Allen et al., 2005, Ball et al., 2004, Pearsall et al., 2004, Williams et al., 2003).

Quite a comprehensive analysis was performed on the effects of prolonged allograft storage by Williams, S.K et al. (Williams et al., 2003). This included analysing chondrocyte viability, viable cell density, PG synthesis, GAG content, and the measurement of four different biomechanical properties (indentation stiffness, compressive modulus, permeability & equilibrium tensile modulus) at intervals of 7, 14 & 28 days. Although minor changes occurred, no significance was witnessed in viability and viable cell density until day 28, whereas a significant decline was seen in proteoglycan (PG) synthesis by the reduction in SO_4 uptake at days 14 & 28. No significant changes were observed to occur in GAG content or in any of the four biomechanical properties at any time period.

Ball et al. examined the effects of refrigeration of allografts within a lactated Ringer's solution against a serum-free culture medium (Ball et al., 2004). A significant decline in chondrocyte viability and metabolic activity was seen in the samples stored in Ringer's solution at 7 days. However, baseline levels remained unchanged for up to 14 days in samples stored in the media culture. It was also observed the noted declines occurred in the superficial zone of the cartilage. Since this region is responsible for resisting shear stresses and reducing contact friction, this finding may have particular significance.

After a mean storage period of 34 days, Pearsall et al. measured the ultrastructure and chondrocyte viability of allografts prior to implantation (Pearsall et al., 2004). Measuring by means of flow cytometry, chondrocyte viability was found to be 67%, quite similar to the 70.7% value quoted by Williams, S.K et al. (Williams et al., 2003) after 28 days of storage. Metabolic activity, structural and mechanical properties were not investigated. Another major drawback with this study was that the tissues were stored in fetal bovine serum, which carries the potential risks of disease transmission and immunological issues.

Allen et al. examined 16 allografts which had been stored commercially for a mean time period of 20.3 days up until the time of surgery (Allen et al., 2005). The hypothesis here

was that laboratory storage conditions may vary in comparison to set commercially stored protocol. Confocal microscopy revealed significant reductions in chondrocyte viability and viable cell density and significant decreases in PG synthesis. A viability of 82% was reported at 20.3 days which corresponds well with the decline of viability reported by Williams, S.K et al. between 14 & 28 days (97.5-70.7%) (Williams et al., 2003). Since no significant changes have already been shown to occur in viability before 14 days, it can hence be deduced the majority of cell destruction occurs after 2 weeks. Like Ball et al. (Ball et al., 2004), there was shown to be preferential chondrocyte death in the superficial zone. Additionally, like Williams, S.K et al. (Williams et al., 2003), no affect was observed in the cartilage matrix, as measured by glycosaminoglycan (GAG) content and biomechanically via indentation stiffness.

1.5.1.2 Patient Outcome

It is clear that major cellular and metabolic problems arise when storing these tissues beyond a threshold period of approximately 2 weeks. However, these tissues are nevertheless still implanted into patients, whose clinical outcome now comes into question. A number of studies have reported follow-up postoperative data after allograft transplantation (Davidson et al., 2007, McCulloch et al., 2007, Williams et al., 2007).

McCulloch et al. reported on a minimum of 2 years follow-up assessment of 25 patients who received allograft treatment for defects of the femoral condyles (McCulloch et al., 2007). The age of patients ranged from 17-49 and the graft was transplanted after an average procurement time of 24 days (range, 15-43 days). In all but two of nine functional indexes used, their overall subjective scores showed significant improvements. For example, the Lysholm score was raised from an average of 39 to 67. Although in most cases significantly better, the magnitudes of functional outcome scores in this study do not in themselves seem particularly encouraging. However, it seems the relief of pain is a powerful influence on patient opinion as patients reported 84% overall satisfaction with their results and that the treated knee functioned at an average of 79%

of their unaffected knee. 22 of the patients showed a normal radiographical contour indicating good incorporation with the host, two developed osteoarthritis and one suffered fragmentation of the graft. The study discovered no link between increasing storage time of the grafts and clinical outcome. However, this author believes since all grafts were used after 2 weeks storage, they were collectively all in a process of decline and no definitive conclusion can be drawn from the absence of a link in this case.

Williams, RJ et al. reported similar functional outcomes in a group of 19 patients who received osteochondral allografts at a mean clinical follow-up time of 48 months (range, 21-68) (Williams et al., 2007). The mean patient age at the time of surgery was 34 years and the Activities of Daily Living scale in conjunction with Short Form-36 assessment (which grades physical and mental responses to treatment) were employed. Increases from baseline scores of 56 to 70 and 51 to 66 were reported for the Activities of Daily Living scale and Short Form-36 respectively. No correlations were attempted between graft storage time, patient age, body mass index etc., due to concerns over the limited sample size of patients studied. Like McCulloch et al. (McCulloch et al., 2007) integration with the host tissue with examined using imaging techniques. On this occasion however, magnetic resonance imaging methods were used, and images were subsequently graded on signal properties to determine tissue incorporation, in addition to morphology and geometry to determine overall congruence. Using this technique, trabecular incorporation was found to positively correlate with Short Form-36 scores.

The clinical outcome of a much larger group was assessed in further detail by Davidson et al. (Davidson et al., 2007). 67 patients received femoral allografts stored at a mean storage time of 36 days and were assessed postoperatively at a mean of 40 months after surgery. Functional scores were representative of McCulloch et al. (McCulloch et al., 2007) and Williams, RJ et al. (Williams et al., 2007) with mean Short From-36 scores improving from 38 to 51 and mean Lysholm scores increasing from 37 to 78. Additionally, 10 knees out of 8 patients underwent second look arthroscopic evaluation and biopsy. A comparison of native cartilage and graft biopsies revealed very little

between mean chondrocyte viability values within the two groups (71% native, 78% grafts). A similar observation was noted for mean cell density values (345 cells/mm^2 native, 429 cells/mm^2 grafts). These results are very similar to those seen in studies previously mentioned (Pearsall et al., 2004, Williams et al., 2003). The fact that the native tissue was found to possess chondrocyte viability and density akin to that seen in grafts after over a month's storage may mean it could be acceptable to do so. However the mean viability value for the native biopsies hides the spread of results recorded (range, 22-97%, SD, 23.7%). Thus, it may be the case that although intentions were to gather native cartilage from a healthy site, they may have been taken from a site in the process of decline secondary to the insult of the original lesion. Furthermore, a number of additional limitations exist in this study as the cell viability and density values for graft and host tissues were not recorded just prior to implantation, and there is no indication as to how metabolically active the biopsied cells are.

1.6 Contact Pressures in the Knee and Osteochondral plugs

1.6.1 Contact Pressures in the Tibiofemoral Joint

In order to understand the particular biomechanical effects due to the presence of osteochondral plugs, it is necessary to acknowledge the biomechanical performance of a healthy knee joint. Perhaps the most relevant of the biomechanical events that occur with regard to OAT treatment are the apparent contact stresses acting on the cartilage surfaces. Thus, before attention is given to the biomechanical effects of the implanted plugs, the stresses present in unaltered joint surfaces will be analysed.

Thambyah et al. examined the contact stresses in the knee joint at various simulated stages of walking but also deep flexion to simulate squatting (Thambyah et al., 2005). Five cadaveric knees were loaded on a materials testing machine under the following loading conditions;

- 2.25 x BW & 5.5° flexion to simulate heel strike (HS)
- 1.85 x BW & 15.5° flexion to simulate single limb stance (SLS)
- 3.5 x BW & 4.5° flexion to simulate toe-off (TO)
- 4 x BW & 90° flexion to simulate deep flexion position 1 (DF1)
- 5 x BW & 120° flexion to simulate deep flexion position 2 (DF2)

where body weight (BW) was assumed to be 700N.

For each of the loading conditions varus/valgus rotations, internal/external rotations, anterior/posterior displacement and medial/lateral displacements remained unrestrained and the final equilibrium position of the joint recorded using scales and markers. Each of the joints was then disarticulated and a Tekscan pressure sensor inserted into the tibiofemoral articulation. Each of the positions determined earlier for the five loading conditions was then reproduced, and so the joint was reconstructed for each scenario. This translated to a varus angulation of 2° for heel strike and toe-off. For the single limb

stance phase, besides the slight varus tilt, an internal rotation of 5° was allowed for also. In deep flexion, some anterior translation (10-12mm) of the tibia was imparted, in addition to internal rotation ranging for 10-20°. Medial and lateral translations were negligible.

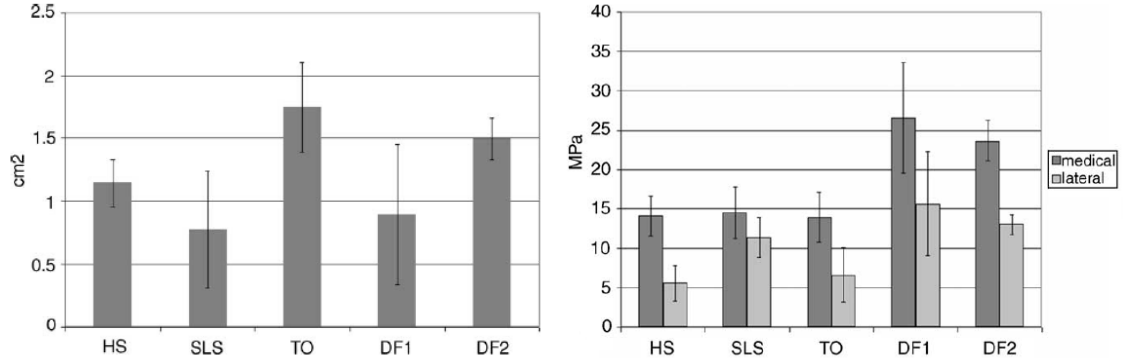

(a) **(b)**

Figure 1-14. Contact areas (a) and Peak pressures recorded (b) in the tibiofemoral joint for the five different loading conditions simulating various walking conditions and squatting (Thambyah et al., 2005).

The contact areas with the medial compartment were smallest at SLS (≈75mm^2) and largest at TO (≈180mm^2) as shown in figure 1-14a. During the conditions that simulated the various cycles of gait (HS, SLS & TO), little variation was observed in the medial compartment pressures (14.1±2.4MPa). However, in deep flexion, pressures were significantly higher, rising by 80% to 26.6±7.1MPa. Figure 1-14b also demonstrates the ratio at which medial and lateral compartments undertake stress. It appears that the lateral compartment encounters only about 50% of what the medial undertakes at HS and TO, both compartments have approximately the same pressures at SLS and the lateral encounters about 70% less stress in deep flexion.

In a later study Thambyah examined this phenomena further in the medial and lateral compartments of four cadaveric knees in stance position alone (Thambyah, 2007). The knees were dissected carefully to expose the tibial plateau with meniscus intact and femoral condyles. A Tekscan pressure sensitive film was placed in between the condyles

and joint compartments to measure contact stresses as the joint was loaded via a specially constructed six degree of freedom apparatus. To simulate stance phase a load in the region of 1000N was applied to the knee in 15.5° flexion and 2° varus tilt, or until the distribution of forces between the medial and lateral compartments were about 70% and 30% respectively.

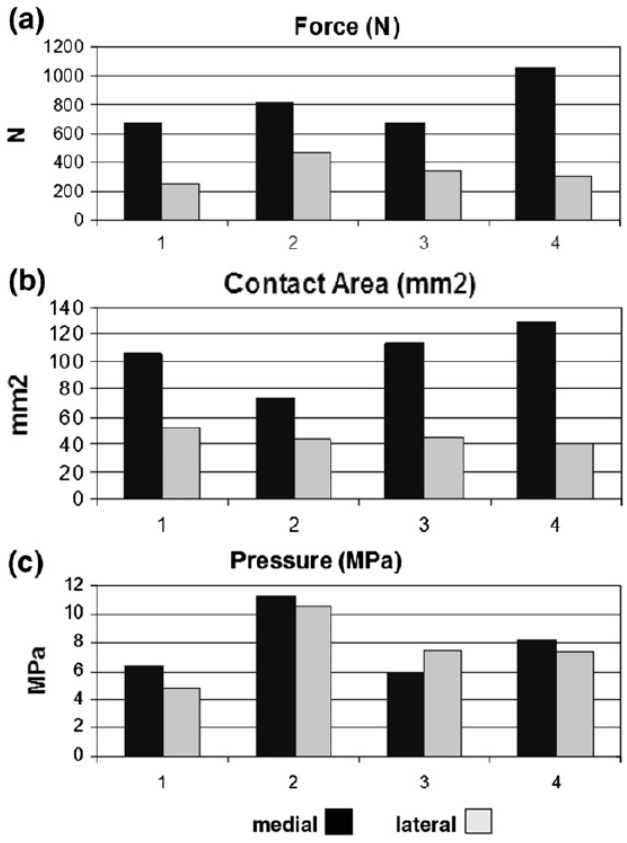

Figure 1-15. The tibiofemoral contact forces (a), contact areas (b), and contact pressures (c) for the medial and lateral compartments of four cadaveric knees (Thambyah, 2007).

The mean forces applied to each knee were found to be approximately 1144N, which was distributed by an average of 806.3N (SD 183.4N) in the medial compartment and 337.5N in the lateral compartment. As expected the contact areas recorded correlated well with the magnitude of force applied, ranging from 40-130mm^2 for forces of 400-1000N. Pressure recordings showed no statistical difference between the medial and

lateral compartments measuring 8MPa and 7.6MPa for the medial and lateral respectively. This agrees with the evidence that both compartments share stress during stance phase in Thambyah et al.'s previously mentioned study (Thambyah et al., 2005). However a >50% difference in the magnitude of the peak loads is observed in all knees but number 2 (figure 1-15). A similar trend appears in the contact areas recorded. Considering, the loading conditions are almost identical, it is difficult to understand why this is the case unless there was some alteration in the preparation that is not explicitly mentioned. Or perhaps, it may simply just be a case of varying gender, donor size and anatomical variations, which were also not referred to prior to testing.

Few studies measure the stress distribution of a healthy joint in its own right, but rather in tandem with altered joints as a control. For example, studies on the effects of meniscal repair (Becker et al., 2005, Marzo and Gurske-DePerio, 2009) or ligament damage (Paci et al., 2009). However, since this particular facet of surgery is distinctly separate from OAT treatment, only the untreated controls used in these studies will be analyzed with the intention of understanding the stresses in a healthy knee joint.

Marzo and Gurske-DePerio studied the effect of medial meniscus posterior horn avulsion on peak contact pressures in the tibiofemoral region of articulation (Marzo and Gurske-DePerio, 2009). Intact knees were inspected for the presence of cartilage damage by performing anterior capsulectomies on 8 knees and to allow the introduction of a Tekscan knee sensor. The knees was held in full extension and measured goniometrically at 0°, allowing for varus/valgus freedom but otherwise constrained. A load of 1800N was then applied axially through the knees. Peak contact pressures were found to be larger in the lateral compartment than the medial compartment, measuring 5.1MPa compared to 3.8MPa. This is an intriguing result, as it seems to be generally witnessed that larger stresses occur in the medial compartment when the joint is under full extension (Becker et al., 2005, Thambyah et al., 2005).

Paci et al. hypothesized that if the anterior intermeniscal ligament was cut, larger pressures would be observed in the medial compartment (Paci et al., 2009). In this study five cadaveric knees, four male and one female, with a mean age of 59 years (range 31-75 years). A Tekscan pressure sensor was inserted inframeniscally into the medial compartment and sutured to extra-articular suture anchors placed in the tibia. The knees were then mounted on a testing machine that allowed or controlled all 6 degrees of freedom of motion. The tibia was mounted on a sliding table connected to an anterior/posterior actuator and the load cell. The anterior/posterior position was dynamically controlled to maintain zero anterior/posterior force on the knee. Similarly, a rotational actuation was dynamically controlled to maintain zero torsional force on the tibia. Free medial/lateral translation and varus/valgus angulation were allowed, limited only by the ligamentous structures of the knees. The loading protocol simply consisted of a maintained axial load of 1000N while the knees were flexed from 0 to 60° at a rate of 0.5°/s.

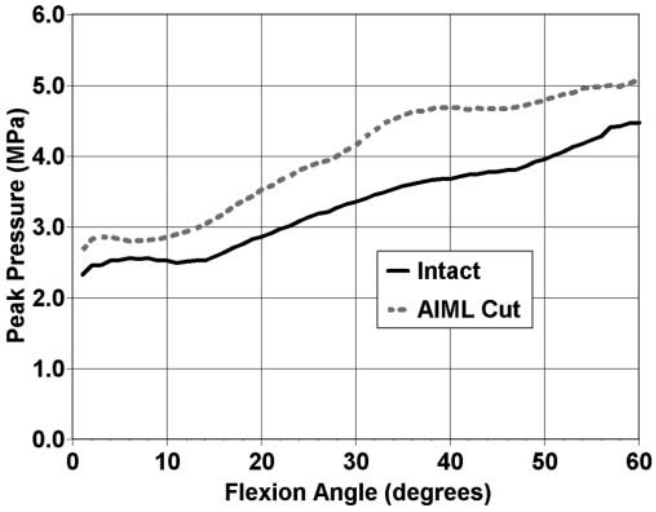

Figure 1-16. Variation of mean peak contact pressures recorded with knee flexion angle. Note: the intact joints are represented by the solid line (Paci et al., 2009).

Peak pressure levels for intact, healthy knees remained steady at approximately 2.5MPa from 0-15°, after which pressures were found to rise linearly up to 4.5MPa at 60° flexion

as shown in figure 1-16. Interestingly, Thambyah et al. also witnessed a maintenance of peak pressures at low flexion angles and higher pressures at greater flexion angles even though, unlike this study, he applied different loads for different flexion angles (Thambyah et al., 2005). The magnitude of these peak values varied, however it may nevertheless be deduced that the shape of the articulating bodies plays a major role (in combination with load) on the pressures encountered within the joint compartments.

In a study performed by Becker et al., meniscofemoral contact pressures were recorded to assess the success of a range of biodegradable implants in correcting meniscal tears (Becker et al., 2005). Thirteen cadaveric knees from donors ranging between 40 and 60 years of age were employed. Parapatellar incisions were performed to expose the anterior portion of the joint. The meniscus, cruciate & collateral ligaments, patella & patellar ligament and quadriceps tendon were all preserved. The femur and tibia regions were then mounted in a testing machined augmented to offer six degrees of freedom, the femoral ends to a hydraulic cylinder with attached load cell and the tibial ends to a base plate. The quadriceps tendons were fixed to a second hydraulic cylinder, also with load cell, which acted to control knee flexion. After mounting, the collateral ligaments were detached to allow the placement of Tekscan pressure sensors into the medial and lateral compartments before being reattached securely. In order to determine the natural mechanical axis, the knees were loaded to 100N under full extension whilst the axis was adjusted to generate equal pressure in both joint compartments. Having found this axis, the joints were then loaded to 350N and contact pressures recorded at the meniscal posterior horns at flexion angles of 0, 30, 60 & 90°.

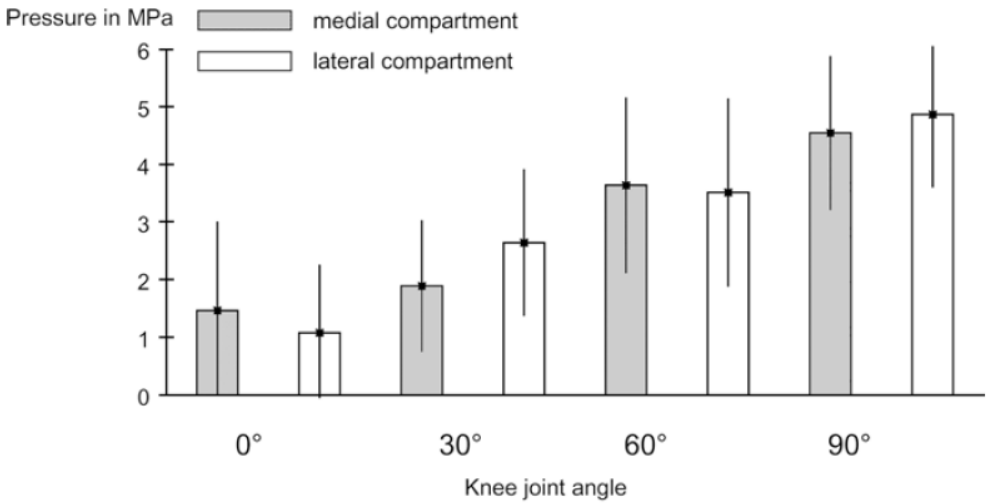

Figure 1-17. Peak contact pressure in the meniscal posterior horns for varying degrees of flexion (Becker et al., 2005).

In full extension the peek contact pressures were found to be 1.46MPa and 1.08MPa in the medial and lateral compartments respectively. No significant difference in the peak pressures were recorded in the early stages of flexion in the medial compartment up until 30°. At this point and beyond, the peak pressures in both compartments began to rise to maximal values of 5.5MPa in the medial compartment and 4.87MPa in the lateral compartment at 90° flexion. This is a trend almost identical to that mentioned by Paci et al. previously (Paci et al., 2009). In fact, a great similarity is observed when figure 1-17 is compared to figure 1-16.

1.6.2 Contact Pressures in the Patellofemoral Joint

Ward and powers examined the influence of patella alta (a condition in which the patella rests in a superior trochlear position) on patellofemoral joint stresses during slow and fast walking (Ward and Powers, 2004). Sagittal and axial MRI images of normal knees and those with patella alta were taken to quantify the extensor mechanics and contact areas of the patellofemoral joints. Gait analysis was performed using a six camera motion analysis system and four force plates in order to measure the kinetics and kinematics of the knee joints. The MRI and gait analysis data was then inputted into

patellofemoral joint stress model. In eleven healthy knees patellofemoral joint reaction forces reached peaks of 500N during slow walking, rising to over 700N during fast walking. Accordingly, joint stresses reached peaks of approximately 2.3MPa and 3.1MPa during slow and fast walking respectively (figure 1-18).

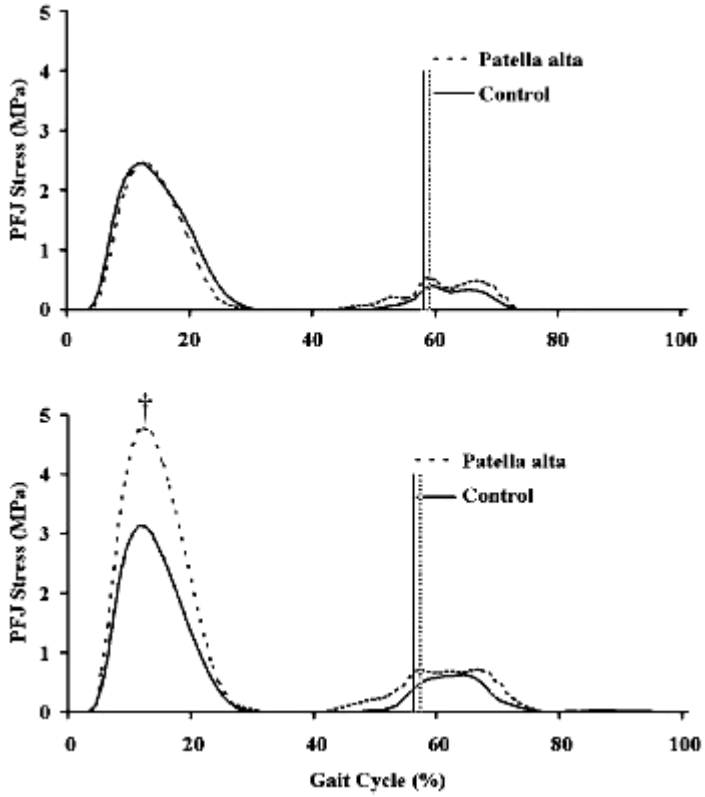

Figure 1-18. The variation of patellofemoral joint contact stress throughout the gait cycle for slow (above) and fast (below) walking conditions (Ward and Powers, 2004).

In another study by the same group utilising an adaptation of the same methods to incorporate a set of stairs, the patellofemoral joint contact stresses were measured during stair ascent and descent in ten patients with and without patellofemoral pain (Brechter and Powers, 2002). In the healthy knee control group joint forces peaked at approximately 3.5 times body weight for both stair ascent and descent. This translated to contact stress of approximately 6-7MPa for both ascent and decent.

Goudakos et al. measured the contact pressure in the patellofemoral joint in eight cadaveric knees using a Tekscan pressure sensitive film (Goudakos et al., 2009). The joints were loaded in two arrangements of flexion, 12 and 30 degrees, whilst static loading was applied via simulated muscle forces. This was achieved via four servo-electronic actuators which generated muscle forces known to occur at those flexion angles during walking and stair climbing. Specifically, the four muscles simulated were the rectus femoris/vastus intermedius, vastus medialis, vastus lateralis and the semimembranosus/semitendinosus. During the walking scenario, average peak pressures of 6.1 & 5.5MPa were recorded at flexion angles of 12 and 30 degrees respectively. However, during stair climbing larger pressures were recorded with average peak values of 7 & 11.8MPa for 12 and 30 degrees of flexion respectively (figure 1-19).

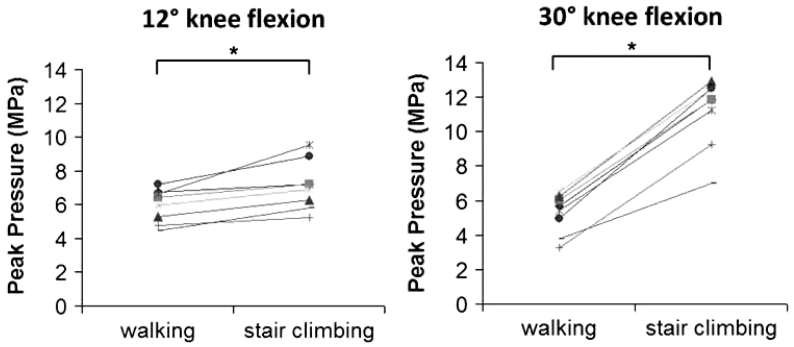

Figure 1-19. Peak pressures recorded for eight cadaveric knees under two different knee flexion angles and two different simulated activities (Goudakos et al., 2009).

Adopting a similar experimental approach, Wilson et al. measured the contact pressure in the patellofemoral joint of nine cadaveric knees under simulated walking whilst wearing different knee braces (Wilson et al., 2010). A Tekscan pressure sensor was positioned in the joint space as physiological dynamic loading was applied to the femur through a custom knee joint driving device and servo-motors controlled flexion/extension and abduction/adduction angles. Peak contact pressures of 3.5 & 4.2MPa were found to occur during the instances of the gait cycle when knee flexion angles peaked (approximately 15 & 70% respectively). Interestingly this is not in

accordance with the work performed by Ward and Powers who predicted much lower stresses at approximately 70% of the gait cycle (figure 1-18) (Ward and Powers, 2004).

In a study performed by Ostermeier et al., the contact pressures in the patellofemoral joint were measured in eight human knees having had patellofemoral ligament reconstruction using a number of techniques (Ostermeier et al., 2007). A Tekscan pressure sensitive film was inserted into the paellofemoral joint space by means of performing lateral parapatellar incision and internally everting the patella. Once the sensor was securely in place, the knees were mounted in a kinematic knee simulator and isokinetic extension under dynamic or static physiological loading. When the knees were tested as unaltered, healthy controls, prior to any surgery, contact pressures were found to peak at 4.5MPa under dynamic loading and 3.4, 3.6 & 4.1MPa under static conditions at flexion angles of 30, 60 & 90 degrees respectively. The dynamic values present similar levels of contact pressures to those described by Wilson et al. under similar loading methods (Wilson et al., 2010).

1.6.3 Influence of Osteochondral Defects/Plugs on Contact Pressures

A feel for the standard contact pressures that occur in the knee joint has been established in the previous section. This now allows for a clearer understanding of the alterations that can occur due to osteochondral defects and the benefits from surgical correction.

Guettler et al. investigated the effect of defect size on the defect's rim stress concentration, peak rim stress and load redistribution to the adjacent cartilage (Guettler et al., 2004). Five left and three right cadaveric knees (2 male, 6 female) from 5 sources were used from donors aged 78-91 years. The knees were mounted in a materials testing machine under 30° flexion. An anterior arthrotomy allowed the placement of Tekscan pressure sensors into the medial and lateral compartments of the joint. Each knee was loaded to 100N, at which point small adjustments were made to the specimen's medial/lateral orientation to ensure both compartments were loaded equally. This position was then fixed in place. After a capsulotomy, each intact knee was loaded from

100 to 700N at 100N/s and held at 700N for a period of 5 seconds while pressure measurements were taken. The load center of each condyle was then marked and an osteochondral coring device used to create a 5mm diameter, 9mm deep defect centered on this mark. Loading was then repeated as previously described. Consecutive concentric defects with diameters of 8, 10, 12, 14, 16, 18 & 20mm were then created around the 5mm defect, repeating the loading for each individual defect whilst pressures were recorded. Peak rim pressures were not found to increase significantly from 10mm to 20mm. However, rim stress concentration was shown for defects of 10mm diameter and larger. This was deemed to alter load distribution, prompting implications for the longevity of the cartilage surrounding the defect.

Koh et al performed a study investigating the effect of angularly fitted osteochondral grafts on contact pressure (Koh et al., 2006). The contact stresses were determined in 50 pig knees using Fuji Photo Film under an applied load of 80N applied via a piston and held for 120 seconds. This was carried out under the following conditions:

- On intact articular surfaces;
- On surfaces with a 4.5mm diameter defect;
- On surfaces where the defect was grafted with a flush osteochondral plug from the contralateral condyle;
- On surfaces where the defect was grafted with a 30º plug with the lower edge flush to the adjacent surface;
- On surfaces where the defect was grafted with a 30º plug with the upper edge flush to the adjacent surface;

Peak pressures were found to be 8.57 +/- 2.35kg/cm^2 in intact surfaces but were significantly higher ($P<0.001$) after creation of the 4.5mm diameter defect (11.97 +/- 1.89kg/cm^2). These were reduced to near normal levels after insertion of the flush osteochondral plugs (9.81 +/- 1.01kg/cm^2). When angled plugs were inserted with the lower edge flush, significant rises ($P<0.001$) were observed in the peak pressures, even

larger than when the defect alone was present (14.5 +/- 2.21kg/cm^2). When the angled plugs were inserted with the upper edge flush, contact pressures (9.15 +/- 3.34kg/cm^2) were not significantly (P=0.497) different from the intact cartilage surfaces or where flush plugs were present, but were significantly different than surfaces with empty defects (P<0.001). The study concluded by outlining the importance of maintaining surface conformity and that if and angled plug is inadvertently harvested than it should be fitted in place with the upper edge flush to the adjacent surface.

2 Aims, Objectives & Deliverables

The previous chapter described the OAT procedure, involving the harvesting of osteochondral material from a relatively non-load bearing location and its implantation into a load bearing site where a defect has occurred. Although excellent to good results are obtained in the majority of cases (66-92% depending on the source study) (Treme and Miller, 2008), poor integration and failure nevertheless happens and it is worthy of investigation to determine why this occurs. The work hence-forth hypothesises that the mechanical properties of the cartilage and bone at the harvesting site are different from that required at the site of implantation and that this mismatch could be detrimental to graft integration and ultimate survival.

It has been demonstrated that there can be certain difficulties in fixation of the grafts, with bone losing its embedding capability simply after a week's simulation *in-vivo* (Whiteside et al., 2003), bone resorption if the graft/implantation site interface is exposed to synovial fluid (Changoor et al., 2006) and the use of high impact loads to deliver the grafts (Pylawka et al., 2007) which may also cause damage to the bone element of the graft, not just the surface cartilage. Hence, given that all of this can occur, it is vital that the graft bone is strong enough to match its local environment so as not to exacerbate the situation any further.

It has also been shown that cartilage defects in the knee lead to concentrated contact pressures (Guettler et al., 2004), but that normal pressure distribution is restored if these defects are correctly substituted with the same osteochondral material from the contralateral knee (Koh et al., 2006). However, there is no guarantee that the cartilage in an osteochondral graft from a non-load bearing harvest site will functionally replicate the host site like this. Should the mechanical properties vary, then the function and integration of the cartilage element of the graft may also be adversely affected.

A number of studies were performed determining the mechanical properties of articular cartilage and trabecular bone in regions of the porcine knee correlating to possible implantation sites. Specifically, these included the femoral condyles and the patellofemoral groove. The patellofemoral groove may not bear as much load as the tibiofemoral joint, however the joint load can be as much as body weight during walking (Ward and Powers, 2004) or 3.5 times body weight during stair ascent/descent (Brechter and Powers, 2002), meaning the resulting contact pressures are comparable at both sites (section 1.6). Hence, it proves worthy to investigate whether the mechanical properties of the osteochondral material at these sites are different. Should this be the case, then it is unlikely that grafts harvested from any one non-load bearing site are suitable.

The porcine knee was chosen due to its ease of acquisition but also because of its similarity to the human knee in terms of shape and relative geometry. Essentially, the porcine knee represents a scaled down version (0.7-0.8) of the human joint, even if some differences with regard to the joint's features are found. The evidence of this is presented in appendix A. It is hoped that due to this anthrometrical similarity, load distribution would also be comparable and any regional variations in the mechanical properties of the cartilage and bone would be representative of that in human knees.

The first study is presented in chapter 3 and involves the determination of the aggregate modulus of the cartilage and strength of the bone in the highlighted locations of interest. The aggregate modulus is determined by means of confined compression methodology and fitting the experimental data to a non-linear biphasic equation. The strength of the bone is determined via conventional uniaxial compression. Correlations are then investigated between the cartilage and bone results.

Chapter 4 presents the second study, which determines the Poisson's ratio of cartilage at the same locations as before. This involves optical extensometry to calculate the radial expansion of cartilage discs under compression at the superficial and deep surfaces.

These results are then correlated with the aggregate modulus results from chapter 3 to determine whether any relationship exists between these two parameters.
Chapter 5 presents the results of a histological study. It is hoped that the content and distribution of the structural proteins collagen and PG's may explain the mechanical characteristics witnessed in the previous experimental studies.

The final experimental study into osteochondral tissue is presented in chapter 6. This details an investigation into the frictional properties of the cartilage at the same locations of interest as the other chapters. This is carried out via a simplified pin-on-plate set-up and also examines the temporal effect of loading on friction.

It has been demonstrated that significant decreases in chondrocyte viability, viable cell density and metabolic activity have been observed within time periods of just 30 during the storage of osteochondral allograft tissue (Allen et al., 2005, Ball et al., 2004, Pearsall et al., 2004, Williams et al., 2003). In recognition of this, Chapter 7 presents the design and proof of concept for a novel bioreactor/joint simulator system. This system generates hydrodynamic pressures capable of providing the essential mechanical cues for cell health and proliferation during allograft storage. Furthermore, this concept can be extended to the realm of tissue engineering as an *in-vitro* growth environment for cell seeded scaffolds. This chapter details the design, validation and operation of an early stage prototype involving predicting the fluid pressures it generates for a given set of operating conditions using hydrodynamic lubrication theory and verifying this via experimental measurements. A design proposal for the incorporation of osteochondral tissues and scaffolds is also put forward.

Given that differences exist in the loading and kinematics of certain parts of the knee such as the femoral condyles and patellofemoral groove, it may be expected that at least some regional variation exists in the various mechanical properties of the tissues at these sites. It is proposed that the bioreactor/joint simulator may act as a means to work harden and tailor osteochondral tissues in accordance with their eventual site of

implantation. These tissues could be constructed via cell-seeding in a single phase or two-tier composite of synthetic or biological biomaterials (Cui et al., 2011, Grayson et al., 2008, Lee et al., 2008, Lien et al., 2009, Lima et al., 2004, Oliveira et al., 2006, Sherwood et al., 2002), or by reseeding previously decellularised auto or allograft osteochondral materials with a patient's own cells.

Hence, to summarise the experimental chapters in brief, chapters 4-7 investigate the particular traits (mechanical or otherwise) required of tissues in the femoral condyles and patellofemoral groove and chapter 8 presents a means of delivering bespoke tissue engineered constructs to replace them.

3 General Statistical Methods

Although a modern statistical software package (Minitab™, v.16) was used to perform all statistical analysis, it is perhaps best to first establish what general methods are used throughout this thesis and briefly describe how these techniques operate listing any assumptions that are made.

3.1 Basic Population Description

The mean ($\bar{x}$), standard deviation (*SD*) and standard error (*SE*) relating to the sample populations in all of the forthcoming studies are calculated using equations 3-1, 3-2 & 3-3 respectively.

$$\bar{x} = \frac{\sum_{n}^{1} x_1 + x_2 + \ldots + x_n}{n} \qquad \textbf{Equation 3-1}$$

$$SD = \left(\frac{\sum (x - \bar{x})^2}{n-1} \right)^{0.5} \qquad \textbf{Equation 3-2}$$

$$SE = \frac{SD}{\sqrt{n}} \qquad \textbf{Equation 3-3}$$

Where;
x is the variable,
n is the sample number.

In all cases the true population variances are not known. Hence, confidence intervals can be calculated in accordance with the t-distribution in the following manner;

$$\bar{x} \pm t_{\alpha/2}(v) * SE \qquad \textbf{Equation 3-4}$$

Where;

v is the number of degrees of freedom (defined as $n - 1$),

$t_{\alpha/2}(v)$ is the point on the t-distribution curve where with a confidence interval of α and v degrees of freedom.

3.2 Student t-test

When a comparison between two unpaired populations was required, significance testing using the t-distribution was performed. Initially, samples were evaluated to determine whether they were drawn from normally distributed populations of equal variances. The latter can be tested for by using the F-test statistic.

$$F = \left(\frac{SD_l}{SD_s} \right)^2 \qquad \textbf{Equation 3-5}$$

Where;

SD_l is the larger variance,

SD_s is the smaller variance.

The F value is then compared against known F-distribution data. If no significant differences are found, the variances are pooled (s^2) and the t value determined.

$$t = \frac{\overline{x_1} - \overline{x_2}}{s\sqrt{\frac{1}{n_1} + \frac{1}{n_2}}} \qquad \textbf{Equation 3-6}$$

Where;

s is calculated from $s^2 = \frac{(n_1 - 1)s_1^2 + (n_2 - 1)s_2^2}{n_1 + n_2 - 2}$, **Equation 3-7**

s_1^2 is the variance of population 1,

s_2^2 is the variance of population 2,

n_1 is the sample number for population 1,

n_2 is the sample number for population 2,

Following calculation of *t*, it is compared against known t-distribution data at n_1+n_2+2 degrees of freedom and a significance level of $\alpha = 0.05$.

Assumptions of the t-test include the data in each of the two populations is normally distributed, the two populations should have equal variances and the data is sampled independently from the two populations being compared.

3.3 Correlation

Correlational analysis results in bivariate data sets, which can be best pictured using scatterplots. Linear relationships within this data can be investigated by measuring the Pearson correlation coefficient (*r*).

$$r = \frac{\sum (x-\bar{x})(y-\bar{y})}{\sqrt{\sum (x-\bar{x})^2 \sum (y-\bar{y})^2}}$$ **Equation 3-8**

Following the calculation of the Pearson correlation coefficient, it can be tested for significance by first calculating the *t* value.

$$t = \frac{r\sqrt{(n-2)}}{\sqrt{(1-r^2)}}$$ **Equation 3-9**

Following calculation of *t*, it is compared against known t-distribution data at *n-2* degrees of freedom and a significance level of $\alpha = 0.05$.

Assumptions made in this process include bivariate normality exists (i.e. both data sets are normally distributed and both data sets have equal variances.

3.4 1-way ANOVA

If a comparison between more than two groups was required than a 1-way analysis of variance (ANOVA) was performed. Throughout this thesis, confidence levels of α = 0.05 were used for 1-way ANOVA's. Table 3-1 lists the formulae relevant when performing a 1-way ANOVA.

Table 3-1. Formulae in performing a 1-way ANOVA where Y is the measurement, $\bar{Y}$ is the group mean, $\bar{\bar{Y}}$ is the grand mean, *a* is the number of groups, *n* is the number of measurements per group, SS_{among} us the sum of squares among groups, SS_{within} is the sum of squares within groups, MS_{among} is the mean sum of squares among groups and MS_{within} is the mean sum of squares within groups.

Source of Variation	Degrees of Freedom	Sum of Squares (*SS*)	Mean sum of Squares (*MS*)	*F*'s
Among Groups	*a*-1	$n\sum^{a}(\bar{Y}-\bar{\bar{Y}})^2$	$\frac{SS_{among}}{a-1}$	$\frac{MS_{among}}{MS_{within}}$
Within Groups	*a*(*n*-1)	$\sum^{a}\sum^{n}(Y-\bar{Y})^2$	$\frac{SS_{within}}{a(n-1)}$	
Total	*an*-1	$n\sum^{a}(\bar{Y}-\bar{\bar{Y}})^2+\sum^{a}\sum^{n}(Y-\bar{Y})^2$		

Following the 1-way ANOVA, uplanned or post-hoc test was performed to ascertain whether significance existed between groups using the Tukey HSD (honestly significant difference) method.

Assumptions of the 1-way ANOVA include the independence, homogeneity and normality of the variances of the residuals and equal population variances.

4 Determination of the Aggregate Modulus of Articular Cartilage & Trabecular Bone Strength in the Porcine Knee

4.1 Introduction

The primary structures that absorb stress in any diarthrodial joint (in this case the knee) are the cartilage that provides the covering layer to the articulating surfaces and the trabecular bone beneath it. Moreover, the geometrical configuration and mechanical properties of the articular cartilage and trabecular bone plays an important role in providing effective load transmission throughout an individual's lifetime. As a result, it is apparent that over the millennia their biomechanical properties have been optimised through an evolutionary process for this particular function.

However, the progression of joint disease in some individuals leads to the requirement of radical treatment options such as osteochondral autograft transfer (OAT) which may alter this delicate balance. In fact, on occasion, OAT has been known to suffer from a number of drawbacks, such as the tendency of the harvested cartilage to degenerate (Tibesku et al., 2004) or convert to a more fibris state (Benazzo et al., 2008, Khan et al., 2008, Moriya et al., 2007) and resorption of the trabecular bone, particularly in the early stages of healing (Oshima et al., 2002, von Rechenberg et al., 2003, Benazzo et al., 2008). This may be due to the damage imparted to the grafts at the point of harvesting (Huntley et al., 2005a, Huntley et al., 2005b, Vizesi et al., 2007), or indeed a result of the methods used to fixate the grafts (Patil et al., 2008, Pylawka et al., 2007, Whiteside et al., 2005), but perhaps more importantly there may be a difference in the mechanical properties of the harvested tissues and what the area of implantation demands of them, on which hypothesis, this study is based. The mechanical properties of the articular cartilage and trabecular bone from different regions of the porcine knee were determined. Specifically these regions included areas of the patello-femoral groove (PFG) and the medial and lateral condyles.

The mechanical characteristics of cartilage are complex and have been widely investigated using methods such as indentation (Athanasiou et al., 1994, Froimson et al., 1997, Jurvelin et al., 1990, Korhonen et al., 2002a, Korhonen et al., 2002b, Lu et al., 2009), unconfined compression (Boschetti et al., 2004, Boschetti and Peretti, 2008, Kiviranta et al., 2006, Korhonen et al., 2002a, Laasanen et al., 2003) and confined compression (Ateshian et al., 1997, Boschetti et al., 2004, Boschetti and Peretti, 2008, Hung et al., 2004b, Korhonen et al., 2002a, Willett et al., 2005, Chen et al., 2001). However, although none of these options accurately mimic cartilage mechanics, it is the latter that has been most commonly used to describe it, as it offers a simple, one-dimensional representation of cartilage under deformation. Using biphasic theory, one can calculate the aggregate modulus, a measure of the compressive stiffness of a two phase tissue in confined conditions. Furthermore, it has been demonstrated that the compressive stiffness of cartilage can be related to its proteoglycan (PG) content (Kiviranta et al., 2006, Laasanen et al., 2003, Lu et al., 2009).

Determining and comparing the mechanical parameters of cartilage from different anatomical locations has been extensively studied. For example, Froimson et al. compared the properties of human patellar and patellofemoral groove cartilage using indentation and discovered that the patellar cartilage had a 30% lower compressive stiffness (Froimson et al., 1997). Korhonen et al. showed that the aggregate modulus of the cartilage on the bovine humeral head was greater than that of the patella, which in turn was greater than that of the medial femoral condyle (Korhonen et al., 2002a). In a study more closely related to the locations of interest in this chapter, Willet and co-workers determined at the aggregate modulus of cartilage on both femoral condyles and the patellofemoral groove in porcine knees (Willett et al., 2005). However, although it was shown that the PFG cartilage was twice as stiff as that of the condyles, the primary aim was determine the effect of freezing on cartilage in these areas. Interestingly, this was found to reduce the aggregate modulus up to 20% in some areas. Jurvelin et al. discovered that the aggregate modulus of canine cartilage was greatest in the PFG, then the medial condyle, lateral condyle and finally the tibial plateau (Jurvelin et al., 2000).

As for the trabecular bone, the most common method to determine the mechanical properties of trabecular bone is uniaxial compression as this is the most accurate reproduction of events *in vivo*. This allows material parameters such as the compressive strength and Young's modulus of specimen to be determined. Tensile testing is very rarely used on trabecular bone as it is extremely difficult to obtain thin, elongated specimens of trabecular bone for the testing. Furthermore, Ryan et al. demonstrated that stress distribution in the intervertebral disc correlates with strength distribution in subdiscal bone in the porcine spine (Ryan et al., 2008). It may be expected that such a relationship exists in the knee joint also, with the areas regularly experiencing higher stresses undergoing adaptive morphological changes leading to an increase in overall bone strength and density in accordance with Wolff's law.

Yet, despite all the comprehensive studies that have been carried out on both articular cartilage and trabecular bone, as far as the author is aware, no study has determined and compared the mechanical properties of both cartilage and its trabecular bone in different anatomical locations with a view to OAT treatment. Hence, the following was performed:

- Harvest osteochondral plugs from different regions of the porcine knee representative of the locations where OAT would take plugs from and subsequently implant them;
- Perform confined compression testing to determine the aggregate modulus;
- Perform a biochemical assay to determine whether PG content is correlated to the aggregate modulus;
- Perform uniaxial compression testing on the trabecular bone to determine the compressive strength & elastic modulus and
- Interpret the results to determine if differences exist for both the cartilage and bone in separate harvest location groups and whether or not this may have implications for OAT treatments.

4.2 Methods

4.2.1 Preparation of Osteochondral Tissues

Five knee joints were harvested from 6-8 month old female pigs 5 days after slaughter. Prior to dissection, the animal carcass remained chilled at 4°C, keeping the joint capsule intact and maintaining the sterility of the joint. The joint capsule was carefully dissected to expose the femoral condyles and the femur gripped in a vice mounted on a laboratory work bench. A steel cork borer of 10mm diameter was then used to harvest osteochondral material from several sites with the aid of a plastic mallet. All throughout the harvesting process, PBS was used to irrigate the cartilage and prevent dehydration. Two sites were highlighted on both the medial (M1 & M2) and lateral (L1 & L2) condyles in addition to the patellofemoral groove (PFG1 & PFG2) for harvesting. These sites are highlighted in figure 4-1. For each osteochondral plug, the trabecular bone was maintained for strength testing, whereas the covering articular cartilage was maintained for confined compression testing (figure 4-2).

After removal of the osteochondral plug, the cartilage was carefully removed from the bone with a scalpel before being irrigated once again with PBS and frozen at -20°C. The remaining bone was then shaped slightly at both ends using a band-saw, removing the subchondral bone, to produce a cylindrical plug 10mm diameter, 10-15mm in length. This too was then irrigated and frozen at a temperature of -20°C. Bone samples were thawed overnight and equilibrated in PBS for 30min prior to testing.

Once five specimens for each location had been collected, each frozen cartilage disc was then embedded in a support resin (Thermo Scientific Shandon Cryomatrix^{TM}) and placed on a cryotome maintained at -20°C (Thermo Scientific Shandon Cryotome) for sectioning. Serial 10μm slices were removed from the bottom surfaces until they appeared to be smooth and parallel to the articular surfaces. The prepared samples together with embedding resin were then placed in storage again at -20°C until the day of testing when they were thawed, cleaned of the embedding resin and equilibrated in

PBS for 30min. It was hoped that because the cartilage surfaces were thoroughly irrigated with PBS whilst harvesting, that any relative osmotic swelling effect between the time of harvesting and after equilibrating would be minimal. Thus, the sample should remain close to its size when it was taken from the knee while it was being tested.

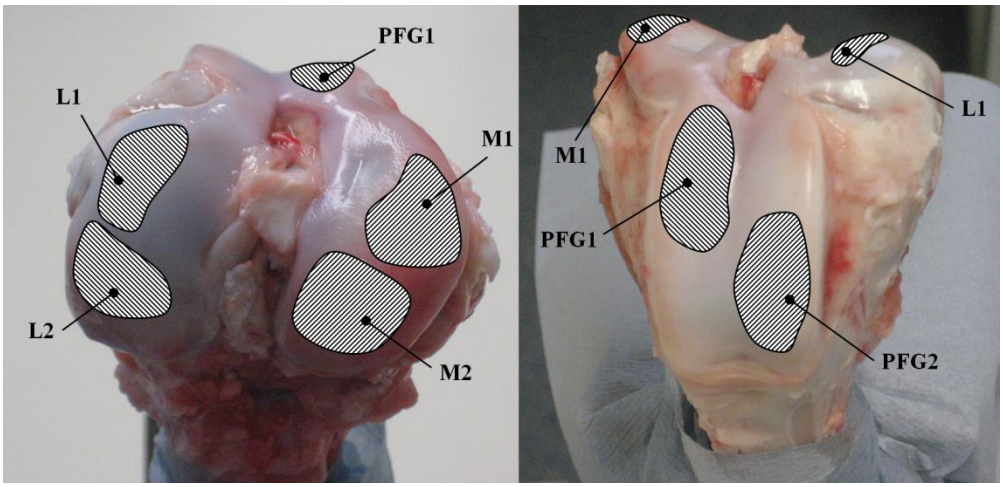

Figure 4-1. Location of osteochondral plug harvesting sites in porcine knee.

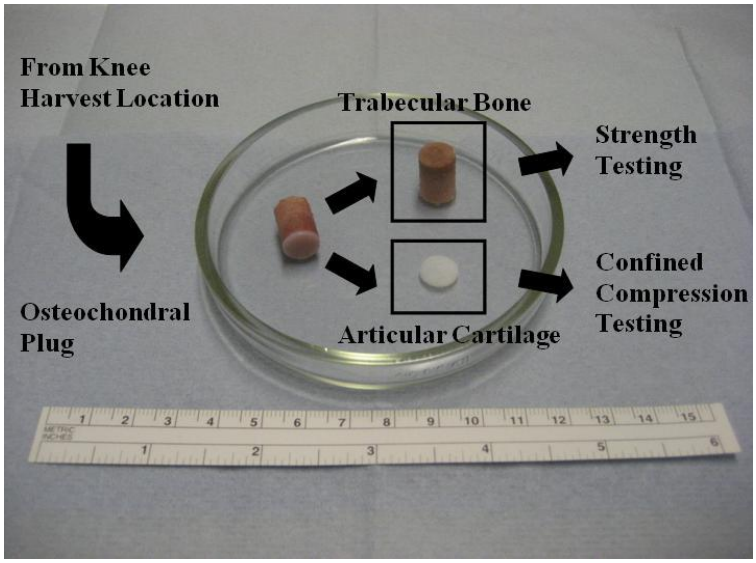

Figure 4-2. Cartilage and trabecular bone are separated from one another. The bone undergoes strength testing whereas cartilage undergoes confined compression.

4.2.2 Mechanical Testing of Cartilage

A Schematic Diagram, along with picture, of the custom made apparatus used for confined compression testing of the prepared cartilage specimens is shown in figures 4-3 & 4-4 respectively. The apparatus consisted of an impermeable Telfon® base section into which a porous 5mm thick polyethylene disc (80-130μm average pore size) (Porex Technologies GmbH, Aachen, Germany) was seated to act as the lower platen for specimen compression. A further impermeable Teflon® section was used as a confinement ring to restrict radial progression of specimen under compression. This was fixed to the before mentioned base section. To act as the upper platen, a solid, stainless steel indenter was employed. Finally, the entire apparatus mentioned thus far was fixed to the base of a Perspex water bath and immersed in PBS at room temperature.

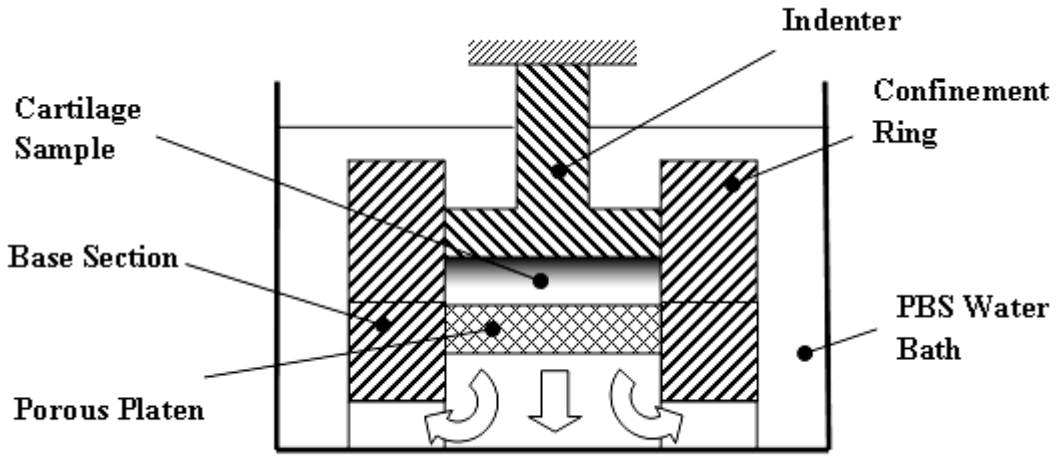

Figure 4-3. Schematic of apparatus used for confined compression testing of cartilage.

Figure 4-4. Picture of confined compression chamber used for cartilage testing; with water bath and indenter (left), and unassembled (right). The coloured marbles were used to reduce the volume of the external solution required to immerse the chamber.

The indentor was connected in series to a load cell on a materials testing system (MTS) (Model Z005, ZwickRoell, Ulm, Germany). A previous study demonstrated that the internal MTS measurement system is reliable and repeatable against externally applied LVDT methods (Heneghan, 2008). Hence, this system was deemed appropriate to be used in conjunction with the load cell for load/displacement measurement.

The indenter was lowered manually prior to each specimen being tested until contact was made with the porous platen and a load of 0.25N was recorded. The digital crosshead position of the MTS (in mm to 4 decimal points) was then noted at this point (LE1), and the indenter was raised for placement of the cartilage.

After thawing and equilibrating in PBS at room temperature for 30min, a 10mm diameter cartilage sample was placed neatly into the confinement chamber with care taken to ensure the articular surface remained flush against the porous surface. The sample was loaded so as to guarantee correct specimen confinement, followed by unloading for a period of time to allow stress relaxation to occur and ultimately determine the specimen thickness. This consisted of the following steps in load control:

- The indenter was lowered into position into the chamber to contact the microtomed surface of the specimen until a load of 0.25N was recorded, and which was maintained for 60s;
- The load was then ramped up to 5N at a rate of 0.05N/s (A);
- The load was maintained at 5N for 60s (B);
- The cartilage was unloaded at a rate of 0.025N/s until the load was once again 0.25N (C); after which
- The load was maintained at 0.25N for 10min (D).

This is a similar methodology to that used by other groups who also tested cartilage under confined compression conditions (Ateshian et al., 1997, Huang et al., 2005). An example of these duties performed by MTS (desired input load profile & actual output load profile performed by MTS) and the response from a cartilage specimen is shown in figure 4-5.

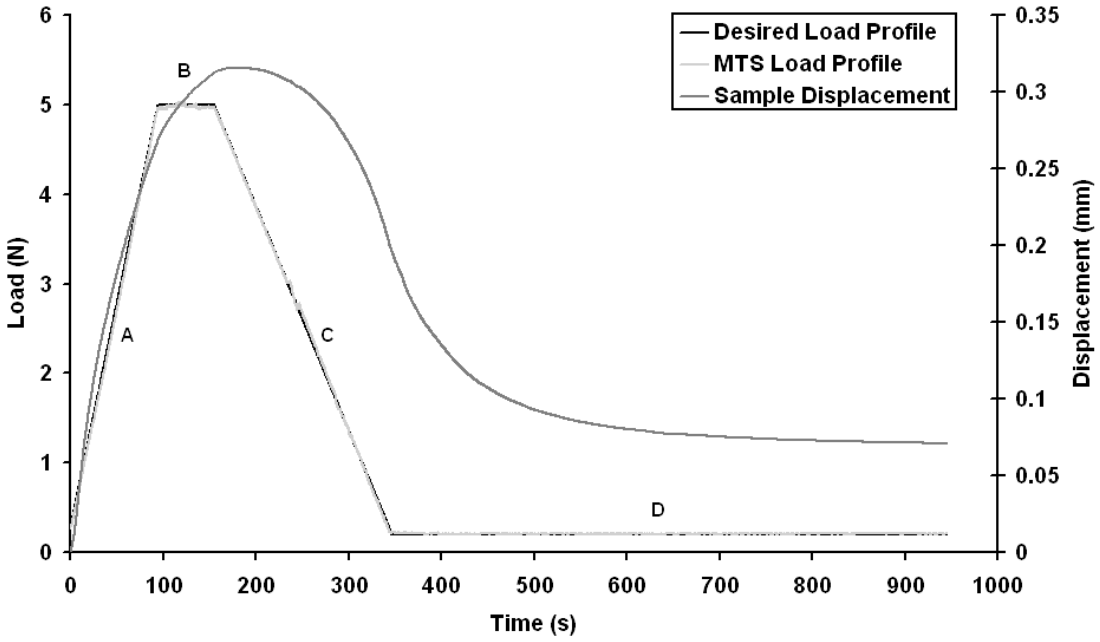

Figure 4-5. An example of the cartilage pre-test program input and sample response.

The digital crosshead position was noted at this location (LE2) and the difference was calculated to determine the cartilage sample thickness (LE1 - LE2). The reference displacement at this point was also defined as zero strain (i.e. ε=0, λ=1). Once the thickness of a sample was known, a series of ramp and hold cycles in steps of 10% strain compression up until 50% strain was performed with the MTS in displacement control. The ramps were performed at a rate of 25μm/min, while the dwell periods were maintained for a period of 30min, during which load was concurrently recorded by the load cell.

Five cartilage samples from each of the six harvest location sites were tested. The equilibrium compressive stresses at each of the 10-50% strain conditions were deemed to be the lowest stresses recorded at each of those corresponding dwell periods. The zero strain aggregate modulus for each sample was also determined using a non-linear biphasic equation for tissue undergoing finite deformation (Holmes and Mow, 1990). This equation has been used previously for determining the aggregate modulus of both cartilage (Ateshian et al., 1997, Huang et al., 2005) and intervertebral disc tissue (Heneghan, 2008, Perie et al., 2006a, Perie et al., 2006b). The equation states that the equilibrium compressive stress can be related to the stretch ratio in the following manner;

$$\sigma^e = \frac{1}{2} H_{A0} \left(\frac{\lambda^2 - 1}{\lambda^{2\beta+1}}\right) e^{\beta(\lambda^2 - 1)} \qquad \textbf{Equation 4-1}$$

Where H_{A0} is the initial zero aggregate modulus and β is a non-dimensional constant which measures the sensitivity of σ^e to large strains. Furthermore, the strain dependent aggregate modulus can be determined by calculating the derivative of equation 4-1 with respect to stretch ratio yielding;

$$H_A = \frac{d\sigma^e}{d\lambda} = \frac{1}{2} H_{A0} \left(\frac{\lambda^2 + 1 + 2(\lambda^2 - 1)^2}{\lambda^{2(\beta+1)}} \right) e^{\beta(\lambda^2 - 1)}$$ **Equation 4-2**

In order to determine the parameters H_{A0} and β in equation 4-1, curve fitting using non-linear least squares regression was performed using Matlab. A typical example of the curve fitting results is shown in figure 4-6 and table 4-1. In this case H_{A0} and β are designated the labels *a* and *b* respectively.

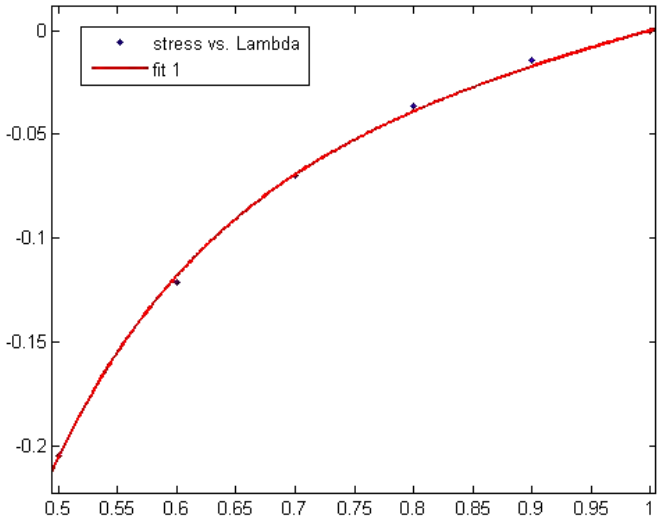

Figure 4-6. Typical example of Matlab curve fitting to equilibrium data.

Table 4-1. Matlab curve fitting results to figure 4-6.

General Model
f(x) = (0.5*a)*((x^2-1)/(x^(2*b+1)))*exp(b*(x^2-1))
Coefficients (with 95% confidence bounds)
a = 0.2332 (0.2153, 0.2512) b = 0.7307 (0.5906, 0.8708)
Goodness of Fit
SSE: 3.344e-005 R-square: 0.9994 Adjusted R-square: 0.9992 RMSE: 0.002891

4.2.3 s-GAG Assay

Once mechanical testing was complete, samples were cut in half with a scalpel, freeze dried for 24 hours, their weight recorded and stored. A digestion solution was then prepared consisting of the following:

- 100ml 0.2M sodium phosphate buffer, pH 6.4.
- 0.1M sodium acetate.
- 0.01M Na_2EDTA.
- 0.005M cysteine.
- After all the above components had dissolved 80µl of crystallised papain suspension was introduced.

The stored tissue samples were then placed in 1.5ml micro-centrifuge tubes and 1ml of the digestion solution was added. The tubes were then placed in a water bath at 65ºC and incubated for 18 hours with agitation every few hours were possible. The tubes were then spun at 10,000rpm for 10 minutes to clarify the solution and the supernatant

decanted for use in a commercial s-GAG assay kit (Blyscan, Biocolor, Carrickfergus, Northern Ireland).

The samples needed to be appropriately diluted to be measured against the assay calibration curve. This was done in the following manner:

- Dry weight of cartilage sample (≈ 20mg) was added to 1ml of digestion solution giving a sample concentration of 20mg/ml.
- Assuming a conservative level of GAG content – 20%, gives 4mg/ml GAG concentration.
- This was then diluted to give 1µg/10µl, which was the same protein concentration used in the standards supplied to generate the calibration curve.
- The calibration curve was accurate up to 5µg of protein, thus 20µl of each sample solution was measured against the calibration curve midway, with some room above this point on the curve as initial GAG approximation was conservative.

Assessment of GAG content in the supplied standards for the calibration curve and the actual tissue samples was performed using a reagent dye (dimethylmethylene blue) and a spectrometer against a reagent blank.

- The sample to be measured was made up to 100µl in a 1.5ml micro-centrifuge tube using the same solvent as the reagent blank (in this case de-ionised H_2O).
- 1ml of the reagent dye was added to the tube. They were then sealed, inverted and placed on a mechanical shaker for 30 minutes.
- Tubes were then transferred to a micro-centrifuge and spun at 12,000rpm for 10 minutes during which time pellets formed.
- The supernatant was carefully drained and replaced with 0.5ml of dissociation fluid. Tubes were then sealed and the dye pellet dissolved using a vortex.
- The resulting solution was then measured on a spectrometer at 656nm.

Duplicates were run for the standards used to generate the calibration curve. The zero standard (blank) was subtracted, the data plotted and fitted to a linear tread line (figure 4-7). Duplicates were also used for all cartilage samples and an average taken. Duplicates were repeated should their value be greater than +/-5% of the mean.

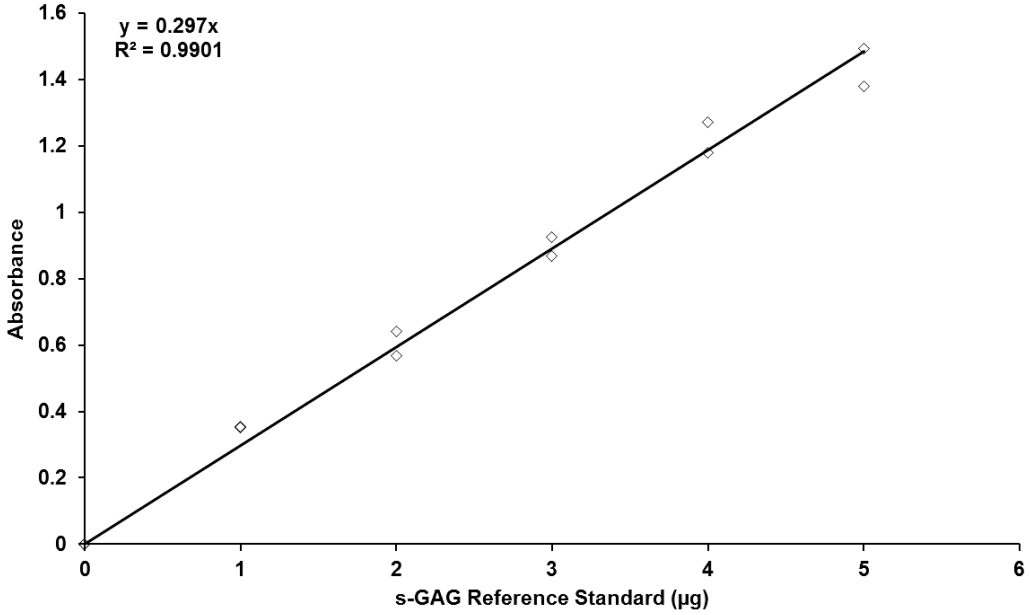

Figure 4-7. Calibration curve used to calculate s-GAG content.

4.2.4 Mechanical Testing of Bone

Cylindrical plugs of trabecular bone were subjected to uniaxial compression using an Instron E10,000 (Instron, Bucks, UK). Hydraulic tensile grips were adapted to become two solid compression platens by means of gripping to pieces of aluminium T-bar between the grips as shown in figure 4-8. The lower grip was connected in series to a 1,000N load cell. Prior, to testing the testing the sample length was measured using a Vernier callipers, then placed centrally upon the lower platen. The upper platen was lowered until contact was made with the top surface of the sample and a load of 0.5N was recorded. The load cell was subsequently tared and a deformation rate of 5mm/min was used to deform each specimen along their long axis until a drop off of load was

detected. The load-displacement curves recorded were converted appropriately to stress-strain curves, from which a number of material parameters including Young's Modulus (E), the ultimate compressive strength (UCS) and the yield strength (σ_y) were determined. The yield strength was calculated at a 0.2% strain offset.

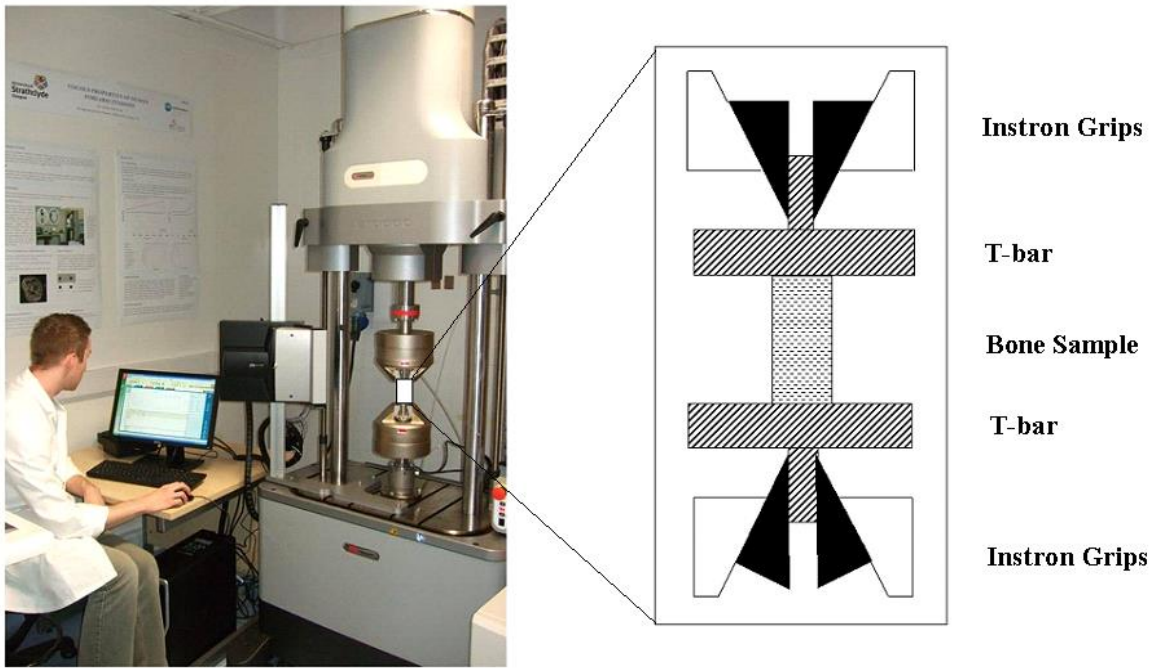

Figure 4-8. Instron E10,000 used for strength testing of bone samples complete with schematic of test set-up incorporating T-bar pieces into the hydraulic grips.

4.2.5 Statistics

Unless otherwise specified, all statistical analyses in chapter 4 were carried out using statistical software (Minitab^{TM}, v.16). Statistical variances between regions were determined by one way analysis of variance (ANOVA). Tukey's honesty significant difference test was used for post hoc evaluation of differences between groups. A student t-test was used to investigate significance between any two groups if so desired. A P-value of <0.05 was considered to be statistically significant.

4.3 Results

4.3.1 Mechanical Properties of Articular Cartilage

4.3.1.1 Cartilage Thickness

The results of the pre-test program to determine the cartilage thicknesses of the samples are presented in figure 4-9. Samples from both lateral groups were found to be significantly thinner than those from both PFG groups. There was also no significant difference between L1 & L2. The medial groups were compared to the PFG groups and both M1 & M2 were significantly thinner than PFG2 but not PFG1. Again, as it was for the lateral groups, no significant difference was found between these inter-condyle groups. However, interestingly, when a comparison was performed between the PFG groups, PFG1 was found to be significantly thinner. Finally, when the lateral groups were compared to the medial groups, L1 was significantly thinner than both medial groups, but L2 was only significantly different than M2. Overall, the mean cartilage thicknesses ranged from 1.57-1.69mm on the lateral condyle, 1.98-2.0mm in the medial compartment and 2.07-2.35mm on the patellofemoral groove region of the knee. Thus, the mean lateral to medial cartilage thickness ratio ranged from 0.79-0.85.

4.3.1.2 Cartilage Sample Compression

Thereafter, when all cartilage samples were tested they experienced a rise in compressive stress during the displacement phases with peak stresses occurring at the end of each of the ramp strains. These were followed by characteristic stress relaxation curves for each of the holding phases. A typical example of the strain applied to the samples and the stress recorded against time is shown in figure 4-10.

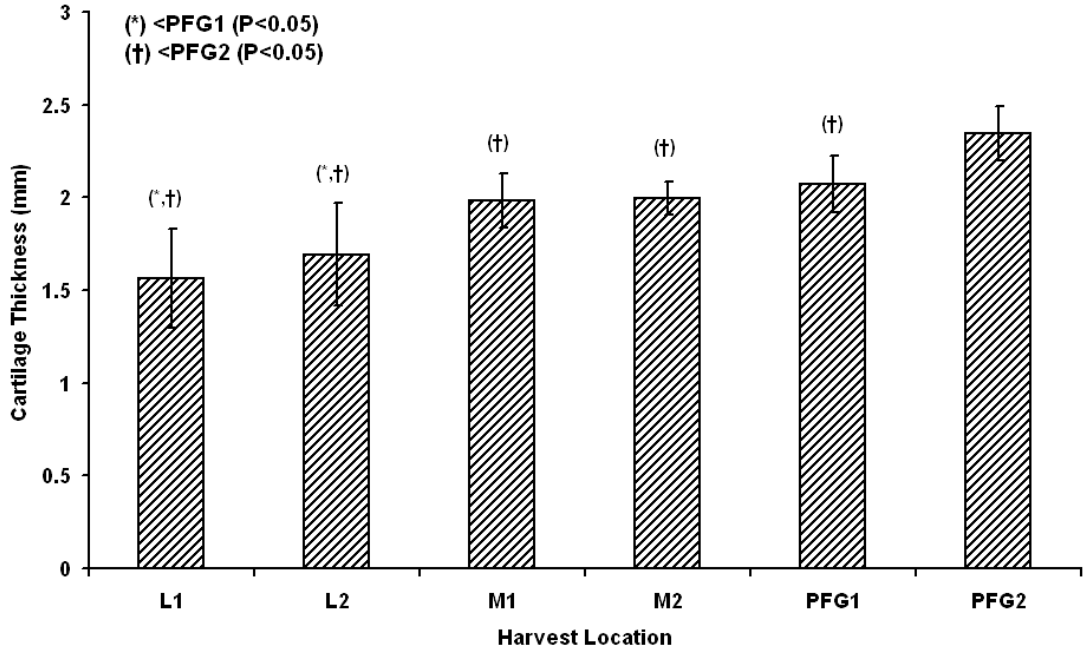

Figure 4-9. Cartilage thickness determined for each harvest location group. Results shown as mean +/- SD (n=5). Data was analysed using a 1-way ANOVA. Significant differences are found to exist between the lateral groups and both the medial and PFG groups.

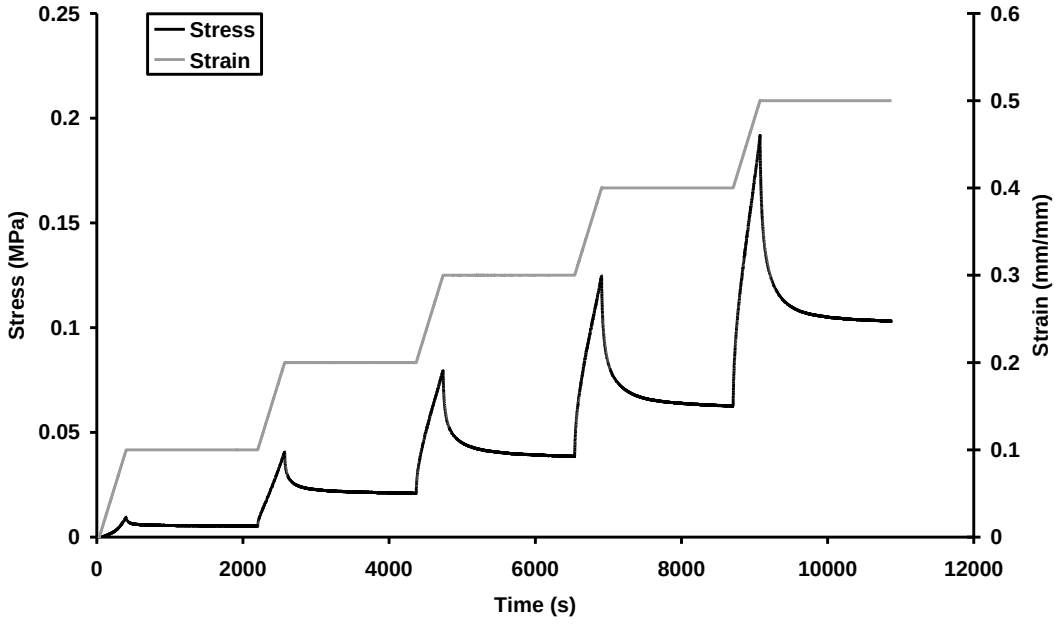

Figure 4-10. Typical example of step strain ramp and hold input and resulting stress recorded.

4.3.1.3 Equilibrium Stress

Figure 4-11 presents plots of the mean equilibrium stresses for each harvest location against strain (σ^e vs. ε). Equilibrium stresses are found to rise steadily against strain in an exponential fashion consistent with equation 3-1. At nearly all levels of strain, the patellar femoral groups were significantly greater ($P<0.05$) than the medial and lateral condyle groups. Exceptions did occur however for PFG1 against M1 & and for PFG2 against M1 at 0.1mm/mm strain. Differences between all the condyle groups were not significant, with the exception of groups M1 & L2 at 0.5mm/mm strain. A significant difference was also found to occur between both PFG groups at 0.3mm/mm strain levels onwards. Table 4-2 is intended to complement Figure 4-11, by highlighting the levels of strain where significant differences in equilibrium stresses occur between harvest site groups.

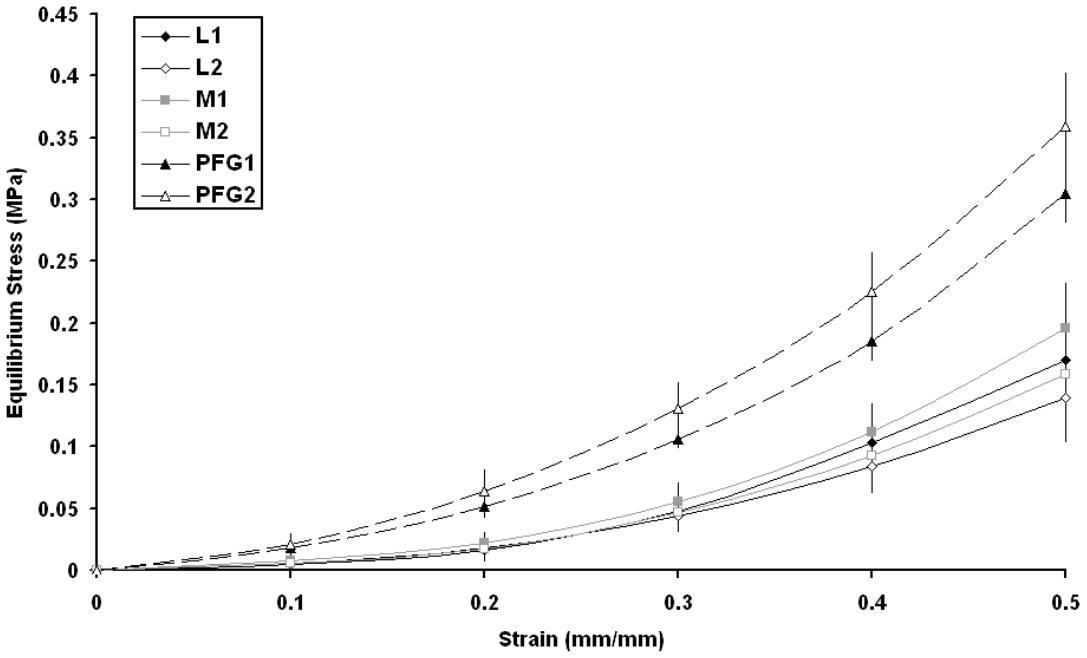

Figure 4-11. Equilibrium stresses recorded for each harvest location group against input strain. Results shown as mean +/- SD (n=5). Data was analysed using a 1-way ANOVA. Cartilage appears to be stiffer in the PFG rather than the femoral condyles.

Table 4-2. Areas where significant differences in equilibrium stresses were found to occur between harvest location groups. Values indicate the strain in mm/mm where significance occurs.

	L1	L2	M1	M2	PFG1	PFG2
L1	n/a	-	-	-	-	-
L2		n/a	-	-	-	-
M1		0.5	n/a	-	-	-
M2				n/a	-	-
PFG1	All	All	0.2 to 0.5	0.2 to 0.5	n/a	-
PFG2	All	All	0.2 to 0.5	All	0.3 to 0.5	n/a

4.3.1.4 Aggregate Modulus

The zero strain aggregate modulus (H_{A0}) was determined for all samples in each group according to equation 4-1. The calculated means for the groups are displayed in figure 4-12. The mean aggregate modulus for both PFG1 & PFG2 was found to be significantly larger than all the medial and lateral condyle groups ($P<0.05$). In all cases the magnitudes of the PFG groups were greater than twice those of the condyle groups. A near significant difference was also found to exist between both PFG1 & PFG2 when the groups were analysed separately using a student t-test ($P=0.052$).

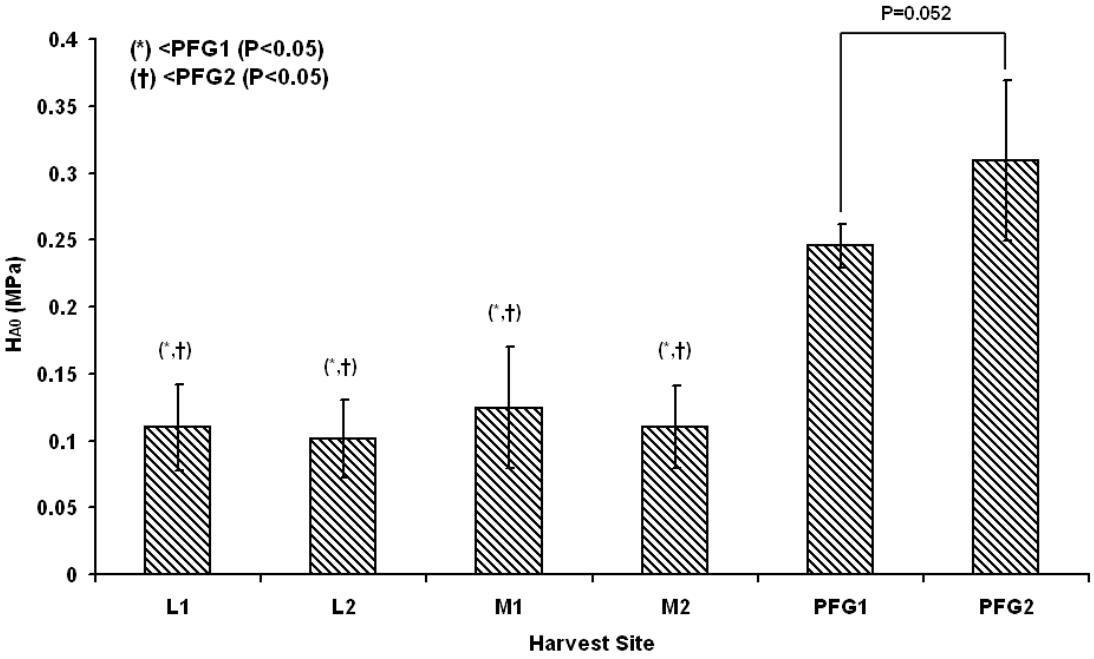

Figure 4-12. Calculated aggregate modulus for each harvest location group. Results shown as mean +/- SD (n=5). Data was analysed using a 1-way ANOVA. The significantly higher aggregate modulii in the PFG sites indicates once again cartilage is stiffer here.

Having calculated the zero strain aggregate modulus (H_{A0}), the strain dependent aggregate modulus (H_A) was calculated for each harvest site group using equation 4-2. Figure 4-13 presents a plot of H_A against strain for each of the harvest groups. It was found that the aggregate modulii in the PFG groups were significantly greater than the M1, M2, L1 & L2 groups at all strains, except in the M1 group at 0.5 mm/mm were no significant differences occurred against both PFG1 and PFG2 (P>0.05).

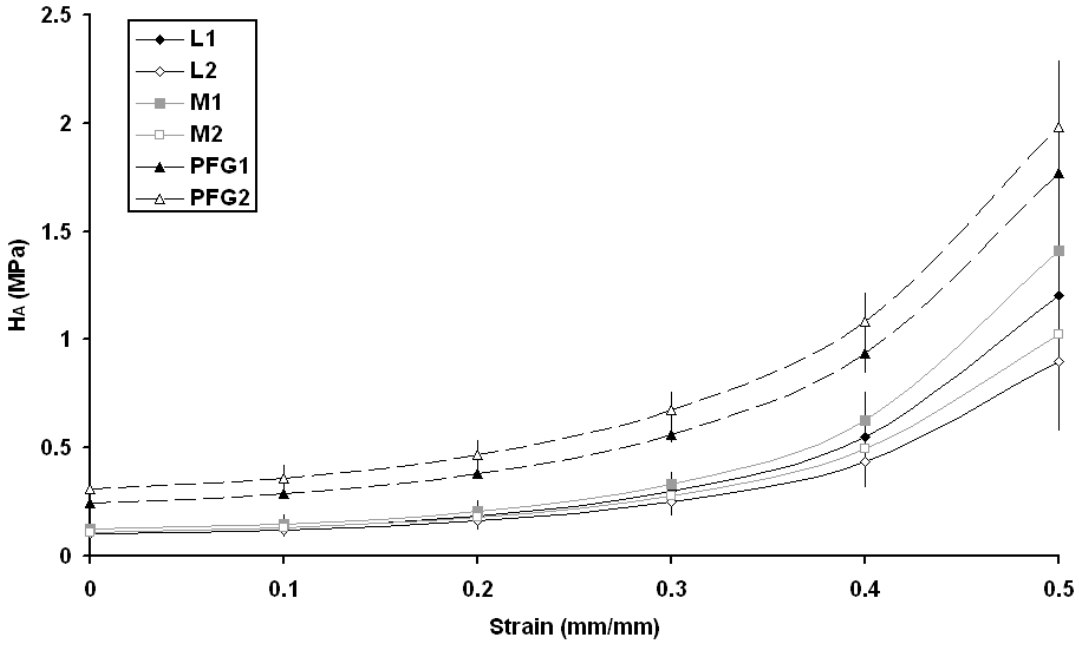

Figure 4-13. Calculated aggregate modulus for each harvest location group against strain.. Results shown as mean +/- SD (n=5). Data was analysed using a 1-way ANOVA. In all cases (except M1 at 0.5mm/mm) the differences in cartilage stiffness between the condylar and PFG groups is independent of applied strain.

Table 4-3 compiles the mean values of equilibrium stress (σ_e) and aggregate modulus (H_A) for each harvest location group at each level of applied strain (ε). The areas of significance against both the PFG1 & PFG2 are indicated in order to highlight the emerging trend of stiffness mismatch between the femoral condyles and the patellofemoral grove regions of the porcine knee.

Table 4-3. The equilibrium stress (σ_e) and aggregate modulus (H_A) for each harvest location group at levels of applied strain (ε). Values reported as mean (SD) (n=5). Data was analysed using a 1-way ANOVA. Black shading indicates <PFG1 & PFG2 whereas grey indicates <PFG2 alone (P<0.05).

	L1		L2		M1		M2		PFG1		PFG2	
ε	**σ_e (kPa)**	**H_A x10^3 (kPa)**	**σ_e (kPa)**	**H_A x10^3 (kPa)**	**σ_e (kPa)**	**H_A x10^3 (kPa)**	**σ_e (kPa)**	**H_A x10^3 (kPa)**	**σ_e (kPa)**	**H_A x10^3 (kPa)**	**σ_e (kPa)**	**H_A x10^3 (kPa)**
0	0	0.110 (0.032)	0	0.101 (0.029)	0	0.125 (0.045)	0	0.110 (0.031)	0	0.246 (0.016)	0	0.309 (0.060)
0.1	4.8 (1.9)	0.131 (0.036)	4.9 (2.1)	0.119 (0.033)	8.1 (3.9)	0.149 (0.050)	5.5 (4.3)	0.131 (0.035)	18.2 (12.1)	0.288 (0.019)	20.6 (8.8)	0.360 (0.066)
0.2	16.5 (7.5)	0.184 (0.041)	18.1 (7.1)	0.162 (0.042)	22.4 (9.1)	0.207 (0.053)	17.3 (10.6)	0.178 (0.042)	51.7 (9.4)	0.380 (0.024)	63.9 (18.3)	0.467 (0.075)
0.3	47.7 (14.4)	0.297 (0.046)	44.3 (13.2)	0.249 (0.063)	55.3 (16.8)	0.333 (0.061)	46.9 (12.8)	0.278 (0.053)	106.0 (7.7)	0.563 (0.042)	131.4 (21.4)	0.673 (0.089)
0.4	103 (15.6)	0.553 (0.040)	84.3 (22.0)	0.438 (0.123)	111.6 (23.6)	0.627 (0.136)	93.1 (15.0)	0.495 (0.078)	185.5 (16.4)	0.936 (0.092)	225.2 (32.5)	1.085 (0.136)
0.5	170.4 (17.2)	1.201 (0.068)	139.1 (35.9)	0.899 (0.322)	195.5 (37.3)	1.410 (0.508)	158.1 (25.5)	1.023 (0.180)	305.1 (24.6)	1.771 (0.238)	359.0 (44.4)	1.981 (0.312)

4.3.2 Mechanical Properties of Trabecular Bone

4.3.2.1 Bone Sample Compression

A typical loading curve is shown in figure 4-14. The load-deformation response of the uniaxial compressive tests consisted of an initial non-linear region (A), followed by a linear, elastic region (B) and a region of yield (C). Loading then continued until failure occurred, defined here as the first detectable decrease in load. An extensive region of plastic behaviour was witnessed post-yield. Initially strains are considerable with little change in stress (D), but this is then followed by a final rise in stiffness before failure (E).This post-yield behaviour can be related to the structural changes that occur in the specimen. Plates of bone collapse upon one another, explaining the slight wavering of the curve, until the material becomes compacted and fracture finally occurs.

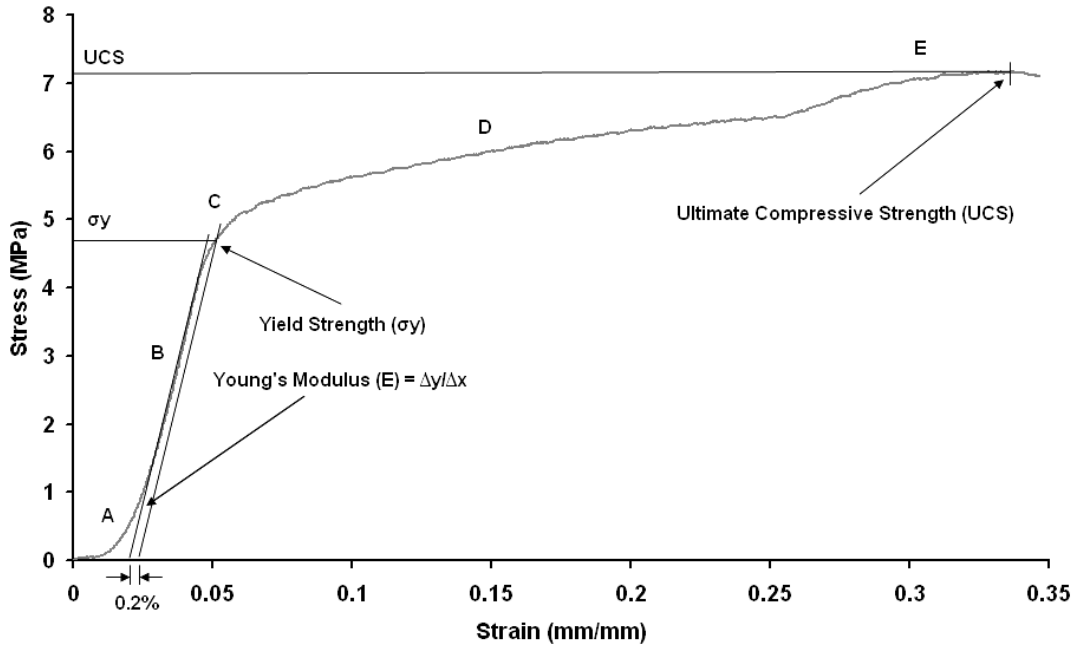

Figure 4-14. Typical loading curve associated with bone samples (in this case a M1 specimen) under uniaxial compression.

4.3.2.2 Bone Strength

Figure 4-15 presents the ultimate compressive strength (UCS) and yield strength (σ_y) results for all six of the harvest location groups. Beginning with the UCS results, significant differences are observed to occur between the L2, M1 & M2 groups and both PFG groups, while the L1 group was found to be significantly higher to the PFG2 group but not the PFG1 group. There was no statistically significant difference between the UCS of PFG1 & PFG2. Within the condyle groups, no significant difference emerged between L2, M1 & M2, but L1 was found to be lower than L2 & M1 but not M2.

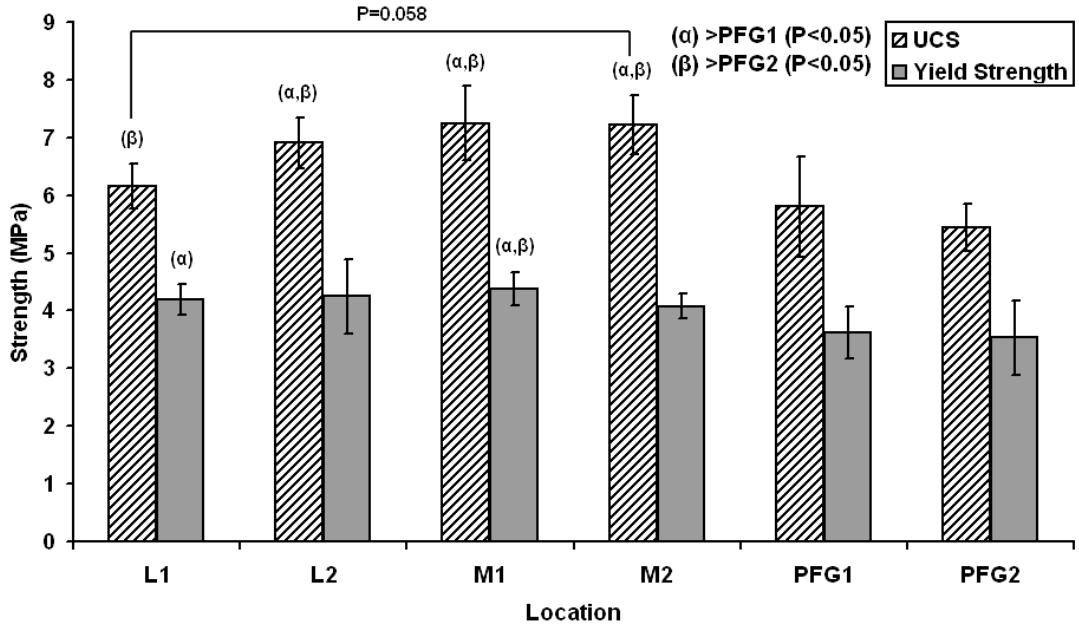

Figure 4-15. Ultimate compressive strength (UCS) and yield strength (σ_y) at sites of harvest. Results shown as mean +/- SD (n=5). Data was analysed using a 1-way ANOVA. Bone is significantly stronger in femoral sites, particularly the medial groups, compared to PFG sites.

In terms of yield strength, only the M1 & L1 groups of the load bearing areas showed any significant difference against the PFG groups. M1 was significantly higher than both PFG1 & PFG2, whereas L1 was higher than PFG1 alone ($P<0.05$). No significant difference was discovered between all of the condyle groups or indeed the PFG groups.

The UCS and yield strength results indicate that the bone harvested in the femoral condyles, especially the medial condyles, is stronger that the patellofemoral grove sites.

4.3.2.3 Young's Modulus

The results for the Young's modulii of the harvest groups are displayed in figure 4-16. The medial groups emerge as the stiffest harvest locations. In fact, bone is found to be significantly stiffer in the M1 group when compared to the PFG1 & PFG2 groups ($P<0.05$). The same trend is seen with M2 against PFG1 & PFG2. No statistical difference was discovered between the lateral groups and the PFG groups. Although the lateral groups are lower, particularly L1, no statistical significance was also found in their modulii and those of the medial groups.

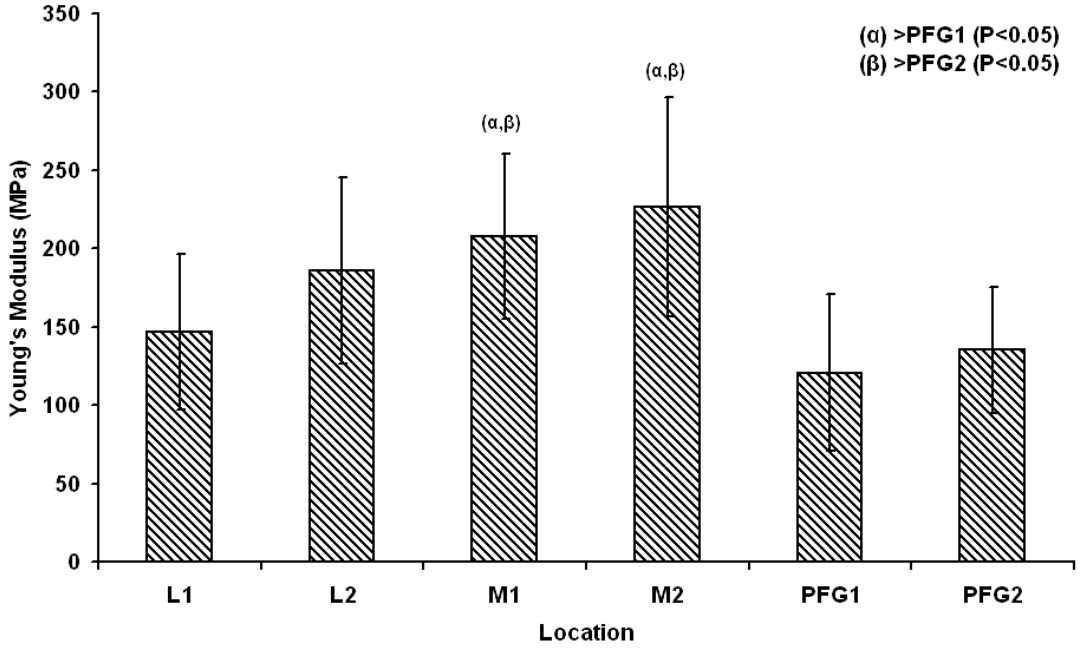

Figure 4-16. Young's Modulus results for harvest location groups. Results shown as mean +/- SD (n=5). Data was analysed using a 1-way ANOVA. Bone is found to be significantly stiffer in the medial condyle sites compared to the PFG sites.

4.3.3 s-GAG Assay Results

No significant difference in s-GAG content was found to exist between the majority of location groups, the only exception being L2 < PFG2 ($P<0.05$). All groups were found to contain approximately between 25 & 30% dry weight s-GAG (figure 4-17).

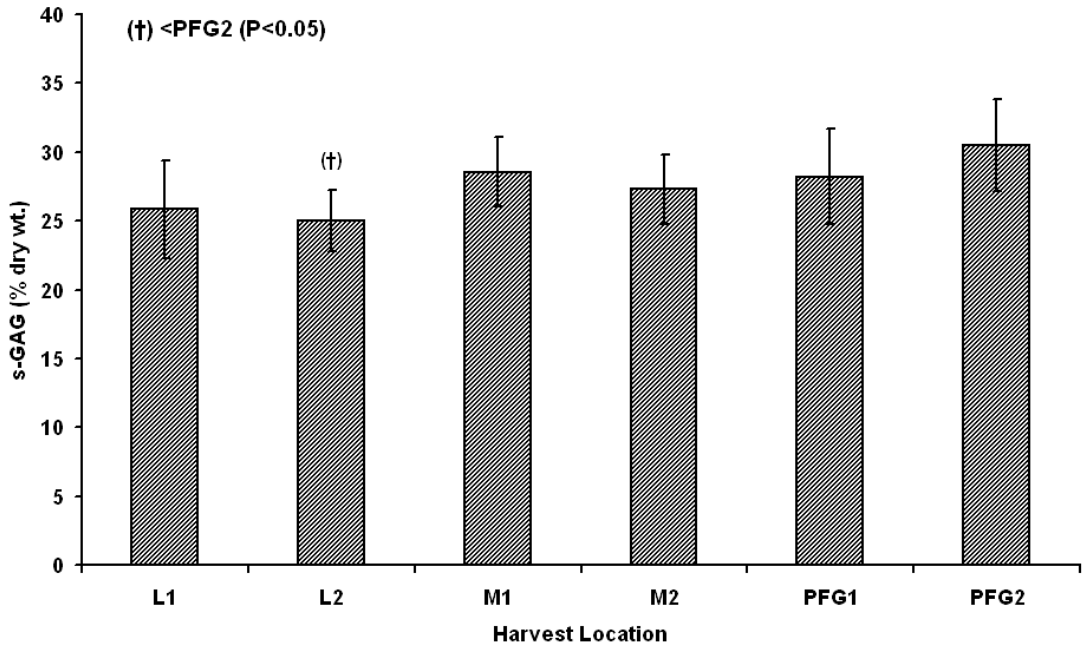

Figure 4-17. s-GAG content in cartilage for each harvest location. Results shown as mean +/- SD (n=5). Data was analysed using a 1-way ANOVA. No significance was found between groups bar L2 < PFG2.

4.3.4 Correlating the Mechanical & Biochemical Properties of the Cartilage

Scatterplots were created to investigate if any correlations existed between the mechanical and biochemical properties of the cartilage tested. Specifically, these were correlations between cartilage thickness and aggregate modulus, the s-GAG content and the aggregate modulus, and between the cartilage thickness and the s-GAG content.

Figure 4-18 indicates a strong correlation exists between cartilage thickness and aggregate modulus when all harvest groups are analysed as a whole ($r=0.605$, $P<0.001$) but not when condylar and PFG groups are analysed independently. This suggests a specimen's stiffness in confined conditions is due, at least to some extent, on the site dependent thickness in question.

Figure 4-19 presents a scatter plot of s-GAG content against aggregate modulus. In this instance the data suggests correlative trends between s-GAG content and the aggregate modulus for condylar locations ($r=0.771$, $P<0.001$), PFG locations ($r=0.597$, $P=0.068$) and all specimens as a whole ($r=0.606$, $P<0.001$). The higher P-value in the PFG group is most likely due to the smaller sample population. Figure 4-19 is suggestive that greater PG content tends to result in a larger H_{A0}. However, this is unlikely to be the full story as collagen and collagen matrix architecture are also likely to play a role which may also explain the clear separation of condyle and PFG groups in the plot.

Figure 4-20 demonstrates that no correlation exists between cartilage thickness and s-GAG content either for condylar and PFG groups, or all the specimens as a whole. It appears that although both cartilage thickness and s-GAG content both seem to affect the aggregate modulus of the specimen, they do so independently of one another's affects.

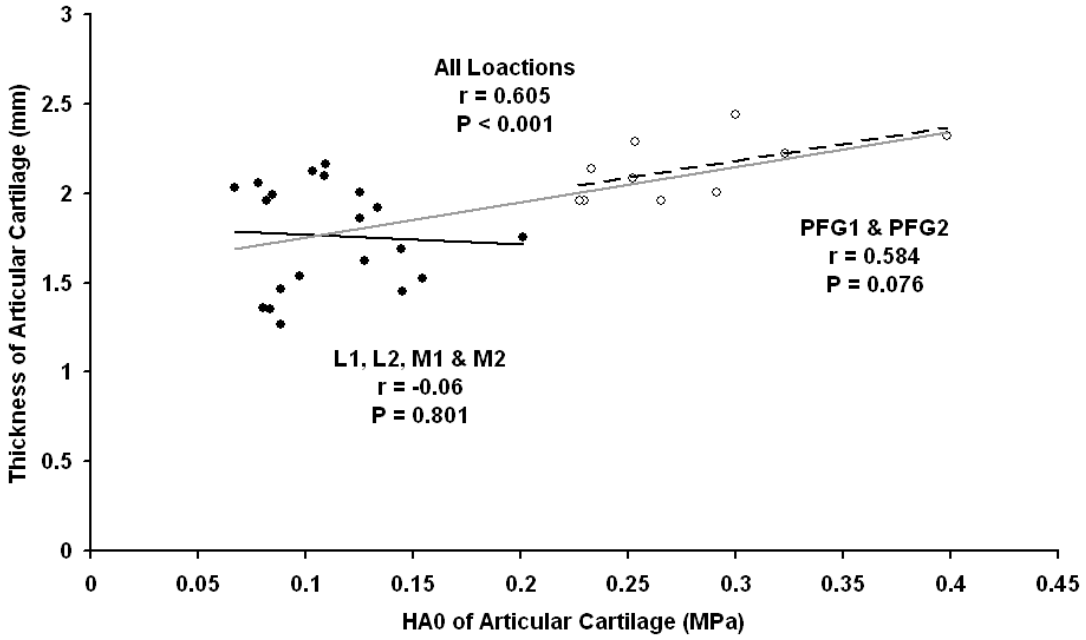

Figure 4-18. Scatterplot of sample thickness vs. H_{A0} for all cartilage specimens tested. Solid black treadline - L1, L2, M1 &M2, dashed treadline - PFG1 & 2, Solid grey treadline – All.

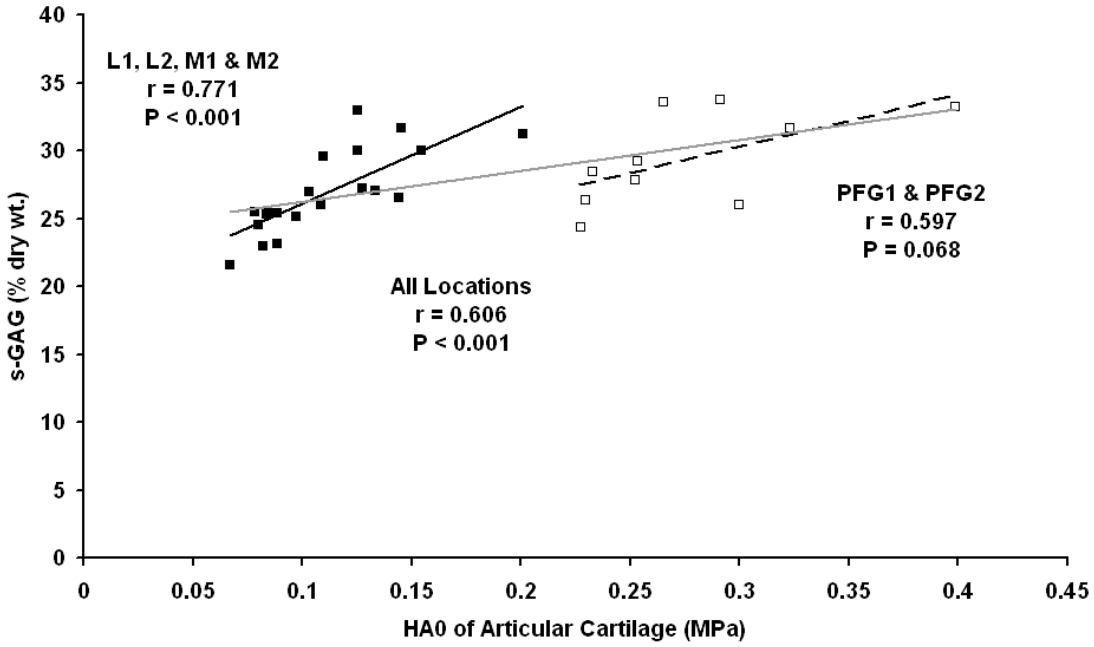

Figure 4-19. Scatterplot of s-GAG content vs. H_{A0} for all cartilage specimens tested. Solid black treadline - L1, L2, M1 &M2, dashed treadline - PFG1 & 2, Solid grey treadline – All.

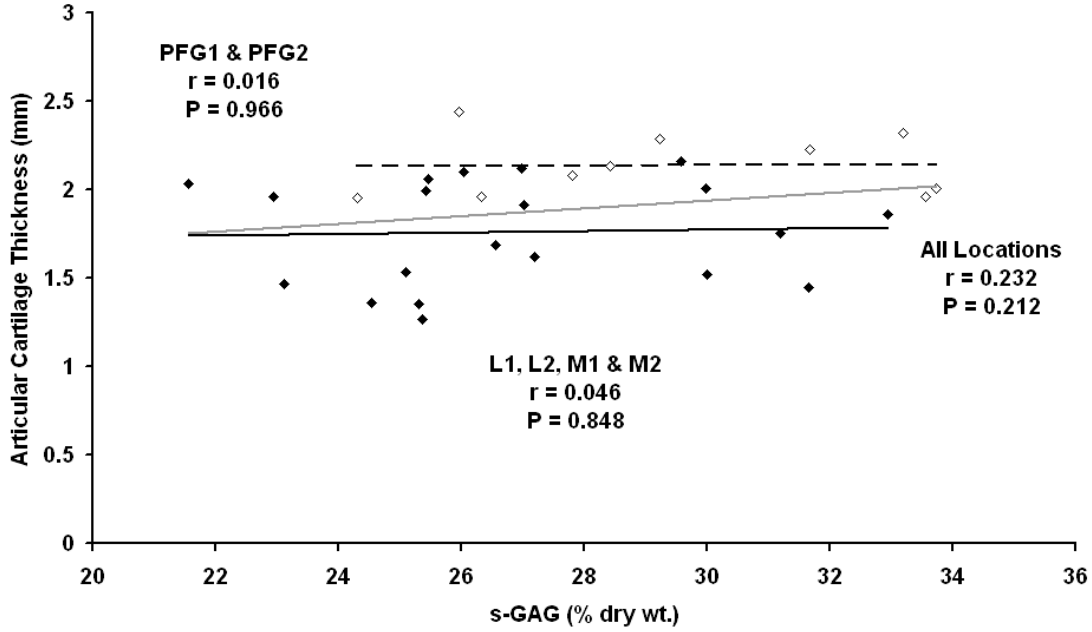

Figure 4-20. Scatterplot of sample thickness vs. s-GAG content for all cartilage specimen tested. Solid black treadline - L1, L2, M1 &M2, dashed treadline - PFG1 & 2, Solid grey treadline – All.

4.3.5 Correlating the Mechanical Properties of the Cartilage & Bone

When the material parameters determined for the trabecular bone (UCS, σ_y & E) are combined with the cartilage material parameter H_{A0} for each harvest location, significant differences occur between particular femoral condyle locations and the patellofemoral groove locations. These are presented in table 4-4. For both cartilage and bone, the areas where most difference is found to occur is in the medial condyle harvest locations. There is striking evidence to suggest that cartilage and bone from both the PFG locations are too stiff and weak respectively compared to medial condyle osteochondral tissues. This is highlighted using the dark background shading.

Table 4-4. The ultimate compressive strength (UCS), yield stress (σ_y) & Young's modulus results for the trabecular bone and the zero strain aggregate modulus (H_{A0}) for the cartilage taken from each harvest location. Values reported as mean (SD) (n=5). Data was analysed using a 1-way ANOVA. Black shading indicates <PFG1 & PFG2, dark grey indicates <PFG2 alone & light grey indicates <PFG1 alone (P<0.05).

	L1	L2	M1	M2	PFG1	PFG2
UCS (MPa)	6.15 (0.39) PFG2	6.90 (0.45) PFG1 & PFG2	7.25 (0.64) PFG1 & PFG2	7.23 (0.51) PFG1 & PFG2	5.80 (0.87)	5.44 (0.41)
σ_y (MPa)	4.19 (0.26) PFG1	4.25 (0.64)	4.37 (0.29) PFG1 & PFG2	4.08 (0.22)	3.62 (0.45)	3.53 (0.64)
E (MPa)	146.92 (49.68)	185.77 (59.57)	207.57 (52.67) PFG1 & PFG2	226.66 (70.19) PFG1 & PFG2	120.73 (50.17)	135.45 (40.25)
H_{A0} (MPa)	0.110 (0.032) PFG1 & PFG2	0.101 (0.029) PFG1 & PFG2	0.125 (0.045) PFG1 & PFG2	0.110 (0.031) PFG1 & PFG2	0.246 (0.016)	0.309 (0.060)

Scatterplots were created to determine if the aggregate modulus of the cartilage correlated with the compressive properties of the bone beneath it. *UCS* & σ_y correlated against H_{A0} only when all groups were analysed as a whole (P=0.001 in both instances), but not for condylar or PFG groups alone in figures 4-21 & 4-22 respectively. However the weight bearing and non-weight bearing sites correlated independently for *E* against H_{A0} (P<0.001 & 0.052 respectively), indicating a site-specific relationship (figure 4-23).

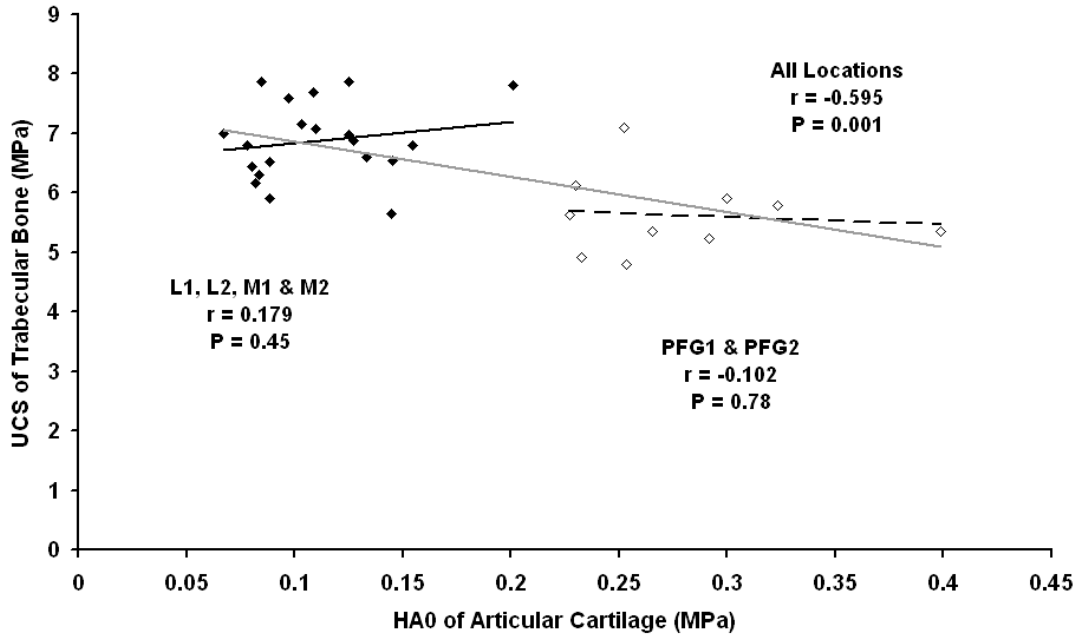

Figure 4-21. Scatterplot of UCS of bone vs. H_{A0} of the cartilage above it for all specimens tested. Solid black treadline - L1, L2, M1 & M2, dashed treadline - PFG1 & 2, Solid grey treadline – All.

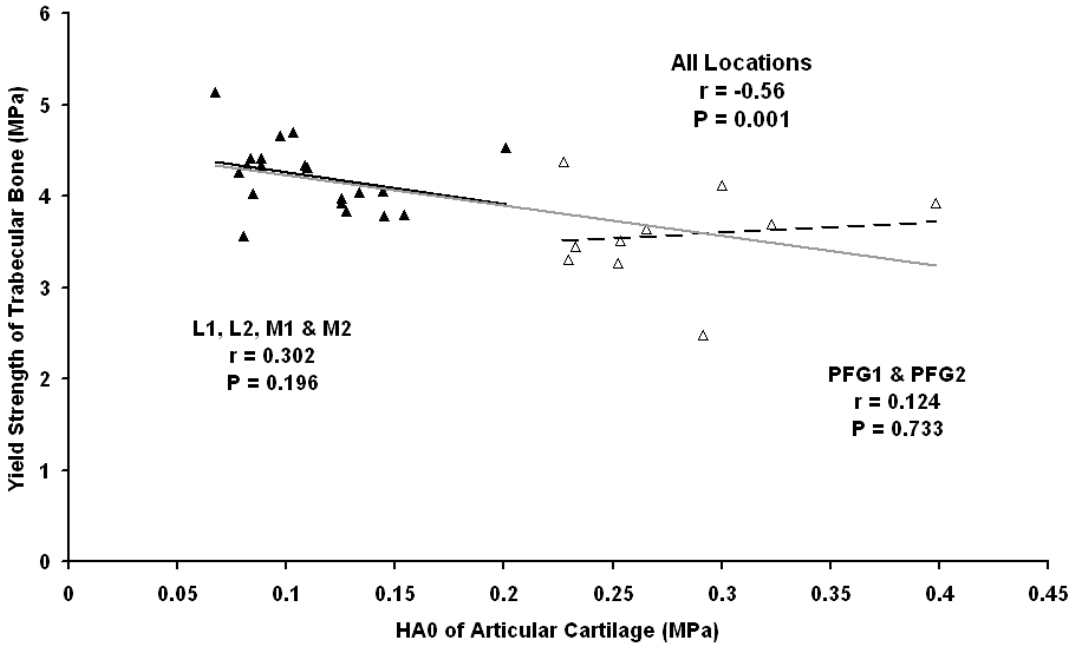

Figure 4-22. Scatterplot of σ_y of bone vs. H_{A0} of the cartilage above it for all specimens tested. Solid black treadline - L1, L2, M1 &M2, dashed treadline - PFG1 & 2, Solid grey treadline – All.

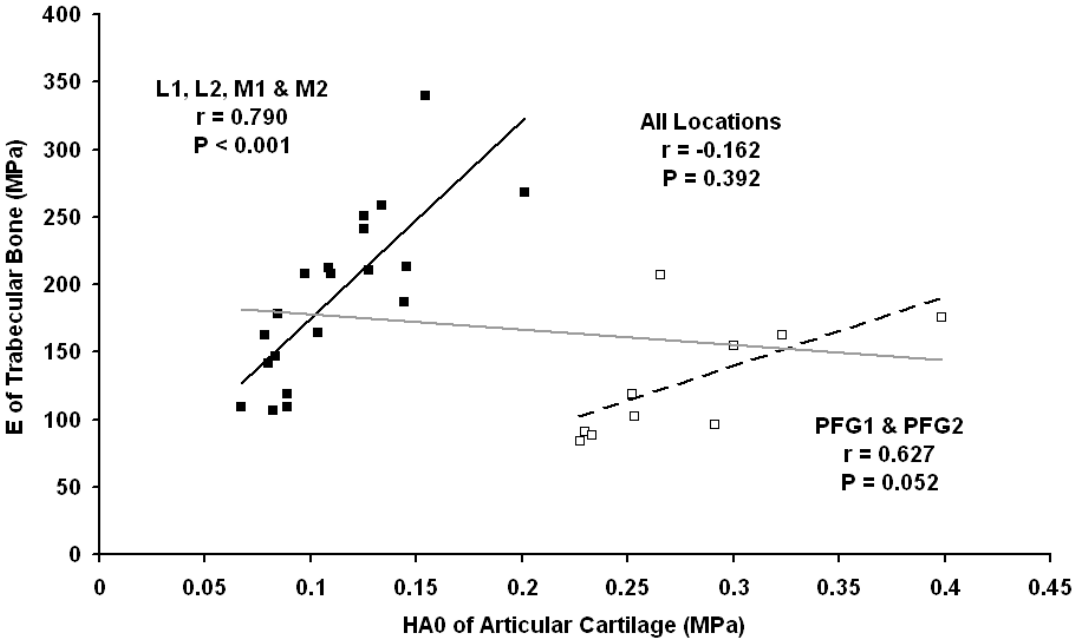

Figure 4-23. Scatterplot of *E* of bone vs. H_{A0} of the cartilage above it for all specimens tested. Solid black treadline - L1, L2, M1 &M2, dashed treadline - PFG1 & 2, Solid grey treadline – All.

4.4 Discussion

This chapter aimed to discover the regional variation in the mechanical characteristics of articular cartilage and trabecular bone in the porcine knee. This was achieved by mechanically testing these tissues in six areas of interest across the knee; two on the medial condyle (M1 & M2), two on the lateral condyle (L1 & L2) and two on the patellofemoral groove (PFG1 & PFG2). The condyles and the patellofemoral groove are known to be sites through which large joint forces are transmitted. However, the kinematics and magnitude of forces vary in these joints and consequently these sites were selected on the principle that their properties may vary in accordance with activity. This is of particular interest when considering OAT procedures, particularly mosaicplasties, where multiple osteochondral plugs are routinely harvested from non-load bearing sites to replace a defect in a load bearing site as these grafts are unlikely to truly replicate the mechanics of the host site.

The mean thicknesses calculated for L1 & L2 were 1.57±0.27 & 1.69±0.28mm respectively. This corresponds well with a study performed by Wayne et al., who used both radiographic and optical methods to determine cartilage thickness across the entire width of porcine lateral condyles (1.843±1.163 & 1.844±1.161mm respectively) (Wayne et al., 1998). The cartilage thickness in the PFG2 location was found to be significantly greater than PGF1. Furthermore, both PFG groups had significantly thicker cartilage than both lateral groups, whereas both medial groups were only significantly different to PFG2 (figure 4-9). Similar results to these were found in bovine knees, with cartilage on the lateral femoral groove found to be more than 30% thicker than the medial femoral groove (Kiviranta et al., 2006). In fact, thicker cartilage has been shown to be present in the patellofemoral groove for bovine and human species but not so for dog, monkey or rabbit (Athanasiou et al., 1991).

The overall thickness of cartilage on the medial condyle was found to be significantly thicker than the lateral condyle. This was a phenomenon also seen in ovine knees by

Armstrong et al., where central areas of the medial condyle were found not only to have thicker cartilage, but also a thicker subchondral bone plate beneath it, suggesting that more load passed through the medial joint compartment (Armstrong et al., 1995). Furthermore, it has been demonstrated that medial femoral cartilage is thicker in bovine, dog, rabbit, monkey (Athanasiou et al., 1991), ovine (Armstrong et al., 1995) and now porcine models (this study). Intuitively, like these animal models, one may suspect that there may be thicker cartilage on human medial condyles, as the knee adduction moment during stance phase should cause a greater proportion of load to pass through the medial joint compartment. Yet, this does not seem to be the case, as there appears to be thicker cartilage present on the lateral condyle rather than the medial (Eckstein et al., 2001, Koo and Andriacchi, 2007, Li et al., 2005).

To say this is simply because the animals previously mentioned are quadrupeds seems a rather simplistic deduction. However, it is not unwarranted to deduce there may be interspecies structural variations in the knee that may cause a greater quantity of cartilage to develop in the opposite compartment. For example, it has been demonstrated that the ovine lateral femoral condyle and tibial plateau are larger than their medial counterparts (Armstrong et al., 1995), whereas the reverse is the case in humans (Koo and Andriacchi, 2007, Iwaki et al., 2000). Therefore, it is most likely that it is the presence of a greater contact pressure in a compartment rather than the magnitude of dynamic load that governs cartilage thickness (Koo and Andriacchi, 2007).

Confined compression testing was performed on cartilage samples from each location to initially discover their aggregate modulus (H_{A0}), which once known, allows for determining of their strain-dependent aggregate modulus (H_A). This was achieved by performing multiple ramp and hold cycles and using the corresponding equilibrium data recorded to develop a relationship between the compressive equilibrium stress (σ^e) and the stretch ratio (λ). This relationship was then interpreted using a non-linear biphasic equation which can determine H_{A0} (Holmes and Mow, 1990).

After applying sequential displacement ramping to the cartilage, the equilibrium stresses were found to increase in an exponential fashion with increasing strain as expected and in line with previous studies (Ateshian et al., 1997, Huang et al., 2005). In the majority of cases, the equilibrium stresses at both PFG1 & 2 were found be increasingly larger than all of the condyle groups. Furthermore, little significant difference was found between the stresses observed within the condyle groups with increasing levels of strain (figure 4-11 & table 4-2). As a consequence of the significant differences found between the equilibrium stress curves of condylar and patellofemoral locations, it is not surprising therefore that this pattern is translated into the values determined for the aggregate modulus and strain-dependent aggregate modulus. Indeed, following the curve-fitting procedure, values for the aggregate modulus were found to range from approximately 0.1-0.125MPa in the condyles and 0.2-0.3MPa in the patellofemoral groove (figure 4-12). These values of the aggregate modulus were found to correlate with sample thickness when both condyle and patellofemoral groups were analysed as a whole ($r=0.606$, $P=0.001$). However, as no significant correlation was found to exist within these groups when taken on their own, any relationship between cartilage thickness and H_{A0} must be put into doubt for this porcine model at least.

Previous studies quote aggregate modulus values of 0.4MPa for bovine glenoid cartilage (Ateshian et al., 1997), 0.178 & 0.141MPa for bovine glenoid and humeral cartilage respectively (Huang et al., 2005), 0.754MPa for bovine humeral cartilage (Jurvelin et al., 1997), 1.113-2.084MPa for canine knee articular cartilage (Jurvelin et al., 2000), 0.87, 0.66 & 0.38MPa for bovine humeral, patellar and femoral cartilage respectively (Korhonen et al., 2002a), 0.38 & 0.47MPa for bovine patellofemoral cartilage (Chen et al., 2001, Schinagl et al., 1997) and 0.11-0.31MPa for bovine femoral condyle and patellofemoral cartilage (Williamson et al., 2001). Little investigation has been invested into determining the aggregate modulus of porcine articular cartilage.

In a study by Willet et al., porcine cartilage from the femoral condyles and the patellofemoral groove were subjected to confined compression to determine the effect of

freezing at -20ºC on the tissue mechanics (Willett et al., 2005). The aggregate modulus was found to be 0.239 & 0.191MPa for the femoral condyles and 0.464 & 0.402MPa for the patellofemoral grove, before and after freezing respectively. It is noticeable that the magnitude of values for the aggregate modulus are markedly different from the values determined in this thesis, however distinctions in the methodologies can explain this feature, including a final applied strain of 0.35mm/mm and a shorter hold time of 1000s. Furthermore, an alternate means to calculate the aggregate modulus was employed which was based on a finite deformation model developed by Kwan et al. (Kwan et al., 1990). Nevertheless, what is apparent is the ratio between the aggregate modulus in the two investigated regions is remarkably similar in both studies, and that cartilage on the patellofemoral grove is significantly stiffer than that found on the condyles in pigs.

The work of Athanasiou et al. demonstrated that amongst other mammalian species this relationship did not seem to exist (Athanasiou et al., 1994). No difference in the cartilage aggregate modulus was discovered between the condyles and the patellofemoral groove in humans and dogs. In fact, in rabbits the medial condyle modulus was significantly higher than the groove, whereas monkey and bovine species had stiffer cartilage in both condyles rather than the patellofemoral grove – the reverse of the porcine model in this thesis. Yet, there is evidence to dispute the results of Athansiou & co-workers as, for example, Jurvelin et al. found cartilage in the patellofemoral groove to be stiffer than the condyles in dogs (Jurvelin et al., 2000), and Williamson et al. found no difference between the grooves and the condyles of adult cows (Williamson et al., 2001). Interpreting between such studies is not entirely routine, as there exists a broad range of methodologies in literature yielding an equally broad range of results. This does not solely rest on the experimental set-up, loading protocol or simply the species of animals used, but also the maturity of the animals in question.

In OAT, cartilage is routinely harvested from margins of the condyles and inter-condylar notch. The absence of sustained contact pressures in these harvest locations are therefore likely to result in thinner cartilage being present. Thaunat et al. found this to be the case,

postulating that gross mismatch in cartilage thickness may lead to abnormal stresses developing and poor function (Thaunat et al., 2007). In total, seven donor sites were analysed against four recipient sites and statistically different thicknesses were observed in 28 out of a possible 34 combinations. Nevertheless, it appears this particular shortfall may be accommodated for by countersinking the implanted graft slightly. Huang et al. found that when grafts are seated no more than 1mm below the native articular surface, the graft cartilage will thicken to meet the surface (Huang et al., 2004). What is worrying however is that human cartilage thickness has been found to be inversely correlated with its compressive modulus (Shepherd and Seedhom, 1999). Thus, one may deduce that cartilage grafts harvested from relatively non-weight bearing sites are inherently stiffer than their site of implantation and may produce some degree of stress shielding.

The s-GAG levels were found to be between 25-30% dry weight across all groups tested. No significant difference was found in the amount of s-GAG between any of the groups bar one pairing (PFG2>L2). This result was somewhat surprising considering that stiffer cartilage is often reported to be related to increased levels of PG (Julkunen et al., 2007, Kiviranta et al., 2006) and the patella-femoral groove sites had already proven to be significantly stiffer. Hence, a scatterplot was constructed plotting s-GAG levels against the H_{A0} of the sample. This plot was found to demonstrate a significant level of correlation when all groups when analysed as a whole ($r=0.606$, $P<0.001$). Thus, it may be proposed that although the quantitative difference in PG levels between certain condylar and patella-femoral groups may not be significant statistically, it is adequate to induce statistically relevant differences in the aggregate modulus between the same groups. The correlation of PG content and tissue stiffness across anatomical locations in this study compares well to the bovine model, as correlations have been observed between not only the Young's modulus and collagen content, but also the PG content of tibial, femoral condyle, patellar and humeral cartilage when grouped together ($P<0.01$ in both instances) (Kiviranta et al., 2006). Furthermore, this has also been demonstrated

between the equilibrium modulus and PG content of cartilage in the same harvest locations discussed here ($P<0.001$) (Julkunen et al., 2007).

The trends of regional cartilage PG content in this porcine knee model can be translated to more significant levels in human knees. Rogers et al. determined the GAG content in what were deemed to be non-weight bearing (patellar groove, margins of the medial & lateral condyles) and weight bearing (medial & lateral femoral condyles) areas in 13 human knees (Rogers et al., 2006). These of course are areas of osteochondral harvest and implantation respectively. Results demonstrated a significantly greater amount of GAG in the weight bearing sites. Given what has just been discussed about the relationship between GAG content and the aggregate modulus in these sites, it may be extended that GAG content alone does not contribute to increased stiffness and that other factors such as collagen content and distribution may play a role.

Alterations may occur during the development of cartilage with age such as its thinning/thickening or changes in the structure of macromolecules or indeed the quantity of these molecules (Hyttinen et al., 2009, Julkunen et al., 2009, Rieppo et al., 2009, Williamson et al., 2001). These changes are the most likely explanation as to why the aggregate modulus of the patellofemoral groove is greater than the condyles in the porcine model as they are relatively young at slaughter (6-8 months), effectively at adolescence when translated to human models. This will be discussed in much more detail in chapter 6 when reviewing the histological work performed, as it will encompass collagen as an accompanying structural macromolecule to PG and their distribution rather than simply their content alone.

A correlative investigation was also found to reveal that no relationship existed between s-GAG content and cartilage thickness ($r=0.046$, $P=0.848$). This proved to be an interesting discovery considering that cartilage thickness has already been shown to correlate significantly with H_{A0} which, as we have just discussed, correlates with s-GAG content. It must be repeated however that cartilage thickness correlates with H_{A0} only

when all groups are taken as a whole and condyle and patellofemoral groove sites correlate poorly (r=-0.06, P=0.802 for condyles & r=0.584, P=0.076 for patellofemoral groove). Thus, it may be that cartilage thickness is an artefact of the anatomical site in this instance and is linked to the aggregate modulus in an alternative manner than its PG structural contributors such as collagen content. Evidence also exists demonstrating significant differences between rabbit femoral and tibial cartilage thicknesses can be reduced with maturation (Julkunen et al., 2009). Perhaps, a similar effect may occur with the femoral and PFG cartilage in pigs and hence the thickness/H_{A0} relationship is present merely because just two anatomical sites were analysed and at a relatively early developmental stage. Correlation is always a likely outcome when only two distinct sites are grouped so must be given due scepticism. Including an additional anatomical site, say from the tibia may destroy this correlation, indicating no overall relationship exists between thickness and the aggregate modulus.

After bone testing no eventful macroscopic changes were evident in both the medial and lateral groups, but such changes were observed in the patellofemoral groove groups, when marrow was often found to exude between the rapidly collapsing trabeculae. A larger proportion of marrow to bone material seemed to exist at these locations, with a greater concentration of bone present in the condyles. No microscopic observations were performed. The magnitude of results for UCS, yield strength and Young's modulus are approximately half of what has been determined in porcine vertebral trabecular bone (Ryan et al., 2008, Teo et al., 2006), but the UCS of porcine humeral trabecular bone appears to be very similar (approx. 6MPa when converted from failure load data) (Matter et al., 2001).

The UCS of the trabecular bone beneath the articular cartilage was found to be significantly higher in the condyle sites compared to the PFG sites in nearly all cases. This trend is not surprising in light of Wolff's law which states that a stress/structural morphology relationship exists in most biological tissues. Given that the femoral condyles distribute body weight more so than the PFG, the bone in the condyles would

encounter more stresses during daily activates which provides greater stimuli for adaptive remodelling to occur.

Interestingly, the observation of PFG bone being inferior was found only to occur significantly in the medial condyle with regard to Young's modulus. This feature relates well to the cartilage thickness results discussed previously. Cartilage was significantly thicker in the medial condyle over the lateral condyle, most likely a result of greater stresses existing in the medial joint compartment. If the Young's modulus of bone in the medial condyle, but not the lateral condyle, is significantly greater than that of the PFG, then this also tends to suggest that greater stresses exist and/or more load passes through the medial compartment.

The results of the regression analyses highlight that although there appears to be a correlation between both the UCS and yield strength of the bone against H_{A0} of the cartilage, this is only the case when all harvest sites are taken as a whole. There was distinctly no correlation found between these respective properties within the femoral and PFG groups. As was the case with the correlation between cartilage thickness and H_{A0}, and for the same reasons, this result should be viewed in a rather critical light. However, there certainly appears to be a correlation between the Young's modulus of the bone and the aggregate modulus of the cartilage above it. This was found to be more significant in the condyles ($r=0.790$, $P<0.001$) than the PFG ($r=0.627$, $P=0.052$), but the PFG group suffered from a distant outlier. Given the two well-defined correlations, it appears that this stiffness relationship between the cartilage and bone is specific to a particular anatomical site.

A relationship has also been demonstrated between the stiffness of cartilage and bone in human tibias and then extended to demonstrate a further correlation between the elastic energies of the tissues (Ding et al., 1998, Rohl et al., 1997). This indicates that articular cartilage and trabecular bone may act together as a unit in response to mechanical loading.

The testing performed in this chapter to determine the aggregate modulus was of a quasi-static nature, that is, it was performed a rate slow enough to almost be static. Under such conditions there are no the acceleration dependent inertial effects and, more importantly, the velocity dependent damping effects are eliminated. However, the physiological loading experienced in the knee joint is obviously dynamic and these acceleration and velocity effects are present. Under cyclic loading it has been demonstrated that the greater the applied frequency of loading, the greater the pressurisation of the interstitial fluid and as a result the lesser the deformation of the cartilage over time (Soltz and Ateshian, 2000, Suh et al., 1995, Wu et al., 1998, Park et al., 2004). Such deformational behaviour is linked to the diffusional phenomenon between the solid and fluid states. The rate of diffusion can be approximated by the primary diffusion characteristic time, τ_d, and the critical frequency at which dynamic loading becomes significant is $1/\tau_d$ (Suh et al., 1995). That is to say, for loading at frequencies lower than $1/\tau_d$, low interstitial pressurisation is present and large matrix deformation occurs. Similarly, for loading at frequencies greater than $1/\tau_d$, large interstitial pressurisation is present and low matrix deformation occurs. If the tissue freely deforms then it cannot be considered to be as stiff as the case when it does not deform easily. Hence, as no cyclic loading was applied to the tissues discussed in this chapter, large deformations occurred which are not representative of *in-vivo* deformations and the magnitude of aggregate moduli derived are similarly askew. In fact, the compressive modulus has been shown to increase by over a factor of 30 when a frequency of 1Hz is applied in contrast to standard quasi-static conditions (Gannon et al., 2012).

Therefore, the quasi-static testing performed here clearly has its limitations. However, quasi-static testing due to its simplicity is largely used in the field of tissue mechanics. As a result, the data generated here offers a simple means for comparison to similar quasi-static testing on cartilage published in the literature. Furthermore, for a simple comparison between cartilage properties at various sites of the knee, quasi-static testing is more than sufficient.

5 Determination of the Poisson's Ratio of Articular Cartilage in the Porcine Knee

5.1 Introduction

Along with the aggregate modulus, another fundamental material property of cartilage is Poisson's ratio i.e. the ratio of transverse strain to applied axial strain. The ability of contacting joint tissues to deform laterally in the appropriate manner may be essential in providing joint conformity under load and effective stress distribution. As such, there have been many investigations into directly measuring the Poisson's ratio of cartilage (Ficklin et al., 2007, Jurvelin et al., 2000, Jurvelin et al., 1997, Kiviranta et al., 2006, Korhonen et al., 2002a, Wang et al., 2003, Williams et al., 2010, Wong et al., 2000) but also other similarly load-bearing tissues such as the intervertebral disc (Cloyd et al., 2007, Elliott and Setton, 2001).

For over 20 years, the leading pioneers in direct measurement of the Poisson's ratio of cartilage have been the group of J.S. Jurvelin in Kuopio University Hospital, Finland (Jurvelin et al., 2000, Jurvelin et al., 1997, Kiviranta et al., 2006, Korhonen et al., 2002a, Wong et al., 2000). The first publication of note determined the Poisson's ratio of bovine humeral cartilage optically, and compared this against a theoretical vale based on experimentally derived data for the equilibrium Young's (unconfined) and aggregate (confined) modulus (Jurvelin et al., 1997). This was achieved by assuming the cartilage was an isotropic linearly elastic material and solving for v_s in the following equation;

$$H_A = \frac{1-v_s}{(1+v_s)(1-2v_s)} E_s \qquad \textbf{Equation 5-1}$$

where,

H_A = aggregate modulus,

E_s = equilibrium Young's modulus &

v_s = Poisson's ratio.

Cartilage discs were compressed and Poisson's ratio was calculated at two time points; at the end of the ramp phase and after lateral recoil homeostasis was achieved at the end of the hold phase. Thus, a short term (or apparent) and equilibrium value for Poisson's ratio could be determined. Although inhomogenousity was observed at low strains, results indicated that cartilage could be successfully interpreted as an isotropic linearly elastic material between strains of 5 & 20% (v_s = 0.185+/-0.065 vs. 0.174+/-0.106 for direct and indirect methods respectively).

This optical technique was employed further in a number of follow-up studies. Korhonen et al. attempted to again determine Poisson's ratio indirectly using the equilibrium Young's and aggregate modulus but also using indentation data (Korhonen et al., 2002a). This was achieved using a combination of equation 4-1 and the following equation assuming a single phase, elastic material;

$$E_s = \frac{(1-v_s^2)\pi a}{2\kappa h} E \qquad \textbf{Equation 5-2}$$

where,

a = radius of the indenter,

h = cartilage thickness,

E = slope of equilibrium stress-strain curve in indentation,

κ = theoretical scaling factor – obtained from Hayes et al. (Hayes et al., 1972).

This was performed on humeral, patellar and femoral cartilage and again results indicated that cartilage could be successfully interpreted as an isotropic linearly elastic

material when using confined and unconfined data. However, this was not found to be the case when indentation techniques are applied. According to the authors, the most likely explanation for this was due to the tangential collagen fibrils of the superficial zone being placed in tension as the tissue is indented, causing an increased compressive stiffness. Hence, the values for Poisson's ratio obtained using this indirect method did not agree with those determined optically.

The contribution of the structural proteins to the Poisson's ratio of cartilage has also been investigated by Jurvelin's Group. The topographical variation of Poisson's ratio over a number of key locations in the canine knee were analysed and found to inversely correlate with the collagen/PG content ratio of the tissues (Jurvelin et al., 2000). The Poisson's ratio of the medial condyle was found to be greater than the lateral condyle, which in turn was greater than the PFG. Wong et al. demonstrated that adult bovine humeral cartilage had a greater instantaneous and equilibrium Poisson's ratio than immature cartilage after a step input strain of 5%. This however, was found not to depend on collagen or PG content as such, but rather the degree to which the proteins had become cross-linked over time (Wong et al., 2000). Finally, Kiviranta et al. measured the Poisson's ratio and Young's modulus of bovine cartilage from the tibial plateau, medial femoral condyle, patella and humeral head, along with determining quantitative data for PG and collagen content (Kiviranta et al., 2006). It was discovered that not only did Poisson's ratio correlate well with Young's modulus ($P<0.01$), but also with the collagen content ($P<0.01$). Poisson's ratio did not correlate well with PG content ($P=0.07$). Hence, it was concluded that it is the collagen content that primarily controls the Poisson's ratio of cartilage.

Although it is apparent there have been studies that investigate the Poisson's ratio of cartilage in anatomical locations that relate to OAT treatment, none have specifically investigated with this therapy in mind or in a porcine model. As such, the following will be carried out:

- Prepare discs of cartilage from different regions of the porcine knee representative of the locations where plugs are taken from and then implanted;
- Perform compression testing whilst simultaneous measuring the lateral strain of the cartilage discs using digital video extensometry in order to determine the Poisson's ratio at each anatomical site.
- Correlate these results with the aggregate modulus results from chapter 3.
- Interpret the results to ascertain whether there are possible implications for AOT.

5.2 Methods

5.2.1 Sample Preparation

Circular discs of cartilage were harvested in the same manner as described in section 3.2.1. However, on this occasion after the osseous end has been microtomed, the diameters of the samples were further reduced to 7mm using an appropriately sized cork borer and frozen at a temperature of -20°C for storage purposes. Samples were thawed and equilibrated in PBS for one hour prior to testing.

A bluntly tipped needle was used to stain five dots of India ink onto the articular surface of the thawed specimen in the pattern shown in figure 5-1. In order to achieve the spacing of the dots accurately, a PTFE stencil was placed atop each cartilage sample and the needle placed through the holes provided. Even though the needle tip was blunted, great care was taken not to damage the cartilage surface. After removal of the stencil, the ink was left to dry for a minute before drops of 0.1M acetic acid were gently placed over the markings to seal them in place. Again the sample was left untouched for 60 seconds then turned to reveal the opposite osseous interface which was patterned in the same manner.

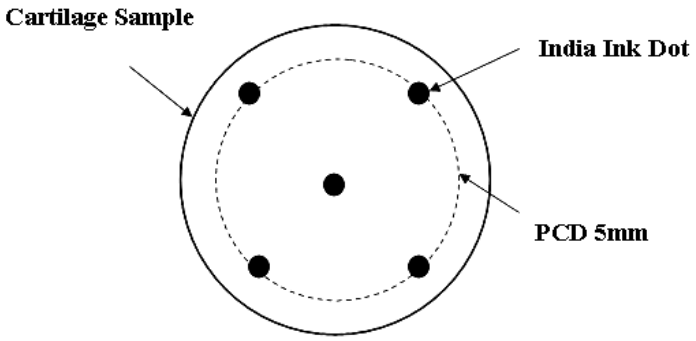

Figure 5-1. Marking system employed on cartilage specimen for video extensometry.

5.2.2 Measurement of Poisson's Ratio

A schematic Diagram, along with picture of the custom experimental set-up is shown in figure 5-2. A Bose Electroforce 3200 series with 450N load cell (Bose Corporation, Electroforce Systems Group, USA) was employed to subject the cartilage tissue to deformation. A preload of 0.5N was imparted onto the tissue to ensure contact had been made. This was followed by a single ramp to 20% deformation at $0.05s^{-1}$ strain rate and a 15 minute hold period. This methodology is in line with previous studies determining the Poisson's ratio of articular cartilage (Kiviranta et al., 2006, Korhonen et al., 2002a, Laasanen et al., 2003). The lower, fixed crosshead was adapted to hold a piece of polished glass which would act as the lower platen. A modified indenter was employed, having a contact surface that was also covered in a sheet of polished glass. The use of glass platens allowed for an unhindered view of the tissue sample by a Prosilica GE digital video extensometer camera (Allied Vision Technologies, USA) directly beneath, which would track the displacement of the India ink markings. Polished glass was used to reduce friction and allow easy radial expansion under deformation. This was further enhanced by coating the glass with a commercial, water based, transparent lubricant which was mixed with PBS solution approximately 1:2 by volume.

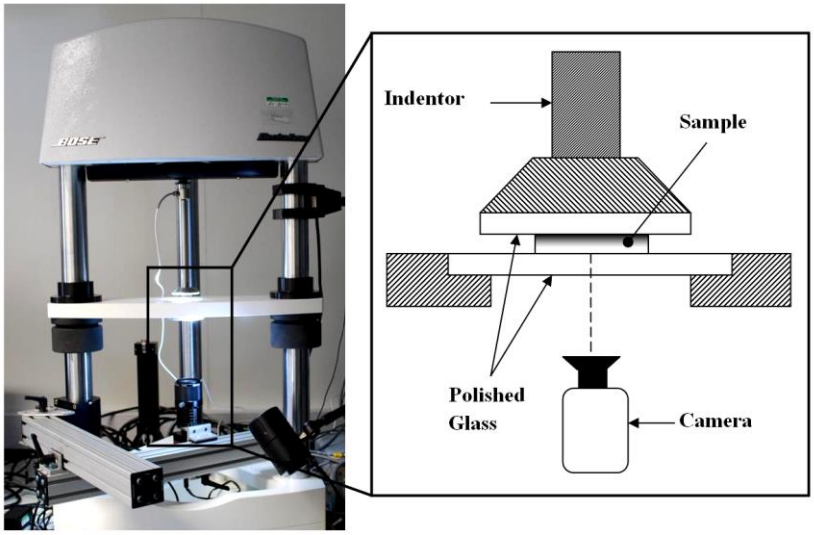

Figure 5-2. Left, picture of the Bose Electroforce 3200 and video camera and right, a close-up schematic of the experimental set-up.

The Digital Video Extensometer (DVE) uses digital video techniques along with an integrated DVE software application to optically monitor two dimensional (planar) displacement relationships between five markers made on a specimen. Using these five markers, the extensometer software acquires primary strain, secondary strain, and shear strain values as the specimen is subjected to mechanical stress. The DVE software also calculates two principle strain values at the same time

The strain measurements (ε_{11}, ε_{12} and ε_{22}) that are calculated by the software are based on the Green-Langrange strain calculation, and the '11' and '22' represent the axis of the camera. Due to the specimen orientation adopted to measure the Poisson's ratio of a sample in compression, ε_{12} is not required. Figure 5-3 displays the realtime user interface of the software used to measure the radial strain of the tissue. Figures 5-3a displays the image of the tissue sample recorded by the camera and the centroids of the markers tracked by the system respectively. Figure 5-3b displays the graphs recorded for the two orthogonal strains (ε_{11} & ε_{22}) in addition to the load encountered. The radial strain (E_{rr}) can then be calculated using the following equation (the derivation of which can be found in Appendix B);

$$\varepsilon_{rr} = \frac{1}{\sqrt{2}}(\varepsilon_{11}{}^2 + \varepsilon_{22}{}^2)^{0.5} \qquad \textbf{Equation 5-3}$$

Two parameters were to be calculated from the recorded data; the apparent Poisson's ratio and the equilibrium Poisson's ratio. The former was defined as the radial strain divided by the axial strain directly at the end of the ramp phase, whereas the latter was defined as the radial strain divided by the axial strain at the end of the hold phase when stress relaxation had reached equilibrium. These parameters were measured for the articular surface (superficial) and the opposite osseous interface (deep) of each cartilage specimen. Finally, these parameters could then be plotted against the $H_{A0.2}$ (aggregate modulus at 20% strain) results determined in section 4.3.1.2 to investigate if any correlation exists across harvest locations.

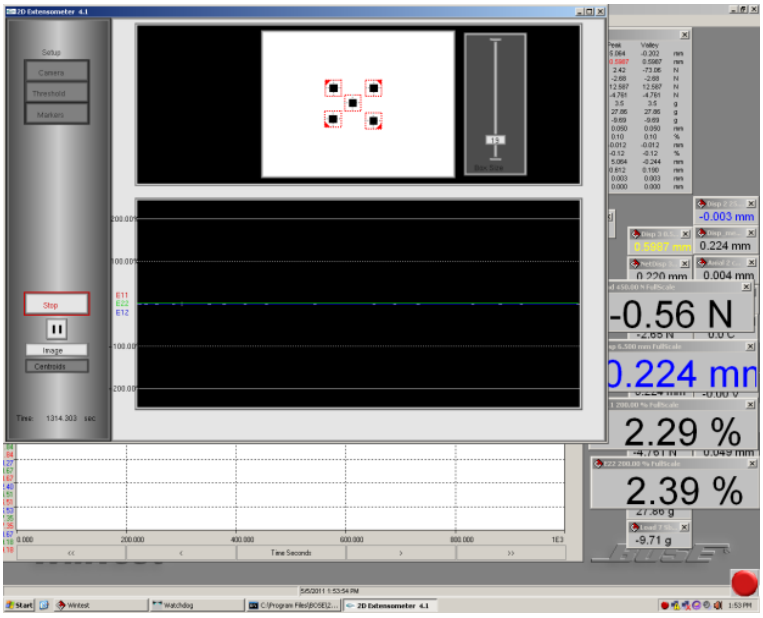

(a)

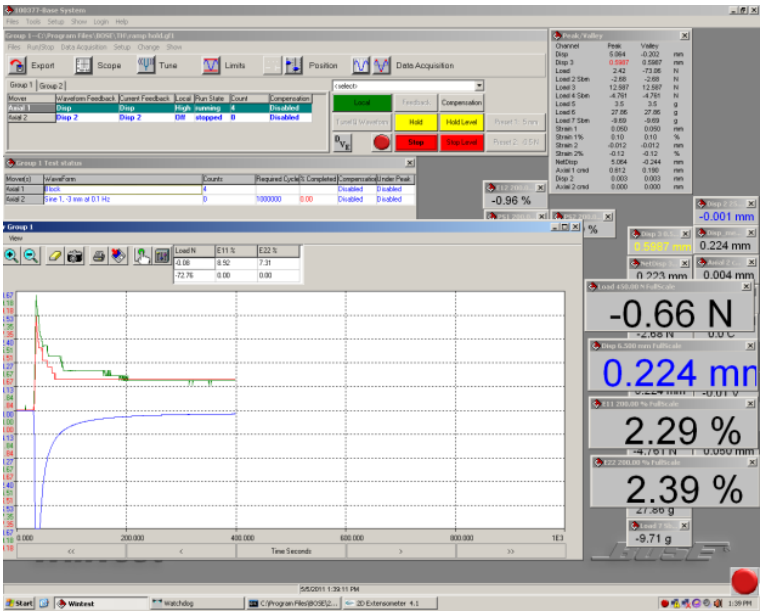

(b)

Figure 5-3. (a) A screen shot of the centroids determined by the DVE software and (b) real time data capture of the two strains and load.

However, before any testing could be performed on cartilage, the accuracy of the system needed to be verified using a material of known Poisson's ratio. The rubber family of materials are said to be incompressible, i.e. they are known to possess a Poisson's ratio of 0.5. Thus, this was deemed to be an ideal test material for verifying the measurement system. There is also a precedent for this validation technique in previous studies (Cloyd et al., 2007).

A silicone analogue (Rhodorsil RTV 3428, Bentley Creative Chemicals, Kidderminster, UK), 10mm diameter x 4mm thickness, was created from a mould. This was then subjected to the same test protocol mentioned earlier for the cartilage. As was the case for the cartilage specimen, a stencil with 5mm PCD holes was used to mark up the rubber sample with India ink. However, a second stencil with 9mm PCD holes was also employed to ensure there was no variation in Poisson's ratio depending on where the markers where placed. The 5mm and 9mm marker systems were designated "inner" and "outer" respectively. In both cases, this was repeated 3 times, with an hour between each successive test to allow the sample to recover sufficiently.

5.2.3 Statistics

All statistical analyses in chapter 5 were carried out using statistical software (Minitab^{TM}, v.16). Statistical variances between regions were determined by one way analysis of variance (ANOVA). Tukey's honesty significant difference test was used for post hoc evaluation of differences between groups. A student t-test was used to investigate significance between any two groups if so desired. A P-value of <0.05 was considered to be statistically significant.

5.3 Results

Figure 5-4 presents the results of the tests performed on the rubber sample. The apparent Poisson's ratio was found to be 0.51 (0.0041 SD) and 0.51 (0.011SD) for the inner and outer marker systems respectively. This is remarkably close to the predicted values of 0.5, indicating that the system is indeed sufficient to measure Poisson's ratio in a predictable and reliable fashion. No statistical significance was found between the apparent Poisson's ratio values and their corresponding equilibrium values. This was expected to be the case as rubber is a hyper-elastic material in nature and as such does not exhibit stress relaxation characteristics.

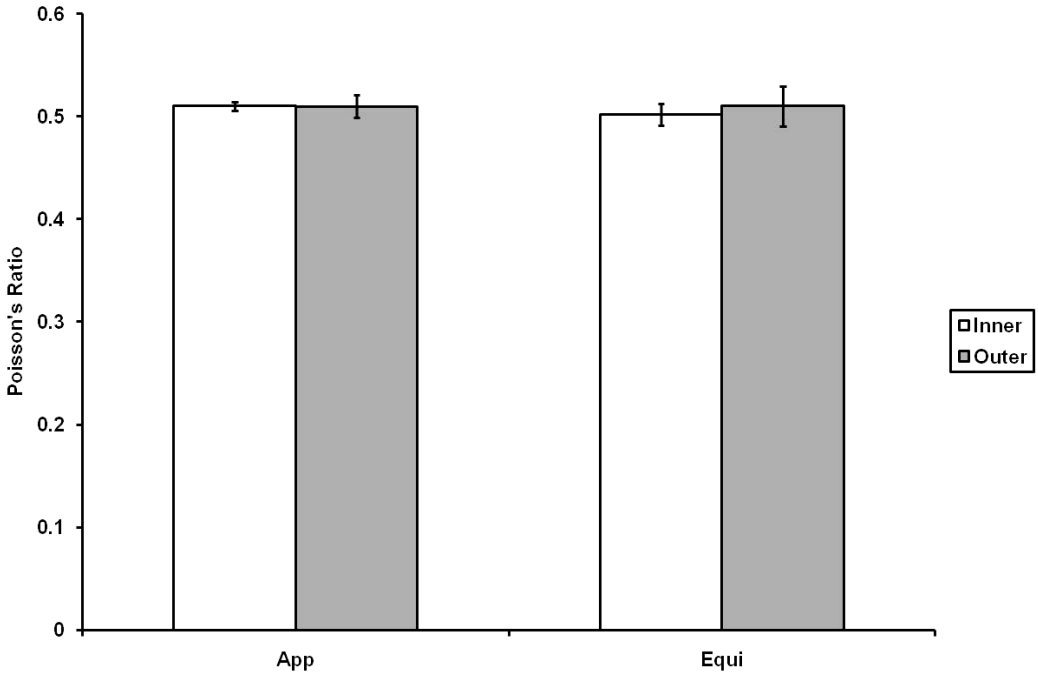

Figure 5-4. Apparent and equilibrium Poisson's ratio calculated for the silicone analogue. Both inner and outer marker system results are displayed. Results shown as mean +/- SD. Data was analysed using a 1-way ANOVA.

Figure 5-5 presents the apparent Poisson's ratio of cartilage determined for the various harvest locations. For superficial surfaces, all medial and lateral condyle cartilage results were found to be significantly higher than PFG1 ($P<0.05$). M1 superficial was also

found to be significantly higher than PFG2 superficial. For deep surfaces, no significant differences were found. But, when both superficial and deep results were combined into an average, all medial and lateral condyle cartilage results were again found to be significantly higher than PFG1 (P<0.05).

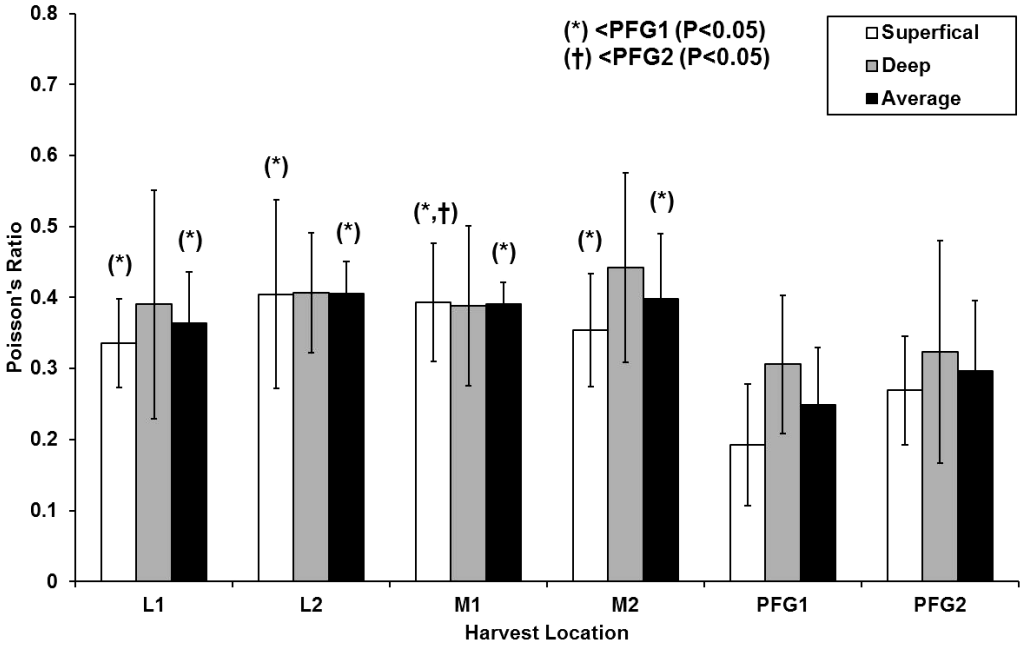

Figure 5-5. The apparent Poisson's ratio measured at each harvest location. Results are shown as mean +/- SD (n=5 for superficial and deep results, n=10 for averaged). Data was analysed using a 1-way ANOVA.

The results for the equilibrium Poisson's ratio are shown in figure 5-6. For superficial surfaces, L2 & M1 were found to be significantly higher than both PFG1 & PFG2 (P<0.05). For deep surfaces, L2 was found to be significantly higher than both PFG1 & PFG2 and M2 was significantly higher than PFG1 (P<0.05). When the superficial and deep results were combined, L2 & M1 were found to be significantly higher than both PFG1& PFG2 and M2 greater than PFG1 (P<0.05). Finally, L2 deep and averaged results were significantly higher than their L1 counterparts (P<0.05). This was further investigated using a student t-tests reporting P-values of 0.026 & 0.029 respectively.

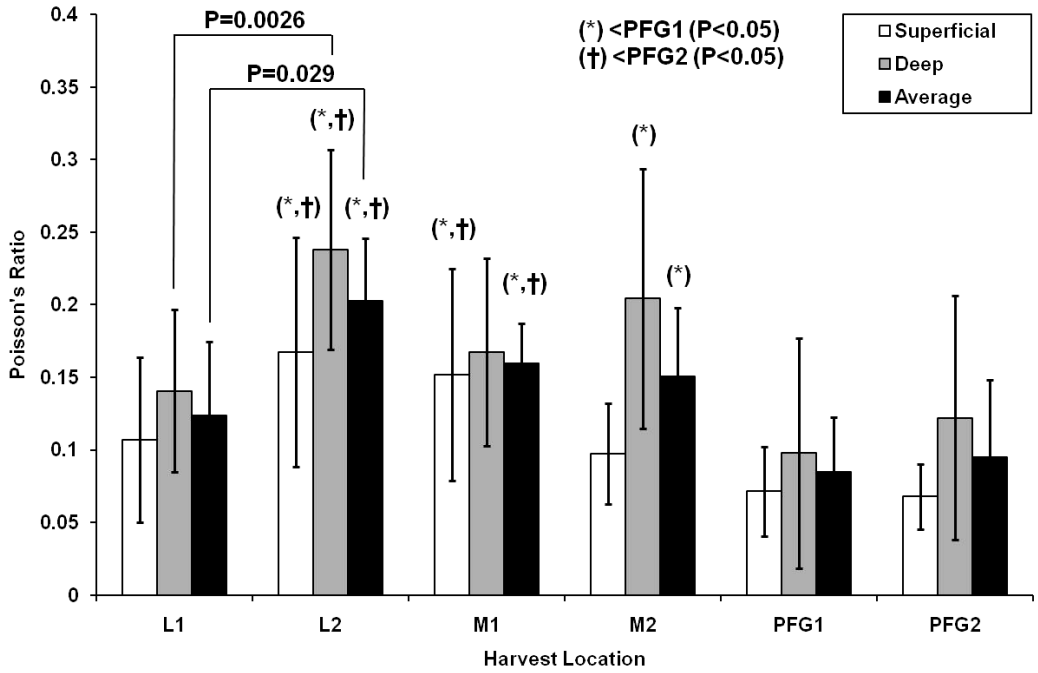

Figure 5-6. The equilibrium Poisson's ratio measured at each harvest location. Results are shown as mean +/- SD (n=5 for superficial and deep results, n=10 for averaged). Data was analysed using a 1-way ANOVA.

Figures 5-7 to 5-9 plot the apparent and equilibrium Poisson's ratio results against the $H_{A0.2}$ results determined in section 3.2.1.4. In all the figures, each individual data point represents a particular harvest location. In Figure 5-7, a significant correlation is found to exist between the apparent superficial Poisson's ratio and $H_{A0.2}$ (r=-0.815, P=0.048), but significance is not witnessed between the equilibrium superficial Poisson's ratio and $H_{A0.2}$ (r=-0757, P=0.082). Figure 5-8 shows that a similar trend exists for the apparent deep Poisson's ratio against $H_{A0.2}$ and equilibrium deep Poisson's ratio against $H_{A0.2}$, with significance achieved in the former but not the latter (r=-0.888, P=0.018 & r=-0.760, P=0.079 respectively). Unsurprising, when superficial and deep results are pooled, again significance is witnessed in the apparent Poisson's ratio results but not the equilibrium Poisson' ratio results (r=-0.877, P=0.022 & r=-0.801, P=0.052 respectively).

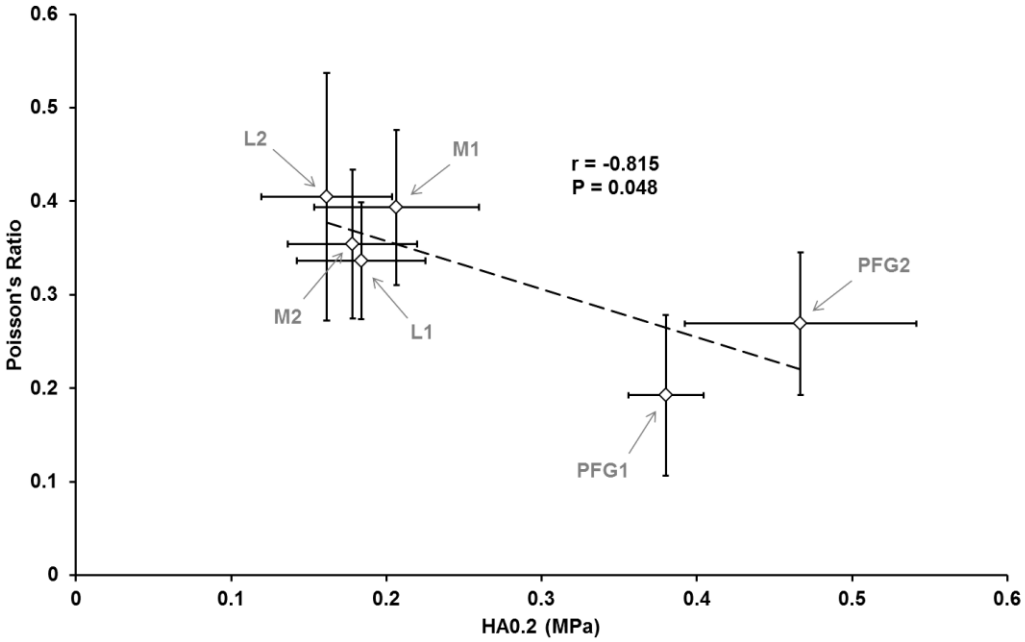

(a)

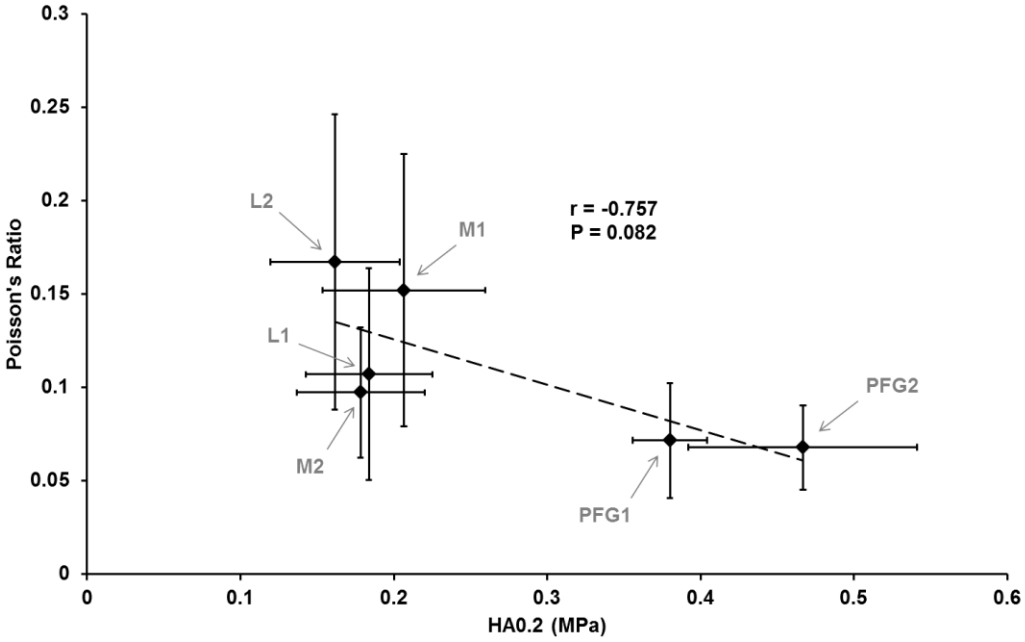

(b)

Figure 5-7. (a) Apparent Poisson's ratio & (b) equilibrium Poisson's ratio of superficial cartilage surface vs. Aggregate modulus at 0.2 strain. Results shown as mean +/- SD (n=5).

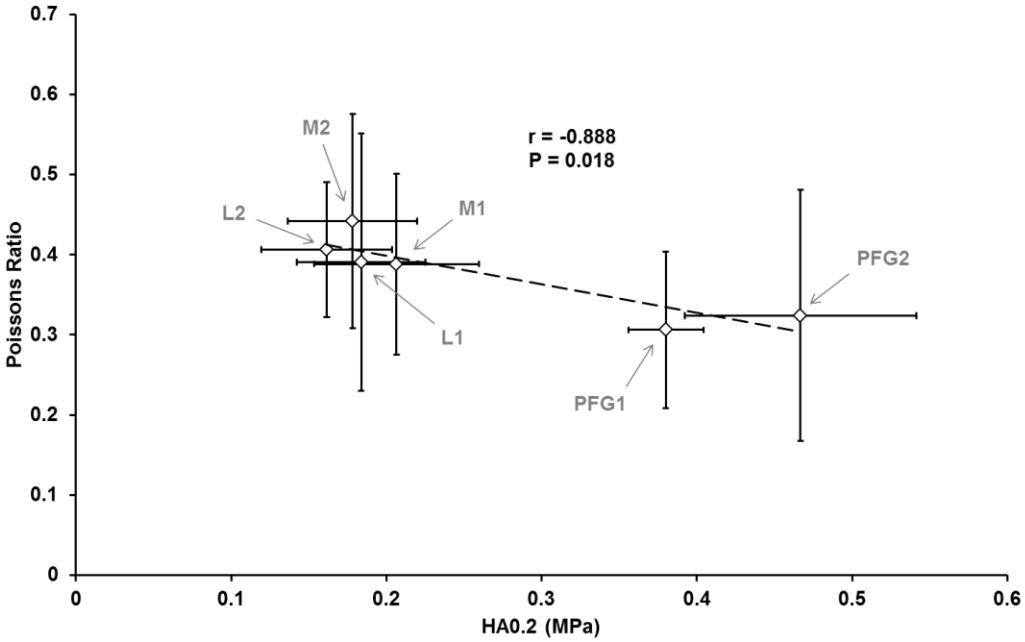

(a)

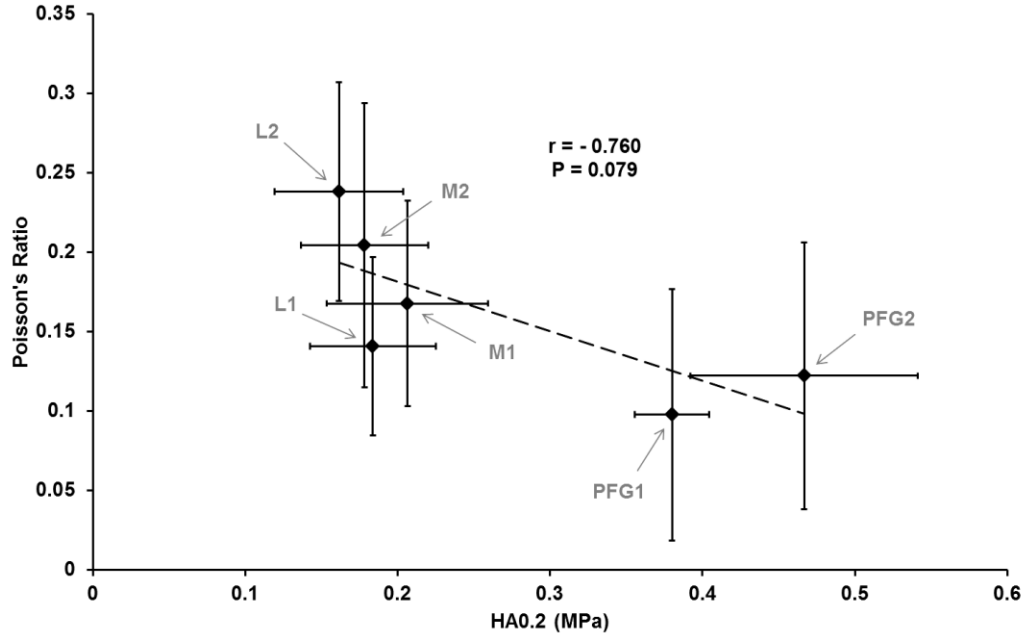

(b)

Figure 5-8. (a) Apparent Poisson's ratio & (b) equilibrium Poisson's ratio of deep cartilage surface vs. Aggregate modulus at 0.2 strain. Results shown as mean +/- SD (n=5).

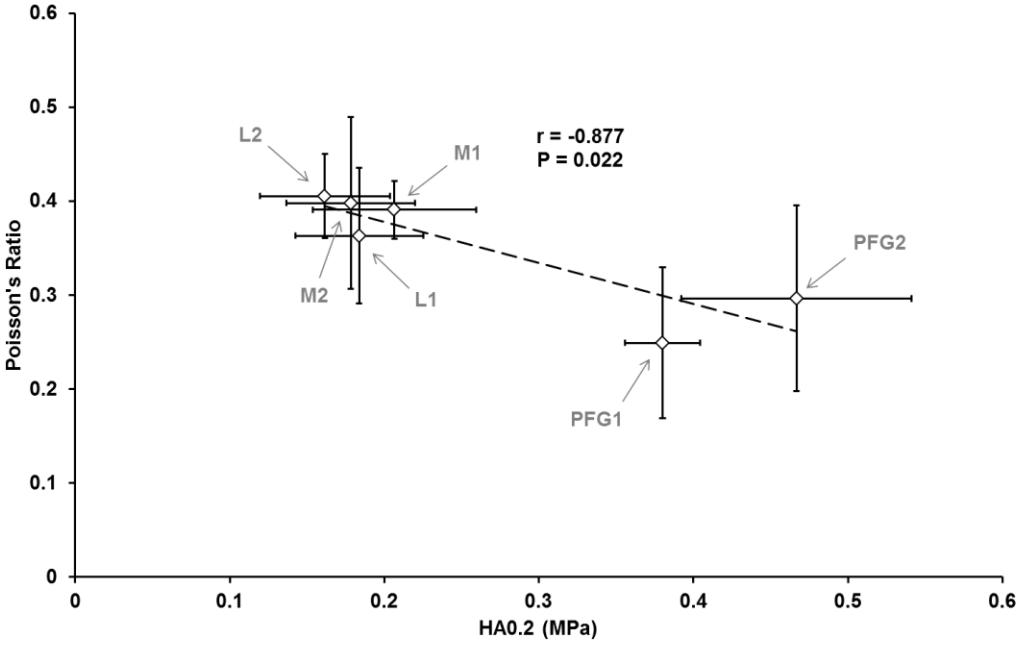

(a)

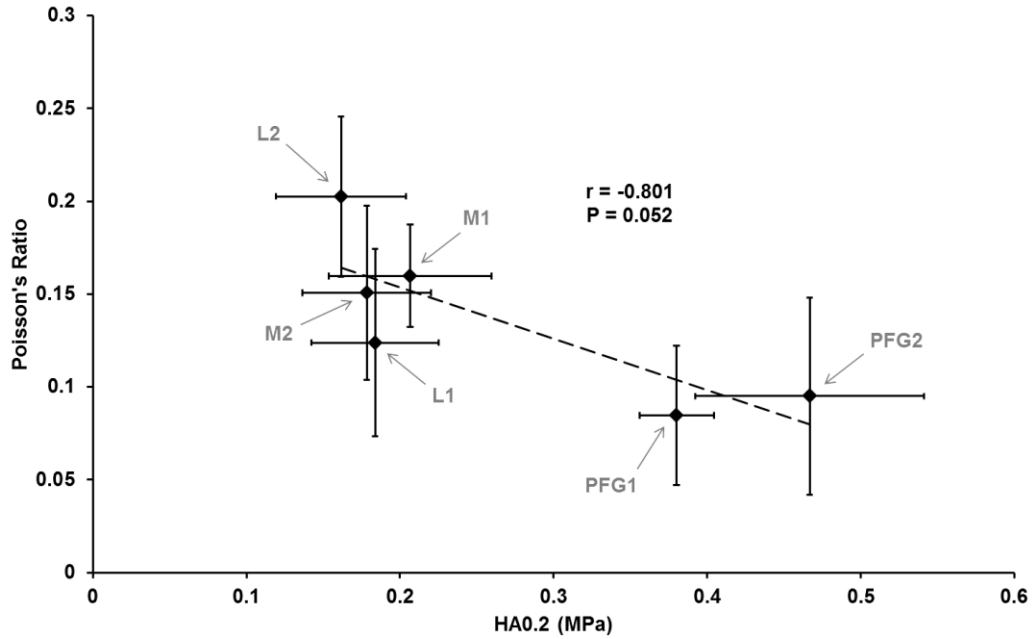

(b)

Figure 5-9. (a) Apparent Poisson's ratio & (b) equilibrium Poisson's ratio of superficial & deep cartilage combined vs. Aggregate modulus at 0.2 strain. Results shown as mean +/- SD (n=10).

5.4 Discussion

This chapter aimed to discover if any regional variation in Poisson's ratio existed in the porcine knee. The mean values of apparent Poisson's ratio ranged from 0.33 to 0.44 in all four condyle harvest sites with no statistical difference found between any of them (figure 5-5). The mean apparent Poisson's ratio of the PFG sites was lower, ranging from 0.19 to 0.32. All superficial and average (superficial & deep combined) values for the condyles sites were found to significantly greater than their PFG1 counterparts, whereas only the superficial value for the M1 site was significantly greater than PFG2. There also appeared to be a more discernible difference between respective superficial and deep values in the PFG sites. These larger deep apparent Poisson's ratio values in the PFG are responsible for the lack of significance when compared to deep condyle values.

The mean values for equilibrium Poisson's ratio ranged from 0.1-0.4 for L1, 0.17-0.24 for L2, 0.15-0.16 for M1, 0.1-0.2 for M2 and 0.07-0.12 for both the PFG groups (figure 5-6). Within the condyle groups, L2 was significantly greater than L1 for deep and averaged measurements. L2 was significantly greater than both PFG groups in all aspects and M1 was significantly greater than both PFG groups in superficial and averaged measurements. M2 was only significantly greater than PFG1 and in deep and averaged measurements alone.

The higher values of Poisson's ratio in the condyle harvest sites indicate that cartilage in these locations expands laterally more readily under compression than the cartilage in the PFG. Poisson's ratio is related to many elastic moduli such as the bulk modulus, shear modulus and Young's modulus. However, these moduli are all ratios of stress and strain and hence essentially measures of stiffness, so it can be inferred that Poisson's ratio can be viewed in a similar light. Intuitively of course this makes a great deal of sense. If a specimen is more resistive to uniaxial compression, then it is less likely to expand laterally. Thus, the presence of a lower Poisson's ratio in the cartilage of the

PFG compared to that of the condyles is indicative of the cartilage being stiffer in the PFG, which has already been shown to be the case in chapter 4.

The magnitude of the various Poisson's ratio values compare favourably with bovine humeral cartilage studies. Jurvelin et al. found apparent values of 0.129 & 0.593 for superficial and deep zones respectively and equilibrium values of 0.068 & 0.225 for superficial and deep zones respectively (Jurvelin et al., 1997). However, it must be stated that these were measured using a considerably different method. The overall lateral expansion of thin slices taken from the deep and superficial zones was measured, whereas in this study the lateral expansion of the most superior and deep surfaces of full thickness specimens was tracked. Nevertheless, in the same study Jurvelin et al. also measured full thickness specimens using the same method yielding apparent Poisson's ratio values of 0.38 and equilibrium values of 0.185 which again compare well with the values reported in this study (Jurvelin et al., 1997).

As was observed in the PFG groups for the apparent Poisson's ratio, the deep values appeared to be greater than the superficial equilibrium values but now across all harvest sites. In fact in many of the groups, there appeared to be a larger drop in apparent to equilibrium Poisson's ratio in the superficial zone. This was also observed by Jurvelin et al. for bovine humeral cartilage where the superficial zone values reduced 53% compared to 37% in the deep zone (Jurvelin et al., 1997). The differences between superficial and deep zones are further emphasised in work by Wang et al where a rise in apparent Poisson's ratio is seen from values as low as 0.01 in the superficial zone to approximately 0.2 in the deep zone in bovine carpometacarpal cartilage (Wang et al., 2003). Furthermore it was discovered that the rise in apparent Poisson's ratio throughout the depth became less pronounced for greater applied strains. Hence, averaged values over the entire thickness of a specimen were found to become lower for greater applied strains.

In a further study, Jurvelin et al. determined the topographical variation of Poisson's ratio in the canine knee (Jurvelin et al., 2000). This was achieved using the exact same method discussed in the group's earlier work on bovine humeral cartilage (Jurvelin et al., 1997). Samples were taken at the patellar groove, medial & lateral femoral condyle and the medial & lateral tibial plateau. Equilibrium values of Poisson's ratio at these sites were found to be 0.07, 0.159, 0.079, 0.236 and 0.167 respectively. These values for the patellofemoral groove and the condyles are again similar to those determined at the same anatomical sites in the porcine knee in this thesis.

Yet, interestingly a regional variation of Poisson's ratio was not found to be the case in the bovine cartilage by Korhonen et al. (Korhonen et al., 2002a). In this study, cartilage from humeral, femoral and patellar regions was subjected to not only confined & unconfined compression but also indentation. Using the data from two different combinations of these three methods, the equilibrium Poisson's ratio was determined indirectly via analytical methods (see equations 4-1 & 4-2). These indirect values were then compared to direct optical measurements made upon the same specimens. When indentation data was used in conjunction with unconfined data, significant difference was found between indirect and direct measurements of the equilibrium Poisson's ratio. However, when confined & unconfined data were used in combination with one another, no significant differences were discovered across all sample groups between indirect and direct methods. These values were approximately 0.15, 0.16 & 0.21 for humeral, patellar and femoral sites respectively. Although no statistical difference was found between harvest sites, compared to the canine model produced by Jurvelin et al. (Jurvelin et al., 2000), it must be noted that the choice of sites was vastly different; in fact the only common site was the femoral condyles. Thus, the results of canine model remain more relevant to the porcine model in terms of gauging the results against one another between harvest locations.

The marked difference found between direct and indirect values when indentation data was used was a result of a much greater Young's modulus being measured whilst using

this method. When this was inputted into the analytical expression, a greater value for Poisson's ratio was produced. However, the reason as to why a greater Young's modulus is found when using indentation now needs to be explained. It was suggested within the study that as indentation deforms the cartilage *in-situ* the collagen fibres running parallel to the surface remained tensioned. Confined & unconfined compression, along with the direct method of measuring Poisson's ratio, relies on tissue samples being excised from the joint, so it is possible these fibres become slack. Thus, a similarity between direct and indirect results is found in this instance.

Although, there seems to be a lesser degree of inter-species variation in the Poisson's ratio of articular cartilage when compared to the differences encountered in the aggregate modulus results, this is not to say that there may be other factors which may dictate Poisson's ratio. When analysing the aggregate modulus results, one issue that was highlighted with regard to the porcine model was the age and skeletal maturity of the animal tissue used. Thus, Poisson's ratio should also be examined in this regard. The work of Roemhildt et al. sheds light on this issue as they measured the equilibrium Poisson's ratio in rabbits of 4 & 12 months (Roemhildt et al., 2006). The more immature cartilage was found to possess a greater Poisson's ratio (0.32-0.38 vs. 0.25-0.31). However, in this instance Poisson's ratio was determined indirectly by means of fitting indentation data to a non-linear biphasic creep solution. Thus, direct methods may represent a truer indication of the effects of age. Wong et al. found the opposite trend when they measured the instantaneous (apparent) and equilibrium Poisson's ration of adult, calf and fetal bovine humeral cartilage via direct optical methods (Wong et al., 2000). It was discovered that the instantaneous adult value approached their initial assumption of incompressibility (0.49), but that this reduced with decreasing age of the tissue (0.38 & 0.36 for calf and fetal respectively). Furthermore, the same trend was found to exist for the equilibrium Poisson's ratio across the maturity of the specimens (0.26, 0.11 & 0.09 for adult, calf and fetal respectively).

This may explain why the skeletally immature porcine model discussed in this thesis failed to satisfy the assumption of incompressibility, with apparent values of Poisson's ratio in the condyles ranging 0.33-0.44 (figure 5-5). To lend further credence to the similarity of the young bovine and porcine models, the equilibrium values of the condyles are well represented by the young bovine variants. However, although the equilibrium values of the PFG sites are similar to the condyles, the apparent values are vastly different. This may mean that the porcine PFG matures at a slower rate and requires a longer period of time to achieve maturity than the condyles. This may explain the variation of the aggregate modulus found between the condyles and the PFG in chapter 3. Alternatively, it may simply be due to variations of loading and kinematics between these regions and between animals.

Wong et al suggested the likely cause of an increasing Poisson's ratio with age is due to not only an increasing collagen content in the tissue but also an increasing cross-link density (Wong et al., 2000). This alludes to a structure-function relationship within the tissue, which has been proposed by a number of authors. Ficklin et al. demonstrated this trend by examining the equilibrium Poisson's ratio of new born bovine PFG cartilage at day 0 and after 14 days in a non-stimulating *in-vitro* environment (Ficklin et al., 2007). At both time points Poisson's ratio was found to correlate with both collagen and collagen cross-link content. Furthermore, the reduction in collagen and collagen cross-link content at day 14 caused an increase in Poisson's ratio. In an opposite approach, Williams et al. endeavoured to stimulate growth *in vitro* using IGF-1 and TGF-β1 in bovine calf PFG cartilage (Williams et al., 2010). Once again, it was found that there was a negative correlation between both collagen and collagen cross-link content and the equilibrium Poisson's ratio. Finally, Kiviranta et al. found once more that the equilibrium Poisson's ratio was strongly inversely correlated collagen content in mature bovine knee cartilage sites ($P<0.01$) (Kiviranta et al., 2006), again lending credence the suggestion of Wong et al. (Wong et al., 2000). Only a very weak correlation was discovered between Poisson's ratio and PG content ($P=0.07$), hence the hypothesis that collagen content primarily controls Poisson's ratio was suggested.

What is most interesting about these studies is that while they demonstrated that collagen content, and indeed collagen crosslink density, correlated with Poisson's ratio, there also appeared to be a relationship between collagen and compressive stiffness. Kiviranta et al. demonstrated that the greater the collagen content, the greater the Young's modulus ($P<0.01$) (Kiviranta et al., 2006). More importantly with regard to the work in results presented here, it was found that there was a significant negative correlation between Poisson's ratio and Young's modulus. When the 0.2 strain aggregate modulus from chapter 3 was correlated against the Poisson's ratio data from chapter 4 in this thesis a negative correlation was also found for both apparent and equilibrium Poisson's ratios (figure 5-7 to 5-9). Interestingly, this was only significantly so ($P<0.05$) for the apparent Poisson ratio's in all superficial, deep and averaged groups not the equilibrium Poisson's ratio. However, this may be somewhat misleading. Only the means for each of the six harvest sites could be used to generate the plots as both sets of experiments used different cartilage specimen (the cartilage used to determine the aggregate modulus was digested for the s-GAG assay). If the same cartilage specimens were used to determine both the aggregate modulus and Poisson's ratio, the resulting scatter plot would most likely prove significance for both apparent and equilibrium Poisson's ratio cases.

Kiviranta et al. demonstrated the inverse relationship of Poisson's ratio and compressive stiffness explicitly (Kiviranta et al., 2006), but some of the other groups mentioned demonstrated this correlation implicitly. As already discussed both Ficklin et al. and Williams et al. found that as collagen content/cross-linking grew Poisson's ratio fell, but they also found that as collagen content/cross-linking grew the compressive stiffness grew (Ficklin et al., 2007, Williams et al., 2010). Hence, one may extrapolate that cartilage, over a range of different harvest sites (each with site specific collagen/cross-linked collagen content), will also produce a negative correlation between Poisson's ratio and aggregate modulus. This is of course is what was observed in the porcine model (figures 5-7 to 5-9). Therefore it stands to reason that, given the PFG sites position on the correlation curve (due to their higher aggregate modulus and lower

Poisson's ratio), they may possess a lower collagen and/or cross-linked collagen content. This may be a site specific phenomenon (i.e. due to variations in loading and kinematics at these joint sites), but it is more likely due to tissue immaturity, giving further momentum to the argument that this site matures at a slower rate than the femoral condyles. This will become clearer in chapter 5 when the histology is reviewed.

However, if this is a site specific phenomenon, or rather that measurable, significant topographical variations exist in human knees, than this may have great implications for OAT therapy. Evidence exists to suggest that this is indeed the case in canine knees. Jurvelin et al. found that a negative correlation existed not between collagen content and Poisson's ratio but rather with the ratio of collagen/PG content and Poisson's ratio at various locations over the canine knee joint (Jurvelin et al., 2000). Not only could there be a mismatch of the mechanical properties of cartilage at the grafting site but rather the entire osteochondral construct implanted. Such an inference may only be resolved through a complete inter and intra statistical analysis of potential harvest sites and implantation sites in human knees.

As was the case in chapter 4, the testing performed here was of a quasi-static nature. In this instance however, testing was performed in unconfined conditions allowing the cartilage samples to bulge radially under compression. Nevertheless, under dynamic conditions one may expect greater interstitial fluid pressure and lesser deformation with increasing frequency as observed in previous unconfined studies (Gannon et al., 2012). In a study performed by Woo et al., two contacting joint surfaces were idealised as two circular rigid bodies (representing the bone) covered by a thin layer of biphasic material (representing the cartilage) (Wu et al., 1998). As the bodies came in contact with one another a contact radius was generated at the interface between the opposing cartilage layers. As was expected, when placed under cyclic dynamic loading the interstitial fluid pressure grew with increasing frequency and deformation decreased. However, what was also observed was that the dilation of the contact radius decreased with increasing frequency.

Hence, it is reasonable to expect that should the cartilage testing performed in this chapter have been of a dynamic nature, then the radial expansion would have been less. As a result, the Poisson's ratio of all the specimens tested would have been less. Therefore the values of Poisson's ratio presented in this chapter are not truly representative of cartilage under *in-vivo* loading conditions. Yet, as was stated in the previous chapter, quasi-static testing due to its simplicity is largely used in the field of tissue mechanics for determining stiffness and such is also the case for determining the Poisson's ratio. All the literature discussed in this chapter which determined Poisson's ratio adopted quasi-static techniques and so offers a simple means of comparison. Furthermore, as was the case with the aggregate modulus, quasi-static testing is more than sufficient for a simple comparison between the Poisson's ratios at various sites of the knee.

6 Histology of Articular Cartilage in the Porcine Knee

6.1 Introduction

This chapter aims to investigate whether qualitative histology can aid in establishing links between the mechanical properties of porcine articular cartilage presented in chapters 3 & 4 and the extracellular matrix within. As discussed in detail in sections 3.4 & 4.3, many authors have suggested that such links exist, for example between PG content and the equilibrium compressive stiffness (Julkunen et al., 2007, Kiviranta et al., 2006) and between the collagen content and the Poisson's ratio (Ficklin et al., 2007, Kiviranta et al., 2006, Williams et al., 2010).

Specifically, the histological approach discussed here will involve performing a depth wise, qualitative investigation of the content and spatial distribution of collagen and PG's using appropriate staining methodology. This will be also performed for each of the harvest locations employed in the previous mechanical property studies with a view to exploring if regional variations in the mechanical properties are accompanied by with regional histological differences. Furthermore, questions have arisen previously in sections 3.4 & 4.3 as to whether cartilage in certain regions of the porcine knee was structurally immature. A histological examination of these regions would reveal if an adult phenotype was present or not. Thus, the following is to be performed:

- A qualitative, histological analysis of the content and spatial distribution of collagen and PG's in the porcine knee.
- Establishing if regional variations in the mechanical properties can be explained by the histological observations.
- Investigating whether there is evidence to suggest cartilage has not reached maturity in particular locations.

6.2 Methods

The methods discussed in this chapter are based on those proposed by Schmitz et al in a review paper detailing methods in joint tissue histopathology (Schmitz et al., 2010).

6.2.1 Fixation, Decalcification and Embedding

Disks of cartilage were halved along their diameter to expose a plane perpendicular to both the articular and osseous faces (figure 6-1). Any further sectioning would be taken parallel to this exposed surface so that the distribution of the proteins of interest could be observed along the samples full thickness from the articular surface down to the bone.

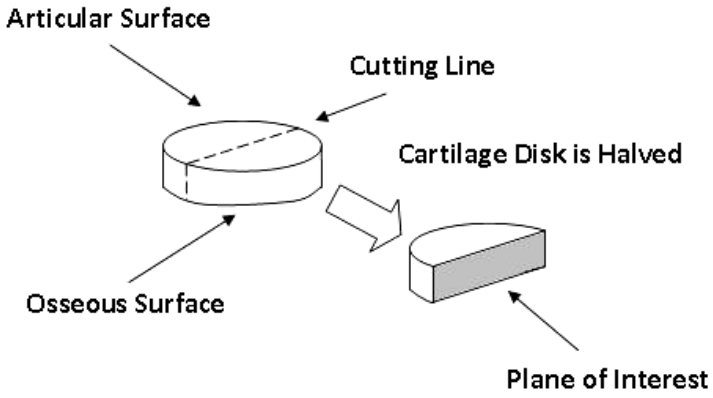

Figure 6-1. Schematic depicting the plane of interest from which all sections were taken parallel to.

To fix the samples they were placed in test tubes of 10% buffered formalin and refrigerated at -4°C for 3 days. Samples were then removed and rinsed in buffer before being decalcified in test tubes of 10% EDTA in 0.1M phosphate buffer (pH 7-8), for two weeks at -4°C, changing the solution half way through. After further rinsing in buffer, specimens were then embedded in paraffin and sectioned along the plane of interest. Serial 8µm slices were taken and placed on glass slides to be stained.

6.2.2 Picrosirius Red Staining Protocol

Solutions required:

Weigert's hematoxylin -	Solution A: 1% hematoxylin in 95% alcohol Solution B: 4ml 30% ferric chloride (anhydrous), 1ml concentrated HCl, 95ml distilled H_2O.. Mix equal parts A & B and use immediately
Acidified water -	5ml acetic acid (glacial) in 1L H_2O.
Picrosirius red solution -	0.5g of Sirius red F3B added to 500ml of saturated picric acid.

Proceedure:

1. Xylene -	4min
2. Xylene -	4min
3. Xylene -	4min
4. 96% alcohol -	1min
5. 96% alcohol -	1min
6. 70% alcohol -	1min
7. Tap water rinse -	1min
8. Weigert's hematoxylin -	8min
9. Running tap water -	10min
10. Picrosirius red solution -	60min
11. Acidified water -	5min
12. Acidified water -	5min
13. 100% alcohol -	5min
14. 100% alcohol -	5min
15. 100% alcohol -	5min
16. Xylene -	5min

17. Mount sample & image.

6.2.3 Toluidine Blue Staining Protocol

Solutions required:

0.2M Acetate Buffer -

0.04% Toluidine blue - Added to 0.2M acetate buffer and mixed on a magnetic stirrer. Before use ensure pH is between 3.75 & 4.25.

Procedure:

1. Xylene - 4min
2. Xylene - 4min
3. Xylene - 4min
4. 96% alcohol - 1min
5. 96% alcohol - 1min
6. 70% alcohol - 1min
7. Tap water rinse - 1min
8. 0.04% Toluidine blue - 10min
9. Tap water rinse - 1min
10. Warm air dry - 9min
11. Xylene - 5min
12. Mount sample & image.

6.2.4 Imaging

All histological sections were imaged using a Zeiss AxioImager Z1 upright microscope (Carl Zeiss Ltd., UK). A magnification level of x2.5 was found to be sufficient to image the sectioned specimens over the entirety of their thicknesses.

6.3 Results

The histological results for all the cartilage harvest locations are shown in figures 6-2 to 6-7. The first of these presents the stains for collagen and PG in location L1. Four distinct bands are observed when stained for collagen as opposed to the three bands observed for PG. L2 possesses two distinct, similarly spaced bands that correspond to both histological sections. Variation in the numbers of bands between stains is seen again for M1, as only one continuous collagen band exists compared to three PG bands. M2 and PFG1 are similar to L2 in that they have the same number of, and similarly spaced corresponding collagen and PG bands. Finally, PFG2 presents singular, uniform collagen and PG stains from the articular surface to the bone interface.

In general it appears that where there are higher levels (darker staining) of collagen content, there are low levels of PG content and vice versa. Furthermore, the banding patterns present are indicative of consecutive variation in the protein content. For collagen, low content is witnessed at the articular surface, changing sequentially down through the specimen thickness. For PG, high content is witnessed at the surface, again sequentially down through the depth.

Substantial variations in the tidemark thickness are also observed from position to position. The anterior parts of both condyles (L1 &M1) and the inferior part of the PFG (PFG1) are located adjacent to one another spatially. These locations all appear to possess thick tidemarks and as one moves away from these locations, whether it be superiorly (to PFG2) or posteriorly (to L2 & M2), the tidemarks become thinner.

Superficial zones are also present in all locations but they appear to be more prevalent relative to the full cartilage thickness in the PFG sites.

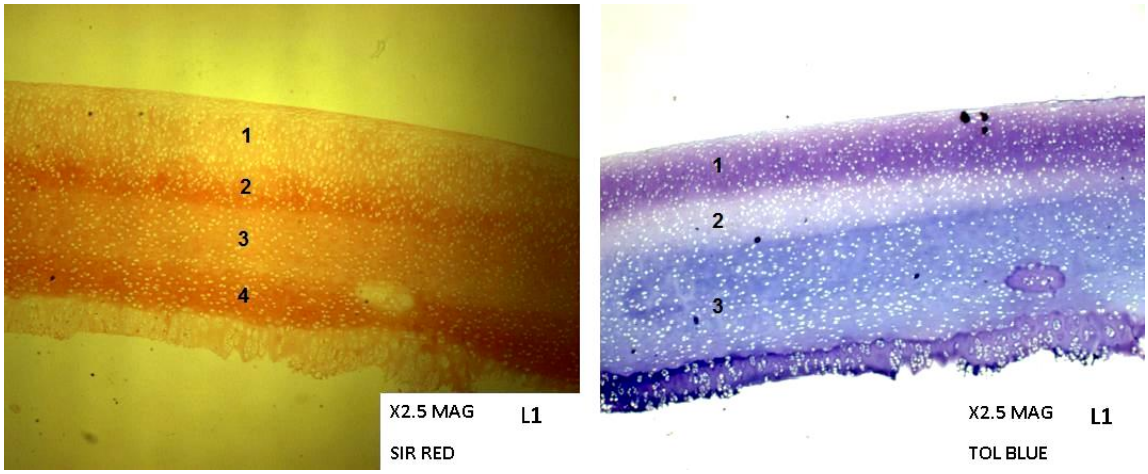

Figure 6-2. Histological depth profile of cartilage take from L1; left - picrosirius red stained for collagen, right - toluidine blue stained for proteoglycan.

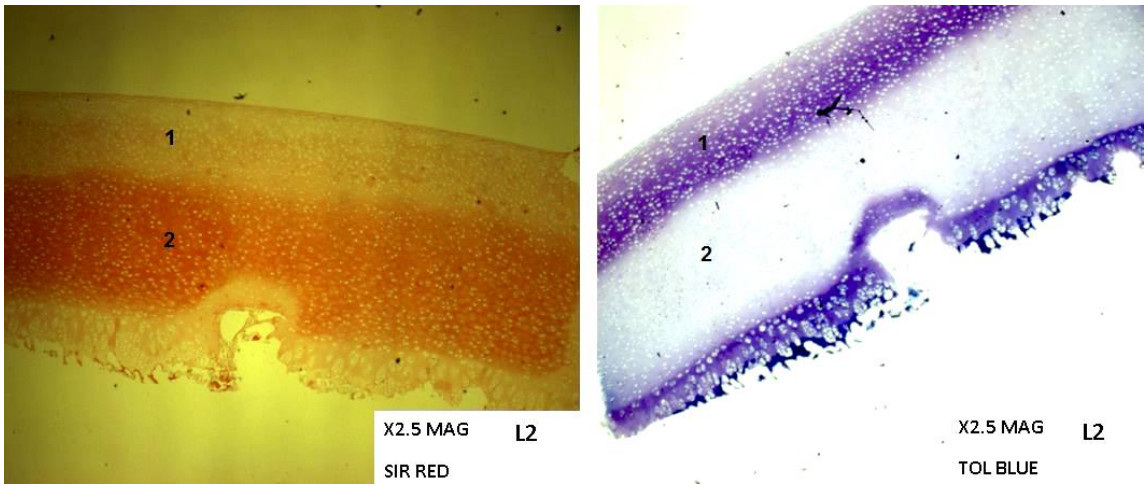

Figure 6-3. Histological depth profile of cartilage take from L2; left - picrosirius red stained for collagen, right - toluidine blue stained for proteoglycan.

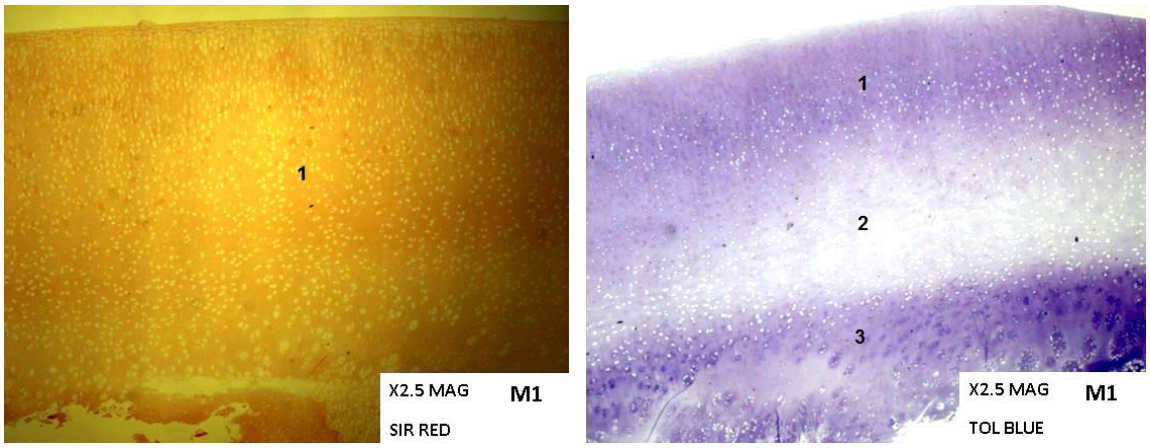

Figure 6-4. Histological depth profile of cartilage take from M1; left - picrosirius red stained for collagen, right - toluidine blue stained for proteoglycan.

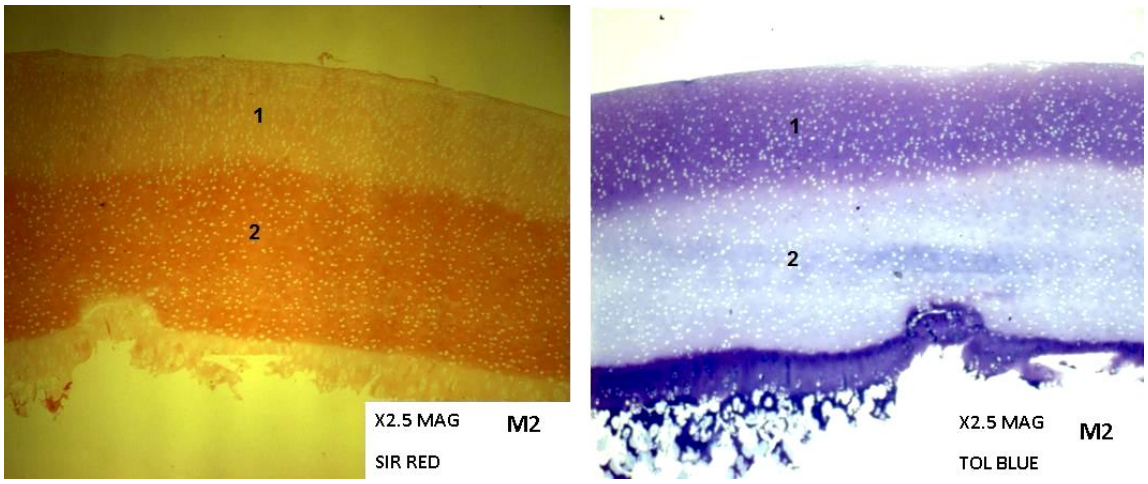

Figure 6-5. Histological depth profile of cartilage take from M2; left - picrosirius red stained for collagen, right - toluidine blue stained for proteoglycan.

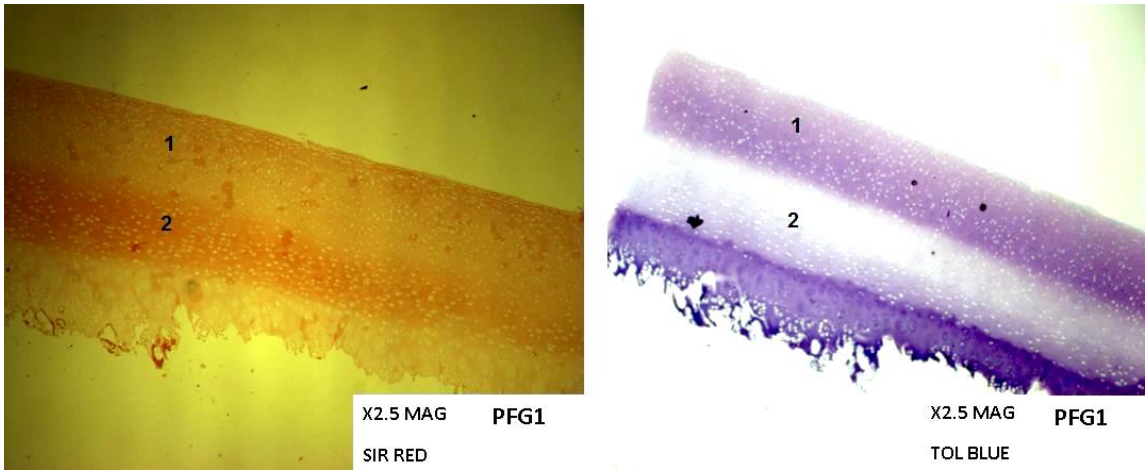

Figure 6-6. Histological depth profile of cartilage take from PFG1; left - picrosirius red stained for collagen, right - toluidine blue stained for proteoglycan.

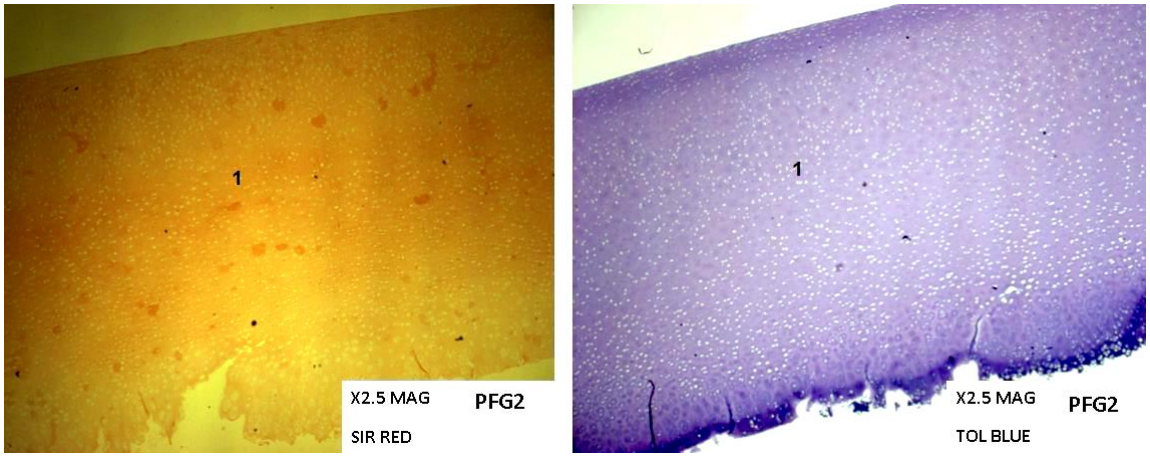

Figure 6-7. Histological depth profile of cartilage take from PFG2; left - picrosirius red stained for collagen, right - toluidine blue stained for proteoglycan.

6.4 Discussion

The histological analysis performed here offers qualitative information about the content and distribution of extracellular matrix proteins, namely collagen and proteoglycans, in all the harvest locations. Given that it has been already demonstrated that the compressive stiffness and Poisson's ratio can be dependent on these proteins, the information presented here may offer a further insight and discussion to the results found for these parameters earlier in this thesis.

The compressive stiffness of cartilage has been strongly linked the tissues PG content both in this thesis and in other literature (see section 3.4) and the aggregate modulus of the cartilage in the PFG sites was found to be significantly higher indicating a greater PG content is present. This certainly appears to be the case with the toluidine blue stain of PFG2 (figure 6-7), with a single constant concentration of PG visible throughout the depth of this sample. The condyles present a layered distribution of PG, ranging from 1-3 layers, beginning with a high concentration at the surface to a low concentration just prior to the calcified zone (figures 6-2 to 6-5). This, however, is not indicative of preferential strain occurring in areas of low PG content. The stiffness of articular cartilage is varied, increasing from the superficial layer in a depth-dependent manner and preferential strain occurs at the articular surface (Schinagl et al., 1997). This acts to improve the congruence between joint surfaces and reduce permeability to maintain interstitial fluid pressurisation. Hence, it is likely that there are other influences contributing to the aggregate modulus rather than just PG content and its distribution.

The Poisson's ratio of cartilage has been found to inversely correlate with collagen content (see section 4.3). Like the toluidine blue staining did for PG's, the picrosirius red stains revealed a layered distribution of collagen content. The number of layers varied from site to site, but what was generally consistent was that the collagen content at the deep surface was generally higher than the articular surface. A greater Poisson's ratio should thus be located at the articular surface. However, Poisson's ratio has been

consistently shown to be greater in the deeper surfaces in most of the harvest locations albeit not statistically. Thus, there appears to be other influences at work in dictating the mechanics of the structure rather than protein content alone.

The collagen network structure and the age-related development of this structure is the most likely explanation. Rieppo et al. examined the changes in collagen content and the collagen network with time in the cartilage of the porcine patellofemoral groove (Rieppo et al., 2009). In animals of 4 months of age, relatively constant low collagen content and a fibril organisation parallel to the surface was witnessed throughout the depth of the cartilage. At 11 months, collagen content began to rise with depth together with substantial heterogeneity in fibril organisation and after 21 months a characteristic adult cartilage phenotype was observed. The distribution of collagen in PFG1 and PFG2 observed in figure 6-6 & 6-7 is similar to that found in the patellofemoral grove by Rieppo et al. in pigs of 11/21 and 4 months respectively. The pigs used for the studies in this thesis were sacrificed at 6-8 months of age. Thus, it may be the case that maturation of cartilage in the patellofemoral groove is occurring earlier inferiorly nearer the condyles (PFG1) and progressing superiorly (PFG2). Cartilage thickness was also found to be significantly thinner at PFG1 compared to PFG2 (section 3.3.1.1) which is also indicative of tissue maturation (Rieppo et al., 2009). Hence, there appears to be varying stages of maturation occurring within the PFG itself in these animals.

In order to explain the results of some of the mechanical properties, it has previously been suggested that the cartilage in the condyles is at further stage of maturation. For the most part, this appears to be true, except for M1, which possesses a collagen distribution similar to that of PFG2. Further to this hypothesis, is evidence that maturation occurs at different rates in different locations in the rabbit knee by Julkunen et al. (Julkunen et al., 2009). Prior to 3 months of age collagen architecture appeared to mature earlier in the femur rather than the tibia, effecting the thickness and mechanical properties of the tissues. As was shown by Rieppo et al. (Rieppo et al., 2009), there was a dominant

collagen fibril orientation parallel to the surface which accounted for an enhanced apparent stiffness in immature cartilage.

Julkunen et al. also demonstrated that as both femoral and tibial cartilage matured collagen content and cross-linking increased and correlated with the equilibrium moduli of the tissues (Julkunen et al., 2009). However, the rate at which these increased is also likely to vary from site to site depending on the demands of the particular location. Hyttinen et al. examined two sites in equine metacarpophalangeal joints with this in mind (Hyttinen et al., 2009). Sites 1 was exposed to intermittent peak loading and shear, whereas site 2 was exposed to constant, moderate loading. Prior to 5 months of age, both sites appear to have similar amounts of collagen, but a greater rate of collagen synthesis at site 1 thereafter leads to a greater collagen presence in adulthood. Cross-linking and parallelism of the fibrils was also found to be enhanced in site 1. It was thus proposed that the nature and history of govern the local collagen network development.

Hence, it has become clear that a number of factors could be working in conjunction with the distribution of the extracellular matrix proteins seen in the histological images to govern the aggregate modulus and Poisson's ratio results. Beginning with the Poisson's ratio results, the most likely explanation for variations is the orientation of collagen fibrils. Collagen content and crosslinking undoubtedly has an influence on the lateral expansion of the tissue (Ficklin et al., 2007, Kiviranta et al., 2006, Williamson et al., 2001). However, the more collagen that is aligned in this lateral axis (i.e. parallel to the articular surface), the more fibrils are in tension and resisting lateral expansion. The variations between Poisson's ratios in surface and deep zones are also likely to be caused by fibril orientation parallel to the surface in the superficial zone and the axial arrangement deep in the tissue which is likely to be less resistive to lateral shape changes (Jurvelin et al., 1997).

The Poisson's ratio of the PFG sites was significantly lower than the condyles. Rieppo et al. demonstrated high collagen fibril parallelism in immature porcine PFG cartilage

(Rieppo et al., 2009), and it is likely that it is this key feature that produced such a low Poisson's ratio in PFG2. PFG1 appears to be more mature in phenotype so the reason why it is generating a large Poisson's ratio may be related to increased fibril heterogeneity possible in PFG should not be present. Perhaps, as the patellofemoral joint is subject to different loading conditions than the condyles, maturation has caused greater collagen content and crosslinking in a similar manner to that suggested by Hyttinen et al. (Hyttinen et al., 2009). Although perhaps not in a parallel orientation, any strengthening of the fibrils due to crosslinking would nevertheless increase lateral resistance to expansion and so reduce the Poisson's ratio.

As previously mentioned, the uniform distribution of PG's in PFG2 may uniformly resist axial strain, hence leading to the higher aggregate modulus observed. The stratified arrangement of PG's in the PFG1 site suggests a lower aggregate modulus similar to that found in the condyles. However, although it was lower than PFG2 (not surprising due to the variation in PG distribution), PFG1 produced an aggregate modulus higher than that found in the condyles. Collagen content and crosslinking have been shown to correlate with compressive equilibrium moduli (Ficklin et al., 2007, Julkunen et al., 2009, Kiviranta et al., 2006), confined or unconfined. An increase in collagen content and crosslinking due to site specific maturation may also explain the significant difference discovered in aggregate modulus between PFG1 and the condyle locations. Thus, it may be the case that cartilage in the PFG locations maintains a greater stiffness than the condyles as it matures.

7 The Frictional Properties of Articular Cartilage in the Porcine Knee

7.1 Introduction

Friction may be described as the resistance to motion when two opposing surfaces move relative to one another. This resistance is most commonly due to abrasion between microscopic asperities on the contacting surfaces, but may also be due in part by the shear resistance of the lubricant between the surfaces.

The relative proximity of the asperities causes adhesive contacts due to interatomic attractions. Fundamentally, adhesion can be described as either physical or chemical in nature. Chemical adhesion describes covalent, ionic and electrostatic bonds whereas physical adhesion involves the hydrogen and van der Waals bonds due to intermolecular forces. Physical bonds are weaker than their chemical counterparts because there is no electron exchange in these cases. However, van der Waals bonds are always present between neighbouring asperities and experimental data suggests that adhesion is primarily due to these forces (Bhushan, 2003, Williams, 2005).

Furthermore, any viscoelastic deformation under load such as creep increases the real area of contact (contact between opposing asperities) leading to an increase in adhesion as a function of duration of contact (Bhushan, 2003). This is observed in figure 7-1 for the case of a steel sphere on indium.

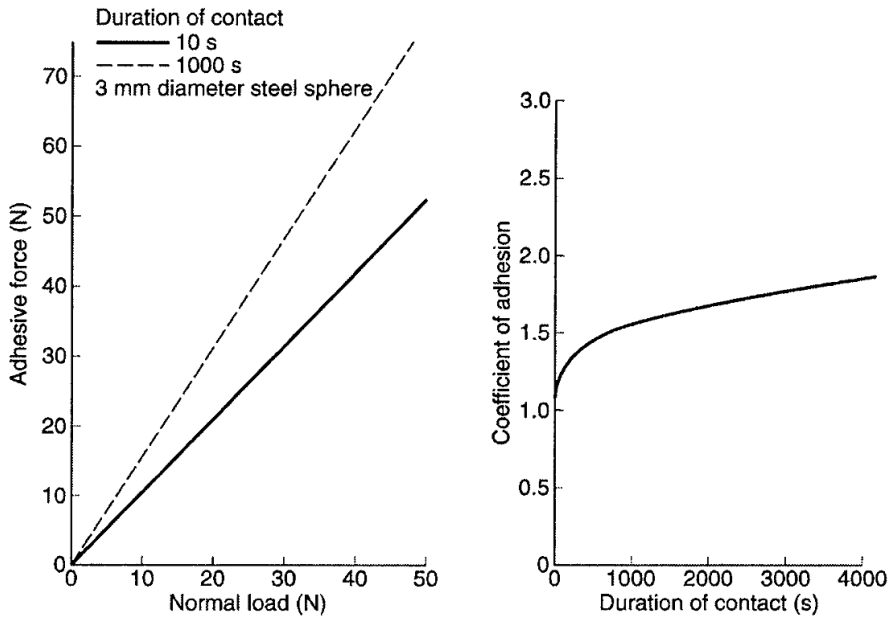

Figure 7-1. (a) Adhesive force versus normal load for a steel sphere on indium after two different time periods and (b) the coefficient of friction for the steel sphere is seen to increase with duration of contact (Bhushan, 2003).

Figure 7-2 presents a graph of frictional force versus time. In this instance, the static frictional force (*Fs*) to initiate sliding is greater than the kinetic or dynamic frictional force (*Fk*) to maintain the sliding. This is known as "stiction". Such is the case in the presence of a thin fluid film separating the contacting surfaces as high static friction can occur due to meniscal and rate dependent viscous effects. Curved menisci form around the contacting asperities due to surface energy effects and an attractive meniscal force is generated from negative Laplace pressure inside the meniscus as a result of surface tension (Bhushan, 2003).

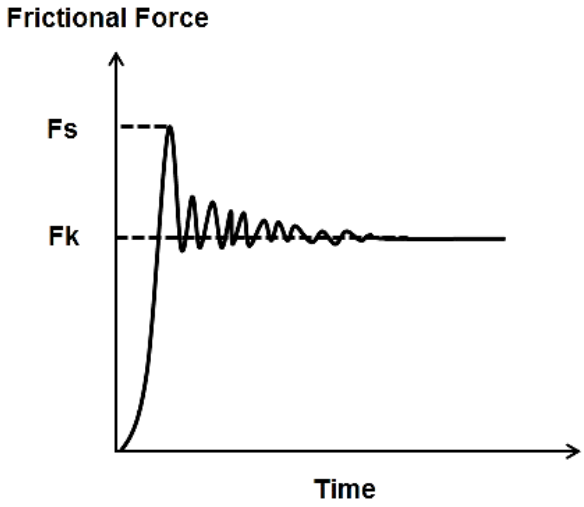

Figure 7-2. Graph depicting the change of frictional force with time for the case of static frictional force being initially higher than the kinetic frictional force.

When linearly applying a load between two surfaces, the applied force changes from meniscal to viscous prior to the separation of the surfaces. Thus, for an applied force less than that of the meniscal force, there is no tendency for separation to occur. When the meniscal force is exceeded, the viscous component in the normal direction is activated until finally separation occurs (figure 7-3). The viscous component of this adhesive force is far more significant in fluids of greater viscosity but can still dominate at high shear rates in fluids of more modest viscosity.

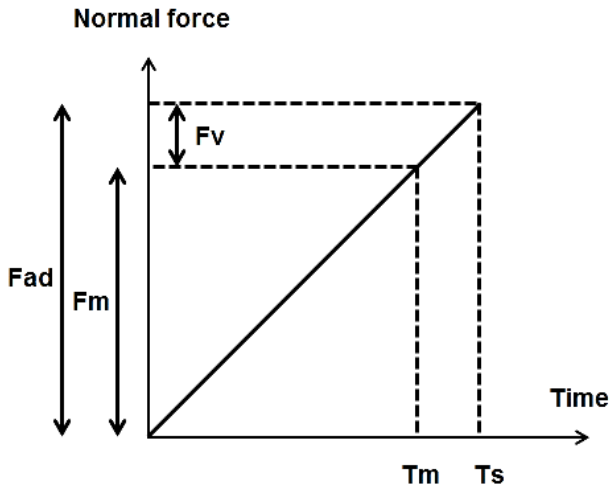

Figure 7-3. The meniscal and viscous contributions of the force-time relationship between two surfaces with a liquid bridge under a ramping load. Adapted from (Bhushan, 2003).

The surface roughness of cartilage may be considered relatively large at 1-6μm (Martin et al., 1998), as the femoral head of metal and ceramic hip prostheses boast surface roughness's of 0.01μm and 0.005μm respectively (Mabuchi et al., 2004, Udofia and Jin, 2003). Yet, despite this the coefficient of cartilage against cartilage has been found to be exceptionally low, in the range of 0.002-0.02 (Mow and Lai, 1980), prompting many hypotheses to be developed as to why this is the case. Many classical engineering theories have been extended to explain the low friction and wear of cartilage. However, no single theory has been able to comprehensively explain all the lubrication characteristics in every loading scenario.

One such theory is hydrodynamic lubrication. This occurs when two opposing surfaces moving at high speeds converge to a 'wedge' shape, generating fluid pressure great enough to push the two surfaces apart. However, hydrodynamic lubrication fails to predict an adequate fluid film thickness greater than the average surface roughness of cartilage. Therefore, it is far more likely that elastohydrodynamic or a mixed lubrication regime is present during the swing phase and boundary lubrication is present throughout the stance phase given the velocity to load ratios over each period (Neu et al., 2008).

Elastohydrodynamic lubrication is a theory generally applied to metal-on-metal and metal-on-plastic joint prostheses (Jalali-Vahid et al., 2003b, Jalali-Vahid et al., 2003a, Scholes and Unsworth, 2000, Udofia and Jin, 2003, Wang et al., 2008, Wang et al., 2004, Yew et al., 2004). The underlying principle here is that when the fluid pressure generated between the surfaces is sufficiently high, elastic deformation of the surfaces takes place which in turn causes the pressure to drop off. As for cartilage, Dowson and Jin developed the theory of micro-elastohydrodynamic lubrication, whereby the asperities are deformed and flattened causing an overall increase in the surface roughness to film thickness ratio (Dowson and Jin, 1986).

If a lubrication film thickness capable of separating the joint surfaces cannot be generated, then the only potential barrier preventing direct contact is an adsorbed molecular monolayer (Neu et al., 2008). This is known as boundary lubrication. A number of synovial fluid constituents has been shown to adhere to and significantly reduce the friction coefficient (Schmidt et al., 2007). This was been shown for hyaluronan (Bell et al., 2006, Schmidt et al., 2007), lubricin (Jay, 1992, Schmidt et al., 2007, Swann et al., 1981, Swann et al., 1985) and both combined together (Jay et al., 1992, Schmidt et al., 2007). The lubricious effect of surface-active phospholipids also been investigated but was shown to play no significant role (Schmidt et al., 2007). Superficial zone protein (SZP) however has been highlighted as potential source of friction reduction.

Another form of lubrication is the squeeze-film variant. This is said to occur if the viscosity of the lubricant is sufficiently high that it is slow to be squeezed out of the cartilage as the surfaces approach each other. A slowly reducing film thickness is formed, separating the joint articulations. However, if this form of lubrication is to exist, the proposed time for the surfaces to touch should be greater than that found physiologically.

Perhaps, the most recognised form of lubrication is bi-phasic lubrication. The hypothesis that interstitial fluid may have a role to play in lubrication was first put forward by Lewis and McCutchen in 1959 as ‘weeping’ lubrication (Lewis and McCutchen, 1959). This exists when cartilage is brought in contact with an opposing surface of metal or glass and enough interstitial fluid is exuded to separate the surfaces. However, this principle had to wait until 1980 when Mow described bi-phasic theory (Mow et al., 1980) until it could be adapted to form bi-phasic lubrication theory (Mow and Lai, 1980). According to this theory it is the load sharing between solid and fluid phases, primarily the fluid phase, which causes such a minimal coefficient of friction. However the longer cartilage is loaded, the more it is increasingly supported by the solid phase resulting in an increasing coefficient of friction. This occurrence was demonstrated experimentally by Forster and Fisher for cartilage against metal on a pin-on-plate setup for time periods of up to 120 minutes (Forster and Fisher, 1999). Further evidence was provided by Krishnan et al. using a similar cartilage against polished glass pin-on-plate arrangement (Krishnan et al., 2004).

It is proposed that it is worthy of investigation to determine the coefficient of friction of cartilage from anatomical sites relevant to OAT therapy in a bi-phasic lubrication context. It may be possible that a different coefficient of friction occurs at the harvest site than that is normally at the site of the condyles, either initially, or with time under with applied load. The following is to be performed to examine this possibility:

- Harvest osteochondral plugs from different regions of the porcine knee representative of the locations where OAT would take plugs from and subsequently implant them.
- Calculate the coefficient of friction of the cartilage using a simplified cartilage against polished glass pin-on-plate setup.
- This shall be carried out with varying sliding velocity against loading time.
- Interpret the results to ascertain whether there are possible implications for AOT therapy.

7.2 Methods

7.2.1 Sample Preparation

Osteochondral plugs were harvested from a further five porcine knee joints from the same anatomical locations (L1, L2, M1, M2, PFG1 & PFG2) and using the same method described in section 4.2.1, however, an alternative cork borer was employed to yield 7mm diameter plugs. On this occasion, cartilage was not removed but the bone ends of the plugs were squared using a band-saw, then well irrigated with PBS and frozen at a temperature of -20°C for storage purposes. Samples were thawed and equilibrated in PBS for one hour prior to testing.

7.2.2 Friction Testing

A Schematic Diagram, along with picture, of the custom made apparatus used for friction testing of the prepared osteochondral specimens is shown in figure 7-4a & b respectively. The apparatus consisted of a fixed linear bearing with accompanying aluminium shaft (igus® UK Ltd, Brackmills, Northampton). One end of the aluminium shaft was machined to accept the insertion of a 7mm osteochondral plug with a press-fit tolerance. The remaining end of the shaft was fitted with a nylon cap, upon which weights could be mounted. A polished glass dish was fixed to a linear carriage and railing system (igus® UK Ltd, Brackmills, Northampton) with adhesive. The dish was half filled with PBS and the shaft-bearing assembly arranged vertically above it so as to insert the osteochondral plug into the PBS with the cartilage end flush against the glass surface. Fishing line was attached to the carriage and run horizontally to a pulley from which it ran in a vertical path to the MTS. When the line was taut a 90 degree angle was formed by the line and pulley system. This was achieved by incurring a pre-load of 0.2N. With all elements in place, the MTS crosshead could be raised at a predefined rate to slide the glass plate beneath a weighted cartilage specimen a distance of 40mm. The force required to cause translation of the glass plate was recorded by the MTS. Hence, a

frictional force was determined corresponding with the applied normal load to the cartilage (weight applied plus aluminium shaft & nylon cap).

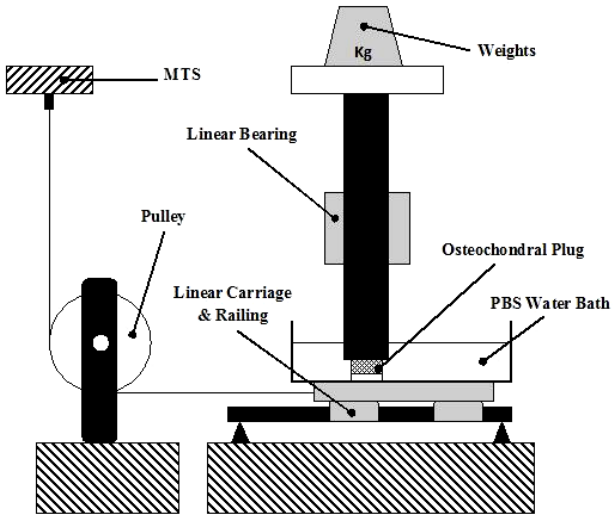

(a)

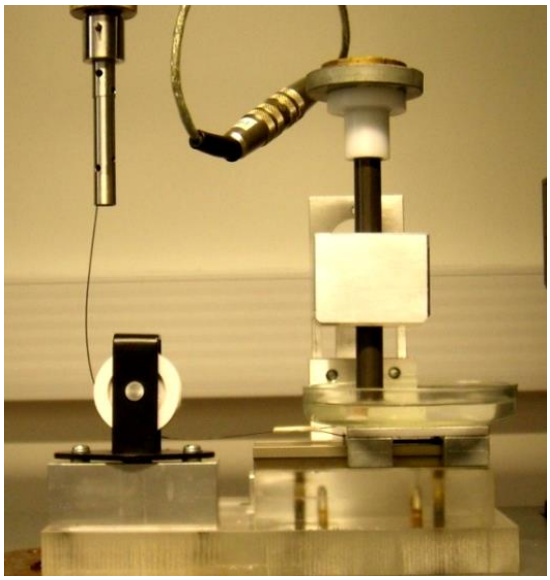

(b)

Figure 7-4. (a) Schematic and (b) picture of rig used in friction testing.

Weight was applied in five successive stages; 98, 196, 391, 587 & 799g, translating to normal loads of 0.961, 1.923, 3.836, 5.758 & 7.838N. For each weight applied, 5 minutes was allowed to elapse before testing began, at which point the frictional force was recorded for sliding velocities of 1, 2 & 3mm/s in quick succession. These velocities were chosen as they satisfy the range specified by Katta et al. in a review of pin-on-plate biotribology (Katta et al., 2008). Often synovial joints are considered to operate in a mixed lubrication regime in simple elastic contact. Hence, these slow sliding velocities are adopted in pin-on-plate testing in an attempt to replicate these conditions *in-vitro*. Higher speeds may result in the formation of elastohydrodynamic lubrication. This was repeated every 5 minutes until 20 minutes under constant loading had elapsed upon which time the next successive weight was then added and the routine repeated.

It has previously been demonstrated that the engineering frictional coefficient of cartilage (i.e. the ratio of frictional force to normally applied load) decreases with increasing normal loads or contact stresses (Katta et al., 2008, Lizhang et al., 2011) and that this is particularly evident over greater sliding distances (10mm) (Katta et al., 2008). The decline of the engineering frictional coefficient will eventually equilibrate at a value known as the true frictional coefficient at high contact stresses. However, this can be more readily calculated be measuring the slope of a plot of frictional force versus normal load (Chan et al., 2011). This method was performed in this study, as it not only calculated a frictional coefficient representative of *in-vivo* loading, but it also allowed this single representation of friction to be analysed independently with, or with a combination of other parameters such as sliding velocity and the duration of loading.

Prior to any testing however, it was essential to determine the force required to slide the carriage and glass plate (with PBS) alone so that this could be deducted when measuring the frictional force of cartilage specimen within the set-up. To this end, ten trials were performed for each of the sliding velocities so that their average values could be ascertained and deducted from any points of interest. Again, a pre-load of 0.2N was employed to ensure the line was taut. The results of the trial assessment of the carriage

and plate are presented in figure 7-5. No significant differences were observed between velocity groups so an average value of 0.6N was taken to be the static friction at 0mm and 0.52N to be the dynamic friction at 40mm translation for all velocities concerned.

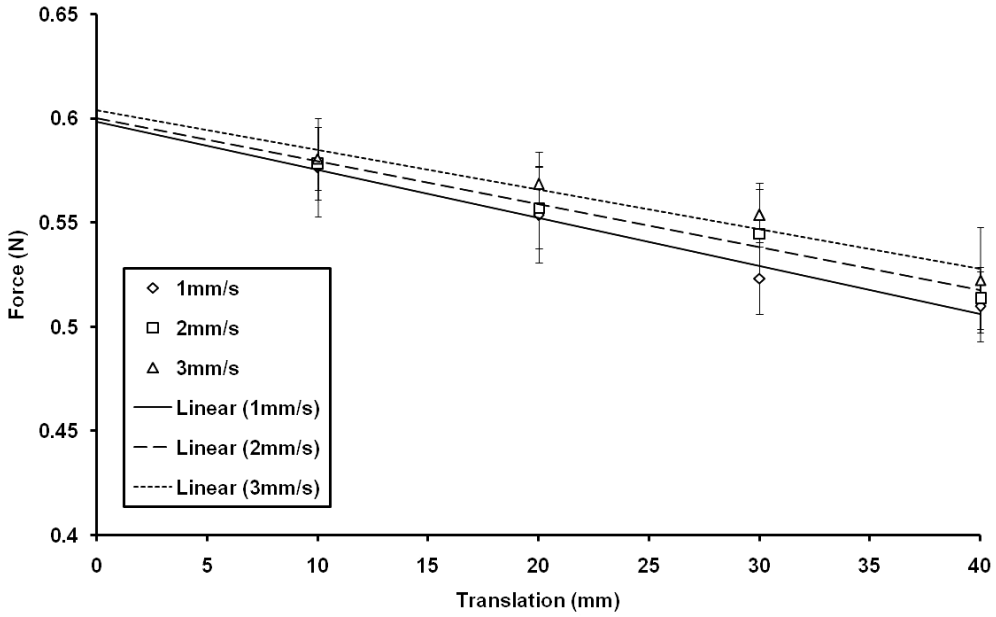

Figure 7-5. Frictional force produced by carriage and glass plate alone. An average static friction of approximately 0.6N and dynamic friction of approximately 0.52N exists after 40mm translation for all three sliding velocities.

7.2.3 Statistics

A 4-way repeated measures ANOVA was performed for the purposes of statistical analysis in chapter 7. Friction type, sliding velocity and time were within-subjects factors, whilst sample location was a between subjects factor. The model included main effects and all two-way interactions between the within-subjects variables. The Greenhouse-Geissersphericity correction factor was employed over the less conservative Huynh-Feidt correction factor to calculate P-values. A P-value of <0.05 was considered to be statistically significant

7.3 Results

A typical load curve recorded for the frictional force of cartilage on glass is presented in figure 7-6. The presence of "stiction" is clearly observed. A rapid rise is observed initially from the 0.2N pre-load to peak and steadily relax to an equilibrium force over the majority of the translation. The peak recorded was attributed to be the force to overcome static friction, whereas the dynamic frictional force was defined as the force recorded after the full 40mm translation. The trials of the unloaded rig specified that 0.6N be deducted from the static frictional value and 0.52N be deducted from the dynamic value to determine a cartilage specimen's corresponding frictional values without interference from the test rig. Furthermore, since both the trials and the actual tests both employed the same pre-load of 0.2N, it was essentially negated in calculating the difference.

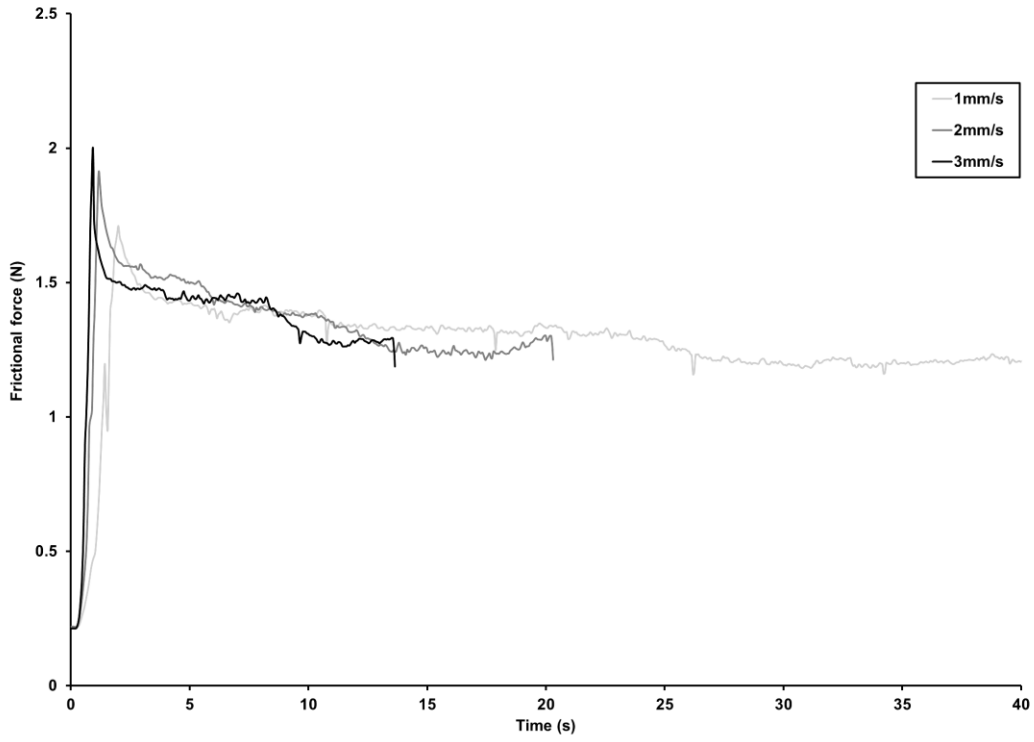

Figure 7-6. Example of a typical load curve recording the frictional force of cartilage within the experimental rig (Site: PFG1, Load: 1.923N, Time: 10mins).

For each sample, at each given time period and velocity, a scatter plot was created plotting the recorded frictional forces against the normally applied load increments. An example of such a plot for the dynamic coefficient of friction is shown in figure 7-7. The slope of the line of best fit to this data was deemed to be the true coefficient of friction in accordance with the following equation;

$$F = \mu R \qquad \textbf{Equation 7-1}$$

Where,

F = Frictional force,

R = Normal applied load,

μ = Coefficient of friction.

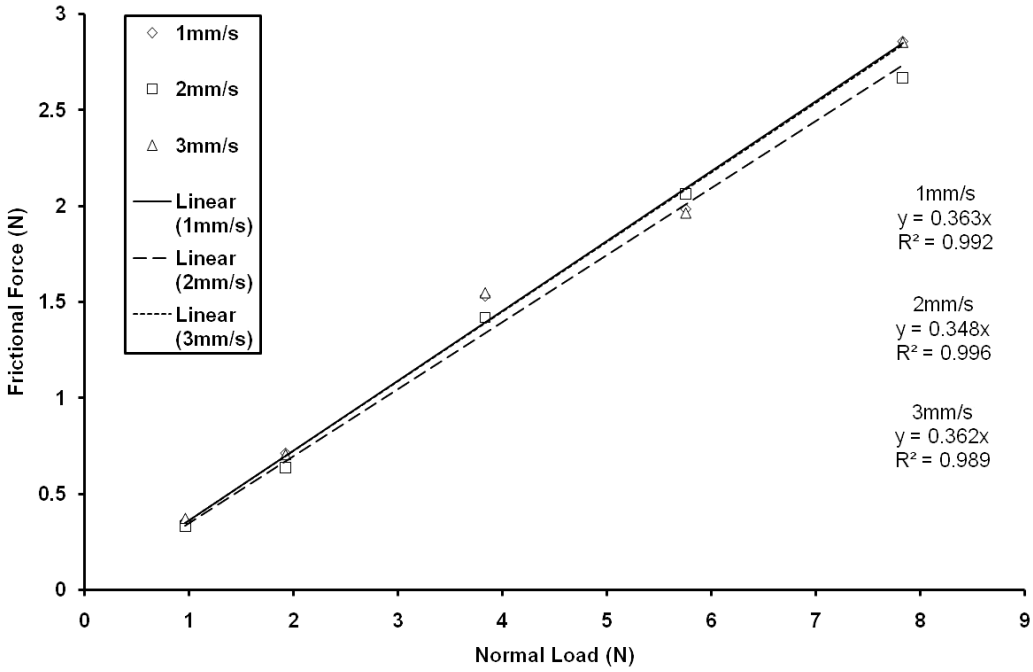

Figure 7-7. Plot of the dynamic frictional force measurements of cartilage (Y-axis) after being subjected to 5mins of their corresponding normal applied loads (X-axis). The specimen in this case was from the L1 group. In this instance, friction coefficients of 0.363, 0.348 & 0.362 were found for 1, 2 & 3mm/s sliding velocities.

Figures 7-8 through to 7-13 display all the complied calculations of friction coefficient for L1, L2, M1, M2, PFG1 & PFG2 groups respectively. Each chart shows the effect of time on friction for velocities of 1, 2 & 3mm/s. On first observations of the charts, it is intuitively evident that for both friction types (static & dynamic) the more time a cartilage specimen spends loaded, the larger the friction becomes. It also appears that an increase in velocity can increase friction, though this is far more evident for static friction rather than dynamic friction. On first observation, there appears to be no obvious effect of anatomical location on the magnitude of the friction types, for any given time period or velocity. However, a full in-depth analysis demands a statistical examination of the data to reveal any trends emerging.

The relationships between friction and time, and friction and sliding velocity were found to be different for both static and dynamic conditions combined ($P<0.001$ in both cases). There was some evidence suggestive of a trend that the relationship between friction and time may depend on sliding velocity, but found to be inconclusive ($P=0.067$). There was no effect on sample harvest location to any of the variables ($P=0.867$).

Due to the main effect and significant interaction of static and dynamic friction with time and sliding velocity, it was deemed valid to analyse each type of friction (static and dynamic) independently. Time and velocity were found to have a highly significantly different influences on static and dynamic friction groups ($P<0.001$ in all cases). On this occasion, the relation between friction and time was found to be significantly affected by sliding velocity within static groups ($P=0.016$). However, this did not appear to be the case within dynamic friction groups ($P=0.069$). Finally, sample harvest location introduced no significant affect to either static or dynamic friction groups ($P=0.644$ & 0.876 respectively).

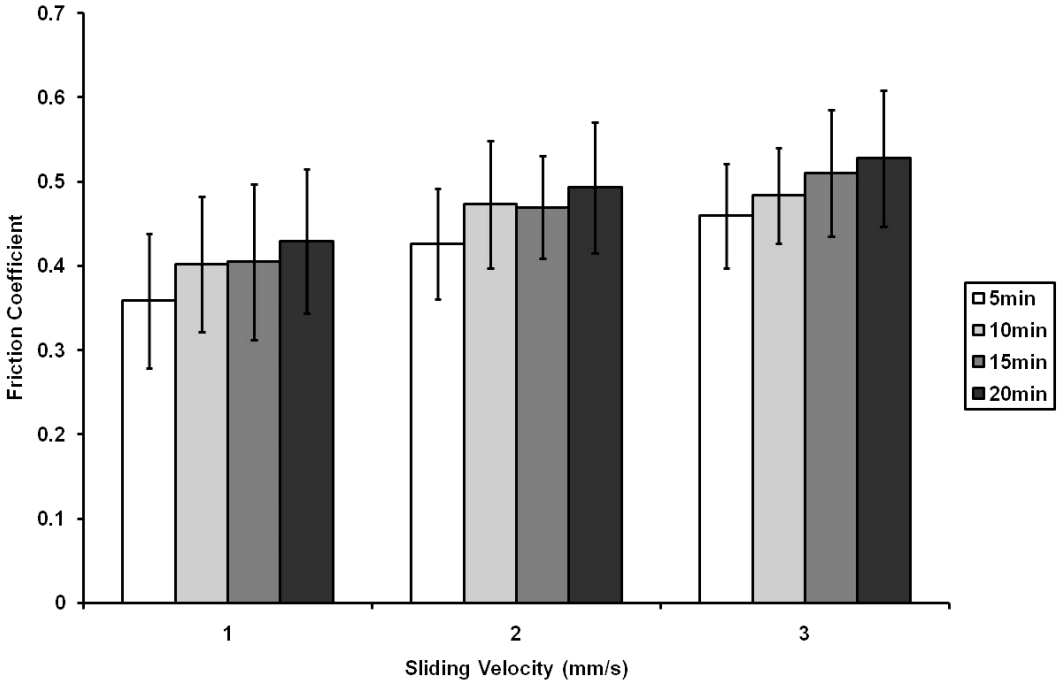

(a)

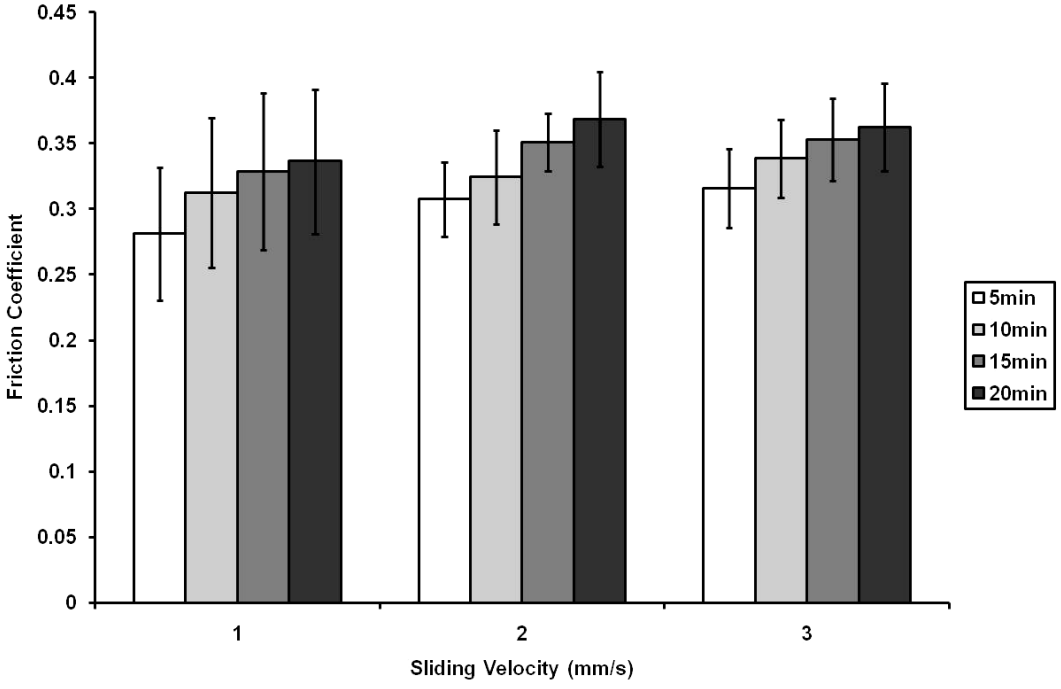

(b)

Figure 7-8. (a) The static coefficient of friction & (b) dynamic coefficient of friction for L1. Results shown as mean +/- SD (n=5). Time indicates duration of applied loading.

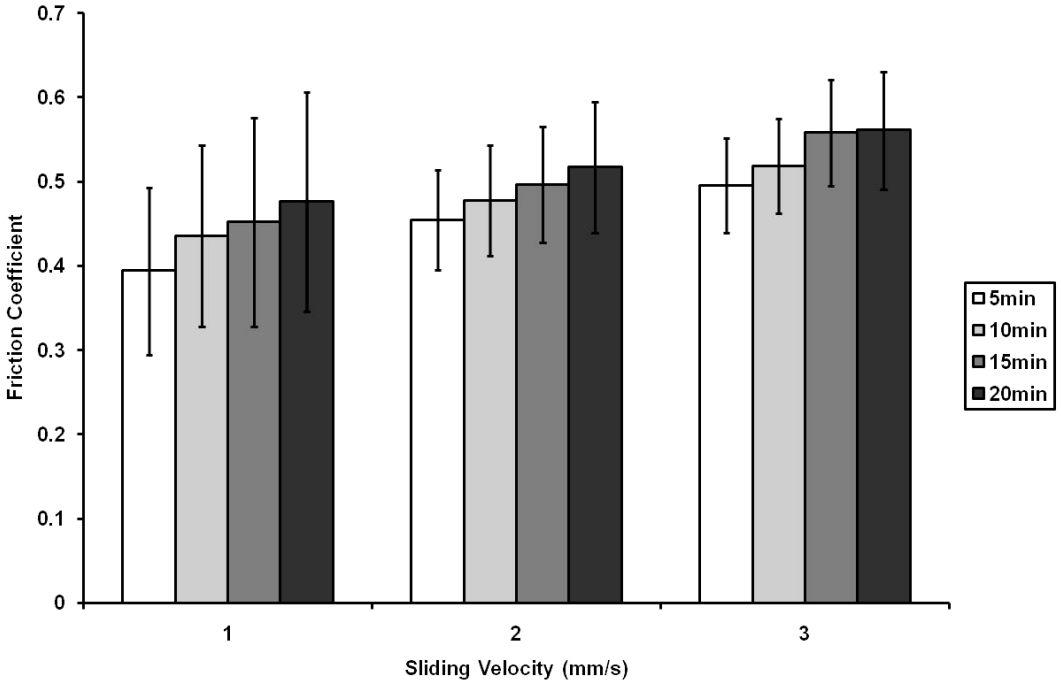

(a)

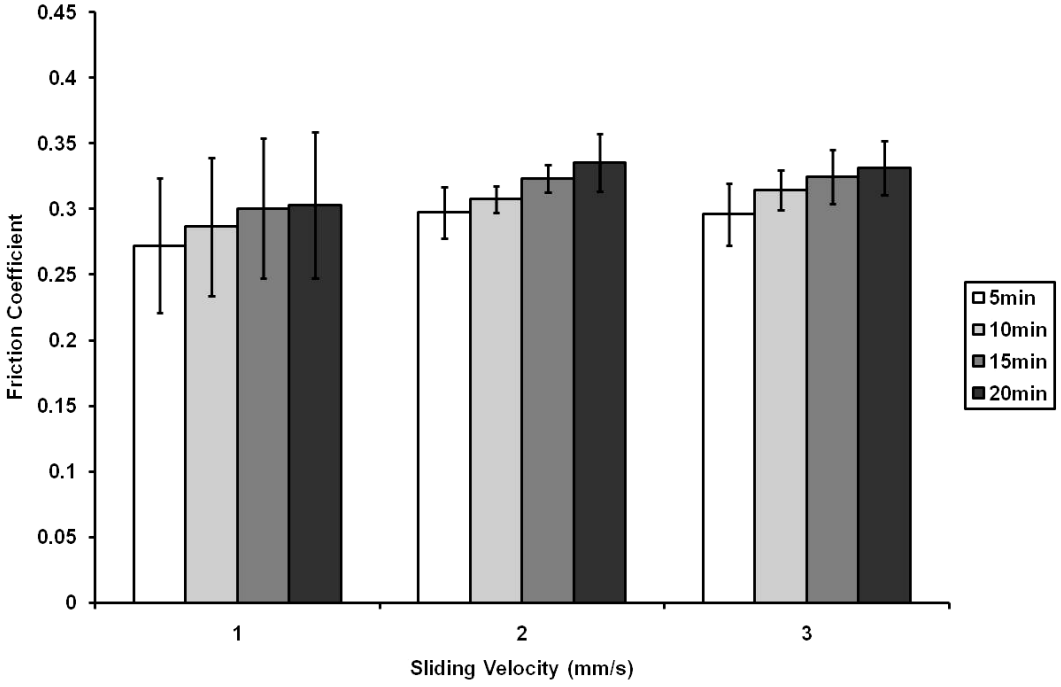

(b)

Figure 7-9. (a) The static coefficient of friction & (b) dynamic coefficient of friction for L2. Results shown as mean +/- SD (n=5). Time indicates duration of applied loading.

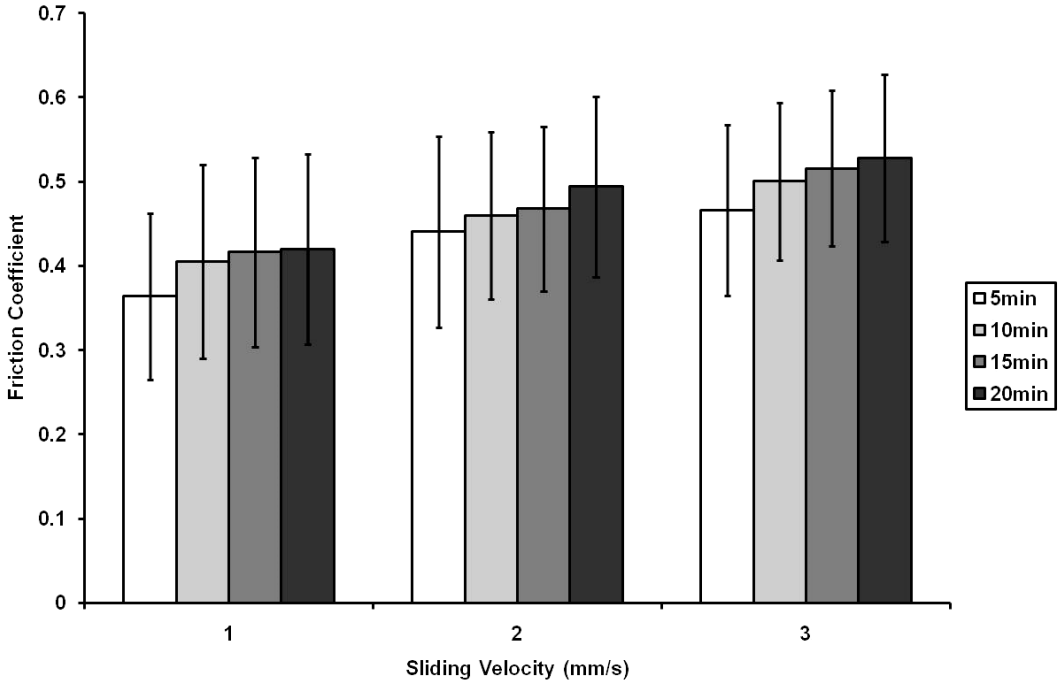

(a)

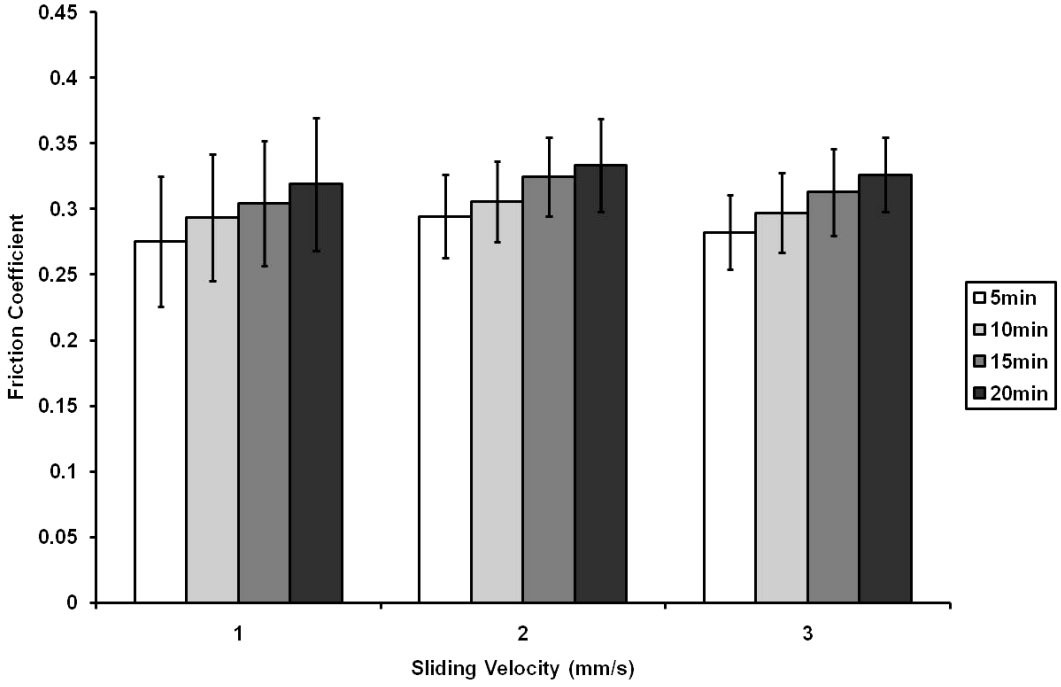

(b)

Figure 7-10. (a) The static coefficient of friction & (b) dynamic coefficient of friction for M1. Results shown as mean +/- SD (n=5). Time indicates duration of applied loading.

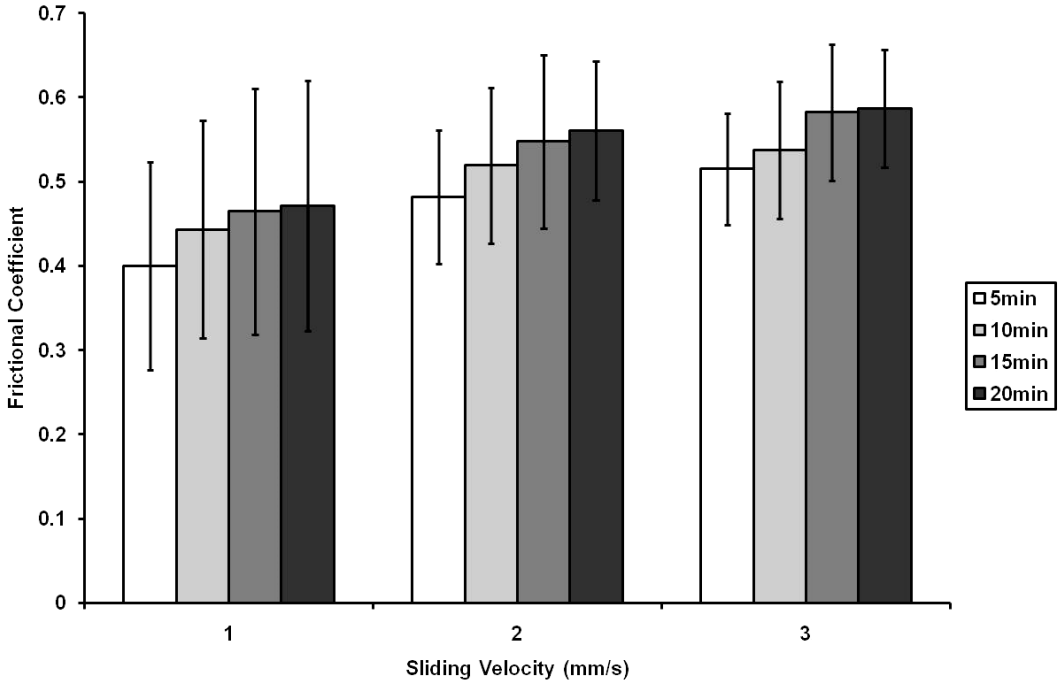

(a)

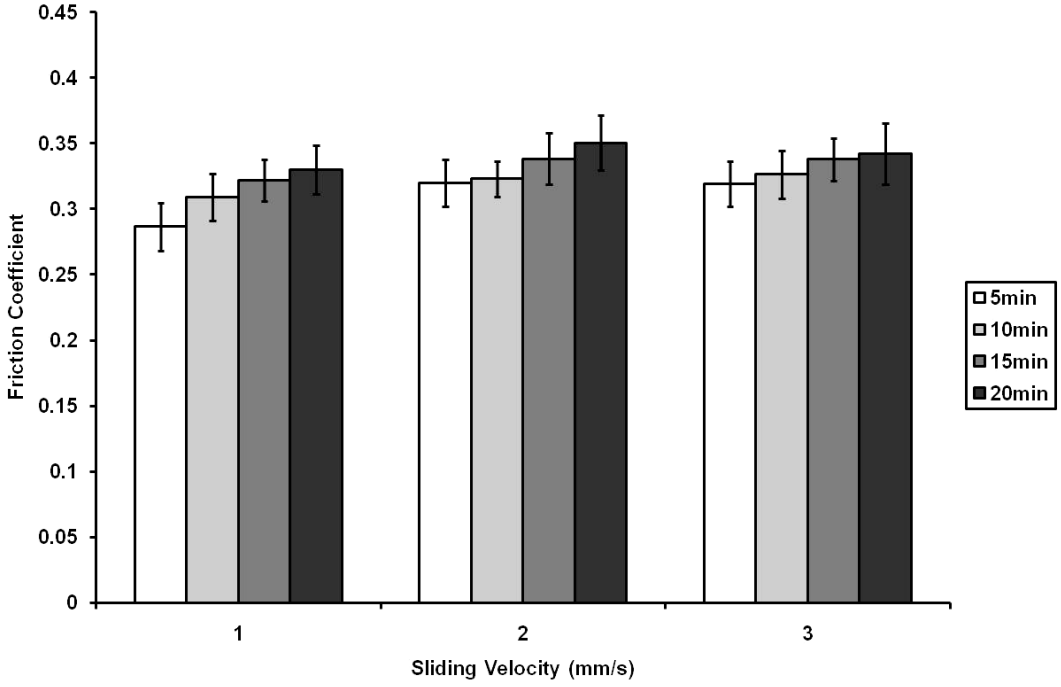

(b)

Figure 7-11. (a) The static coefficient of friction & (b) dynamic coefficient of friction for M2. Results shown as mean +/- SD (n=5). Time indicates duration of applied loading.

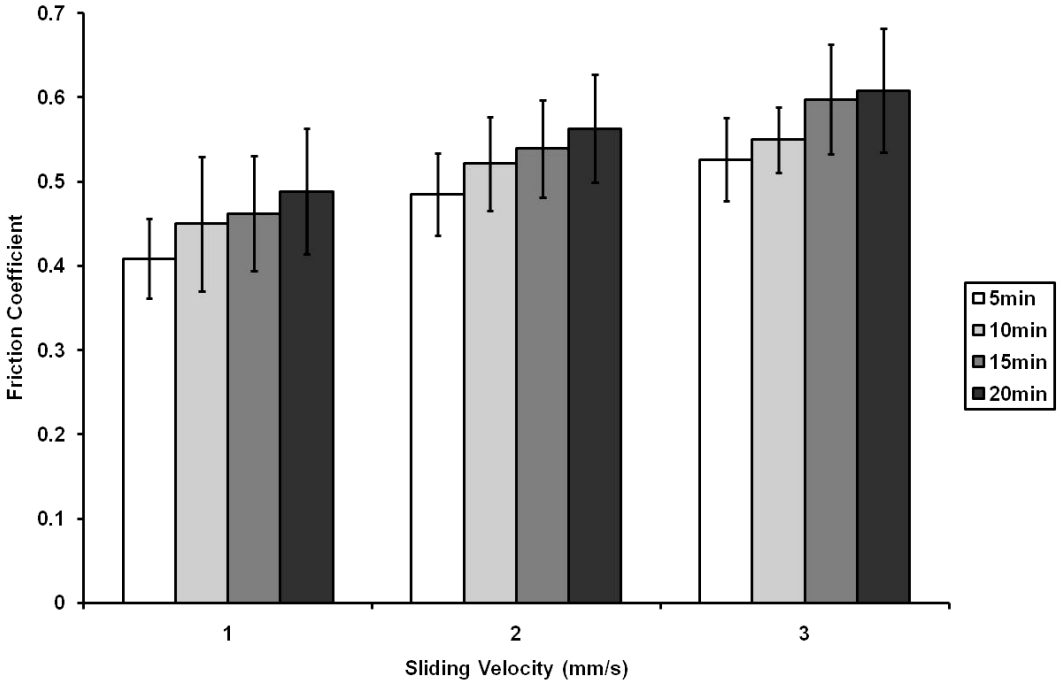

(a)

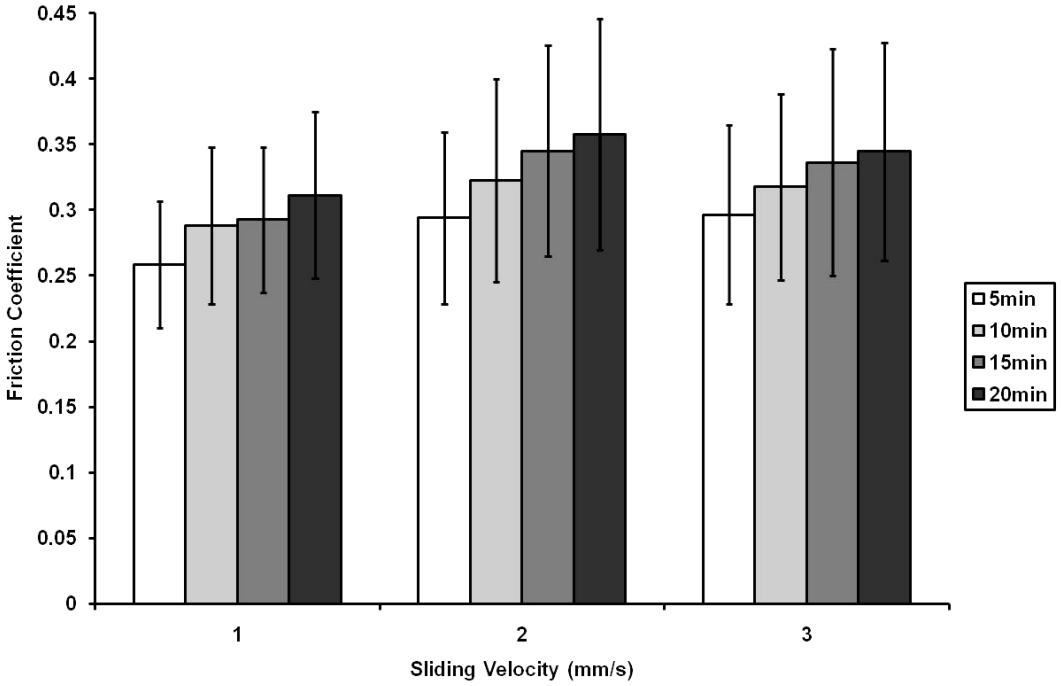

(b)

Figure 7-12. (a) The static coefficient of friction & (b) dynamic coefficient of friction for PFG1. Results shown as mean +/- SD (n=5). Time indicates duration of applied loading.

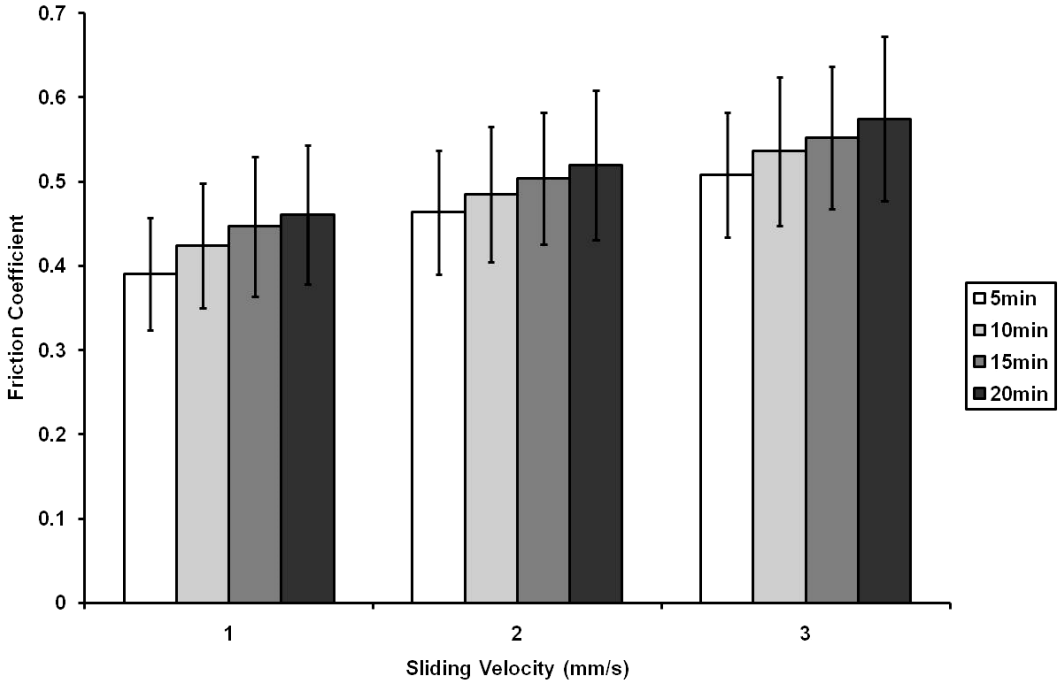

(a)

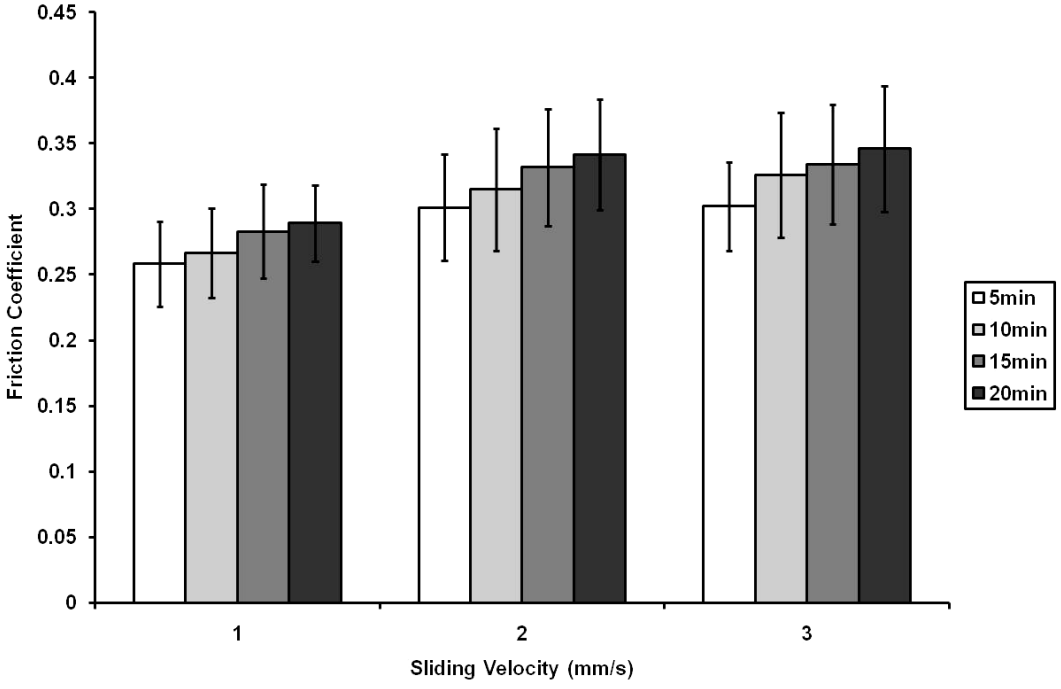

(b)

Figure 7-13. (a) The static coefficient of friction & (b) dynamic coefficient of friction for PFG2. Results shown as mean +/- SD (n=5). Time indicates duration of applied loading.

7.4 Discussion

The range of values determined for the frictional coefficients are similar to those specified by many other authors for cartilage on glass and cartilage on metal plate configurations. For example, Krishnan et al. and Forster and Fisher found coefficients of friction that ranged to upward values of 0.25 and 0.35 for cartilage on glass and cartilage on metal respectively (Forster and Fisher, 1996, Krishnan et al., 2004).

One of the dominant findings of this study was the temporal response of the coefficient of friction to loading. For either static or dynamic conditions, friction was found to increase with loading time, a trait consistent with biphasic lubrication theory and the findings of many other authors whether the normal load is static (Forster and Fisher, 1996), dynamic (Krishnan et al., 2005) or multi-directional (i.e. with rotation) (Northwood and Fisher, 2007). Friction becomes elevated in cartilage with time due to the increasing influence of its solid phase. Therefore, friction can be kept at a very low level as long as the fluid phase load support is maintained at a very high level (Katta et al., 2008). The fluid phase load support is generated in a number of ways. In addition to osmotic pressure due to physiochemical effects, the interstitial fluid of the tissue will pressurise as a result of mechanical loading (Ateshian, 2009). Due to the very low permeability of cartilage (in the region of 10^{-15} to 10^{-16} m^4Ns), any mechanically induced internal fluid flow generates large drag forces and pressure gradients. However, the mechanical load applied to cartilage is only initially supported by this interstitial fluid pressurisation and as time increases the fluid pressurisation decreases as fluid escapes, transferring more of the load to the solid phase of the cartilage. Hence, the friction increases as the fluid load support decreases.

Shi et al demonstrated this loss in fluid load support and rise in friction for a similar set-up to that described here (Shi et al., 2011). Using a bovine cartilage pin on a reciprocating alumina plate, the fluid load support was found to drop from an initial value of 71% to 0% after 1885 seconds. The corresponding coefficient of friction was

found to rise from 0.099 to 0.271 over this period. Even after periods as short as 5mins, it appeared the coefficient of friction had risen to over 0.25, similar to values presented in section 6.3. Krishnan et al. found that a fluid load support drop of 88.8% to 8.7% corresponded to an increase in friction from 0.01 to 0.243 in a cartilage on glass configuration (Krishnan et al., 2004). However further to this, it was also demonstrated that this loss in interstitial fluid load support was inversely correlated to both the fictional coefficient and the creep displacement. The frictional study performed in this thesis also demonstrates a significant association between friction and time, confirming that interstitial fluid pressurisation is the primary mechanism in regulating the frictional response.

Only the static coefficient of friction was found to be influenced by the sliding velocity applied. Furthermore, this friction was found to increase with increasing velocity regardless of the loading time. It has previously been discussed in section 7.1 that the force of adhesion grows with increasing time under creep loading conditions (figure 7-1). Furthermore, it has also been shown that, in the presence of thin film of fluid between contacting surfaces, the force of adhesion is comprised of meniscal and viscous components (figure 7-3). The viscous component is time-dependent and so sensitive to varying sliding velocities. Either one of these suggestions, or possibly a combination of both, may explain this apparent increase in the static friction.

The dynamic coefficient of friction appeared to be unaffected by sliding velocity. This agrees with Coulomb's law of kinetic (dynamic) friction which states that the dynamic friction is independent of the sliding velocity. However, this is in contrast to the work of other authors (Gleghorn and Bonassar, 2008, Shi et al., 2011). Shi et al. demonstrated a decreasing coefficient of friction as sliding velocity increased from 0.2 to 0.5, 1 & 5mm/s for alumina pins on cartilage (Shi et al., 2011). The coefficient of friction decreased from 0.095 at the 0.2mm/s to 0.044 at 5mm/s, although the decrease was more dramatic at lower rather than higher changes in velocities. A similar observation was made by Gleghorn and Bonassar (Gleghorn and Bonassar, 2008). For cartilage on glass

interfaces, an increase in sliding velocity was found to reduce the coefficient of friction. Furthermore, using Stribeck curves (used determine lubrication regimes) it was found that increasing the sliding velocity was found to cause a transition from boundary lubrication to mixed lubrication even under applied strains as large as 40%.

However, the differences between the influence of sliding velocity in this study and that observed by others can be explained by the experimental set-up and methodology. The method employed in this study had cartilage pins under constant loading periods but not subject to constant translation of the glass plate. Translation was initiated only after the specifically allocated loading periods (i.e. 5, 10, 15 & 20mins). Previous experimental studies maintained constant reciprocating translation in their studies (Gleghorn and Bonassar, 2008, Krishnan et al., 2004, Shi et al., 2011). Thus, the length of time the pin is loaded in combination with continuous translation is a key factor.

There may also be another factor that is contributing to increased resistance at start-up to explain the differences between the static and dynamic frictional values. It is likely that the test rig itself, more specifically the carriage and rail system upon which the glass rests could have introduced a degree of resistance. The carriage possesses a series of polymer bearings to provide smooth transition along the rail. However, there will always be some degree of friction in these bearings. Although the frictional resistance of this system was measured so as to be deducted when cartilage pins were introduced, it was done without including the effects of the normally applied loads on the bearing friction. The result of this would have a much greater impact on the static friction rather than the dynamic friction, although both would no doubt be affected. For each successive weight that was applied it is likely that resistance of the sliding system grew greater and hence, a greater force was required to overcome it and cause motion. Once this resistance was overcome, it is unlikely that such small loads had any effect on the dynamic friction. To eliminate this adverse static affect, it is recommended that any future pin-on-plate work employ a calibrated actuator with embedded force sensor to measure frictional force.

The differences found between the static and dynamic values of friction are not evidence that elastohydrodynamics are taking place. This is very unlikely to occur at the very low velocities detailed here (1-3mm/s), as sufficiently thick fluid films cannot be generated. In contrast, Forster and Fisher determined the "stationary" coefficient of friction of 3 and 9mm diameter cartilage pins on metal plates and found that these were similar to the steady state friction values (Forster and Fisher, 1996). It was deduced that the low-velocity sliding was not sufficient enough to generate fluid film lubrication and that boundary lubrication was maintained. Similarly, in this study, the theoretical static and dynamic film thickness values are much lower than the surface roughness of cartilage (approximately 1μm). Hence, boundary lubrication conditions occur at both start-up and running conditions. These calculations are shown in Appendix C.

Interestingly, the harvest locations of the osteochondral plugs were found to cause no significant difference in the coefficient of friction for ant given sliding velocity or loading time. Given that the PFG cartilage has already proved to possess significantly a significantly higher aggregate modulus, one would expect these sites to lose interstitial load support at a slower rate than the condyles and so exhibit superior time-dependent frictional properties. The results are also contrary to the work of Chan et al. who discovered differences in the 'true' frictional coefficient of bovine femoral cartilage from load bearing and non-load bearing locations (0.13 & 0.2 respectively) (Chan et al., 2011). However, although no analyses of mechanical properties were performed, a greater expression of superficial zone protein was expressed in the load bearing sites, which is known to be an important boundary lubricant in cartilage (Neu et al., 2008). It may be possible that this protein is not as of yet present in significant amounts at the load bearing sites in immature animals, or indeed that this may reduce at non-load bearing sites as maturity progresses. However, it is most likely due care was not given to preserving this protein and it may have been washed away.

It is unclear what effects osteochondral transplantation would have on the frictional properties of the altered composite articular surface. Although the coefficients of friction

were found to be similar in all harvest locations, there are nevertheless a number of issues to be considered. The PFG cartilage has been shown to be stiffer than the condyles in chapter 4. Stiffer cartilage has been reported to have a slower recovery rate, presumably due to its lower permeability (Barker and Seedhom, 2001). Thus, the coefficient of friction after prolonged loading periods may remain at a high level, running the risk of subsequent damage. Furthermore, all the plugs employed from all the locations were of all the same size, but the contact areas of the cartilage in the condyles and the PFG is undoubtedly different and alter throughout the gait cycle. The temporal response of the frictional coefficient has been found to depend on the contact area, with larger areas maintaining interstitial fluid load support for longer (Carter et al., 2007). Hence, given that the surface area of the transferred osteochondral plug is smaller than that of the surrounding native tissue, the surface of the plug may lose fluid load support and have a frictional rise at a much faster rate than its surroundings due to fluid loss at the perimeter of the implant cartilage. This may be significant not only tribologically, but also a factor in the time taken for full integration of both cartilage surfaces to occur.

8 Development of an *in-vitro* Hydrodynamic Environment for Osteochondral Tissue Constructs

8.1 Introduction

The growing incidence of younger patients contracting bone and joint disease presents a considerable challenge to the bioengineer. There is a limited amount of donor material, the possibility of donor site morbidity and difficulty in matching the surface topology (Wendt et al., 2005). Allografts are also associated with some major disadvantages such as limited availability, immunological rejection and pathogen transmission (Mahmoudifar and Doran, 2005). One alternative avenue of approach is that of tissue engineering, and in particular a procedure known as Autologous Cell Implantation (ACI). In this practice, a patient's own cells are harvested in a minimally invasive manner and processed in culture *in vitro* using degradable polymeric scaffold structures and specialised analytical equipment. This is not a new concept, and as such subsequent technology is currently available in the form of devices such as Carticel®, yielding implantable cartilage repair products or plugs to replace the affected area. However, any tissue engineered cartilage constructs are highly dependent on the environment in which they are developed as poor matrix production is a consequence of inadequate mechanical stimuli and poor transport of nutrients and oxygen. Therefore, the greatest challenge lies in the optimisation of the *in vitro* environments in which these constructs are grown (bioreactors), in order to promote successful cartilage integration and repair *in vivo*.

It has previously been demonstrated that osteochondral extracellular matrix can be promoted by applying mechanical stimuli within physiological ranges, leading to enhanced mechanical properties (Angele et al., 2003, Shieh and Athanasiou, 2003). However, the mode by which mechanical stimulus is applied is by no means standardised, with many differing methodologies still being employed, including static and dynamic compression, hydrostatic pressure, strain induced shear and flow induced shear. Ideally, any bioreactor system should attempt to mimic the natural environment of

the tissue in question. Hence, for osteochondral tissue, none of the previously mentioned methodologies alone is truly representative, but rather a combination of them. With this in mind, it is postulated that the predominant mechanical factors are the applied pressure in combination with shear.

There have to date been many varied intermittent and cyclic applications of hydrostatic pressure and shear to culture systems (Angele et al., 2003, Carver and Heath, 1999, Frank et al., 2000, Jin et al., 2001, Parkkinen et al., 1993). Many of these technologies have been found to produce beneficial outcomes. For example, Parkkinen et al discovered that proteoglycan (PG) synthesis can be enhanced in both chondrocyte cultures and bovine cartilage tissue using hydrostatic pressure but that this was highly dependent on load duration and magnitude (Parkkinen et al., 1993). Furthermore, the relative effects of duration and magnitude were found to vary between culture systems. Carver and Heath applied intermittent pressurisation to scaffolds seeded with juvenile and adult horse chondrocytes (Carver and Heath, 1999). GAG concentrations were found to resemble those of native cartilage in the juvenile seeded scaffolds but not the adult. However, disappointingly collagen levels never even reached 10% of native cartilage concentrations in either case. Angele et al. examined the effects of cyclic hydrostatic pressure on aggregates of bone marrow derived mesenchymal progenitor cells (Angele et al., 2003). It was found that loading for multiple days rather than single days statistically increased collagen and PG concentrations and the overall cell/matrix ratio. As for the application of strain-induced shear, Frank et al. compressed 1.1mm thick bovine cartilage explants to 1mm whilst they were subjected to 1% cyclic shear deformation yielding 25 and 41% increases in PG and protein content (Frank et al., 2000). This work was followed up by Jin et al. by subjecting explants to shear loading of 1-3% producing an increase of approximately 25 and 50% in PG and protein synthesis (Jin et al., 2001).

From such studies it is apparent that the application of cyclic hydrostatic pressure is principally successful in synthesising PG, whereas the direct application of shear is more

successful in producing collagen matrix. This thesis will discuss the design and construction of a novel test apparatus capable of combining these mechanical stimulus methodologies. The design utilises hydrodynamic lubrication theory, creating fluid flow through a reducing annular space to induce fluid pressure and shear effects. This is achieved by attempting to mimic the components of load and rotation experienced by the femoral condyles *in vivo*. The test apparatus does not include control systems for pH, temperature, gas exchange, humidity etc., but merely aims to reproduce the mechanical environment experienced by osteochondral tissue in the knee, and in doing so is hoped will be the first step in the design of a complete bioreactor system. Additionally, it is hoped that this device could double as a joint simulator for the storage of osetochondral allografts over prolonged periods of time. The same mechanical cues employed to grow tissue engineered constructs are also likely to maintain the health of osteochondral tissue prior to implantation.

The design of the apparatus revolves around an eccentric cylinder concept subject to a recent patent publication (Black et al., 2007, Black et al., 2013). As such, the feasibility of this concept in being able to provide the correct mechanical cues is vital. The following shall be performed in this section to address this matter:

- A description and experimental evaluation of a pre-existing device known as version 1, highlighting the apparent shortcomings and suggesting potential solutions to overcome them.
- The proposal of a new bioreactor/joint simulator incorporating these solutions (version 2), including finite element analysis of the design.
- The construction and experimental evaluation of the test apparatus, experimentally recording the hydrodynamic pressures it can generate.
- Comparison of the recorded experimental data to a mathematical model governed by lubrication theory.

8.2 Methods

8.2.1 Experimental Apparatus

A pre-existing rig had been constructed before the author's involvement in this study, but a subsequent evaluation found the device to be inadequate. Please refer to Appendix D for a full description of this assessment. Based on these shortcomings, a second custom experimental test rig (version 2) was designed and built for the purposes of generating and measuring hydrodynamic pressures. This particular rig was designed to resemble that of a journal bearing, consisting of a solid S.S. journal supported and sealed at either end with bearings and rotary seals housed within an A-frame and a S.S. bearing surface (or bushing) of larger diameter which encompassed the shaft. This bushing was housed in a subassembly which was constrained to move vertically up and down (z-axis) via four alignment pins anchored in the carriage base plate. This base plate was in turned attached to a carriage on a guide rail which allows freedom of the journal housing to translate in the x-axis via a guide rail and carriage assembly (igus® UK Ltd, Brackmills, Northampton). A CAD model of the newly designed system is presented in figure 8-1.

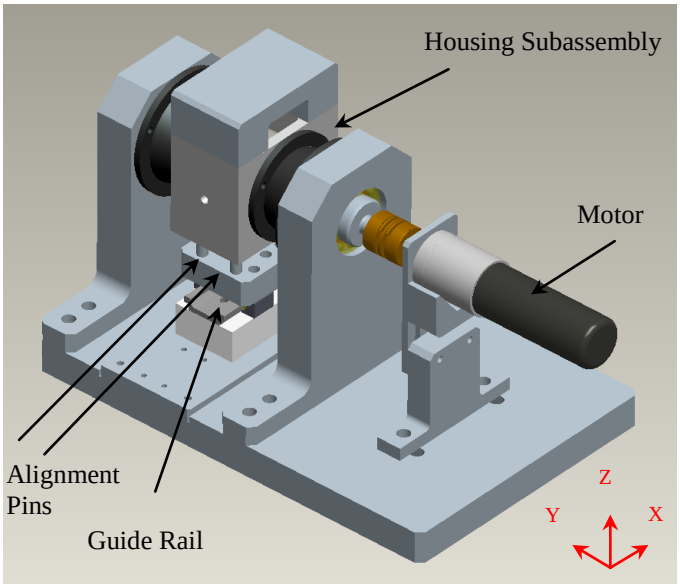

Figure 8-1. A CAD model of hydrodynamic test rig: version 2 using Pro-Engineer Wildfire 4.0.

Two specially moulded silicone rubber bellows (Rhodorsil RTV 3428, Bentley Creative Chemicals, Kidderminster, UK) linked the two A-frames to the journal housing, encasing any remaining rotating elements that may be exposed, sealing in the lubrication fluid and maintaining a fluid filled environment for the journal. Load was applied to the top of the journal housing via a housing cap, reducing the fluid gap between the bushing and rotating journal, causing hydrodynamic lubrication to occur.

The journal was coupled to a servomotor with encoder feedback that maintained the prescribed speed of rotation at all loading conditions (Maxon Motor & Motor Control, Switzerland). Load is applied to the housing cap via a Zwick-Roell materials testing system (MTS). The magnitude of the load is controlled by the user via a software interface on a desktop computer assigned to the MTS.

The housing subassembly itself consists of a number of components. Figure 8-2a presents a section of the subassembly, highlighting each individual component. Two concentric cylinders pass through the core of the journal housing, the housing insert and the shell liner. The shell liner is initially composed of stainless steel, and acts as the bushing to the shaft ensuring a metal-on-metal interface. A 1.5mm port was drilled as shown in order to allow access for measurement of the hydrodynamic pressure within. Connection products for chromatography and fluidic applications (IDEX® Health & Science 2009/2010 Catalogue) are used to connect the 1.5mm diameter port in the bearing surface to a 2.5MPa capacity gauge pressure transducer (Keller Piezoresistive Transmitters, Switzerland). By correctly aligning the port in the shell liner with a drilled and tapped hole in the housing insert, a PEEK M6 bolt can then be used to secure the shell liner, housing insert, ferrule and tubing all together and create a hydraulic seal. This is shown in the highlighted area named detail ‘A’ (figures 8-2a & b).

One further feature is a keyway on the surface of the housing insert. This interacts with two M3 bolts in the journal housing so the housing insert can be rotated radially by a set number of degrees and then fixed in place. This allows for positioning of the port in the

shell liner at any radial position for the measurement of the local hydrodynamic pressure.

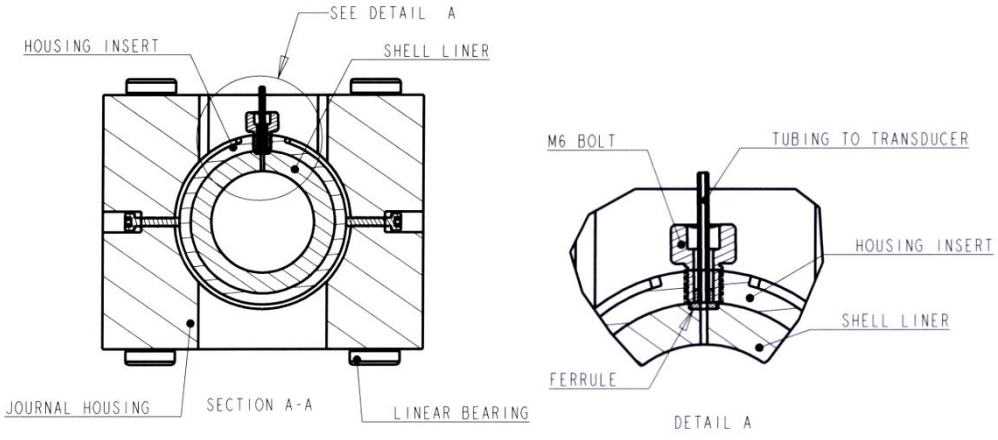

(a) **(b)**

Figure 8-2. (a) Section of journal housing subassembly, (b) closer look at detail 'A'.

Voltage signals from the pressure transducer are captured via a data acquisition system (National Instruments, US), then converted and recorded as pressure readings by purpose/user written software program on a laptop computer (NI LabView, U.S.A.). Figure 8-3 displays a schematic of the overall experimental set-up and a picture of the hydrodynamic rig during testing.

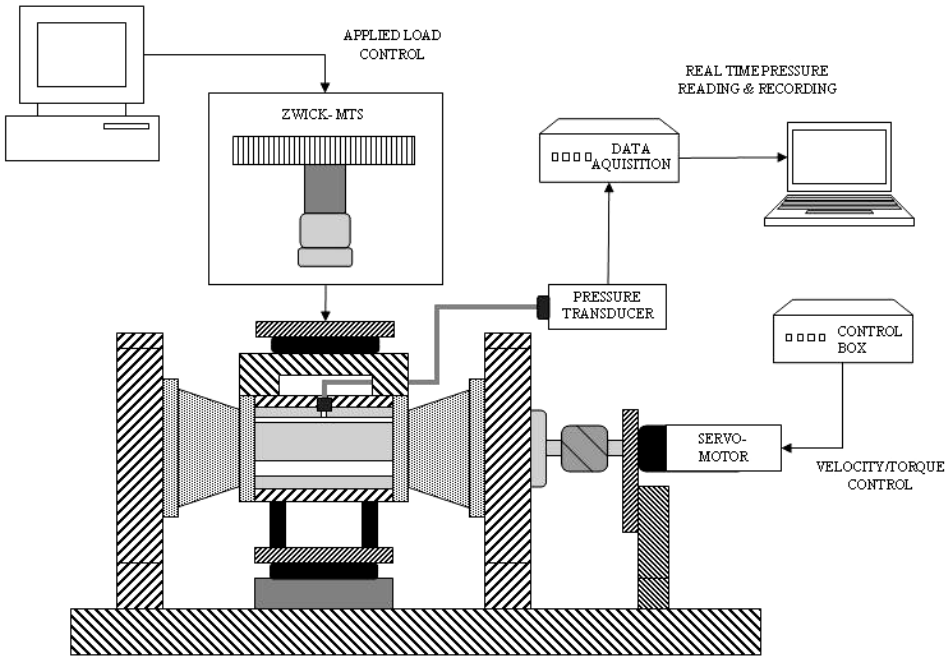

(a)

(b)

Figure 8-3. Hydrodynamic test rig, (a) schematic of test set-up, (b) during testing.

8.2.2 Finite Element Validation of Apparatus Design

Having designed all of the components of the hydrodynamic test rig and suitably assembling them, a three dimensional finite element analysis of the structure was performed to validate the design. This was achieved using ANSYS© Workbench version 11.0. The model of the structure was generated by simply saving the assembly as a SAT file in Pro Engineer Wildfire 4.0. Subsequently, this SAT file was uploaded into ANSYS Workbench and geometry defined.

However, one of the limitations of the software is the finite number of nodes available to the user. In this case, 32,000 nodes were available to mesh a large assembly of components. Hence, a decision had to be made either to mesh all of the components with a very low density and corresponding loss of resolution, or mesh the more critical components with a finer density and yielding more genuine results. Intuitively, the latter presented the better option and so the directly loaded components of the housing subassembly and the journal shaft itself were selected for analysis.

A worst case scenario of hydrodynamic pressure breakdown and contact occurring between the shaft and journal housing was postulated as a good indicator of the rig's structural strength. Hence, an initial line contact was created between the journal housing and the shaft. Material properties were assigned to all of the components; aluminium for the housing cap, journal housing, and housing insert, whereas stainless steel was chosen for the journal shaft and the shell liner. Non-essential components such as the bolts were excluded for simplicity.

The ends of the shaft were constrained radially, while the all the components of the journal housing subassembly were restricted in all degrees of freedom except the z-axis to mimic the action of the alignment pins. A ramped load of 750N was applied to the housing cap over a period of 0.25s, simulating twice the eventual load that will be

applied. Finally, a mesh was generated with a density as fine as was allowable, and the von-Mises stresses, displacements and factors of safety calculated.

8.2.3 Contact Mechanics

8.2.3.1 Hertzian Contact Theory

The contact mechanics theory originally developed by Hertz allows for simple calculation of the stresses generated between a contacting journal shaft and shell liner. When contact occurs between a solid cylinder (radius R_1) and the internal surface of another cylinder (radius R_2) of equal length (l) due to an external load (W), a narrow rectangular area of contact is formed with width $2b$ and length l. The half width b is given by the following equation;

$$b = \left(\frac{4WR'}{\pi l E'}\right)^{0.5} \qquad \textbf{Equation 8-1}$$

Where;

R' = Effective radius, given by $R' = \left(\frac{1}{R_2} - \frac{1}{R_1}\right)^{-1}$

E' = Effective elastic modulus, given by $E' = \left(\frac{1-\nu_1^2}{E_1} + \frac{1-\nu_2^2}{E_2}\right)^{-1}$

E_1, υ_1, E_2, υ_2 are the elastic constants of each respective cylinder.

The maximum contact stress can then be found using;

$$\sigma_{MAX} = \frac{2W}{\pi b l} \qquad \textbf{Equation 8-2}$$

and the maximum deflection is determined by;

$$\delta = 0.319(\frac{W}{E'l})[\frac{2}{3} + \ln(\frac{4R_1R_2}{b^2})] \qquad \textbf{Equation 8-3}$$

8.2.3.2 2D Finite Element Analysis

A 2 dimensional finite element analysis was performed to validate the Hertzian contact theory using ANSYS© version 11. An axisymmetric plane stress model was created using line and curve commands in the model space and two different areas created within them representing the journal shaft and the shell liner. The lines and curves were divided using the NDIV and aspect ratio commands to ensure an ever increasing availability of nodes towards the region of contact. The number of divisions was increased x2, x6, and x8 for each simulation to generate finer mesh densities and achieve solution convergence. The elements chosen were solid 4-node quadrilaterals, the appropriate material properties were entered and the mesh created. Appropriate axisymmetric boundary conditions and loads were then applied. The nodes at the contact interface were then coupled and all their degrees of freedom limited but that of the line of action of the applied force. The simulation was run for each mesh density case and the von-Mises stress results and displacements incurred analysed in the post processor.

8.2.4 Calibration of Pressure Transducer

Calibration of the pressure transducer was achieved by connecting the pressure transducer, via the same fluidic application products mentioned earlier, to a bespoke test rig comprising of a piston and cylinder arrangement. Fluid within the cylinder was pressurised by applying load to the piston and this pressure was in turn recorded by the transducer in terms of a voltage value. If the applied load was known, then the pressure within the cylinder could be determined, and related to the recorded voltage. Thus, various increments of load and pressure could be plotted against their corresponding recorded voltages and a calibration curve generated.

Load was transmitted by connecting the piston to an Instron 5800. A preload of 5N was initially applied for 20 seconds to steady the system, before a sequence of ramp-and-hold cycles were performed. This consisted of 7 consecutive ramps of 50N at a rate of 12.5N/s and dwell periods of 60 seconds. Thus, the load was ramped from 5 to 355N in 50N increments.

The pressure in the cylinder for each dwell period was determined by dividing the load by the cross-sectional area, which was then plotted against the corresponding average voltage. A line of best fit was then applied to each of the 7 dwell data points and an equation relating voltage to pressure derived. Thereafter all acquired voltage signals were converted within LabView software to units of to pressure in MPa.

8.2.5 Determining the Absolute Viscosity of Glycerol

Prior to any experimentation being performed, it was essential to know the viscosity of the lubricant used in the test rig. The viscosity of glycerol was determined by employing the well-established Stokes falling sphere method, which was in turn then verified by means of cone and plate viscometry of various glycerol/water blends.

8.2.5.1 Falling Sphere Method

A 250ml measuring cylinder (diameter 37.35mm) was filled with glycerol to approximately 60mm above the upper 250ml marking. A steel ball bearing (diameter 4.75mm, mass 0.441g) was carefully lowered into contact with the glycerol surface centrally within the cylinder using wide-gripped plastic tweezers and then released. After passing through the first 60mm in height of glycerol, the ball bearing reached the 250ml marking on the cylinder, upon which a stopwatch was activated. This was allowed to continue until the bearing had reached the 30ml marking, upon which the stopwatch was stopped. Each 10ml marking on the cylinder was found to be 9mm apart,

so the distance travelled during this period of time was calculated to be 198mm. In all, the time for the ball bearing to complete this distance was measured 20 times.

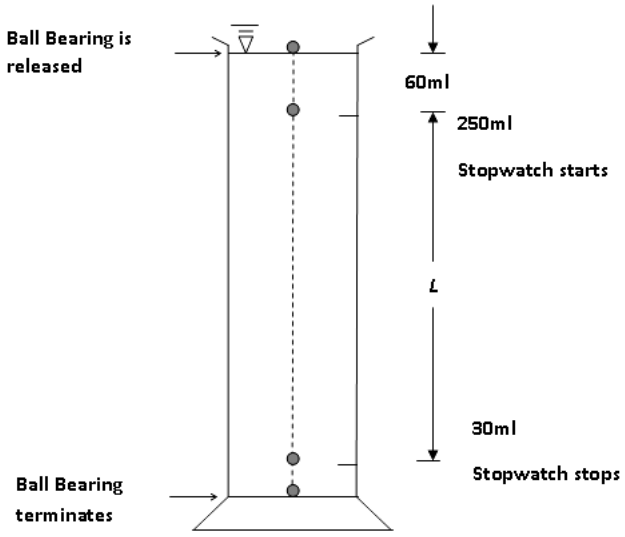

Figure 8-4. Schematic of falling sphere method set-up.

Using the times measured, in addition to knowledge of some physical characteristics of the set-up, the viscosity of the glycerol can be calculated using the following method:

According to Stokes, the force required for a sphere to separate the molecules of any fluid is;

$$F = 6\pi R_S \mu v_S \qquad \textbf{Equation 8-4}$$

where,

R = Radius of the sphere,

μ = Absolute viscosity of the fluid,

v_S= Velocity of the sphere.

This force can be equated with the gravitational force, modified to include buoyancy effects,

$$6\pi R_S \mu v_S = \frac{4}{3}\pi R_S^3(\rho_S - \rho_L)g \qquad \textbf{Equation 8-5}$$

where,

ρ_S = Density of the sphere,

ρ_L = Density of the liquid,

g = Acceleration due to gravity (9.81m/s^2).

The velocity term can be replaced by L/t (distance travelled/time taken) and the equation solved for μ yielding;

$$\mu = \frac{2gR_S^2(\rho_S - \rho_L)t}{9L} \qquad \textbf{Equation 8-6}$$

However, this equation calculates μ based on a falling sphere in an infinite fluid. For this particular experimental set-up, edge and end effects will play a role and should be accommodated for. The velocity term can be modified be modified to include edge effects and the finite falling distance using the following;

$$v_S = v_S(1+2.4x)(1+1.65y) \qquad \textbf{Equation 8-7}$$

Where,

x = Ratio of the sphere diameter to cylinder diameter,

y = Ratio of the sphere diameter to total liquid height.

Finally, incorporating the new continuous velocity term, the viscosity can be expressed as;

$$\mu = \frac{2gR_S^2(\rho_S - \rho_L)t}{9L(1+2.4x)(1+1.65y)}$$ **Equation 8-8**

The density of the sphere was found by simply calculating its mass/volume. The density of glycerol was found by determining the mass of 5, 10, 15 20 & 25 ml volumes of solution and after applying the mass/volume relationship to each of them, then calculating the average (1230.11kg/m^3).

Of course the viscosity and density of glycerol is temperature dependent, so all measurements described were performed in the same operating environment as the hydrodynamic test rig in which it will be used. This was an enclosed materials testing laboratory maintained at 22°C via air conditioning.

8.2.5.2 Cone & Plate Viscometry

A Well-Brookfield cone and plate viscometer was employed which consists of a cone element rotating at a constant angular velocity relative to a fixed plate. The conical spindle rotates at a precise speed and measures the torque necessary to overcome the viscous resistance to the induced movement caused by the fluid sample situated between the cone and the plate. This is achieved by driving the spindle through a calibrated beryllium copper spring. The degree at which the spring is wound is proportional to the viscosity of the fluid and is indicated by a dial and pointer as a per cent of the full scale torque reading.

However, in this instance, the spring available was found to be not stiff enough for full concentrations of glycerol. Hence, the viscosity of glycerol and deionised water blends were determined. Three concentrations of glycerol were measured, 25%, 50% and 75%

glycerol by volume. The experimental viscosity results of these blends can then be reproduced using a theoretical method described by Cheng (Cheng, 2008) using data from the falling sphere results. Hence, it is hoped one each method will validate the other.

The equation described by Cheng (Cheng, 2008) for calculating glycerol/water blends is as follows;

$$\mu_b = \mu_w^{\alpha} \mu_g^{1-\alpha}$$ **Equation 8-9**

Where,

μ_b = Viscosity of the blend,

μ_w = Viscosity of water (taken to be 0.001Pa.s),

μ_g = Viscosity of glycerol (calculated from falling sphere test),

α = Weighting factor, varying from 0 to 1 depending on glycerol/water concentration.

The α term must be solved independently using the following equation;

$$\alpha = 1 - C_m + \frac{abC_m(1-C_m)}{aC_m + b(1-C_{m)}}$$ **Equation 8-10**

Where;

C_m = Mass concentration of glycerol against water,

a & b = Temperature sensitive coefficients given by

$a = 0.705 - 0.0017T$ & $b = (4.9 + 0.036T)a^{2.5}$

Where;

T = Temperature of the glycerol/water blend.

8.2.6 *Hydrodynamic Lubrication Theory*

In order to mathematically model the pressures occurring within the system hydrodynamic lubrication theory was employed. Consider a section of the two articulating bodies within the hydrodynamic test rig (figure 8-5).

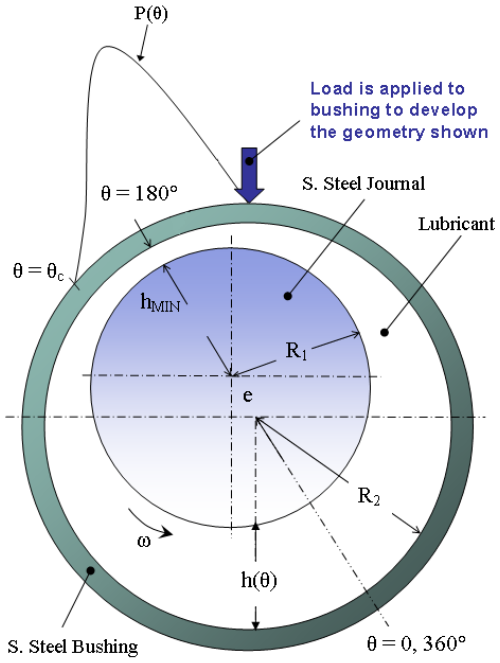

Figure 8-5. Section of the articulating bodies within the hydrodynamic rig.

A solid shaft of radius R_1, surrounded by a cylindrical bushing of inner radius R_2, with their centres offset by a distance e. A fluid lubricant separates the two bodies. The theory defines the maximum fluid film thickness as h_{max} at $\theta = 0$ and the minimum film thickness as h_{min} at $\theta = 180°$, yielding an expression for the film thickness;

$$h = c(1 + \varepsilon Cos\theta) \qquad \textbf{Equation 8-11}$$

Where;

c is the radial clearance, given by $R_2 - R_1$,

ε is the eccentricity ratio, given by e/c.

For a journal of infinite length $4R_1/l \leq 1$) and lubrication fluid of constant viscosity, the Reynolds equation may be reduced to the following polar coordinate expression;

$$\frac{\partial}{\partial\theta}(h^3.\frac{\partial P}{\partial\theta}) = 6\mu\omega R_1^2 \frac{\partial h}{\partial\theta} \qquad \textbf{Equation 8-12}$$

where;

P is the fluid pressure,

μ is the kinematic viscosity of the fluid,

ω is the angular velocity of the shaft.

The fluid pressure can be determined by solving the Reynolds equation for P and implementing the following Swift-Stieber (Reynolds) boundary conditions;

(i) $P = 0$ at $\theta = 0$,

(ii) $P = 0$ at $\theta c \leq \theta \leq 360°$,

(iii) $dP/d\theta = 0$ at $\theta = \theta c$ (θc is known as the cavitation angle).

Solving requires a complicated back-substitution procedure known as the Sommerfeld method and determining the cavitation angle requires iterative techniques. These actions were solved numerically using Maple 13, a mathematical analysis software package. A more detailed description of the derivation involved and the script for the software programs can be found in the appendices.

8.2.7 Operating Conditions

The input values to the theoretical model were based on the conditions at which the hydrodynamic test rig was operated, namely the geometry of the articulating bodies, the viscosity of the lubricant (in this case glycerol), the rotation velocities applied by the motor and the load applied by the Zwick MTS. These are listed as follows:

- R_1 = 0.015m, R_2 = 0.016m, meaning c = 0.001m.
- The viscosity (μ) of glycerol is approximately 0.715Pa.s.
- The angular velocity (ω) was taken as 1 & 2rev/s.
- The applied load (W) was 375N (Half body weight).

The value of ε was determined by Raimondi-Boyd charts (based on empirical data) graphing ε against the bearing characteristic number (Sommerfeld number);

$$S = (\frac{R_1}{c})^2 (\frac{\mu\omega}{P_b})$$ **Equation 8-13**

Where P_b is the nominal bearing pressure, $P_b = \frac{W}{2R_1 l}$ (l = bushing length = 0.06m).

The charts described were digitised and a 5th order polynomial used to describe the chart and calculate ε for a given S.

8.3 Results

8.3.1 Finite Element Validation of Apparatus Design

Figures 8-6a, b & c present the 3 dimensional finite element analyses to validate the design of the hydrodynamic test rig v2. Figure 8-6a demonstrates the von-Mises stresses present under load. It is evident that the highest stresses occur at the shaft ends where they are fixed in position by the bearings. A maximum value of 7.76MPa is recorded here. Other areas of stress accumulation occur at the interface of the journal shaft and shell liner as would be expected. Average values at this interface range from 1.72-3.45MPa, however precise peak contact values cannot be determined from this model, due to the highly localised nature of this contact area involved and the relatively coarse mesh employed. However, the Hertzian contact analysis will achieve this goal and these results are presented at a later stage.

Figure 8-6b presents the deformation that occurs to the journal housing subassembly under load. Results again are not surprising with now deformation occurring at the fixed ends of the journal shaft, and maximum deformation occurring at the site of load application. A deformation value of 1.1958×10^{-6}m is recorded here. This is partially due to the lower elasticity value of the aluminium of the loading area to the steel of the journal shaft, but also due to the vent incorporated directly before the load area which allows for exit of the PEEK tubing to the pressure transducer. Although this vent allows for minor three-point bending to occur, they are minor and not significant to the workings of the overall apparatus.

Finally, figure 8-6c displays the factor of safety of the model. It is apparent that the minimum factor exceeds a value of 15 which is considered more than an adequate level for such an apparatus.

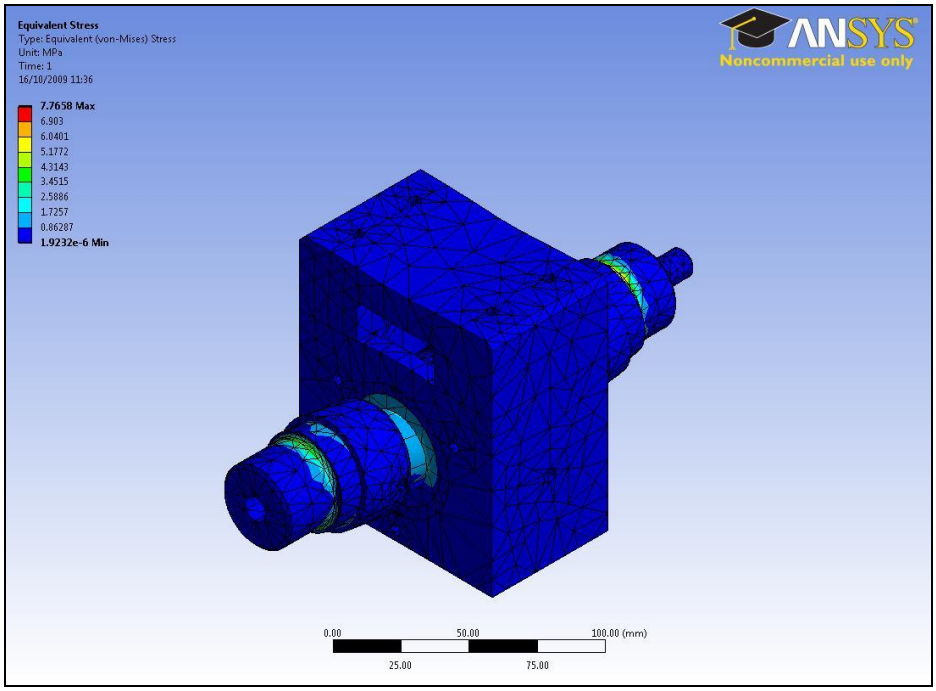
Equivalent Stress
Type: Equivalent (von-Mises) Stress
Unit: MPa
Time: 1
16/10/2009 11:36
7.7658 Max
6.903
6.0401
5.1772
4.3143
3.4515
2.5886
1.7257
0.86287
1.9232e-6 Min
ANSYS
Noncommercial use only
0.00
50.00
100.00 (mm)
25.00
75.00

(a)

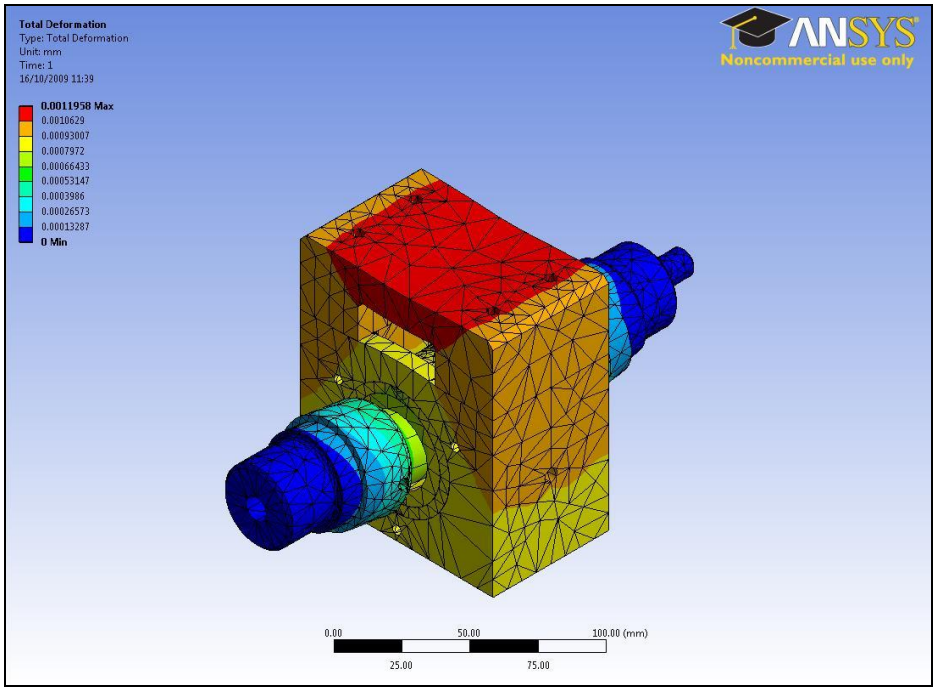
Total Deformation
Type: Total Deformation
Unit: mm
Time: 1
16/10/2009 11:39
0.0011958 Max
0.0010629
0.00093007
0.0007972
0.00066433
0.00053147
0.0003986
0.00026573
0.00013287
0 Min
ANSYS
Noncommercial use only
0.00
50.00
100.00 (mm)
25.00
75.00

(b)

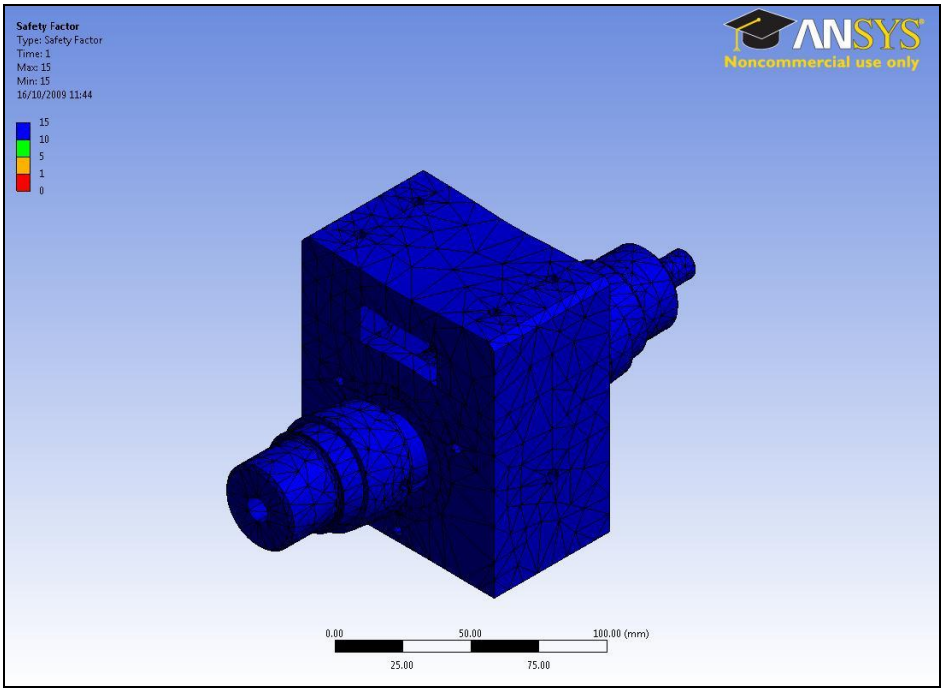

(c)

Figure 8-6. Finte element validation of test apparatus, (a) von Mises Stress distribution, (b) deformation & (c) safety factor.

8.3.2 Contact Mechanics

Hertzian contact theory calculates a maximum stress and a maximum deflection of 63.6MPa and 4.399 x 10^{-8}m respectively at the contact interface. Using the 2 dimension finite element model with the greatest mesh density (figure 8-7a), a maximum stress value of 60.46MPa and a maximum deflection value of 4.15 x 10^{-8}m is determined. These results are observed in figure 8-7b, where a closer look at the stress distribution at the interface is highlighted. Figure 8-8 presents a graph emphasising the convergence of the finite element solution to the Hertzian value using increasing mesh densities. This is a good indicator of the robustness of the simulation, it having been validated against established contact theory. Finally, table 8-1 presents a summary of the data collected from both methods and the percentage difference that exists between them.

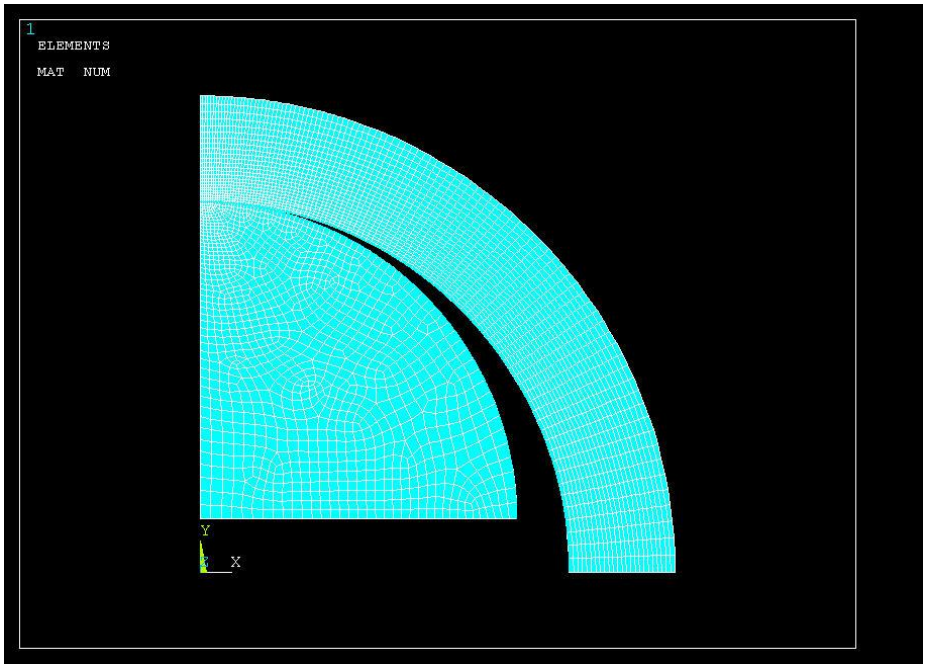

(a)

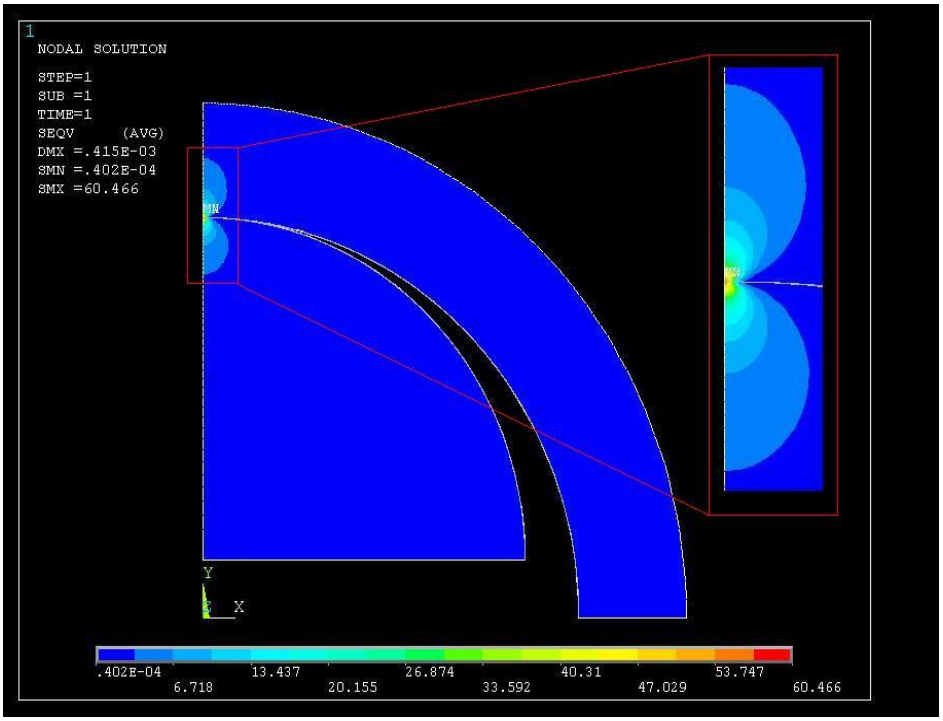

(b)

Figure 8-7. 2-D Analysis of Hertzian contact region, (a) highest and final mesh density used, (b) von-Mises stress distribution.

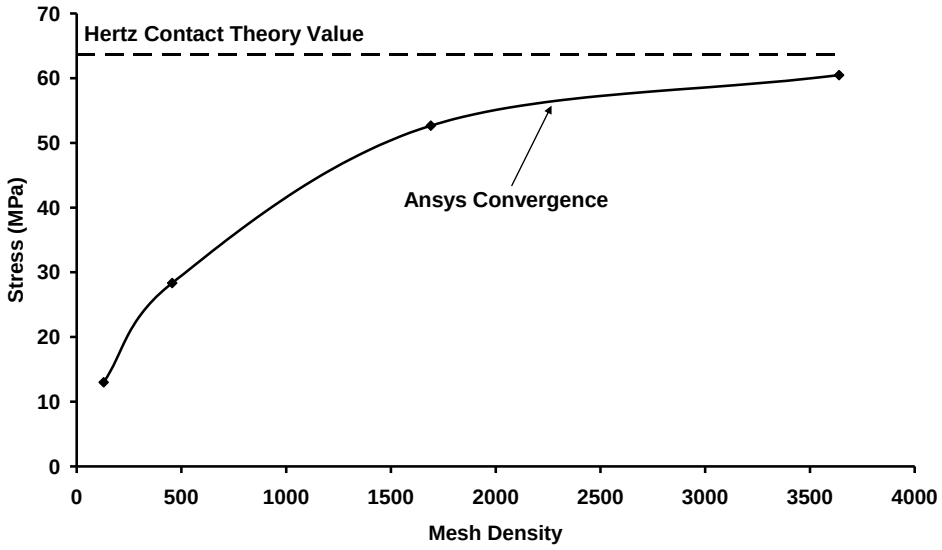

Figure 8-8. Convergence of Ansys solution to Hertzian contact value.

Table 8-1. Contact analysis results.

Hertz Contact Theory		**Finite Element Model**		**% Difference**	
Stress (MPa)	Deflection (m)	Stress (MPa)	Defection (m)	Stress	Deflection
63.6	4.399×10^{-8}	60.46	4.15×10^{-8}	2.17	5.68

8.3.3 Calibration of Pressure Transducer

The load applied by the Instron along with the voltage recorded by the pressure transducer is displayed in figure 8-9a. As one would expect, for each ramp and hold load cycle imparted by the Instron, a similar pattern is observed in the corresponding trace generated by the pressure transducer. The appearance of the two curves to converge on one another is explained simply by the fact that the scale of linearity to which transducer relates pressure to voltage (which we are trying to determine), is different to that at which the load was scaled when they were being recorded.

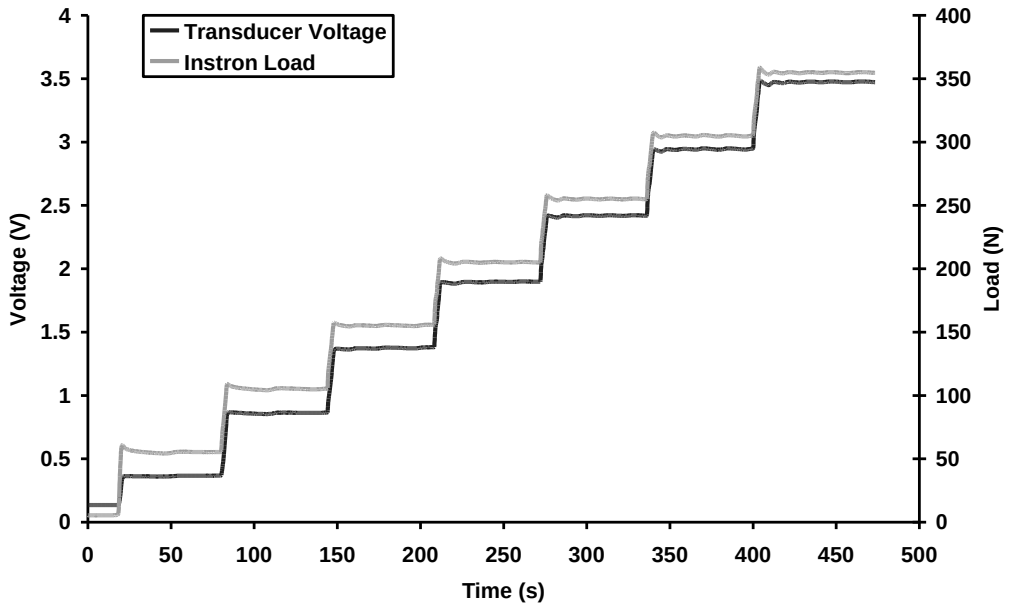

(a)

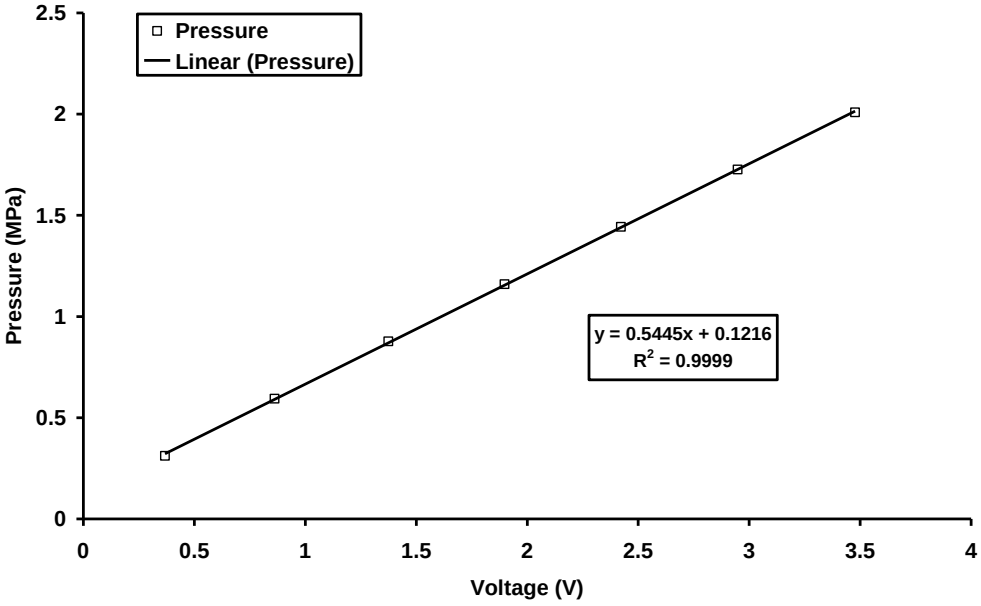

(b)

Figure 8-9. Calibration of 2.5MPa capacity pressure transducer, (a) voltage recordings as Instron imparts ramp and hold loads onto calibration rig, (b) transducer calibration curve.

Figure 8-9b presents a plot of Instron loads during the dwell periods against the average values of the corresponding voltages generated by the transducer. The line of best fit suggests a strong degree of linearity (R^2 = 0.9999), and so the equation used to describe this line was used hence forth to measure the pressure experienced by the transducer when incorporated into the hydrodynamic test rig.

8.3.4 Viscosity of Glycerol

For the falling sphere method, an average time of 2.33 (+/- 0.039 SD) seconds was taken for the sphere to descend through the glycerol between the two reference points. When this was used to determine the glycerol's viscosity using equation 6-7, it was found to be 0.715+/- 0.012Pa.s. When this value was used to determine the viscosity of 75, 50 & 25% glycerol/H_2O blends using the method described by Cheng (Cheng, 2008), these were calculated to be 0.03677, 0.00668 & 0.00220Pa.s respectively.

Figure 8-10 presents a graph of shear stress against shear rate for the three Glycerol / H_2O Blends. The Newtonian behaviour of the fluid mixtures is demonstrated by the strongly linear relationship. This is an indicator that the viscosity is not independent of shear rate and that the shear stress is directly proportional to the strain rate. The constant of proportionality in each case is of course the fixed absolute viscosity of the blend, specifically 0.03928, 0.00674 & 0.00253Pa.s for the 25, 50 & 75% volumetric concentrations respectively. These values compare quite favourably with those determined using theory and the falling sphere result, indicating that the 100% glycerol concentration viscosity value is indeed correct and can be used for any other calculations regarding its role in the hydrodynamic test rig. All the viscosity results are summarised in table 8-2.

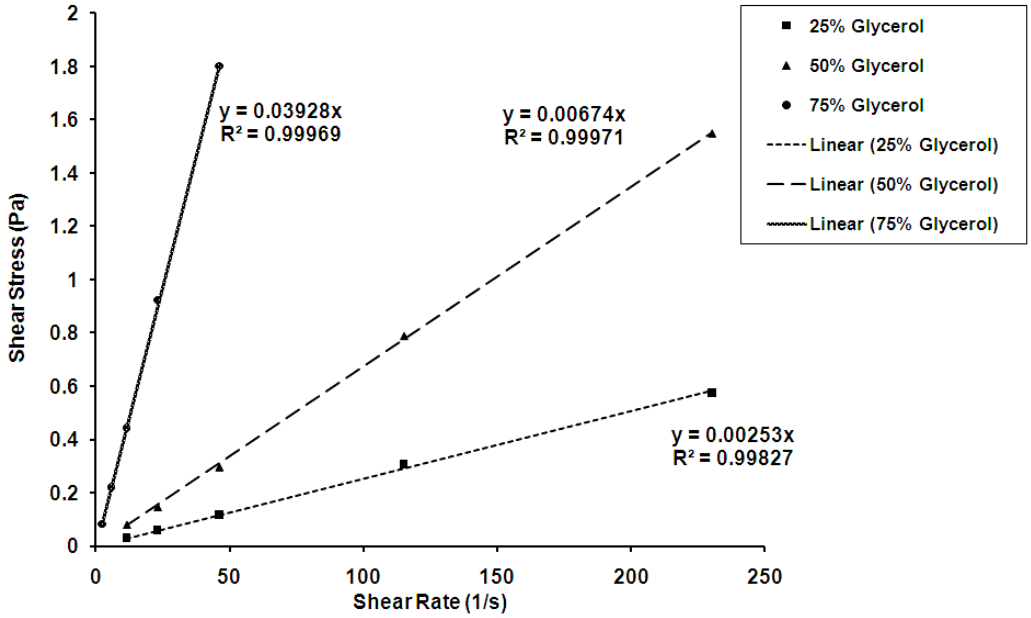

Figure 8-10. Flow curves for 25, 50 & 75% by volume glycerol/H_2O blends.

Table 8-2. Summary of viscosity results. The direct viscosity results were found to closely resemble those that were calculated by employing theory and the falling sphere result.

Method Used	**Viscosities of Glycerol/H_2O Blends (Pa.s)**			
	100%	**75%**	**50%**	**25%**
Falling Sphere	0.715 (0.012)			
Viscometer		0.03928	0.00674	0.00253
Theory using Falling Sphere Result		0.03677	0.00668	0.00220

8.3.5 Hydrodynamic Test Rig and Lubrication Theory

Figure 8-11 presents typical recording of pressure at one particular port location. For each port location, pressure was measured three times, halting the applied load and shaft rotation between attempts and allowing the system to come to rest. It is very apparent that the results generated by the test rig are very repeatable as in each instance the results vary very little. It is also evident that a period of time (in this case between $t \approx 50$ & 100s) is required for the pressure recordings to stabilise after load is applied. An average of the steady state values over the three attempts was taken as the pressure reading for each individual port location.

During the ramp phases shown in figure 8-9a it is clear that the transducer is quite responsive to the application of load. Hence, there must either be a delay in the test rig equilibrating under load, or something else is delaying the pressures encountered at the area of interest from reaching the transducer (such as shear forces in front of the recording port). Either of these explanations could well be true, however once the pressure recordings had stabilised the readings were highly reproducible.

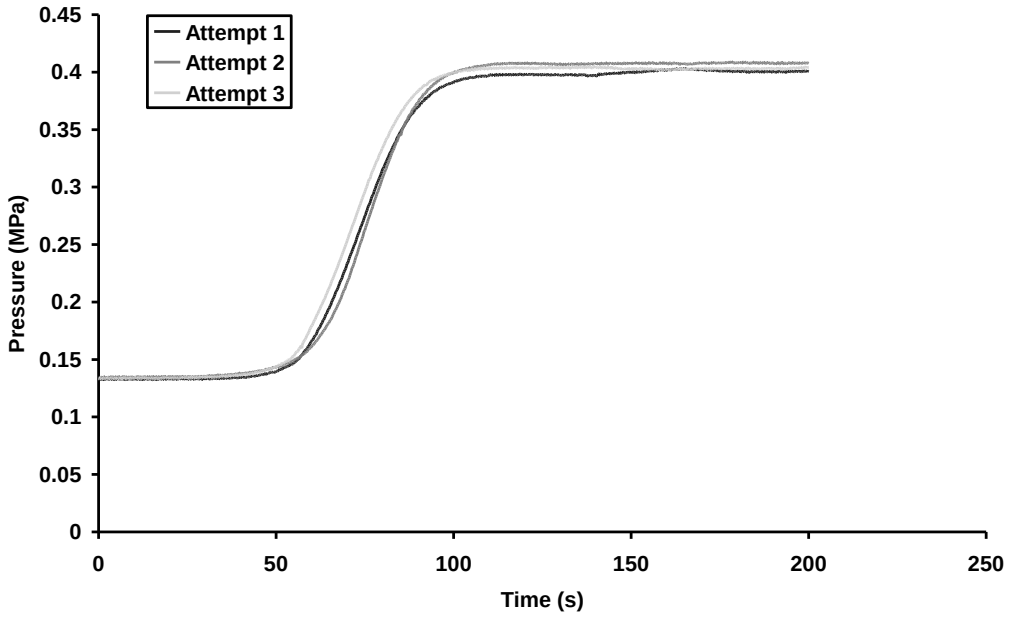

Figure 8-11. **Repeatability of pressure measurements in the test rig.**

Figure 8-12 displays the pressure distributions that would be expected to exist for two different scenarios according to the hydrodynamic lubrication theory described in the methods. However, also present is the experimental measurements made at various port locations for the same conditions applied to the model. Whether the shaft angular velocity is 1 or 2rev/s, it is clear that the experimental results tend to describe the magnitudes, as well as profiles of the pressures quite well. In the case of an angular velocity of 2rev/s, pressures rise steadily around the bushing to a maximum of approximately 0.9MPa, whereas, in the case of an angular velocity of 1rev/s, pressures rise on a much steeper gradient to approximately 1.5MPa. Furthermore, it is not just the magnitude of the maximum pressures that vary, but also the position at which they occur.

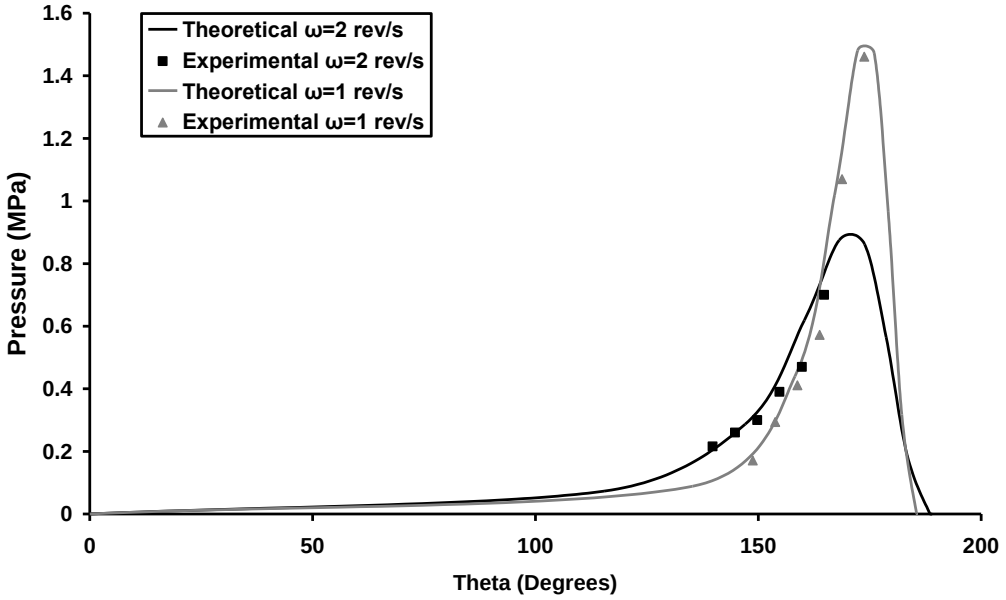

Figure 8-12. Experimental measurements from test rig compared to the theoretical model.

However, having now validated the model against experimental results, these can be predicted quite easily as seen in figure 8-13a. A decrease in viscosity results in a decrease in film thickness and corresponding increase pressure (figure 8-13b). In fact, for the kinematic conditions described, a viscosity of 0.1Pa.s will generate a peak pressure of approximately 5.5MPa which is in the *in-vivo* range of pressures found in the contact areas of the tibio-femoral joint.

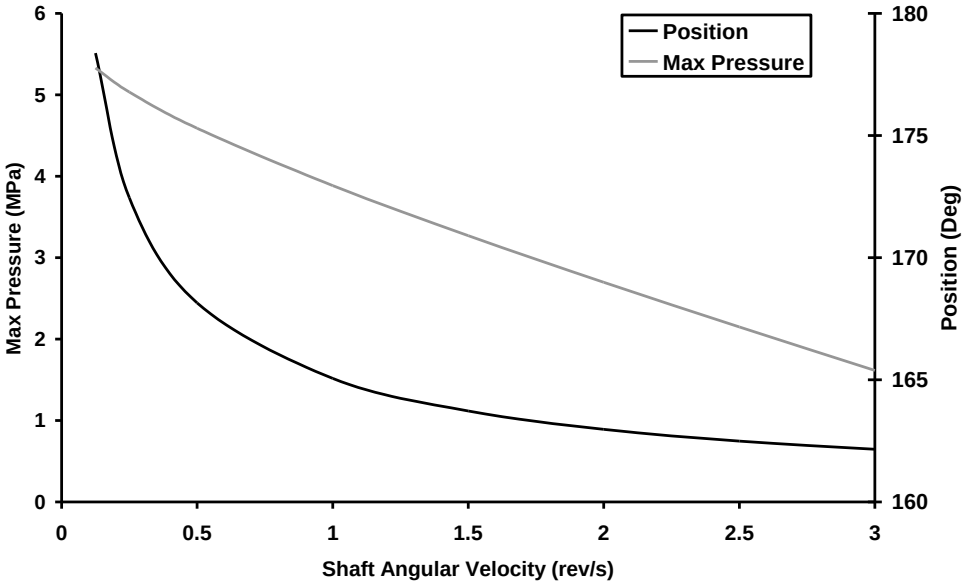

(a)

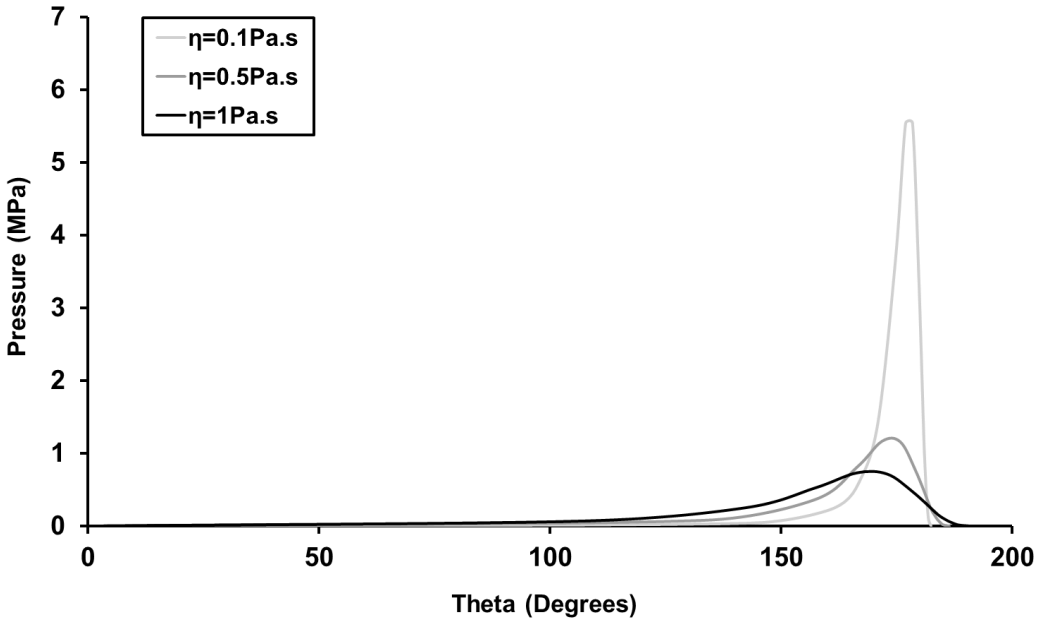

(b)

Figure 8-13. (a) Predictions of maximum pressures and their locations (b) pressure variations with viscosity.

8.4 Discussion

A hydrodynamic test rig has been designed and built for the purposes of generating fluid pressures similar to those experienced by cartilage *in vivo*. This rig was then subjected to controlled input performance parameters such as shaft angular velocity and the load applied to the bearing surfaces. Measurements of pressure were taken at various locations within this closed system using a calibrated pressure transducer and data acquisition system. It was discovered that a great degree of repeatability existed between measurement attempts at any particular location.

A generalised mathematical model was created in an attempt to predict these pressures based on the fundamental principles established by lubrication theory. Swift-Stieber (Reynolds) boundary conditions were employed over more simplistic Full-Sommerfeld or Half-Sommerfeld boundary conditions. Although their application may result in a reasonable depiction, the Full-Sommerfeld conditions gives rise to the presence of negative pressures and the Half-Sommerfeld conditions fail to satisfy the continuity of mass flow. However, these are shortcomings overcome by utilising the Swift-Stieber boundary conditions, albeit at the cost of a more demanding computational process.

Good agreement was found to exist between the predictions provided by the model and the measurements taken form the experimental apparatus. Hence, both the theoretical model and the test rig can be interpreted as being verified against one another.

The magnitudes of the pressures were found to peak at 1.5 and 0.9MPa for shaft angular velocities of 1 & 2rev/s respectively. In section 1.7.1, it was found that the contact pressures that cartilage experiences in the knee can range from 1MPa up to as large 15MPa, although the majority of studies citied values of less than 10MPa. Tailoring of the pressure magnitude in the test rig towards a particular value can be readily carried out. As observed increasing angular velocity, increases the film thickness and lowers the pressure. Conversely, increasing load will reduce the film thickness and increase the

pressure within the rig. Furthermore, the experimental and theoretical models here are based on a single lubricant, glycerol, having a viscosity of 0.8Pa.s. The range of viscosity of non-Newtonian synovial fluid is approximately 0.01-1Pa.s (Fam et al., 2007), and it has been seen that choosing a fluid with lower viscosity will result in higher peak pressures. However, choosing lubricants with too low a viscosity is not advised as this leads to overly thin fluid films, isolated pressure peeks of great magnitude and potential damage to the bearing surfaces. Hence, due consideration must be given to choosing a more suitable lubricant, such as fetal calf serum, for future studies on the test rig. Fetal calf serum is an often employed lubricant in wear testing of various joint prostheses and hence must be considered as a strong candidate for an alternative lubricant in this system.

Although the agreement between experimental and theoretical results remains a key area of interest, the primary focus is the application of this system to the medical device industry and the clinical need of cartilage repair. Thus, harvested osteochondral plugs can now be incorporated into the test rig and an updated mathematical model produced. Once inside the system, parameters such as the fluid flux through the tissue could be accessed directly. Adequate mass transfer is critical in maintaining or growing cartilage constructs in order to deliver nutrients, maintain pH levels and remove waste products. The shear stresses upon the chondrocytes generated by this fluid flow may also be beneficial as media flowing through cartilage constructs as low as 1μm/s has been previously been shown to increase matrix synthesis (Kim et al., 1995).

In principle, this technology also has applications in the tissue engineering of cartilage replacement constructs. Engineered tissues grown in mechanically active environments generally possess superior composition, morphology and mechanical properties compared to those grown in static environments (Vunjak-Novakovic et al., 2005). Cell death has been found to occur preferentially in the superficial tangential zone of cartilage rather than middle or deep zones under applications of high axial and even transverse static strains (65%) (Chahine et al., 2007). This apparent depth-dependence in

chondrocyte behaviour is most likely due to their cell properties/metabolism and/or the depth-specific extracellular matrix in which they rest. However encouragingly, true physiological dynamic loading (4.8MPa peak stress at frequencies of 0.1-40Hz in this case) together with the complex viscoelastic material behaviour of cartilage can maintain strains below 20% (Park et al., 2004).

Furthermore, mechanical stimuli presented within physiological values can promote the synthesis of cartilage extracellular matrix and enhance the mechanical properties of the tissue (Shieh and Athanasiou, 2003). Bioreactors providing cyclic hydrodynamic pressures, within the range of those expected *in vivo*, have been demonstrated to induce significant changes in aggregan and collagen II mRNA in bovine chondrocyte monolayers (Smith et al., 2000), increased GAG and collagen production in equine chondrocyte seeded PGA scaffolds (Carver and Heath, 1999) and enhanced sGAG incorporation in bovine explants (Parkkinen et al., 1993).

Another avenue of interest is the continued upkeep and preservation of explants in storage such as allografts. Traditionally, osteochondral allograft material has been transplanted within 1 week of sourcing, but due to safety concerns involving bacterial contamination and disease transmission, in addition to logistical issues, this may be extended to as much as 40-42 days (Allen et al., 2005, Williams et al., 2003). Although it appears that maintenance of the extracellular matrix is achieved, significant decreases in chondrocyte viability, viable cell density and metabolic activity have been observed within time periods of just 30 days (Allen et al., 2005, Ball et al., 2004, Pearsall et al., 2004, Williams et al., 2003). It has been demonstrated that physical stimuli can control the metabolism of chondrocytes and osteoblasts and can up-regulate the production of extracellular matrix when applied with specific magnitudes and frequencies (Wendt et al., 2005). Joint simulators similar to the hydrodynamic test rig have been previously shown as a successful means of preserving cartilage grafts for future implantation, boasting improved cell vitality and the elimination of central necrosis consistent with statically maintained tissue (Cohen et al., 2000). Furthermore, dynamic mechanical

loading has been shown to have a much more substantial effect on the health and maintenance of articular cartilage over static loading (Hung et al., 2004b). In fact, a decrease in proteoglycan synthesis and release from the extracellular matrix has been demonstrated for static compressive loads (Guilak et al., 1994, Jones et al., 1982), in addition to damaging gene expression and synthesis (Aufderheide and Athanasiou, 2006, Li et al., 2001, Ragan et al., 1999).

Given the potential uses for such a joint simulator/bioreactor, the question remains as to how either osteochondral plugs or scaffolds could be incorporated into the system. One possible envisaging of this is shown in figure 8-14. The osteochondral plug or scaffold could be housed in the shaft (or journal) element of the system. There are a number of reasons for choosing this housing location over the outer annulus. The first is quite intuitive. The vast majority of tissues replaced in AOT procedures in knees are in the medial condyles of patients. The surface topography of the tissue in this location is of course convex and thus the cartilage is more likely to lay flush with the outer surface of the shaft. The shaft itself is also a more readily available of the shelf product than the annulus and can be purchased in a variety of diameters to suit patient specific condyle curvatures. In theory, the smaller the osteochondral plug/scaffold incorporated the more flush the transition of the shaft to the construct will be. A number of 4-6mm diameter plugs/scaffolds could be situated along the length of the shaft, not just one as depicted in figure 8-14. Furthermore, smaller diameter plugs are likely to be more effective in mosaicplasties over larger diameter plugs as there would be less spacing between adjacent plugs.

The second reason for using this particular set-up is that the biological maintenance of the tissues (i.e. adequate nutrient & oxygen supply and removal) can be readily regulated. The septum-divided configuration discussed here is based on the principles of a double-chamber stirring bioreactor developed by Chang et al. (Chang et al., 2004). Consider the specifics of the osteochondral construct placement in figure 8-14. In order to accommodate the constructs, the shaft has been split along its long axis yielding two

sections denoted “Part A” and “Part B”. Part A has a through bore along its long axis and a second through bore that is orthogonal to the first. This second bore has a stepped shoulder on one end at the interface with the first bore, within which a silicon septum has been fixed. A sintered metal tube is placed into the second bore to meet the silicon septum, within which the osteochondral plug/scaffold has been placed. The septum seals around the cartilage/bone interface thereby creating two separate environments above and below this interface. The purpose of the sintered metal tube is to ensure that the bone tissue is secured laterally while experiencing axial micro-motion due to the external hydrodynamic pressures applied to the cartilage above. When Part B is reunited with Part A, the osteochondral construct and sintered metal tube are fixed in place. The shaft assembly can now be fixed at its distal ends by the hubs of two separate suspension shafts mounted in a frame with bearings and rotary seals.

The suspension shafts in the frames possess their own internal bores coupled with rotary valves which allow osteogenic medium to be pumped into the space around the sintered metal tube, then through the sintered metal tube to the bone phase of the construct and out the bore of the second suspension shaft. The environment between the shaft and the annulus is sealed by bellows linking either end of the annulus to the frames. Chondrogenic medium can be pumped into this sealed environment through a port in one frame and out a port in the second frame. This will act as a lubricant for hydrodynamic pressures to be created, but also provide nutrients and remove waste products. Additionally, the rotation of the shaft will provide agitation for mixing of the osteogenic and chondrogenic media inside and outside of the shaft respectively. In-line sensors before the inlets and after the outlets may also be used for real-time measurement and recording of oxygen concentration levels, pH, and temperature.

Lastly, the third and final reason as to why the osteochondral constructs should be housed in the shaft portion of the system is that the periodicity of loading applied to the construct can be readily and simply controlled. The outer annulus could be maintained in a fixed position as the shaft rotates within at a chosen speed and it is this speed that will

determine the frequency of loading. For example, should a speed of 1 rev/s be chosen then the construct will make a complete revolution once a second and so be exposed to the hydrodynamic pressures generated at the pinch point at a rate of once a second. This essentially translates to a frequency of 1 Hz and the standard walking loading rate. Similarly, faster or slower frequencies can be applied by altering the speed of the shaft.

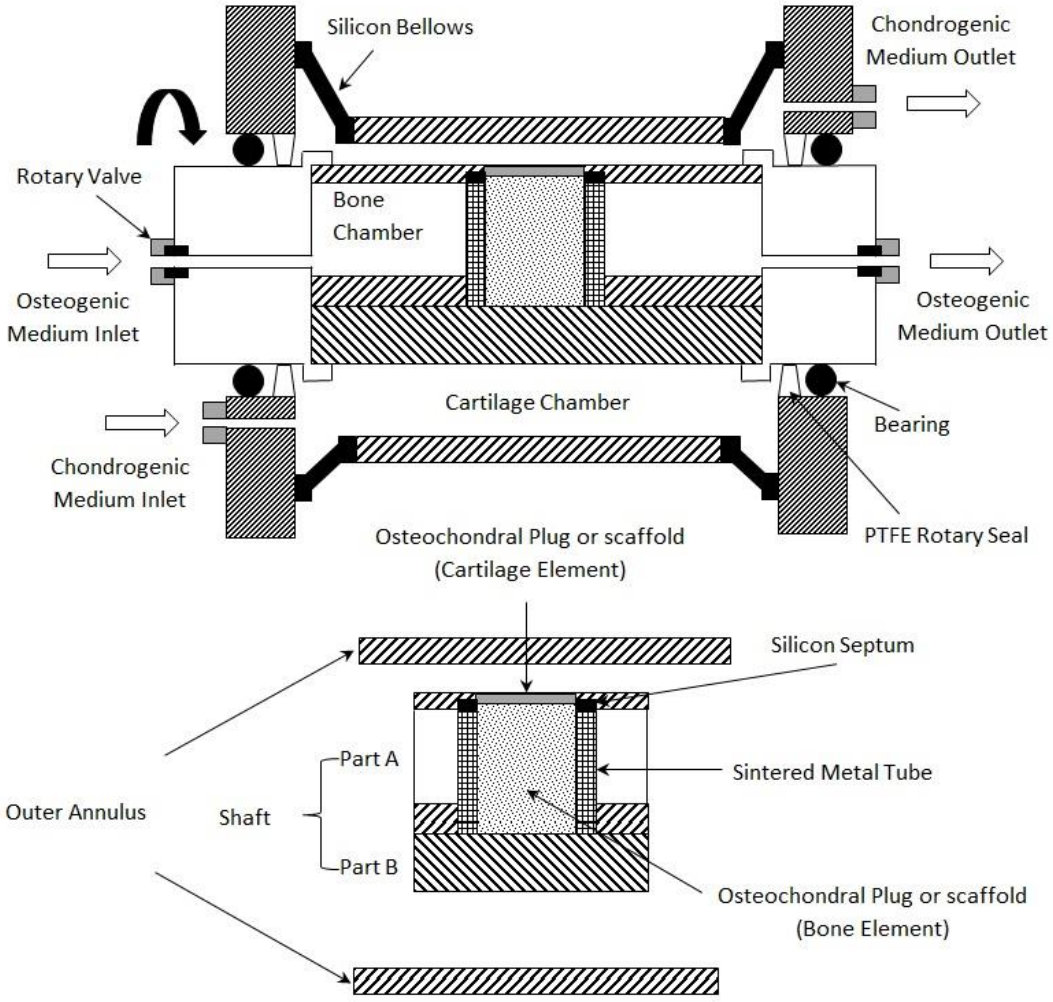

Figure 8-14. Hydrodynamic joint simulator/bioreactor incorporating osteochondral plugs or scaffolds. Two separate media chambers simultaneously but separately provide nutrients & oxygen to the cartilage and bone phases of the tissue/scaffold. Some elements of the diagram are exaggerated and not to scale.

9 Discussion

9.1 General Review

Osteochondral defects affect both the articular cartilage and underlying subchondral bone within the knee joint. They typically originate from traumatic mechanical injuries or osteochondritis, and are often associated with joint instability and associated osteoarthritic degenerative changes (Martin et al., 2007, Wendt et al., 2005). Transplantation of articular cartilage and subchondral bone in the shape of osteochondral plugs has been proven to be useful in clinical practice (Moriya et al., 2007, Zaslav et al., 2009). OAT involves the harvesting of intact cartilage and bone in the form of cylindrical plugs from joint compartments of lesser weight-bearing and their transfer into the defect site. These plugs should maintain similar biomechanical properties as intact cartilage and, once healed, produce a durable hyaline cartilage surface (Treme and Miller, 2008). However, it is not without its drawbacks. Principally, the process suffers from a limited amount of donor material available, the inability to completely match the topology of the graft to the site of injury and poor integration into the surrounding area (Martin et al., 2007, Wendt et al., 2005).

Alternative options include palliative treatments, marrow stimulation, cell therapies and cell/scaffold tissue engineered constructs. Palliative treatments focus entirely on the providing relief to the mechanical symptoms using techniques such as debridement in a strategy angled at removing the sources of pain rather than filling the lesion (Williams, 2006). Marrow stimulation cell therapies rely on the local recruitment of pluripotent stems cells based in the marrow and can be achieved in a number of manners such as abrasion arthroplasty, subchondral drilling and microfracture. The term “marrow stimulation” however, may deemed somewhat as a misnomer, as typically very little to no red bone marrow resides in the subcondral bone meaning the pluripotent cells attracted are no different than those which occur in a clot at a majority of sites in the body (Farr et al., 2011).

Abrasion arthroplasty involves the complete removal of the damaged cartilage and providing the subchondral plate with a gentle superficial burring (Farr et al., 2011). This initiates bleeding, releasing local pluripotent stem cells and the development of a fibrin clot which is used as a scaffold for the formation of the repair tissue (Aroen et al., 1998). Subchondral drilling involves perforating the subchondral plate with small drill holes whilst maintaining the majority of its structure (Aroen et al., 1998). As was the case with abrasion arthroplasty, vascular infiltration is induced, resulting in the formation of a fibrin clot. Cytokines are released during clot formation attracting pluripotent cells and leading to the formation of repair cartilage (Farr et al., 2011). Lastly, the microfracture technique involves the use of an awl to create multiple microfractures spaced 3 to 4mm apart in the subchondral bone which disrupts the vasculature beneath and inducing bleeding. As mentioned previously, this leads to clot formation, an inflammatory response, pluripotent cell infiltration and subsequent defect repair (Aroen et al., 1998).

Cell based therapies for cartilage repair include autologous chondrocyte implantation (ACI) which utilizes an autologous periosteum flap to construct a watertight lid under which a chondrocyte suspension is injected (Farr et al., 2011). The repair tissue has been reported to possess hyaline-like structural elements such as collagen II, cartilage oligomeric protein and aggrecan but at lower percentages than would be expected in healthy articular cartilage (Aroen et al., 1998). As an alternative to periosteum, collagen patches have been introduced (collagen-associated chondrocyte implantation or CACI). These involve additionally cell-seeding the collagen patch and such techniques have been expanded to include further matrix/cell composites such as matrix-associated chondrocyte implantation (MACI) and Hyalograft C (Williams, 2006).

Currently, substantial research is focused on the development of cell-seeded biodegradable scaffolds which, when processed in the correct *in-vitro* environment, are hoped to produce newly generated osteochondral tissue suitable for implantation. Generation of such tissues relies heavily on the principles of the tissue engineering triad. This consists of cell type, scaffold type and environmental factors. Scaffolds composed

of porous biodegradable biomaterials are inhabited by cells whose controlled behavior is the driving force in the formation of repair tissue. Essentially, the type of scaffold employed can be of one or more phases and fits into one of four categories (Martin et al., 2007). These include a scaffold phase for the bone component but scaffold free for cartilage, different scaffolds for bone and cartilage components, one heterogeneous/bi-layered scaffold or one homogeneous/single-layered scaffold. Furthermore, scaffolds can be made from a variety of synthetic and natural materials such as hydrogels (Grayson et al., 2008, Hung et al., 2004a, Lima et al., 2004), PLGA (Cui et al., 2011, Lee et al., 2008, Sherwood et al., 2002), hydroxyapatite (Lee et al., 2008, Oliveira et al., 2006), chitosan (Oliveira et al., 2006) and ceramic (Lien et al., 2009) to name a few.

Critically, the behavior of the cells used is controlled by the environmental circumstances they are exposed to such as chemical, biological and mechanical factors (Chiang and Jiang, 2009). The latter of these, the mechanical environment, has been keenly investigated by many authors as it has been found to govern the structural and mechanical properties of the end product (Hung et al., 2004b, Carver and Heath, 1999, Kim et al., 1995, Parkkinen et al., 1993, Vunjak-Novakovic et al., 2005, Kelly and Prendergast, 2005). The ability to create the correct mechanical environment is a matter that became significant in the formation of this thesis (chapter 8), as it is believed by many that tissue engineering is the future of osteochondral repair.

At the outset, this thesis proposed the hypothesis that that the mechanical properties of cartilage and bone at harvesting sites for osteochondral material are different from those required at the site of implantation and, although patient problems are relatively few, this disparity could influence the integration and survival of the graft *in-situ*. This is due to the fact that osteochondral tissue throughout the joint is likely to vary due to site-specific loading and kinematics. In order to investigate this, a number of studies were performed determining mechanical properties key to the function and performance of an osteochondral graft in sites which experience different joint mechanics. The femoral condyles and patellofemoral groove were chosen as these sites and indeed it was

discovered that the properties of the tissues in these sites were significantly different in a number of aspects. Furthermore, given that such differences are observed throughout the knee joint, a novel bioreactor was discussed with the aim of tissue engineering osteochondral replacements tailored specifically to a chosen site of implantation.

The first step performed in determining the properties in the condyles and PFG was evaluating the basic mechanical properties of these sites. Chapter 4 demonstrated that the aggregate modulus of articular cartilage and strength of trabecular bone at the PFG were significantly different to that of the femoral condyles. A correlation was found between the s-GAG content and the aggregate modulus, but there was no conclusive significant increase in the s-GAG content in the PFG where cartilage was stiffer. This could indicate that other factors may also be contributing to this. The strength of the trabecular bone from the condyles was significantly greater than the PFG, presumably due to functional adaptation of the bone structure in response to the greater joint stresses encountered. Furthermore, separate correlations were found for the PFG and the condyle sites between the aggregate modulus of the cartilage and the Young's modulus of the trabcecular bone beneath, indicating that the cartilage and bone couple to form a functional unit that can vary between different anatomical sites.

The possible ramifications of these results with regard to OAT in human patients come to light when it is considered that osteochondral plugs are taken from non-load bearing sites and so are very likely to have different cartilage/bone functional units. Secure fixation of the osteochondral plugs, particularly in the early stages of weight bearing, is vital to graft integration. Wolff's law dictates that the more bone experiences stress, the more it remodels itself to bare that stress and as a result becomes stronger. If the bone from non-load bearing sites should be weaker, it runs the risk of loosening whether it is through a repetitive process such as micro-motion at the interface, or through a single incident such as yielding of the bone under a sudden impact load. The bone will also experience remodelling once transplanted which may further weaken the already vulnerable graft bone. Furthermore, as it is unlikely that the cartilage from a non-load

bearing site is akin to that of a particular implantation site, then some degree of stress shielding may occur at the site of implantation due to preferential distribution of load through the stiffer material, be it the implant or the immediate area around the implant.

In continuing to examine the variation of the mechanical properties of the osteochondral tissues in the chosen sites, chapter 5 determined the Poisson's ratio of the cartilage. It was revealed that a lower apparent and equilibrium Poisson's ratio existed for the cartilage of the PFG then that of the condyles. These results signify that cartilage from the PFG is more resilient to radial expansion at physiological levels of deformation. When the Poisson's ratio results were examined in combination with the aggregate modulus results, an inverse correlation was realised between the two parameters. Essentially, the cartilage of the PFG possessed a combination of a higher aggregate modulus and a lower Poisson's ratio, whereas in contrast the condylar cartilage presented a lower aggregate modulus and a higher Poisson's ratio.

The ability of any synovial joint to maintain joint conformity is of great importance in reducing contact stresses, friction and tribological wear. In fact, Barker and Seedhom hypothesised that cartilage adapts its matrix constituents to be least susceptible to damage as it minimizes strain by optimising the response of viscous and elastic contributions according to location in the knee (Barker and Seedhom, 2001). It was discovered that there exists an optimal range of cartilage stiffness (8-12MPa dynamic indentation modulus) at which strains are minimised (≈23%). For stiffer cartilage existing beyond that range, larger strains were found to occur that were primarily contributed to by large viscous strains. Alternatively, for softer cartilage which existed below that range, larger strains were also found to occur but this time the primary contributor was large elastic strains. This phenomenon is most likely the driving mechanism by which cartilage in the porcine PFG was found to be stiffer than cartilage in the condyles in the study performed in this thesis.

Also key to joint conformity is the ability of the cartilage to deform under joint load and expand laterally (i.e. the tissue's Poisson's ratio). Given the evidence that there is a site-dependent variation in the Poisson's ratio throughout the knee, it is possible therefore that OAT affects the joints ability to maintain conformity. Further still, given the inverse correlation between Poisson's ratio and the aggregate modulus, it is possible that the cartilage of transferred tissue, should it be stiffer, may remain prominent to the native articular surface under prolonged durations of loading.

The inverse correlation between the Poisson's ratio and aggregate modulus of cartilage has been demonstrated in other animal models (bovine) than simply the porcine model in this thesis (Kiviranta et al., 2006). Thus, it is very likely that it also exists in human articular cartilage. There are further indications that the animal model results of the mechanical properties translate to humans as a correlative relationship between the stiffness of cartilage and trabecular bone beneath has also been demonstrated in human tibias (Ding et al., 1998, Rohl et al., 1997).

Chapter 6 initially set out to understand the regional variations found in the mechanical properties of the cartilage via a simple histological examination, but it also succeeded in raising another issue; that the maturity, or rather the immaturity, of the tissue may be a complex, integrated factor in the results. Prior to this, it had been eluded to that the tissue immaturity may indeed hold relevance. In discussing the aggregate modulus results, it was postulated that this could explain why variations exist between different anatomical locations in different animal models. This issue was raised again with regards regional variations in the Poisson's ratio results, but also to explain why the apparent Poisson's ratio does not satisfy theoretical incompressibility. This incompressibility has been shown previously to exist in mature but not immature cartilage (Wong et al., 2000).

The distribution of the structural proteins collagen and PG should vary though the depth of cartilage in accordance with the standard phenotype of mature cartilage. Laminar

distributions of these proteins were observed in many of the locations, but a homogenous distribution was found at PFG2 in the patellofemoral groove which may indicate that maturation had not occurred there. This is especially interesting as it was been shown that a mature cartilage phenotype occurs in a very similar position in pigs merely a few months older (Rieppo et al., 2009). The presence of what appeared to be a more mature phenotype at PFG1 could suggest that maturation of cartilage within the porcine PFG begins initially inferiorly near the condyles and then progresses superiorly. In time, PFG2 will present the same distribution of proteins as PFG1. This is most likely stimulated by alteration of the joint load and kinematics in these animals as they develop and mature with age.

It is unclear whether these indications of immaturity in the joint cartilage affect the results of the mechanical properties (the aggregate modulus & Poisson's ratio) in any significant way. Ideally, all tissues would be fully mature. However, PFG1 presents a similar level of maturity to the condyles but still remains significantly stiffer than the condyles. Hence, the inference that this increased stiffness is due to its anatomical location (and associated loading conditions) may still hold and with it the application of the porcine knee model.

The results of the friction study in chapter 7 revealed far fewer variations between sites than the mechanical properties determined. In fact, the results demonstrated that the site where an osteochondral plug is taken from has no significant effect on its friction. According to bi-phasic lubrication theory, the longer cartilage is loaded the more interstitial fluid load support is lost and friction rises as a result of this. This trait was clearly demonstrated, but it is surprising that the rate of loss of fluid load support did not vary in the PFG sites given that they were found to possess a higher aggregate modulus. This may be as a result of influences that were not quantified, such as the content of superficial zone protein at the sites, or indeed it may simply be that the test apparatus is not sensitive enough to measure more discrete variations of friction. Furthermore, it may

be due to the cartilage still being attached to be subchondral bone in the friction tests but not attached in the determination of the aggregate modulus.

It was demonstrated however, that the static coefficient of friction was found to be influenced by the sliding velocity applied and that this friction was found to increase with increasing velocity regardless of the loading time. This is likely due to the time-dependent viscous component of the force of adhesion which is sensitive to velocity. The dynamic coefficient of friction appeared to be unaffected by sliding velocity. This agrees with Coulomb's law of kinetic (dynamic) friction, which states that the dynamic friction is independent of the sliding velocity.

Given the evidence that the mechanical properties of osteochondral plugs harvested from different regions around the knee joint are significantly different, the tissue engineering of repair products become an increasingly attractive prospect. This is due to the fact that because of this topographical variation, it is unlikely that osteochondral tissue from any harvest site will match a given implantation site. The bioreactor described in chapter 8 offers a novel approach to growing such constructs in physiologically relevant mechanical conditions. The possible benefits of the specified design include the development of constructs with tailored composition and mechanical properties (Vunjak-Novakovic et al., 2005) including increased GAG and collagen synthesis (Carver and Heath, 1999) and enhanced GAG incorporation (Parkkinen et al., 1993). Hence, this device offers a potential to develop superior osteochondral grafts then those currently employed during AOT procedures. Additionally, since cell viability, cell density and matrix synthesis in osteochondral allografts have been found to reduce during storage periods (Allen et al., 2005, Ball et al., 2004, Pearsall et al., 2004), the apparatus may be employed as a joint simulator to maintain biological homeostasis. Thus, the device has the potential to make a significant impact in the medical device industry, as well as the health and activity of those suffering from osteochondral lesions.

9.2 Limitations & Future Work

The foremost limitation of the work presented in this thesis is the use of a porcine model to characterise the mechanical properties at sites akin to those found in human knees. It was chosen in spite of knowledge that the osteochondral tissues of the porcine knee are unlikely to possess mechanical properties of equal or similar magnitude. However, it was the porcine knee's relatively similar geometry (i.e. features are scaled similarly) and shape to the human knee that formed the basis for its inclusion, suggesting that load distribution and joint movement may also occur in a similar manner to human knees. It was hoped that due to the topographical resemblance, the regional variation in the mechanical properties would also be comparable to human knees, even if they do not present the same magnitude. The ovine model offers a similar quandary to the porcine model, but was excluded due to greater difficulty in its acquisition. In contrast, osteochondral tissues in the bovine knee are known to exhibit comparative mechanical properties to humans, but the topography is considerably different and this formed the basis of its exclusion.

Appendix A presents a brief study examining the suitability of the porcine knee model. Anatomical features representative of the overall shape of the knee joint were measured and compared to similar data for ovine and human knee joints (Osterhoff et al., 2011). The resulting porcine/human feature ratios spanned from approximately 0.7-0.8 for 7 of the 8 anatomical features. The remaining feature was the intercondylar height. Speaking more broadly of the knee, the condylar and tibial aspect ratio were rather comparable, yielding values of 0.91 and 0.99 respectively. On average, this was found to be slightly superior to the ovine/human aspect ratios.

However, these features alone do not necessarily account for the gait patterns, load bearing or movement characteristics of the knee joint, or that the porcine knee is comparable to humans in this respect. Sadly, no such kinematic data appears to exist for

pigs, but examining the knee joint kinematics of sheep may shed some light given its similarity in size and it also being a quadruped.

Slow walking is known to produce a stance and swing phase lasting approximately 1 second in humans and 0.8 seconds in sheep. Hence, a similar porcine/human ratio is found to that describing the shape and relative size of the joint. Furthermore, the stance and swing gait percentages are the same as in human knee joints (Agostinho et al., 2012). The peak load forces that pass through the tibiofemoral joint in sheep exceed twice that of body weight (Taylor et al., 2006, Taylor et al., 2011), which is also similar to the respective human joint when take at a 0.8 ratio. There are some kinematic changes however, most notably that the flexion/extension patterns during the stance phase are different and generally are offset by approximately 30 degrees throughout the entire gait cycle (Cottrell et al., 2008, Darcy et al., 2008, Tapper et al., 2006). It has previously been demonstrated that similar flexion angles induce greater PFG contact pressures in human knees compared to relatively extended angles, especially during activities such as stair climbing (Goudakos et al., 2009). Hence, it is possible a greater proportion of stress is constantly present in the porcine PFG compared as muscle contractions to maintain joint stability. This could be responsible for the generation of stiffer cartilage in this PFG rather than the femoral condyles.

In truth, no animal model can be comprehensively representative of human knees, but they can be used to establish that similar tends could exist. In this thesis, this practice was employed to demonstrate that osteochondral tissues from alternative bearing sites in porcine knees behave differently and that this may translate to human knees, possibly having implications for OAT procedures. Future work may include investigating directly if these trends exist in humans. This could be achieved by broadening the study to encompass clinical input from orthopaedic surgeons, the application for ethical approval in using human osteochondral tissues and gaining access to human tissue banks.

The methodology of the studies performed remains predominately sound, but these investigations could be developed further. The Poisson's ratio study consisted of compressive ramping and holding of the specimens to 20% strain and measuring the resulting apparent and equilibrium radial expansions. Successive ramps and holds of 5% strain are likely to demonstrate a strain dependency for Poisson's ratio. Although, it is known such strain dependencies exist (Jurvelin et al., 1997), the extent and relationship of this dependency may alter from site to site around the knee.

In attempting to understand the results of the cartilage mechanical properties determined (namely H_{A0} & Poisson's ratio), there was some conjecture as to whether the collagen network played a significant role at certain locations. The inclusion of a collagen assay to accompany the s-GAG assay would quantify the collagen content at chosen sites and could also be expanded to measure the presence of cross-linked collagen. Furthermore, the histological analysis could be improved by employing such techniques as polarised light microscopy to determine the spatial orientation and organisation of the collagen network throughout the depth of cartilage specimens (Rieppo et al., 2009).

In determining the aggregate modulus of the articular cartilage and the strength of the trabecular bone, the cartilage was completely removed from the sub-chondral bone and the sub-chondral bone was completely removed from the tested bone plugs. Hence, the sub-chondral plate contributed nothing to the mechanical properties of either material tested. However, *in-vivo*, the sub-chondral plate most likely affects the mechanics of both elements. Removal of sub-chondral bone from cartilage greatly affects the tissue's permeability and by association deformational characteristics, whether it is creating a hole (Suh et al., 1995) or completely removing the plate (Gannon et al., 2012). However, in the study determining the aggregate modulus in this thesis, the cartilage face where bone was attached was loaded with a solid indenter (section 4.2.2). Thus, an effort was made to minimise the removal of the sub-chondral plate by attempting to mimic the attachment of the bone. As for the bone compression testing, the sub-chondral bone is denser the trabecular bone beneath it, so the removal of the sub-chondral bone plate

weakens the properties of the samples tested. Although assumptions are often made about homogeneity in tissue mechanics in order to simply a model, this would certainly not be true should the sub-chondral plate be attached to the bone plugs. One possible way around this would be to model the plugs as composites, using the Reuss model for example. However, this would necessitate determining the volume fractions of both phases, adding more, perhaps unrequired, effort to the process.

Another limitation of the biomechanical studies performed in this thesis, especially chapters 4 and 5, is that the aggregate modulus and Poisson's ratio of cartilage was determined under quasi-static loading conditions. Dynamic conditions, such as those experienced *in-vivo*, elicit a substantially different response over static conditions, generating vast amounts of interstitial fluid pressurisation and in turn significantly reducing the deformational strain (Soltz and Ateshian, 2000, Suh et al., 1995, Wu et al., 1998, Park et al., 2004). Furthermore, the dynamic deformational response is strongly influenced by the loading frequency, which has been attributed to the diffusive momentum changes between solid and fluid phases governing cartilage's viscoelasticity (Suh et al., 1995). When the frequency is low, the deformational response can adapt easily to the applied load. However, when the frequency is high the tissue cannot adapt as quickly, meaning less deformation occurs. For example, this translates to a deformation of approximately 30μm at 0Hz (i.e. static conditions) to near zero deformation at 0.1Hz for calf carpometacarpal cartilage under the same loading conditions. (Soltz and Ateshian, 2000). Hence, this reluctance to deform in tandem with the presence of large interstitial fluid pressures results in a large increase in the apparent stiffness of the tissues (Gannon et al., 2012), which increases the aggregate modulus. Similarly, the dilatory ability of the tissue is reduced (Wu et al., 1998), which decreases the Poisson's ratio.

Therefore, the quasi-static testing performed determining the aggregate modulus and the Poisson's ratio has its limitations. However, quasi-static testing due to its simplicity is largely used in the field of tissue mechanics. Hence, the data generated for these

parameters in this thesis offers a simple means for comparison to similar quasi-static testing published in the literature. In any case, a comparison between cartilage properties at various sites of the knee can be made regardless of it not being loaded in a physiologically relevant manner.

Although simple in its application, and adequate for all intents and purposes, the friction study in chapter 7 presented a number of limitations. Considerable adaptions could be made to the pin-on-plate test-rig if so desired. The first of these is the removal of the carriage and rail system employed for translation and replacing it with an actuator with in-line load sensor. This now frees the materials testing system to apply a choice of constant, stepped or dynamic loads over prolonged time periods. The addition of biocides such as sodium azide to lubrication solutions would ensure no bacterial growth over these periods, or if a simple constant applied load is sufficient, the rig could be mounted in a fume hood to maintain sterility.

One pin-on-plate friction study that could be of particular interest to OAT procedures is the utilisation of a cartilage plate configuration, but with the inclusion of osteochondral plugs of varying diameters. The pin element of the rig could be alumina, steel, or cartilage. The differences in friction could then be measured against a control intact cartilage plate. Further still, differences in friction relating to OAT could be measured by incorporating osteochondral plugs from load bearing and non-load bearing regions, allograft tissues and even tissue engineered constructs.

The study describing the development of the hydrodynamic bioreactor/joint simulator was far from exhaustive and served merely as a proof of concept and to establish the feasibility of such a device. This presents a plethora of potential future work to develop the concept further. The inclusion of a non-Newtonian viscosity lubricant may be considered as a next step, but given that the lubricating solutions will most likely be Newtonian culture media to maintain the health of incorporated tissues, this may not be required. The inclusion of osteochondral constructs presents a considerable

developmental step. Although, suggestions were provided as to how this may be achieved (section 8.4), it is nevertheless a substantial undertaking, worthy of a doctorate in itself.

The hydrodynamic lubrication theory upon which the mathematical predictions were produced in this thesis assumes the articulating surfaces are sufficiently stiff that deformations are minimal under the fluid pressures generated. A reasonable assumption given stainless steel was employed for theses surfaces. The inclusion of osteochondral plugs into one of these surfaces introduces regions susceptible to significant deformation and thus elastohydrodynamic lubrication must be employed to model such a system. Perhaps, as an initial step it may be beneficial to introduce an articulating surface comprising entirely of a polymer, develop the elastohydrodynamic model for the system and verify this with physical pressure measurements. Once this has been achieved, one could attempt to model the inclusion of a composite articulating surface similar to osteochondral plugs being incorporated into the shaft. Given the degree of complexity this presents, perhaps the use of computational fluid dynamics (CFD) software offers a superior route in determining the pressures generated. Furthermore, the deformations of the tissues and fluid flux through the cartilage could also be assessed via a 2-D approximation.

9.3 Conclusions

In a porcine knee model, the aggregate modulus of articular cartilage and the strength of trabecular bone in the femoral condyles differ from those found at the patellofemoral groove. The Poisson's ratio of the articular cartilage also differs between these sites and an inverse correlation with the aggregate modulus appears to exist. It describes sites of higher aggregate modulus possessing a lower Poisson's ratio and conversely sites of lower aggregate modulus possessing higher Poisson's ratios. A frictional study found no significant differences between the coefficient of friction at condylar and patellofemoral groove sites, even though these sites present starkly different mechanical properties. Translating this information to a human model indicates that harvesting osteochondral material from non-load bearing sites and implanting it into load bearing sites such as the condyles or patellofemoral groove may affect the integration and survival of the graft as it is highly unlikely the graft will possess the appropriate properties. Although failure of grafts is relatively rare, this may prove to be a cause in some instances. Hence, the future of repairing osteochondral lesions may lie in tissue engineering. The hydrodynamic bioreactor/joint simulator proposes a promising and novel solution in providing the essential mechanical stimuli required during the tissue engineering of ostoechondral constructs or the storage of similar allograft tissues. In this manner, it may be possible to tailor the mechanical properties of a tissue engineered construct to a particular implantation site. Further still, it may also be possible to work harden auto or allograft tissues to the needs of the implantation site. However, considerably more work is required to be done before this potential can be fully realised.

REFERENCES

AGOSTINHO, F. S., RAHAL, S. C., ARAUJO, F. A. P., CONCEICAO, R. T., HUSSNI, C. A., EL-WARRAK, A. O. & MONTEIRO, F. O. B. 2012. Gait analysis in clinically healthy sheep from three different age groups using a pressure-sensitive walkway. *Bmc Veterinary Research,* 8.

AL-SHAIKH, R. A., CHOU, L. B., MANN, J. A., DREEBEN, S. M. & PRIESKORN, D. 2002. Autologous osteochondral grafting for talar cartilage defects. *Foot & Ankle International,* 23**,** 381-389.

ALLEN, R. T., ROBERTSON, C. M., PENNOCK, A. T., BUGBEE, W. D., HARWOOD, F. L., WONG, V. W., CHEN, A. C., SAH, R. L. & AMIEL, D. 2005. Analysis of stored osteochondral allografts at the time of surgical implantation. *American Journal of Sports Medicine,* 33**,** 1479-1484.

AMIN, A. K., HUNTLEY, J. S., BUSH, P. G., SIMPSON, A. & HALL, A. C. 2008. Osmolarity influences chondrocyte death in wounded articular cartilage. *Journal of Bone and Joint Surgery-American Volume,* 90A**,** 1531-1542.

ANGELE, P., YOO, J. U., SMITH, C., MANSOUR, J., JEPSEN, K. J., NERLICH, M. & JOHNSTONE, B. 2003. Cyclic hydrostatic pressure enhances the chondrogenic phenotype of human mesenchymal progenitor cells differentiated in vitro. *Journal of Orthopaedic Research,* 21**,** 451-457.

ARMSTRONG, S. J., READ, R. A. & PRICE, R. 1995. TOPOGRAPHICAL VARIATION WITHIN THE ARTICULAR-CARTILAGE AND SUBCHONDRAL BONE OF THE NORMAL OVINE KNEE-JOINT - A HISTOLOGICAL APPROACH. *Osteoarthritis and Cartilage,* 3**,** 25-33.

AROEN, A., JONES, D. G. & FU, F. H. 1998. Arthroscopic diagnosis and treatment of cartilage injuries. *Sports Medicine and Arthroscopy Review,* 6**,** 31-40.

ATESHIAN, G. A. 2009. The role of interstitial fluid pressurization in articular cartilage lubrication. *Journal of Biomechanics,* 42**,** 1163-1176.

ATESHIAN, G. A., WARDEN, W. H., KIM, J. J., GRELSAMER, R. P. & MOW, V. C. 1997. Finite deformation biphasic material properties of bovine articular cartilage from confined compression experiments. *Journal of Biomechanics,* 30**,** 1157-1164.

ATHANASIOU, K. A., AGARWAL, A. & DZIDA, F. J. 1994. Comparative-Study of the Intrinsic Mechanical-Properties of the Human Acetabular and Femoral-Head Cartilage. *Journal of Orthopaedic Research,* 12**,** 340-349.

ATHANASIOU, K. A., ROSENWASSER, M. P., BUCKWALTER, J. A., MALININ, T. I. & MOW, V. C. 1991. INTERSPECIES COMPARISONS OF INSITU INTRINSIC MECHANICAL-PROPERTIES OF DISTAL FEMORAL CARTILAGE. *Journal of Orthopaedic Research,* 9**,** 330-340.

AUFDERHEIDE, A. C. & ATHANASIOU, K. A. 2006. A direct compression stimulator for articular cartilage and meniscal explants. *Annals of Biomedical Engineering,* 34**,** 1463-1474.

BALL, S. T., AMIEL, D., WILLIAMS, S. K., TONTZ, W., CHEN, A. C., SAH, R. L. & BUGBEE, W. D. 2004. The effects of storage on fresh human osteochondral allografts. *Clinical Orthopaedics and Related Research***,** 246-252.

BARKER, M. K. & SEEDHOM, B. B. 2001. The relationship of the compressive modulus of articular cartilage with its deformation response to cyclic loading: does cartilage optimize its modulus so as to minimize the strains arising in it due to the prevalent loading regime? *Rheumatology,* 40**,** 274-284.

BECKER, R., WIRZ, D., WOLF, C., GOPFERT, B., NEBELUNG, W. & FRIEDERICH, N. 2005. Measurement of meniscofemoral contact pressure after repair of bucket-handle tears with biodegradable implants. *Archives of Orthopaedic and Trauma Surgery,* 125**,** 254-260.

BELL, C. J., INGHAM, E. & FISHER, J. 2006. Influence of hyaluronic acid on the time-dependent friction response of articular cartilage under different conditions. *Proceedings of the Institution of Mechanical Engineers Part H-Journal of Engineering in Medicine,* 220**,** 23-31.

BENAZZO, F., CADOSSI, M., CAVANI, F., FINI, M., GIAVARESI, G., SETTI, S., CADOSSI, R. & GIARDINO, R. 2008. Cartilage repair with osteochondral autografts in sheep: Effect of biophysical stimulation with pulsed electromagnetic fields. *Journal of Orthopaedic Research,* 26**,** 631-642.

BHUSHAN, B. 2003. Adhesion and stiction: Mechanisms, measurement techniques, and methods for reduction. *Journal of Vacuum Science & Technology B,* 21**,** 2262-2296.

BLACK, R. A., CURRAN, S. J. & BLACKHURST, J. 12/04/2007. *Reactor comprising an annular reaction space*. International patent application number PCT/GB2006/003671.

BLACK, R. A., CURRAN, S. J. & BLACKHURST, J. 01/01/2013. *Reactor comprising an annular reaction space*. US patent number US8342735.

BOSCHETTI, F., PENNATI, G., GERVASO, F., PERETTI, G. M. & DUBINI, G. 2004. Biomechanical properties of human articular cartilage under compressive loads. *Biorheology,* 41**,** 159-166.

BOSCHETTI, F. & PERETTI, G. M. 2008. Tensile and compressive properties of healthy and osteoarthritic human articular cartilage. *Biorheology,* 45**,** 337-344.

BRECHTER, J. H. & POWERS, C. M. 2002. Patellofemoral joint stress during stair ascent and descent in persons with and without patellofemoral pain. *Gait & Posture,* 16**,** 115-123.

BROWN, O., MORGAN, C. & SCUDERI, G. 2009. Osteochondral Autograft Transfer. *In:* COLE, B. & GOMOLL, A. (eds.) *Biologic Joint Reconstruction: Alternatives to Joint Replacement.* Thorofare, NJ: SLACK Inc.

BUGBEE, W. & OSTEMPOWSKI, M. 2006. Osteochondral Allograft Transplantation. *In:* MIRZAYAN, R. (ed.) *Cartilage Injury in the Athlete.* New York, NY: Thieme Medical Publishers Inc.

CARTER, M. J., BASALO, I. M. & ATESHIAN, G. A. 2007. The temporal response of the friction coefficient of articular cartilage depends on the contact area. *Journal of Biomechanics,* 40**,** 3257-3260.

CARVER, S. E. & HEATH, C. A. 1999. Increasing extracellular matrix production in regenerating cartilage with intermittent physiological pressure. *Biotechnology and Bioengineering,* 62**,** 166-174.

CHAHINE, N. O., ATESHIAN, G. A. & HUNG, C. T. 2007. The effect of finite compressive strain on chondrocyte viability in statically loaded bovine articular cartilage. *Biomechanics and Modeling in Mechanobiology,* 6**,** 103-111.

CHAMPE, P. C. & HARVEY, R. A. 1987. *Biochemistry,* Philadelphia, Lippincott.

CHAN, S. M. T., NEU, C. P., KOMVOPOULOS, K. & REDDI, A. H. 2011. Dependence of nanoscale friction and adhesion properties of articular cartilage on contact load. *Journal of Biomechanics,* 44**,** 1340-1345.

CHANG, C. H., LIN, F. H., LIN, C. C., CHOU, C. H. & LIU, H. C. 2004. Cartilage tissue engineering on the surface of a novel gelatin-calcium-phosphate biphasic scaffold in a double-chamber biorector. *Journal of Biomedical Materials Research Part B-Applied Biomaterials,* 71B**,** 313-321.

CHANGOOR, A., HURTIG, M. B. & RUNCIMAN, R. J. 2006. Osteochondral graft fixation using a bioresorbable bone cement. *Journal of Biomechanics,* 39**,** 2887-2892.

CHEN, A. C., BAE, W. C., SCHINAGL, R. M. & SAH, R. L. 2001. Depth- and strain-dependent mechanical and electromechanical properties of full-thickness bovine articular cartilage in confined compression. *Journal of Biomechanics,* 34**,** 1-12.

CHENG, N. S. 2008. Formula for the viscosity of a glycerol-water mixture. *Industrial & Engineering Chemistry Research,* 47**,** 3285-3288.

CHIANG, H. & JIANG, C.-C. 2009. Repair of Articular Cartilage Defects: Review and Perspectives. *Journal of the Formosan Medical Association,* 108**,** 87-101.

CHOW, J. C. Y., HANTES, M. E., HOULE, J. B. & ZALAVRAS, C. G. 2004. Arthroscopic autogenous osteochondral transplantation for treating knee cartilage defects: A 2-to 5-year follow-up study. *Arthroscopy-the Journal of Arthroscopic and Related Surgery,* 20**,** 681-690.

CLOYD, J. M., MALHOTRA, N. R., WENG, L., CHEN, W., MAUCK, R. L. & ELLIOTT, D. M. 2007. Material properties in unconfined compression of human nucleus pulposus, injectable hyaluronic acid-based hydrogels and tissue engineering scaffolds. *European Spine Journal,* 16**,** 1892-1898.

COHEN, I., ROBINSON, D., COHEN, N. & NEVO, Z. 2000. Storing live embryonic and adult human cartilage grafts for transplantation using a joint simulating device. *Biomaterials,* 21**,** 2117-2123.

COTTRELL, J. M., SCHOLTEN, P., WANICH, T., WARREN, R. F., WRIGHT, T. M. & MAHER, S. A. 2008. A new technique to measure the dynamic contact pressures on the Tibial Plateau. *Journal of Biomechanics,* 41**,** 2324-2329.

CUI, W., WANG, Q., CHEN, G., ZHOU, S., CHANG, Q., ZUO, Q., REN, K. & FAN, W. 2011. Repair of articular cartilage defects with tissue-engineered osteochondral composites in pigs. *Journal of Bioscience and Bioengineering,* 111**,** 493-500.

DARCY, S. P., ROSVOLD, J. M., BEVERIDGE, J. E., CORR, D. T., BROWN, J. J. Y., SUTHERLAND, C. A., MARCHUK, L. L., FRANK, C. B. & SHRIVE, N. G.

2008. A comparison of passive flexion-extension to normal gait in the ovine stifle joint. *Journal of Biomechanics,* 41**,** 854-860.

DAVIDSON, P. A., RIVENBURGH, D. W., DAWSON, P. E. & ROZIN, R. 2007. Clinical, histologic, and radiographic outcomes of distal femoral resurfacing with hypothermically stored Osteoarticular allografts. *American Journal of Sports Medicine,* 35**,** 1082-1090.

DING, M., DALSTRA, M., LINDE, F. & HVID, I. 1998. Mechanical properties of the normal human tibial cartilage-bone complex in relation to age. *Clinical Biomechanics,* 13**,** 351-358.

DOWSON, D. & JIN, Z. M. 1986. Micro-elastohydrodynamic lubrication of synovial joints. *Engineering in medicine,* 15**,** 63-5.

DUCHOW, J., HESS, T. & KOHN, D. 2000. Primary stability of press-fit-implanted osteochondral grafts - Influence of graft size, repeated insertion, and harvesting technique. *American Journal of Sports Medicine,* 28**,** 24-27.

ECKSTEIN, F., WINZHEIMER, M., HOHE, J., ENGLMEIER, K. H. & REISER, M. 2001. Interindividual variability and correlation among morphological parameters of knee joint cartilage plates: analysis with three-dimensional MR imaging. *Osteoarthritis and Cartilage,* 9**,** 101-111.

ELLIOTT, D. M. & SETTON, L. A. 2001. Anisotropic and inhomogeneous tensile behavior of the human anulus fibrosus: Experimental measurement and material model predictions. *Journal of Biomechanical Engineering-Transactions of the Asme,* 123**,** 256-263.

ERGGELET, C. & MANDELBAUM, B. 2008. *Principles of Cartilage Repair,* Wurzburg, Steinkopff Verlag.

FAM, H., BRYANT, J. T. & KONTOPOULOU, M. 2007. Rheological properties of synovial fluids. *Biorheology,* 44**,** 59-74.

FARR, J., COLE, B., DHAWAN, A., KERCHER, J. & SHERMAN, S. 2011. Clinical Cartilage Restoration Evolution and Overview. *Clinical Orthopaedics and Related Research,* 469**,** 2696-2705.

FEELEY, B. & WILLIAMS III, R. 2009. Osteochondral Allografts. *In:* COLE, B. & GOMOLL, A. (eds.) *Biologic Joint Reconstruction: Alternatives to Arthroplasty.* First ed. Thorofare, NJ: SLACK Inc.

FICKLIN, T., THOMAS, G., BARTHEL, J. C., ASANBAEVA, A., THONAR, E. J., MASUDA, K., CHEN, A. C., SAH, R. L., DAVOL, A. & KLISCH, S. M. 2007. Articular cartilage mechanical and biochemical property relations before and after in vitro growth. *Journal of Biomechanics,* 40**,** 3607-3614.

FORSTER, H. & FISHER, J. 1996. The influence of loading time and lubricant on the friction of articular cartilage. *Proceedings of the Institution of Mechanical Engineers. Part H, Journal of engineering in medicine,* 210**,** 109-19.

FORSTER, H. & FISHER, J. 1999. The influence of continuous sliding and subsequent surface wear on the friction of articular cartilage. *Proceedings of the Institution of Mechanical Engineers Part H-Journal of Engineering in Medicine,* 213**,** 329-345.

FRANK, E. H., JIN, M., LOENING, A. M., LEVENSTON, M. E. & GRODZINSKY, A. J. 2000. A versatile shear and compression apparatus for mechanical stimulation of tissue culture explants. *Journal of Biomechanics,* 33**,** 1523-1527.

FROIMSON, M. I., RATCLIFFE, A., GARDNER, T. R. & MOW, V. C. 1997. Differences in patellofemoral joint cartilage material properties and their significance to the etiology of cartilage surface fibrillation. *Osteoarthritis and Cartilage,* 5**,** 377-386.

GANNON, A. R., NAGEL, T. & KELLY, D. J. 2012. The role of the superficial region in determining the dynamic properties of articular cartilage. *Osteoarthritis and Cartilage,* 20**,** 1417-1425.

GLEGHORN, J. P. & BONASSAR, L. J. 2008. Lubrication mode analysis of articular cartilage using Stribeck surfaces. *Journal of Biomechanics,* 41**,** 1910-1918.

GOUDAKOS, I. G., KOENIG, C., SCHOETTLE, P. B., TAYLOR, W. R., SINGH, N. B., ROBERTS, I., STREITPARTH, F., DUDA, G. N. & HELLER, M. O. 2009. Stair climbing results in more challenging patellofemoral contact mechanics and kinematics than walking at early knee flexion under physiological-like quadriceps loading. *Journal of Biomechanics,* 42**,** 2590-2596.

GRAY, H. 1973. *Gray's Anatomy,* Longman group

GRAYSON, W. L., CHAO, P. H. G., MAROLT, D., KAPLAN, D. L. & VUNJAK-NOVAKOVIC, G. 2008. Engineering custom-designed osteochondral tissue grafts. *Trends in Biotechnology,* 26**,** 181-189.

GUETTLER, J. H., DEMETROPOULOS, C. K., YANG, K. H. & JURIST, K. A. 2004. Osteochondral deflects in the human knee - Influence of defect size on cartilage rim stress and load redistribution to surrounding cartilage. *American Journal of Sports Medicine,* 32**,** 1451-1458.

GUILAK, F., MEYER, B. C., RATCLIFFE, A. & MOW, V. C. 1994. The effects of matrix compression on proteoglycan metabolism in articular cartilage explants. *Osteoarthritis Cartilage,* 2**,** 91-101.

HAMROCK, B., SCHMID, S. & JACOBSON, B. 2004. *Fundamentals of Fluid Film Lubrication,* New York, Marcel Dekker, Inc.

HAMROCK, B. J. & DOWSON, D. 1978. Elastohydrodynamic Lubrication of Elliptical Contacts for Materials of Low Elastic-Modulus I - Fully Flooded Conjunction. *Journal of Lubrication Technology-Transactions of the Asme,* 100**,** 236-245.

HANGODY, L. & FULES, P. 2003. Autologous osteochondral mosaicplasty for the treatment of full-thickness defects of weight-bearing joints - Ten years of experimental and clinical experience. *Journal of Bone and Joint Surgery-American Volume,* 85A**,** 25-32.

HAYES, W. C., HERRMANN, G., MOCKROS, L. F. & KEER, L. M. 1972. MATHEMATICAL-ANALYSIS FOR INDENTATION TESTS OF ARTICULAR-CARTILAGE. *Journal of Biomechanics,* 5**,** 541-&.

HENEGHAN, P. 2008. *Fluid-solid-chemical interactions of the nucleus pulposus.* Phd, University of Strathclyde, Glasgow.

HOLMES, M. H. & MOW, V. C. 1990. The Nonlinear Characteristics of Soft Gels and Hydrated Connective Tissues in Ultrafiltration. *Journal of Biomechanics,* 23**,** 1145-1156.

HUANG, C. Y., STANKIEWICZ, A., ATESHIAN, G. A. & MOW, V. C. 2005. Anisotropy, inhomogeneity, and tension-compression nonlinearity of human glenohumeral cartilage in finite deformation. *Journal of Biomechanics,* 38**,** 799-809.

HUANG, F. S., SIMONIAN, P. T., NORMAN, A. G. & CLARK, J. M. 2004. Effects of small incongruities in a sheep model of osteochondral autografting. *American Journal of Sports Medicine,* 32**,** 1842-1848.

HUNG, C. T., LIMA, E. G., MAUCK, R. L., TAKAI, E., LEROUX, M. A., LU, H. H., STARK, R. G., GUO, X. E. & ATESHIAN, G. A. 2004a. Anatomically shaped osteochondral constructs for articular cartilage repair (vol 36, pg 1853, 2004). *Journal of Biomechanics,* 37**,** 1953-1953.

HUNG, C. T., MAUCK, R. L., WANG, C. C. B., LIMA, E. G. & ATESHIAN, G. A. 2004b. A paradigm for functional tissue engineering of articular cartilage via applied physiologic deformational loading. *Annals of Biomedical Engineering,* 32**,** 35-49.

HUNTLEY, J. S., BUSH, P. G., MCBIRNIE, J. M., SIMPSON, A. H. & HALL, A. C. 2005a. Chondrocyte death associated with human femoral osteochondral harvest as performed for mosaicplasty. *Journal of Bone and Joint Surgery-American Volume,* 87A**,** 351-360.

HUNTLEY, J. S., MCBIRNIE, J. M., SIMPSON, A. H. & HALL, A. C. 2005b. Cutting-edge design to improve cell viability in osteochondral grafts. *Osteoarthritis and Cartilage,* 13**,** 665-671.

HYTTINEN, M. M., HOLOPAINEN, J., VAN WEEREN, P. R., FIRTH, E. C., HELMINEN, H. J. & BRAMA, P. A. J. 2009. Changes in collagen fibril network organization and proteoglycan distribution in equine articular cartilage during maturation and growth. *Journal of Anatomy,* 215**,** 584-591.

IWAKI, H., PINSKEROVA, V. & FREEMAN, M. A. R. 2000. Tibiofemoral movement 1: the shapes and relative movements of the femur and tibia in the unloaded cadaver knee. *Journal of Bone and Joint Surgery-British Volume,* 82B**,** 1189-1195.

IWASAKI, N., KATO, H., ISHIKAWA, J., MASUKO, T., FUNAKOSHI, T. & MINAMI, A. 2009. Autologous Osteochondral Mosaicplasty for Osteochondritis Dissecans of the Elbow in Teenage Athletes. *Journal of Bone and Joint Surgery-American Volume,* 91A**,** 2359-2366.

IWASAKI, N., KATO, H., KAMISHIMA, T., SUENAGA, N. & MINAMI, A. 2007. Donor site evaluation after autologous osteochondral mosaicplasty for cartilaginous lesions of the elbow joint. *American Journal of Sports Medicine,* 35**,** 2096-2100.

JALALI-VAHID, D., JIN, Z. M. & DOWSON, D. 2003a. Elastohydrodynamic lubrication analysis of hip implants with ultra high molecular weight polyethylene cups under transient conditions. *Proceedings of the Institution of Mechanical Engineers Part C-Journal of Mechanical Engineering Science,* 217**,** 767-777.

JALALI-VAHID, D., JIN, Z. M. & DOWSON, D. 2003b. Isoviscous elastohydrodynamic lubrication of circular point contacts with particular

reference to metal-on-metal hip implants. *Proceedings of the Institution of Mechanical Engineers Part J-Journal of Engineering Tribology,* 217**,** 397-402.

JAY, G. D. 1992. CHARACTERIZATION OF A BOVINE SYNOVIAL-FLUID LUBRICATING FACTOR .1. CHEMICAL, SURFACE-ACTIVITY AND LUBRICATING PROPERTIES. *Connective Tissue Research,* 28**,** 71-88.

JAY, G. D., LANE, B. P. & SOKOLOFF, L. 1992. CHARACTERIZATION OF A BOVINE SYNOVIAL-FLUID LUBRICATING FACTOR .3. THE INTERACTION WITH HYALURONIC-ACID. *Connective Tissue Research,* 28**,** 245-255.

JIN, M., FRANK, E. H., QUINN, T. M., HUNZIKER, E. B. & GRODZINSKY, A. J. 2001. Tissue shear deformation stimulates proteoglycan and protein biosynthesis in bovine cartilage explants. *Archives of Biochemistry and Biophysics,* 395**,** 41-48.

JONES, I. L., KLAMFELDT, A. & SANDSTROM, T. 1982. The Effect of Continuous Mechanical Pressure Upon the Turnover of Articular-Cartilage Proteoglycans Invitro. *Clinical Orthopaedics and Related Research***,** 283-289.

JULKUNEN, P., HARJULA, T., IIVARINEN, J., MARJANEN, J., SEPPANEN, K., NARHI, T., AROKOSKI, J., LAMMI, M. J., BRAMA, P. A., JURVELIN, J. S. & HELMINEN, H. J. 2009. Biomechanical, biochemical and structural correlations in immature and mature rabbit articular cartilage. *Osteoarthritis and Cartilage,* 17**,** 1628-1638.

JULKUNEN, P., KIVIRANTA, P., WILSON, W., JURVELIN, J. S. & KORHONEN, R. K. 2007. Characterization of articular cartilage by combining microscopic analysis with a fibril-reinforced finite-element model. *Journal of Biomechanics,* 40**,** 1862-1870.

JURVELIN, J., KIVIRANTA, I., SAAMANEN, A. M., TAMMI, M. & HELMINEN, H. J. 1990. Indentation Stiffness of Young Canine Knee Articular-Cartilage - Influence of Strenuous Joint Loading. *Journal of Biomechanics,* 23**,** 1239-1246.

JURVELIN, J. S., AROKOSKI, J. P. A., HUNZIKER, E. B. & HELMINEN, H. J. 2000. Topographical variation of the elastic properties of articular cartilage in the canine knee. *Journal of Biomechanics,* 33**,** 669-675.

JURVELIN, J. S., BUSCHMANN, M. D. & HUNZIKER, E. B. 1997. Optical and mechanical determination of Poisson's ratio of adult bovine humeral articular cartilage. *Journal of Biomechanics,* 30**,** 235-241.

KATTA, J., JIN, Z., INGHAM, E. & FISHER, J. 2008. Biotribology of articular cartilage-A review of the recent advances. *Medical Engineering & Physics,* 30**,** 1349-1363.

KELLY, C. M. & WILKINS, R. M. 2004. Treatment of benign bone lesions with an injectable calcium sulfate-based bone graft substitute. *Orthopedics,* 27**,** S131-S135.

KELLY, D. J. & PRENDERGAST, P. J. 2005. Mechano-regulation of stem cell differentiation and tissue regeneration in osteochondral defects. *Journal of Biomechanics,* 38**,** 1413-1422.

KHAN, I. M., GILBERT, S. J., SINGHRAO, S. K., DUANCE, V. C. & ARCHER, C. W. 2008. Cartilage Integration: Evaluation of the Reasons for Failure of

Integration During Cartilage Repair. a Review. *European Cells & Materials,* 16**,** 26-39.

KIM, Y. J., BONASSAR, L. J. & GRODZINSKY, A. J. 1995. The Role of Cartilage Streaming Potential, Fluid-Flow and Pressure in the Stimulation of Chondrocyte Biosynthesis During Dynamic Compression. *Journal of Biomechanics,* 28**,** 1055-1066.

KIVIRANTA, P., RIEPPO, J., KORHONEN, R. K., JULKUNEN, P., TOYRAS, J. & JURVELIN, J. S. 2006. Collagen network primarily controls Poisson's ratio of bovine articular cartilage in compression. *Journal of Orthopaedic Research,* 24**,** 690-699.

KOCK, N. B., VAN SUSANTE, J. L. C., BUMA, P., VAN KAMPEN, A. & VERDONSCHOT, N. 2006. Press-fit stability of an osteochondral autograft - Influence of different plug length and perfect depth alignment. *Acta Orthopaedica,* 77**,** 422-428.

KOH, J. L., KOWALSKI, A. & LAUTENSCHLAGER, E. 2006. The effect of angled osteochondral grafting on contact pressure - A biomechanical study. *American Journal of Sports Medicine,* 34**,** 116-119.

KOMISTEK, R. D., KANE, T. R., MAHFOUZ, M., OCHOA, J. A. & DENNIS, D. A. 2005. Knee mechanics: a review of past and present techniques to determine in vivo loads. *Journal of Biomechanics,* 38**,** 215-228.

KOO, S. & ANDRIACCHI, T. P. 2007. A comparison of the influence of global functional loads vs. local contact anatomy on articular cartilage thickness at the knee. *Journal of Biomechanics,* 40**,** 2961-2966.

KORDAS, G., SZABO, J. S. & HANGODY, L. 2005. The effect of drill-hole length on the primary stability of osteochondral drafts in mosaicplasty. *Orthopedics,* 28**,** 401-404.

KORHONEN, R. K., LAASANEN, M. S., TOYRAS, J., RIEPPO, J., HIRVONEN, J., HELMINEN, H. J. & JURVELIN, J. S. 2002a. Comparison of the equilibrium response of articular cartilage in unconfined compression, confined compression and indentation. *Journal of Biomechanics,* 35**,** 903-909.

KORHONEN, R. K., WONG, M., AROKOSKI, J., LINDGREN, R., HELMINEN, H. J., HUNZIKER, E. B. & JURVELIN, J. S. 2002b. Importance of the superficial tissue layer for the indentation stiffness of articular cartilage. *Medical Engineering & Physics,* 24**,** 99-108.

KRISHNAN, R., KOPACZ, M. & ATESHIAN, G. A. 2004. Experimental verification of the role of interstitial fluid pressurization in cartilage lubrication. *Journal of Orthopaedic Research,* 22**,** 565-570.

KRISHNAN, R., MARINER, E. N. & ATESHIAN, G. A. 2005. Effect of dynamic loading on the frictional response of bovine articular cartilage. *Journal of Biomechanics,* 38**,** 1665-1673.

KWAN, M. K., LAI, W. M. & MOW, V. C. 1990. A FINITE DEFORMATION-THEORY FOR CARTILAGE AND OTHER SOFT HYDRATED CONNECTIVE TISSUES .1. EQUILIBRIUM RESULTS. *Journal of Biomechanics,* 23**,** 145-155.

LAASANEN, M. S., TOYRAS, J., KORHONEN, R. K., RIEPPO, J., SAARAKKALA, S., NIEMINEN, M. T., HIRVONEN, J. & JURVELIN, J. S. 2003. Biomechanical properties of knee articular cartilage. *Biorheology,* 40**,** 133-140.

LAPRADE, R. F. & BOTKER, J. C. 2004. Donor-site morbidity after osteochondral autograft transfer procedures. *Arthroscopy,* 20.

LEE, J. B., LEE, S. H., YU, S. M., PARK, J.-C., CHOI, J. B. & KIM, J. K. 2008. PLGA scaffold incorporated with hydroxyapatite for cartilage regeneration. *Surface & Coatings Technology,* 202**,** 5757-5761.

LEITMAN, E. & MORGAN, C. 2005. Chondral Injuries Treated with Osteochondral Autograft Transfer. *In:* CUSHNER, F., NORMAN SCOTT, W. & SCUDERI, G. (eds.) *Surgical Techniques of the Knee.* New York, NY: Thieme Medical Publishers Inc.

LEWIS, P. R. & MCCUTCHEN, C. W. 1959. EXPERIMENTAL EVIDENCE FOR WEEPING LUBRICATION IN MAMMALIAN JOINTS. *Nature,* 184**,** 1285-1285.

LI, G., PARK, S. E., DEFRATE, L. E., SCHUTZER, M. E., JI, L. N., GILL, T. J. & RUBASH, H. E. 2005. The cartilage thickness distribution in the tibiofemoral joint and its correlation with cartilage-to-cartilage contact. *Clinical Biomechanics,* 20**,** 736-744.

LI, K. W., WILLIAMSON, A. K., WANG, A. S. & SAH, R. L. 2001. Growth responses of cartilage to static and dynamic compression. *Clinical Orthopaedics and Related Research***,** S34-S48.

LIEN, S.-M., CHIEN, C.-H. & HUANG, T.-J. 2009. A novel osteochondral scaffold of ceramic-gelatin assembly for articular cartilage repair. *Materials Science and Engineering: C,* 29**,** 315-321.

LIMA, E. G., MAUCK, R. L., HAN, S. H., PARK, S., NG, K. W., ATESHIAN, G. A. & HUNG, C. T. 2004. Functional tissue engineering of chondral and osteochondral constructs. *Biorheology,* 41**,** 577-590.

LIZHANG, J., FISHER, J., JIN, Z., BURTON, A. & WILLIAMS, S. 2011. The effect of contact stress on cartilage friction, deformation and wear. *Proceedings of the Institution of Mechanical Engineers Part H-Journal of Engineering in Medicine,* 225**,** 461-475.

LU, X. L., MOW, V. C. & GUO, X. E. 2009. Proteoglycans and Mechanical Behavior of Condylar Cartilage. *Journal of Dental Research,* 88**,** 244-248.

MABUCHI, K., SAKAI, R., OTA, M. & UJIHIRA, M. 2004. Appropriate radial clearance of ceramic-on-ceramic total hip prostheses to realize squeeze-film lubrication. *Clinical Biomechanics,* 19**,** 362-369.

MAHMOUDIFAR, N. & DORAN, P. M. 2005. Tissue engineering of human cartilage and osteochondral composites using recirculation bioreactors. *Biomaterials,* 26**,** 7012-7024.

MARTIN, I., MIOT, S., BARBERO, A., JAKOB, M. & WENDT, D. 2007. Osteochondral tissue engineering. *Journal of Biomechanics,* 40**,** 750-765.

MARTIN, R. B., BURR, D. B. & SHARKEY, N. A. 1998. *Skeletal Tissue Mechanics,* New York, Springer.

MARZO, J. M. & GURSKE-DEPERIO, J. 2009. Effects of Medial Meniscus Posterior Horn Avulsion and Repair on Tibiofemoral Contact Area and Peak Contact Pressure With Clinical Implications. *American Journal of Sports Medicine,* 37**,** 124-129.

MATTER, H. P., VON GARREL, T., BILDERBEEK, U. & MITTELMEIER, W. 2001. Biomechanical examinations of cancellous bone concerning the influence of duration and temperature of cryopreservation. *Journal of Biomedical Materials Research,* 55**,** 40-44.

MCCULLOCH, P. C., KANG, R. W., SOBHY, M. H., HAYDEN, J. K. & COLE, B. J. 2007. Prospective evaluation of prolonged fresh osteochondral allograft transplantation of the femoral condyle - Minimum 2-year follow-up. *American Journal of Sports Medicine,* 35**,** 411-420.

MINIACI, A., JAMBOR, C. & PETRIGLIANO, F. 2007. Autologous Osteochondral Transfer. *In:* WILLIAMS III, R. (ed.) *Cartilage Repair Strategies.* Totowa, NJ: Humana Press.

MORIYA, T., WADA, Y., WATANABE, A., SASHO, T., NAKAGAWA, K., MAINIL-VARLET, P. & MORIYA, H. 2007. Evaluation of reparative cartilage after autologous chondrocyte implantation for osteochondritis dissecans: histology, biochemistry, and MR imaging. *Journal of Orthopaedic Science,* 12**,** 265-273.

MOW, V. C. & HUNG, C. T. 2001. Biomechanics of Articular Cartilage. *In:* NORDIN, M. & FRANKEL, V. H. (eds.) *Basic Biomechanics of the Musculoskeletal System.* Third ed. Philadelphia: Lippincott Williams & Wilkins.

MOW, V. C., KUEI, S. C., LAI, W. M. & ARMSTRONG, C. G. 1980. Biphasic Creep and Stress-Relaxation of Articular-Cartilage in Compression - Theory and Experiments. *Journal of Biomechanical Engineering-Transactions of the Asme,* 102**,** 73-84.

MOW, V. C. & LAI, W. M. 1980. RECENT DEVELOPMENTS IN SYNOVIAL JOINT BIOMECHANICS. *Siam Review,* 22**,** 275-317.

MOW, V. C., RATCLIFFE, A. & POOLE, A. R. 1992. CARTILAGE AND DIARTHRODIAL JOINTS AS PARADIGMS FOR HIERARCHICAL MATERIALS AND STRUCTURES. *Biomaterials,* 13**,** 67-97.

NEU, C. P., KOMVOPOULOS, K. & REDDI, A. H. 2008. The interface of functional biotribology and regenerative medicine in synovial joints. *Tissue Engineering Part B-Reviews,* 14**,** 235-247.

NORTHWOOD, E. & FISHER, J. 2007. A multi-directional in vitro investigation into friction, damage and wear of innovative chondroplasty materials against articular cartilage. *Clinical Biomechanics,* 22**,** 834-842.

OLIVEIRA, J. M., RODRIGUES, M. T., SILVA, S. S., MALAFAYA, P. B., GOMES, M. E., VIEGAS, C. A., DIAS, I. R., AZEVEDO, J. T., MANO, J. F. & REIS, R. L. 2006. Novel hydroxyapatite/chitosan bilayered scaffold for osteochondral tissue-engineering applications: Scaffold design and its performance when seeded with goat bone marrow stromal cells. *Biomaterials,* 27**,** 6123-6137.

OSHIMA, Y., WATANABE, N., MATSUDA, K. I., TAKENAKA, N., KAWATA, M. & TAKAI, S. 2002. Behavior of graft and host cells in underlying subchondral

bone after transplantation of osteochondral autograft. *Microscopy Research and Technique,* 58**,** 19-24.

OSTERHOFF, G., LOEFFLER, S., STEINKE, H., FEJA, C., JOSTEN, C. & HEPP, P. 2011. Comparative anatomical measurements of osseous structures in the ovine and human knee. *Knee,* 18**,** 98-103.

OSTERMEIER, S., HOLST, M., BOHNSACK, M., HURSCHLER, C., STUKENBORG-COLSMAN, C. & WIRTH, C.-J. 2007. Dynamic measurement of patellofemoral contact pressure following reconstruction of the medial patellofemoral ligament: An in vitro study. *Clinical Biomechanics,* 22**,** 327-335.

PACI, J. M., SCUDERI, M. G., WERNER, F. W., SUTTON, L. G., ROSENBAUM, P. F. & CANNIZZARO, J. P. 2009. Knee Medial Compartment Contact Pressure Increases With Release of the Type I Anterior Intermeniscal Ligament. *American Journal of Sports Medicine,* 37**,** 1412-1416.

PARK, S., HUNG, C. T. & ATESHIAN, G. A. 2004. Mechanical response of bovine articular cartilage under dynamic unconfined compression loading at physiological stress levels. *Osteoarthritis and Cartilage,* 12**,** 65-73.

PARKKINEN, J. J., IKONEN, J., LAMMI, M. J., LAAKKONEN, J., TAMMI, M. & HELMINEN, H. J. 1993. Effects of Cyclic Hydrostatic-Pressure on Proteoglycan Synthesis in Cultured Chondrocytes and Articular-Cartilage Explants. *Archives of Biochemistry and Biophysics,* 300**,** 458-465.

PATIL, S., BUTCHER, W., D'LIMA, D. D., STEKLOV, N., BUGBEE, W. D. & HOENECKE, H. R. 2008. Effect of osteochondral graft insertion forces on chondrocyte viability. *American Journal of Sports Medicine,* 36**,** 1726-1732.

PAUL, J., SAGSTETTER, A., KRINER, M., IMHOFF, A. B., SPANG, J. & HINTERWIMMER, S. 2009. Donor-Site Morbidity After Osteochondral Autologous Transplantation for Lesions of the Talus. *Journal of Bone and Joint Surgery-American Volume,* 91A**,** 1683-1688.

PEARSALL, A. W., TUCKER, J. A., HESTER, R. B. & HEITMAN, R. J. 2004. Chondrocyte viability in refrigerated osteochondral allografts used for transplantation within the knee. *American Journal of Sports Medicine,* 32**,** 125-131.

PERIE, D., IATRIDIS, J. C., DEMERS, C. N., GOSWAMI, T., BEAUDOIN, G., MWALE, F. & ANTONIOU, J. 2006a. Assessment of compressive modulus, hydraulic permeability and matrix content of trypsin-treated nucleus pulposus using quantitative MRI. *Journal of Biomechanics,* 39**,** 1392-1400.

PERIE, D. S., MACLEAN, J. J., OWEN, J. P. & IATRIDIS, J. C. 2006b. Correlating material properties with tissue composition in enzymatically digested bovine annulus fibrosus and nucleus pulposus tissue. *Annals of Biomedical Engineering,* 34**,** 769-777.

PYLAWKA, T. K., WIMMER, M., COLE, B. J., VIRDI, A. S. & WILLIAMS, J. M. 2007. Impaction affects cell viability in osteochondral tissues during transplantation. *J Knee Surg,* 20**,** 105-10.

PYLIOS, T. & SHEPHERD, D. 2004. Prediction of lubrication regimes in wrist implants with spherical bearing surfaces. *J. of Biomechanics,* 37**,** 405-11.

RAGAN, P. M., BADGER, A. M., COOK, M., CHIN, V. I., GOWEN, M., GRODZINSKY, A. J. & LARK, M. W. 1999. Down-regulation of chondrocyte aggrecan and type-II collagen gene expression correlates with increases in static compression magnitude and duration. *Journal of Orthopaedic Research,* 17**,** 836-842.

REDDY, S., PEDOWITZ, D. I., PAREKH, S. G., SENNETT, B. J. & OKEREKE, E. 2007. The morbidity associated with osteochondral harvest from asymptomatic knees for the treatment of osteochondral lesions of the Talus. *American Journal of Sports Medicine,* 35**,** 80-85.

RIEPPO, J., HYTTINEN, M. M., HALMESMAKI, E., RUOTSALAINEN, H., VASARA, A., KIVIRANTA, I., JURVELIN, J. S. & HELMINEN, H. J. 2009. Changes in spatial collagen content and collagen network architecture in porcine articular cartilage during growth and maturation. *Osteoarthritis and Cartilage,* 17**,** 448-455.

ROEMHILDT, M. L., COUGHLIN, K. M., PEURA, G. D., FLEMING, B. C. & BEYNNON, B. D. 2006. Material properties of articular cartilage in the rabbit tibial plateau. *Journal of Biomechanics,* 39**,** 2331-2337.

ROGERS, B. A., MURPHY, C. L., CANNON, S. R. & BRIGGS, T. W. R. 2006. Topographical variation in glycosaminoglycan content in human articular cartilage. *Journal of Bone and Joint Surgery-British Volume,* 88B**,** 1670-1674.

ROHL, L., LINDE, F., ODGAARD, A. & HVID, I. 1997. Simultaneous measurement of stiffness and energy absorptive properties of articular cartilage and subchondral trabecular bone. *Proceedings of the Institution of Mechanical Engineers Part H-Journal of Engineering in Medicine,* 211**,** 257-264.

RYAN, G., PANDIT, A. & APATSIDIS, D. 2008. Stress distribution in the intervertebral disc correlates with strength distribution in subdiscal trabecular bone in the porcine lumbar spine. *Clinical Biomechanics,* 23**,** 859-869.

SCHINAGL, R. M., GURSKIS, D., CHEN, A. C. & SAH, R. L. 1997. Depth-dependent confined compression modulus of full-thickness bovine articular cartilage. *Journal of Orthopaedic Research,* 15**,** 499-506.

SCHMIDT, T. A., GASTELUM, N. S., NGUYEN, Q. T., SCHUMACHER, B. L. & SAH, R. L. 2007. Boundary lubrication of articular cartilage - Role of synovial fluid constituents. *Arthritis and Rheumatism,* 56**,** 882-891.

SCHMITZ, N., LAVERTY, S., KRAUS, V. B. & AIGNER, T. 2010. Basic methods in histopathology of joint tissues. *Osteoarthritis and Cartilage,* 18**,** S113-S116.

SCHOLES, S. C. & UNSWORTH, A. 2000. Comparison of friction and lubrication of different hip prostheses. *Proceedings of the Institution of Mechanical Engineers Part H-Journal of Engineering in Medicine,* 214**,** 49-57.

SHEPHERD, D. E. T. & SEEDHOM, B. B. 1999. Thickness of human articular cartilage in joints of the lower limb. *Annals of the Rheumatic Diseases,* 58**,** 27-34.

SHERWOOD, J. K., RILEY, S. L., PALAZZOLO, R., BROWN, S. C., MONKHOUSE, D. C., COATES, M., GRIFFITH, L. G., LANDEEN, L. K. & RATCLIFFE, A. 2002. A three-dimensional osteochondral composite scaffold for articular cartilage repair. *Biomaterials,* 23**,** 4739-4751.

SHI, L., SIKAVITSAS, V. I. & STRIOLO, A. 2011. Experimental Friction Coefficients for Bovine Cartilage Measured with a Pin-on-Disk Tribometer: Testing Configuration and Lubricant Effects. *Annals of Biomedical Engineering,* 39**,** 132-146.

SHIEH, A. C. & ATHANASIOU, K. A. 2003. Principles of cell mechanics for cartilage tissue engineering. *Annals of Biomedical Engineering,* 31**,** 1-11.

SMITH, R. L., LIN, J., TRINDADE, M. C. D., SHIDA, J., KAJIYAMA, G., VU, T., HOFFMAN, A. R., VAN DER MEULEN, M. C. H., GOODMAN, S. B., SCHURMAN, D. J. & CARTER, D. R. 2000. Time-dependent effects of intermittent hydrostatic pressure on articular chondrocyte type II collagen and aggrecan mRNA expression. *Journal of Rehabilitation Research and Development,* 37**,** 153-161.

SOLTZ, M. A. & ATESHIAN, G. A. 2000. Interstitial fluid pressurization during confined compression cyclical loading of articular cartilage. *Annals of Biomedical Engineering,* 28**,** 150-159.

SUH, J. K., LI, Z. F. & WOO, S. L. Y. 1995. DYNAMIC BEHAVIOR OF A BIPHASIC CARTILAGE MODEL UNDER CYCLIC COMPRESSIVE LOADING. *Journal of Biomechanics,* 28**,** 357-364.

SWANN, D. A., HENDREN, R. B., RADIN, E. L., SOTMAN, S. L. & DUDA, E. A. 1981. THE LUBRICATING ACTIVITY OF SYNOVIAL-FLUID GLYCOPROTEINS. *Arthritis and Rheumatism,* 24**,** 22-30.

SWANN, D. A., SILVER, F. H., SLAYTER, H. S., STAFFORD, W. & SHORE, E. 1985. THE MOLECULAR-STRUCTURE AND LUBRICATING ACTIVITY OF LUBRICIN ISOLATED FROM BOVINE AND HUMAN SYNOVIAL-FLUIDS. *Biochemical Journal,* 225**,** 195-201.

TAPPER, J. E., FUKUSHIMA, S., AZUMA, H., THORNTON, G. M., RONSKY, J. L., SHRIVE, N. G. & FRANK, C. B. 2006. Dynamic in vivo kinematics of the intact ovine stifle joint. *Journal of Orthopaedic Research,* 24**,** 782-792.

TAYLOR, W. R., EHRIG, R. M., HELLER, M. O., SCHELL, H., SEEBECK, P. & DUDA, G. N. 2006. Tibio-femoral joint contact forces in sheep. *Journal of Biomechanics,* 39**,** 791-798.

TAYLOR, W. R., POEPPLAU, B. M., KOENIG, C., EHRIG, R. M., ZACHOW, S., DUDA, G. N. & HELLER, M. O. 2011. The Medial-Lateral Force Distribution in the Ovine Stifle Joint during Walking. *Journal of Orthopaedic Research,* 29**,** 567-571.

TEO, J. C. M., SI-HOE, K. M., KEH, J. E. L. & TEOH, S. H. 2006. Relationship between CT intensity, micro-architecture and mechanical properties of porcine vertebral cancellous bone. *Clinical Biomechanics,* 21**,** 235-244.

THAMBYAH, A. 2007. Contact stresses in both compartments of the tibiofemoral joint are similar even when larger forces are applied to the medial compartment. *Knee,* 14**,** 336-338.

THAMBYAH, A., GOH, J. C. H. & DAS DE, S. 2005. Contact stresses in the knee joint in deep flexion. *Medical Engineering & Physics,* 27**,** 329-335.

THAUNAT, M., COUCHON, S., LUNN, J., CHARROIS, O., FALLET, L. & BEAUFILS, P. 2007. Cartilage thickness matching of selected donor and

recipient sites for osteochondral autografting of the medial femoral condyle. *Knee Surgery Sports Traumatology Arthroscopy,* 15**,** 381-386.

TIBESKU, C. O., SZUWART, T., KLEFFNER, T. O., SCHLEGEL, P. M., JAHN, U. R., VAN AKEN, H. & FUCHS, S. 2004. Hyaline cartilage degenerates after autologous osteochondral transplantation. *Journal of Orthopaedic Research,* 22**,** 1210-1214.

TREME, G. & MILLER, M. D. 2008. Autograft Osteochondral Transfer. *Operative Techniques in Sports Medicine,* 16**,** 81-88.

UDOFIA, I. J. & JIN, Z. M. 2003. Elastohydrodynamic lubrication analysis of metal-on-metal hip-resurfacing prostheses. *Journal of Biomechanics,* 36**,** 537-544.

VIZESI, F., OLIVER, R., SMITHAM, P., GOTHELF, T., YU, Y. & WALSH, W. R. 2007. Influence of surgical preparation on the in-vivo response of osteochondral defects. *Proceedings of the Institution of Mechanical Engineers Part H-Journal of Engineering in Medicine,* 221**,** 489-498.

VON RECHENBERG, B., AKENS, M. K., NADLER, D., BITTMANN, P., ZLINSZKY, K., KUTTER, A., POOLE, A. R. & AUER, J. A. 2003. Changes in subchondral bone in cartilage resurfacing - an experimental study in sheep using different types of osteochondral grafts. *Osteoarthritis and Cartilage,* 11**,** 265-277.

VON WACHENFELT, H., NILSSON, C. & PINZKE, S. 2010. Gait and force analysis of provoked pig gait on clean and fouled rubber mat surfaces. *Biosystems Engineering,* 106**,** 86-96.

VON WACHENFELT, H., PINZKE, S. & NILSSON, C. 2009. Gait and force analysis of provoked pig gait on clean and fouled concrete surfaces. *Biosystems Engineering,* 104**,** 534-544.

VUNJAK-NOVAKOVIC, G., MEINEL, L., ALTMAN, G. & KAPLAN, D. 2005. Bioreactor cultivation of osteochondral grafts. *Orthod Craniofac Res,* 8**,** 209-18.

WANG, C. C. B., CHAHINE, N. O., HUNG, C. T. & ATESHIAN, G. A. 2003. Optical determination of anisotropic material properties of bovine articular cartilage in compression. *Journal of Biomechanics,* 36**,** 339-353.

WANG, C. J. 2002. Treatment of focal articular cartilage lesions of the knee with autogenous osteochondral grafts - A 2-to 4-year follow-up study. *Archives of Orthopaedic and Trauma Surgery,* 122**,** 169-172.

WANG, F. C., BROCKETT, C., WILLIAMS, S., UDOFIA, I., FISHER, J. & JIN, Z. M. 2008. Lubrication and friction prediction in metal-on-metal hip implants. *Physics in Medicine and Biology,* 53**,** 1277-1293.

WANG, F. C., LIU, F. & JIN, Z. M. 2004. A general elastohydrodynamic lubrication analysis of artificial hip joints employing a compliant layered socket under steady state rotation. *Proceedings of the Institution of Mechanical Engineers Part H-Journal of Engineering in Medicine,* 218**,** 283-291.

WARD, S. R. & POWERS, C. M. 2004. The influence of patella alta on patellofemoral joint stress during normal and fast walking. *Clinical Biomechanics,* 19**,** 1040-1047.

WAYNE, J. S., BRODRICK, C. W. & MUKHERJEE, N. 1998. Measurement of articular cartilage thickness in the articulated knee. *Annals of Biomedical Engineering,* 26**,** 96-102.

WENDT, D., JAKOB, M. & MARTIN, I. 2005. Bioreactor-based engineering of osteochondral grafts: from model systems to tissue manufacturing. *Journal of Bioscience and Bioengineering,* 100**,** 489-494.

WHITESIDE, R. A., BRYANT, J. T., JAKOB, R. P., MAINIL-VARLET, P. & WYSS, U. P. 2003. Short-term load bearing capacity of osteochondral autografts implanted by the mosaicplasty technique: an in vitro porcine model. *Journal of Biomechanics,* 36**,** 1203-1208.

WHITESIDE, R. A., JAKOB, R. P., WYSS, U. P. & MAINIL-VARLET, P. 2005. Impact loading of articular cartilage during transplantation of osteochondral autograft. *Journal of Bone and Joint Surgery-British Volume,* 87B**,** 1285-1291.

WILLETT, T. L., WHITESIDE, R., WILD, P. M., WYSS, U. P. & ANASTASSIADES, T. 2005. Artefacts in the mechanical characterization of porcine articular cartilage due to freezing. *Proceedings of the Institution of Mechanical Engineers Part H-Journal of Engineering in Medicine,* 219**,** 23-29.

WILLIAMS, G. M., DILLS, K. J., FLORES, C. R., STENDER, M. E., STEWART, K. M., NELSON, L. M., CHEN, A. C., MASUDA, K., HAZELWOOD, S. J., KLISCH, S. M. & SAH, R. L. 2010. Differential regulation of immature articular cartilage compressive moduli and Poisson's ratios by in vitro stimulation with IGF-1 and TGF-beta 1. *Journal of Biomechanics,* 43**,** 2501-2507.

WILLIAMS, J. 2005. *Engineering Tribology*, Cambridge University Press.

WILLIAMS, R. J. 2006. Articular Cartilage Repair: Clinical Approach and Decision Making. *Operative Techniques in Orthopaedics,* 16**,** 218-226.

WILLIAMS, R. J., RANAWAT, A. S., POTTER, H. G., CARTER, T. & WARREN, R. F. 2007. Fresh stored allografts for the treatment of osteochondral defects of the knee. *Journal of Bone and Joint Surgery-American Volume,* 89A**,** 718-726.

WILLIAMS, S. K., AMIEL, D., BALL, S. T., ALLEN, T., WONG, V. W., CHEN, A. C., SAH, R. L. & BUGBEE, W. D. 2003. Prolonged storage effects on the articular cartilage of fresh human osteochondral allografts. *Journal of Bone and Joint Surgery-American Volume,* 85A**,** 2111-2120.

WILLIAMSON, A. K., CHEN, A. C. & SAH, R. L. 2001. Compressive properties and function-composition relationships of developing bovine articular cartilage. *Journal of Orthopaedic Research,* 19**,** 1113-1121.

WILSON, N. A., MAZAHERY, B. T., KOH, J. L. & ZHANG, L.-Q. 2010. Effect of bracing on dynamic patellofemoral contact mechanics. *Journal of Rehabilitation Research and Development,* 47**,** 531-541.

WONG, M., PONTICIELLO, M., KOVANEN, V. & JURVELIN, J. S. 2000. Volumetric changes of articular cartilage during stress relaxation in unconfined compression. *Journal of Biomechanics,* 33**,** 1049-1054.

WU, J. Z., HERZOG, W. & EPSTEIN, M. 1998. Articular joint mechanics with biphasic cartilage layers under dynamic loading. *Journal of Biomechanical Engineering-Transactions of the Asme,* 120**,** 77-84.

YEW, A., UDOFIA, I., JAGATIA, M. & JIN, Z. M. 2004. Analysis of elastohydrodynamic lubrication in McKee-Farrar metal-on-metal hip joint replacement. *Proceedings of the Institution of Mechanical Engineers Part H-Journal of Engineering in Medicine,* 218**,** 27-34.

ZASLAV, K., COLE, B., BREWSTER, R., DEBERARDINO, T., FARR, J., FOWLER, P. & NISSEN, C. 2009. A Prospective Study of Autologous Chondrocyte Implantation in Patients With Failed Prior Treatment for Articular Cartilage Defect of the Knee Results of the Study of the Treatment of Articular Repair (STAR) Clinical Trial. *American Journal of Sports Medicine,* 37**,** 42-55.

APPENDIX A – Comparative Features of the Porcine Knee

Introduction

Experimentation on ostehochondral tissues throughout this thesis were performed on tissues excised from porcine knees. Hence, it worth discussing some of the features of the porcine knee and how they compare to other animal models such as the ovine model and more importantly, the human knee. To begin with, a study will be performed measuring the dimensions of a number of key anatomical features. These will then be discussed with regard to human knee joints and then the discussion further extended to include other important parameters such as joint load and kinematics.

Methods

Six knee joints were harvested from 6-8 month old female pigs 5 days after slaughter. Prior to dissection, the animal carcass remained chilled at 4°C, keeping the joint capsule intact and maintaining the sterility of the joint. The joint capsule was opened to expose the articular surfaces of the joint. The patellar tendon was transected immediately prior to its insertion point on the tibial tuberosity and the fat pad behind it removed. The medial, lateral and cruciate ligaments were transected along with any remaining joint capsule so as to separate the femoral and tibial potions of the joint. The meniscus, transected joint ligaments, joint capsule and any other excess soft tissue was removed to leave the condyles and patellofemoral groove of the femur, in addition to the tibial plateau of the tibia. All exposed areas were cleaned via irrigation using phosphate buffered saline (PBS).

Key anatomical features of the femoral condyles, patellofemoral groove and tibial plateau were then measuring using Vernier callipers in accordance with techniques established by Osterhoff et al. for human and ovine knee joints (Osterhoff et al., 2011). These anatomical features comprised of the following:

- Epicondylar width (ECW),
- Lateral condyle width (LCW),
- Medial condyle width (MCW),
- Intercondylar width (ICW),
- Troclear width (TW),
- Intercondylar height (ICH),
- Anterior-posterior tibial width at the plateau (APTW),
- Medial-lateral tibial width at the plateau (MLTW).

The results were tabulated and compared to similar gross values for these features in human and ovine knees published by Osterhoff et al. (Osterhoff et al., 2011). Ratios were calculated between species for each feature to compare feature sizes relative to one another. Finally, aspect ratios were calculated for the femoral condyles (ICW*100/ECW) and the tibial plateau (MLTW*100/APTW) and compared to human and ovine data.

Unless otherwise specified, all statistical analyses in appendix A were carried out using statistical software (Minitab^{TM}, v.16). A student t-test was used to investigate significance between any two groups if so desired. A P-value of <0.01 was considered to be statistically significant.

Results

Table A-1 presents the gross values of the measurements taken from porcine knee joints against human and ovine data published by Osterhoff et al. (Osterhoff et al., 2011). Additionally, the ratios between each of the three species groups are presented for each anatomical feature. It is apparent first of all that the dimensions of both animal models are less than the human knee for each recorded feature. For the most part, based on the ovine/human ratios, the ovine model appears to be a two-thirds scaled model of the human knee. The porcine model appears simply to be a slightly larger version of the

ovine model for most anatomical features (ovine/porcine ratios ranging from 0.77-0.87) bar the intercondylar height (1.22).

Table A-1. The results of measurements made to anatomical features of the porcine tibiofemoral joint compared against those made by Osterhoff et al. (Osterhoff et al., 2011).

	Human	Ovine	Porcine	Ovine/Human	Porcine/Human	Ovine/Porcine
ECW	81.2 (6.2)	47.2 (1.8)	58.6 (1.2)	0.58	0.72	0.81
LCW	29.7 (3.0)	20.1 (1.8)	23.2 (0.6)	0.68	0.78	0.87
MCW	29.1 (2.9)	18.1 (1.6)	23.6 (1.0)	0.62	0.81	0.77
ICW	19.9 (3.4)	10.8 (1.2)	13.1 (0.5)	0.54	0.66	0.82
TW	44.4 (5.1)	21.9 (1.5)	29.6 (0.8)	0.49	0.67	0.74
ICH	24.9 (4.4)	13.9 (3.4)	11.4 (1.6)	0.56	0.46	1.22
APTW	52.0 (3.7)	21.5 (1.9)	42.2 (2.7)	0.63	0.81	0.78
MLTW	76.4 (5.4)	14.6 (1.4)	61.9 (2.7)	0.68	0.81	0.84

The results from the condylar and tibial aspect ratio calculations (Table A-2) indicate that no statistical difference is found between all three groups ($P>0.01$ in all cases). In this respect, it appears overall that the porcine model appears to be slightly more representative of the human knee joint. Although the porcine condylar aspect ratio is slightly lower than the ovine compared to humans (0.91 vs. 0.93), the tibial aspect ratio is far closer (0.99 vs. 1.10).

Table A-2. The calculated condylar aspect ratios (CAR) & tibial aspect ratios (TAR) of the porcine knee joint compared against ovine and human data published by Osterhoff et al. (Osterhoff et al., 2011)

	Human	Ovine	Porcine	Ovine/Human	Porcine/Human	Ovine/Porcine
CAR	24.6 (3.8)	23.0 (2.6)	22.4 (0.9)	0.93	0.91	1.03
TAR	147.4 (9.3)	162.2 (29.4)	146.9 (8.8)	1.10	0.99	1.10

Discussion

The results of this study indicate that the porcine knee joint, like the ovine knee joint, represents a scaled version of the human knee joint. However, it is far from being a perfectly scaled model. The measured porcine/human feature ratios ranged from approximately 0.7-0.8 for seven of the eight measured features (Table A-1). The remaining feature, the intercondylar height, had a ratio of merely 0.49. However, this is unlikely to be significant in altering the mechanics to such a degree that joint mechanics would alter. More globally speaking, the results of the condylar and tibial aspect ratios were quite encouraging with ratios of 0.91 and 0.99 respectively (Table A-2). This would seem to indicate that the porcine knee model is similar in many respects to human knees if only based on anthrometrical data describing its shape.

However, it is important to remember that this animal is a quadruped and as such may have joint forces and kinematics that are quite different from humans. Unfortunately, a literature review revealed there were sparse studies which have analysed the kinematics of the porcine knee joint. In fact, the only reasonable studies of relevance found were more concerned about the friction and slipping of the animals on different types of flooring (von Wachenfelt et al., 2010, von Wachenfelt et al., 2009). Hence, in the absence of this data, pig kinematics will be assumed to be akin to sheep. This may not be such a stretch given that both animals are both quadrupeds and possess very similar knee joints in terms of the size of their anatomical features (Table A-1).

The joint forces in the tiobiofemoral compartment of the human knee can be expected to peak at approximately 2 to 3 times body weight throughout normal gait (Thambyah et al., 2005). In the patellofemoral joint, they can be expected to reach at least body weight (Ward and Powers, 2004). Although there appears to be no studies examining the joint reaction force in the patellofemoral compartment in sheep, there are however studies that quote the joint forces in the tibiofemoral compartment at having peak values that exceed 2 times body weight (Taylor et al., 2006, Taylor et al., 2011). Given the scaled size of

the knee joint, these values of tibiofemoral joint forces appear to be reasonable enough to be interpreted as a model of the human joint.

It is generally accepted that the periodic gait cycle during walking in humans is approximately 1Hz (i.e. one combined stance and swing phase per second). Hence, repetitive joint contact forces within the human knee occur at a frequency of 1Hz. Furthermore, approximately 60% of the gait cycle is accounted for by the stance phase and the remaining 40% by the swing phase (Ward and Powers, 2004). In a study examining the gait cycle of three different age categories of sheep, the length of the gait cycle in the hind limbs was found to be consistently in the region of 0.8 seconds for all ages (Agostinho et al., 2012). Again, this matches the previously mentioned scaling factor against humans for joint dimensions and forces. Furthermore, the percentages of the gait cycle split into stance and swing phase were found to be 60 & 40% respectively.

However, there does appear to be variations in the flexion and extension patterns of the knees between sheep and humans. Typically, the knee flexion angle varies between 0 and 20 degrees in sinusoidal manner throughout the stance phase in humans. This then continues in one smooth peak from 20 to 60 and back to 0 degrees in the swing phase (Ward and Powers, 2004). In sheep this flexion/extension profile of the knee is notably different for two main reasons. The first of these is that there is an initial offset of 30-40 degrees in the flexion angle of sheep (Cottrell et al., 2008, Darcy et al., 2008, Tapper et al., 2006). That is to say sheep knees are already flexed by an initial extra 30-40 degrees compared to human knees. Secondly, the shape of the flexion/extension profile during the stance phase is different (Cottrell et al., 2008, Darcy et al., 2008, Tapper et al., 2006). The flexion angle rises from approximately 40 to 60 and back to 40 degrees in one smooth peak rather than a two peaked sinusoidal pattern. However, the change of the flexion angle during the swing phase is very similar to humans, albeit at a 40 degree offset.

It has already been mentioned that the length of the stance and swing phases are in sheep and humans are comparable. However, due to the differences in the flexion/extension pattern in the stance phase, it is likely that the joint rotation speeds are different. Conversely, as the flexion/extension pattern is very similar in the swing phase and operating over the same flexion angle range (even if at an offset), it may be deduced the joint rotations speed during this phase are comparable to humans.

No animal model is capable of completely representing the human condition, whether it is the knee joint or any other facet. However, there appears to be enough evidence detailing the porcine knee as being representative enough of its human equal to justify its use. There will be differences, as mentioned above, and these will be highlighted in due respect to any study performed. One important difference not discussed in this section is the maturity of the porcine model. However, this will be discussed in detail in the chapters of the main body of the thesis.

APPENDIX B – Derivation of Expression for Radial Strain

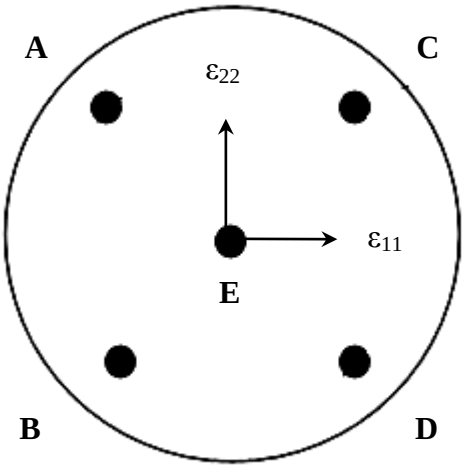

CAMERA MARKER SYSTEM

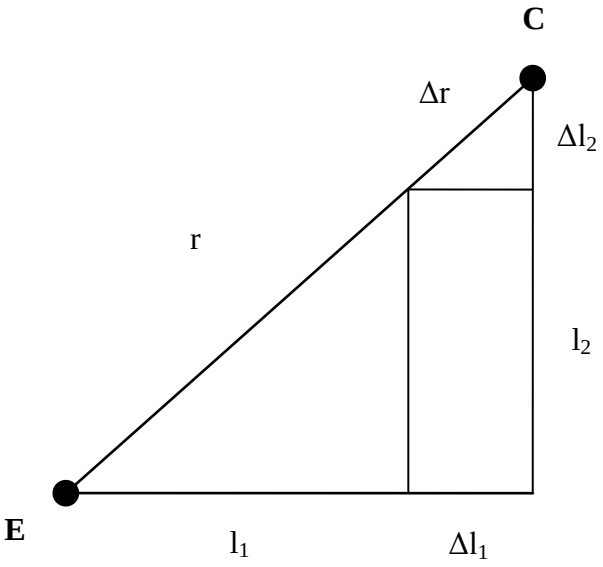

$$\varepsilon_{rr} = \frac{\Delta_r}{r}$$

$$\varepsilon_{11} = \frac{\Delta l_1}{l_1}$$

$$\varepsilon_{22} = \frac{\Delta l_2}{l_2}$$

$$\Delta r^2 = \Delta l_1^2 + \Delta l_2^2$$

$$r^2 = l_1^2 + l_2^2$$

$$\Delta l_1^2 = \varepsilon_{11}^2 l_1^2$$

$$\Delta l_2^2 = \varepsilon_{22}^2 l_2^2$$

Originally square ⇒

$$l_1 = l_2 = l$$

$$\varepsilon_{rr}^2 = \frac{\Delta l_1^2 + \Delta l_2^2}{l_1^2 + l_2^2}$$

$$\varepsilon_{rr}^2 = \frac{\varepsilon_{11}^2 l_1^2 + \varepsilon_{22}^2 l_2^2}{l_1^2 + l_2^2}$$

$$\varepsilon_{rr}^2 = \frac{\varepsilon_{11}^2 l_1^2 + \varepsilon_{22}^2 l_2^2}{2l^2}$$

$$\varepsilon_{rr}^2 = \frac{l^2(\varepsilon_{11}^2 + \varepsilon_{22}^2)}{2l^2}$$

$$\varepsilon_{rr} = \sqrt{\frac{(\varepsilon_{11}^2 + \varepsilon_{22}^2)}{2}}$$

APPENDIX C – Elastohydrodynamic Calculations

The following is based on theoretical predictions made by Forster and Fisher (Forster and Fisher, 1999).

(a) Squeeze film (for stationary loading periods)

The squeeze film thickness (h) is given by the following;

$$h = a^2\sqrt{\frac{3\pi\eta}{4Wt}} \qquad \textbf{Equation C-1}$$

where;
η = viscosity of the lubricant (Pa.s)
W = normal load (N)
t = squeeze film time (s)
a = contact radius (m)

Parameters chosen were based on constructing a best possible scenario. (i.e. lowest load & lowest loading time) For this study η of PBS was taken as 0.001Pa.s, W = 0.961, t = 300s, a = 0.0035m.

$\Rightarrow h$ = 0.035μm

(b) Minimum film thickness for entraining action

The cartilage disc is approximated to a square pad such that the length of the square, L, was such that $L^2 = \pi r^2$.

The minimum film thickness (h_{min}) is given by;

$$h_{\min} = \sqrt{0.071(\frac{\eta u L}{W})} * L$$ **Equation C-2**

where;

η = viscosity of the lubricant (Pa.s)

W = normal load (N)

u = sliding velocity (m/s)

$L = \sqrt{\pi r^2}$ (m)

Again parameters chosen were based on constructing a best possible scenario. (i.e. lowest load & highest sliding velocity) For this study η of PBS was taken as 0.001Pa.s, W = 0.961, u = 0.003m/s, a = 0.0035m.

$\Rightarrow h_{min}$ = 0.23μm

APPENDIX D – Hydrodynamic Test Rig: Version 1

Introduction

This section shall detail the design of an earlier version (version 1) of the hydrodynamic test rig discussed in chapter 8. Furthermore, a feasibility study and the results thereof are also presented, followed by a discussion highlighting the weaknesses of the sytem and how these could possibly be overcome in the improved version of the test rig.

Methods

Version 1 of the hydrodynamic test rig is shown in figure D-1a. This device pre-existed the beginning of this studentship, but was deemed as an appropriate starting point in order to familiarise oneself to working with such systems. The apparatus consisted of a solid stainless steel shaft (or journal) located between two semi-cylindrical Perspex bushings which were machined to mate rigidly at a split-line so as to encompass the entire solid journal. The annular space created was filled with glycerol to act as a lubricating agent. The journal was supported at either end by simple rotary bearings housed in aluminium blocks and linked in series to a servomotor to provide input rotation speed.

The journal itself was not located concentrically within the bushings, but was in fact offset vertically so as to almost contact the upper bushing. The intention was to create a reducing space for the fluid to flow through, with the minimum gap directly on the journals vertical line of centre (figure D-1b). As a consequence of this, it was proposed that a fluid film and hydrodynamic pressure would be created to balance any applied load.

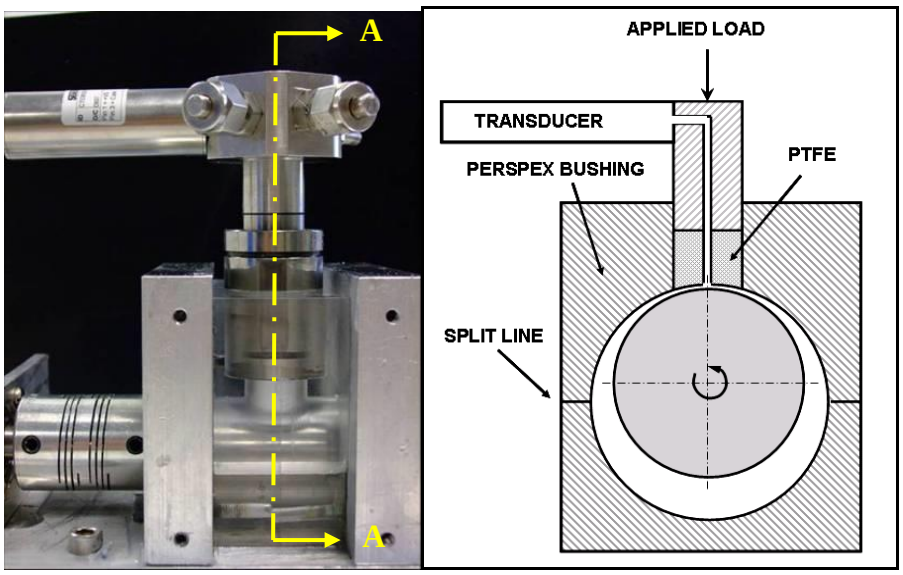

(a) **(b)**

Figure D-1. (a) Test apparatus used, (b) schematic of section A-A.

A bore was located centrally in the upper bushing to accommodate a PTFE tipped insert, specially machined to match the inner profile of the bushing. A conduit existed within this insert linking the fluid interface at the minimum gap to an external 20bar pressure transducer (Sensortechnics GmbH, Puchheim, Germany). As the journal rotated, load could be applied to the insert from above and excite pressure within the system which was measurable via the voltage produced by the transducer. Although this test rig may have been simple in design and application, it nevertheless should promote an understanding of the scale of pressures that are achievable using such a set-up.

Load was applied to the insert by the careful placement of calibration weights on its outer end. Weight was applied in 0.5kg intervals up to 3kg. 2kg was then added, with 2.5kg additions subsequently applied to reach 25kg, approximately a third of body weight. This was deemed an appropriate watershed for device assessment. This process was performed for four journal speeds, 1, 1.5, 2 and 2.5Rev/s. Each test cycle was repeated twice for statistical purposes.

Elastohydrodynamic lubrication (EHL) of elliptical conjunctions was first applied to low elastic modulus materials (soft EHL) by Hamrock and Dowson (Hamrock and Dowson, 1978). A least squares fit of experimental data was used to obtain the following formula for minimum film thickness;

$$H_{\min} = 7.43U^{0.65}W^{-0.21}(1-0.85EXP^{-0.31k}) \qquad \textbf{Equation D-1}$$

Where;

H_{min} = Dimensionless minimum film thickness,

U = Dimensionless speed parameter,

W = Dimensionless load parameter,

k = Ellipticity parameter.

Furthermore,

$$U = \frac{\mu u}{E' R_x},\ W = \frac{w_z}{E' R_x^2} \text{ and } k = \frac{D_y}{D_x}$$

Where,

μ = Absolute viscosity of lubricant,

u = Entraining mean velocity, given by $u = \frac{u_A + u_B}{2}$

Where,

u_A and u_B are the velocities of the inner and outer conjunctions respectively.

E' = Effective elastic modulus, given by $E' = (\frac{1-\nu_A^2}{E_A} + \frac{1-\nu_B^2}{E_B})^{-1}$

Where,

υ_A and υ_B are the Poisson ratios of the inner and outer conjunctions respectively,

E_A and E_B are the elastic modulii of the inner and outer conjunctions respectively,

R_x = Effective radius, given by $R_x = (\frac{1}{R_A} + \frac{1}{R_B})^{-1}$

Where,

R_A and R_B are the radii of the inner and outer conjunctions respectively.

w_z = Applied load,

D_y = Elliptical contact diameter in transverse direction,

D_x = Elliptical contact diameter in the direction of entraining motion.

This has been an approach used by many previous authors to determine the film thicknesses of various hip prostheses (Jalali-Vahid et al., 2003b, Scholes and Unsworth, 2000, Udofia and Jin, 2003, Wang et al., 2004, Yew et al., 2004), in addition to wrist prostheses (Pylios and Shepherd, 2004) and various other types of bearing (Hamrock et al., 2004, Hamrock and Dowson, 1978). In all of these cases, the ellipticity factor k was chosen to be 1, in accordance with prosthesis design. However, based on the design of the test apparatus discussed in this paper, an ellipticity factor of k = 19/30 was chosen (diameter of PTFE insert divided by diameter of steel journal). Values for the radii mentioned were found by measuring apparatus geometry. All other parameters where found by choosing them as set input conditions such as journal velocity or applied load (discussed previously), determining the lubricant viscosity (section 7.2.2.1) and by estimating material properties ($E_A = E_{STEEL}$ = 213GPa, $E_B = E_{PTFE}$ = 0.73GPa, $\upsilon_A = \upsilon_{STEEL}$ = 0.3, $\upsilon_B = \upsilon_{PTFE}$ = 0.47).

The lubrication regime of a system is determined via the dimensionless film parameter, which is expressed as follows;

$$\Lambda = \frac{h_{\min}}{(Ra_A^2 + Ra_B^2)^{0.5}} \qquad \textbf{Equation D-2}$$

Where,

Λ = Film parameter,

h_{min} = Minimum film thickness,

Ra_A & Ra_B are the surface roughness of the inner and outer conjunctions respectively.

This formulation again has been used readily in the analysis of implanted prostheses. The film parameter can define four important lubrication regimes, useful for assessing how affective a device is in providing lubrication for any particular load scenario (Hamrock et al., 2004). The regimes and the range of Λ required for each of these regimes are as follows;

- Boundary lubrication, $\Lambda < 1$
- Partial lubrication, $1 < \Lambda < 5$
- Elastohydrodynamic lubrication, $3 < \Lambda < 10$
- Hydrodynamic lubrication, $5 < \Lambda < 100$

The value of h_{min} was determined from the previously mentioned calculation of minimum film thickness (equation D-1), whereas the values of Ra_A and Ra_B were estimated ($Ra_A = Ra_{STEEL} \approx 0.05$ microns, $Ra_B = Ra_{PTFE} \approx 1$ micron).

Results

Figure D-2 presents a graph of the fluid film parameter (lambda ratio) against load. As load increases it is observed that the film parameter decreases steadily in a non-linear fashion. This is a tread witnessed for all rotation velocities, with higher film parameter values for greater rotation velocities. In addition, it is also apparent that the rate of film parameter decrease with load is greater at with larger rotation velocities. The reduction in film parameter values ranges from 0.37-0.23 for 2.5Rev/s, to 0.20-0.12 for 1Rev/s.

Figure D-3 presents a graph of the fluid film parameter against journal velocity, and highlights a non-linear increase of the film parameter as the velocity increases. This is witnessed for all applied load scenarios, but film parameter values are comparatively higher at lower loads rather than higher. Furthermore, it is witnessed that the rate of increase of the film parameter with velocity is higher at these lower loads. The increase in film parameter values ranges from 0.17-0.32 for 50N, to 0.12-0.23 for 250N. The

fluid film parameter at all times in both figure D-2 and D-3 is less than 1 indicating boundary lubrication.

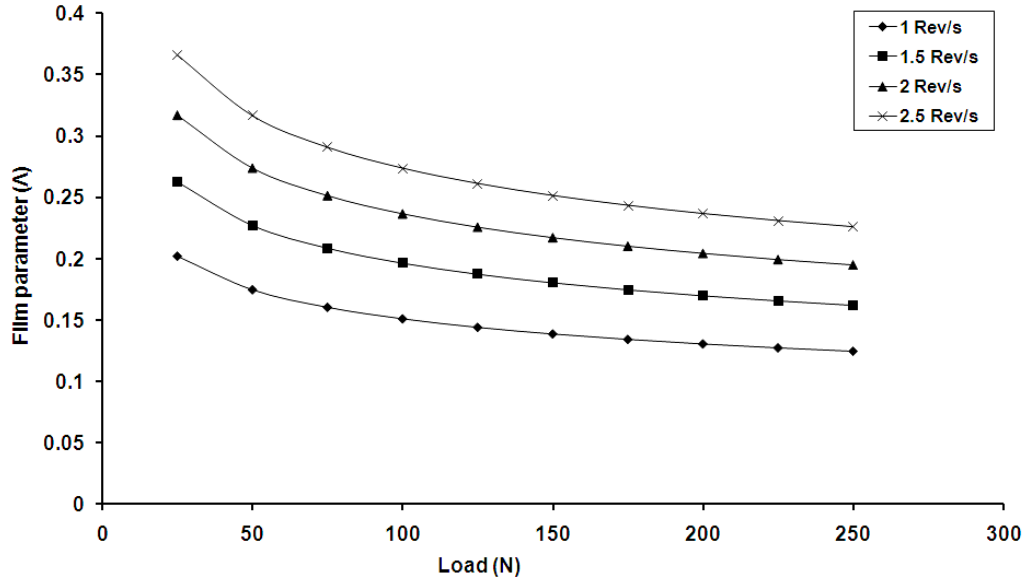

Figure D-2. Calculated film parameter vs. applied load. Film parameter decreases steadily in a non-linear fashion with increased load.

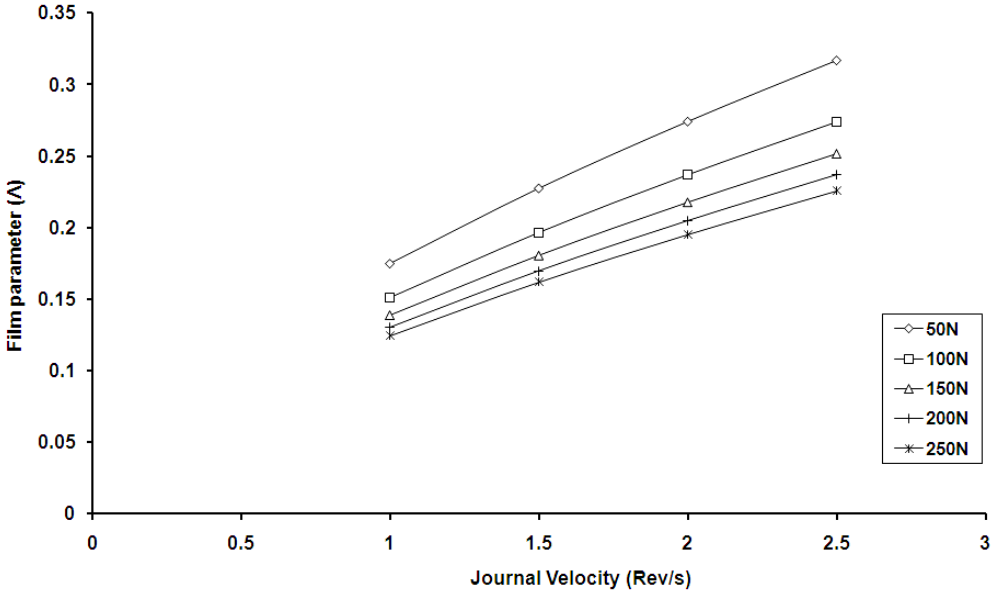

Figure D-3. Calculated film parameter vs. journal velocity. Film parameter increases steadily in a non-linear fashion with increased journal velocity

Consider the data presented in figure D-4. It is observed that the pressure rises steadily for a period before decreasing at a lower rate, and that this occurs for all rotation velocities. This is not an expected event given the low loads applied. Pressure is expected to rise continuously (i.e. inversely with the film parameter). Increasing the rotation velocity appears to prolong this event, as the peak pressures drift along the x-axis, but not only to a minor extent. Peak pressures range from 0.096MPa for 1Rev/s up to 0.184MPa for 2.5Rev/s. Figure D-5 plots the experimentally recorded pressure against journal rotation velocity for the various applied loads. Pressure seems to increase linearly with increasing rotation velocity. However, the pressure differences between successive load scenarios increases only between 50-100N and then decreases for all others (100-150N, 150-200N etc.). The unexpected pressure drop first witnessed in figure D-4 is evident once again.

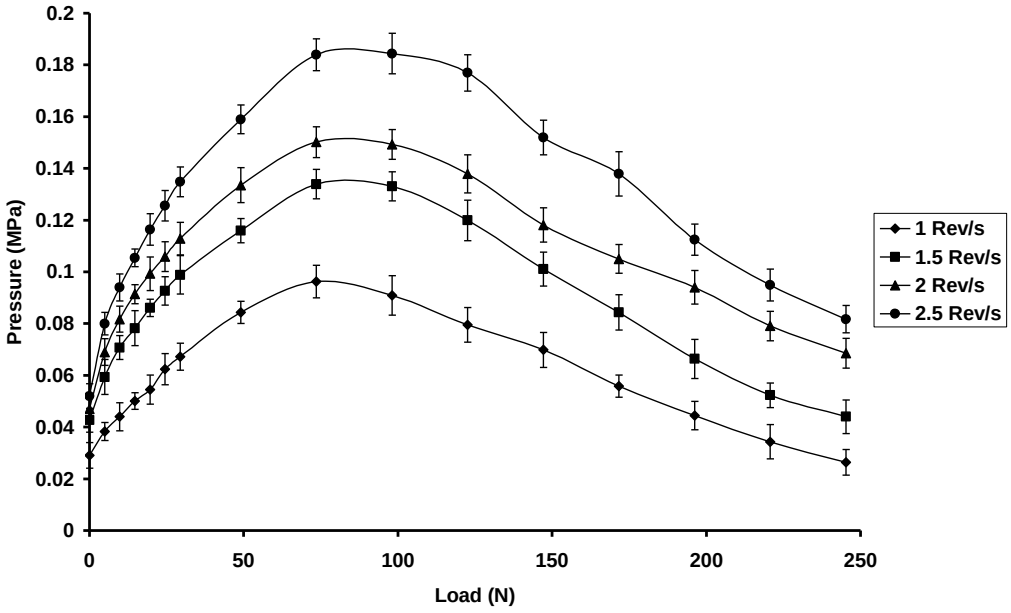

Figure D-4. Experimental pressures recorded vs. load using version 1 test rig. Results shown as mean ± SD (n=3).

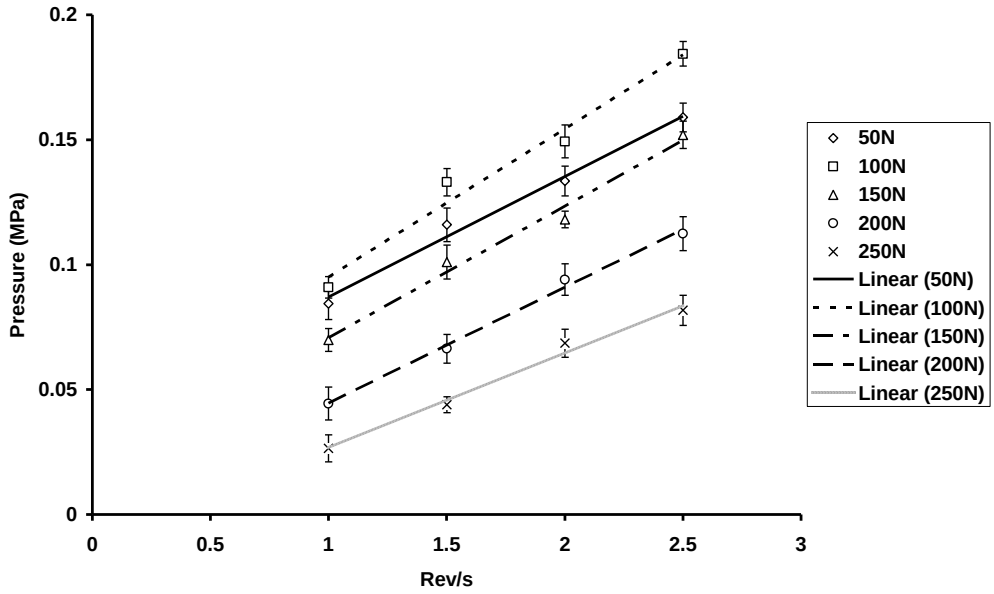

Figure D-5. Experimental pressures recorded versus journal rotation velocity using version 1 test rig. Results shown as mean ± SD (n=3).

Discussion

The response of the film parameter to load, as seen in figure D-4, demonstrates a reduction of the difference in the parameter between various rotation speeds with increasing load. This would tend to indicate that although the parameter is decreasing, the importance of rotation speed also decreases with increasing load. Figure D-5 highlights a similar trend where it is observed that the importance of load becomes more of an issue with increasing revolution speed. However, throughout gait, various combinations of load and revolution speed occur, and the effect of this is unclear and demands further assessment.

The lubrication regime analysis for the articulation surfaces also suggests that for the given conditions, boundary lubrication occurs. This suggests that the surfaces are in direct contact, which is of course, not a desirable event. The apparent limiting of the curves in figure D-4 is self-evident of this. One possible method of rectifying the issue is

to increase load/rotation speed combinations. However, it is not entirely likely that this will occur at conditions resembling a physiological range of motion. Similar results are to be found in prosthetic implant systems using metal against UHMWPE surfaces (Pylios and Shepherd, 2004, Scholes and Unsworth, 2000) but generally not metal on metal articulations (Jalali-Vahid et al., 2003b, Udofia and Jin, 2003, Yew et al., 2004). So the problem lies in the uses of a polymer in the system, as these materials cannot achieve the same level of smoothness as their metal counterparts. Hence, another solution to this problem is to replace the PTFE component with a stainless steel version. Entering this parameter into the calculation made for the test apparatus results in lubrication regimes in the elastohydrodynamic region. Altering the geometry of the structures also has a positive effect but to a much lesser extent. Hence, it is perhaps best to adopt both the introduction of new materials and geometry alteration for further development of the device.